UNIVERSITY OF BIRMINGHAM

Anion Substitution in Perovskite Related Materials For Fuel Cell Applications

By

Cathryn Hancock

Supervisor: Prof Peter Slater

Collaborative Supervisor: Dr John Varcoe

A thesis submitted to The University of Birmingham

for the degree of Doctor of Philosophy

The School of Chemistry

College of Engineering and Physical Sciences

The University of Birmingham

Sept 2012

ii. Abstract

The work presented in this thesis focuses on two different structures, the Ruddlesden Popper and perovskite, which have shown promise as catalysts in fuel cell devices.

The Ruddlesden Popper materials have interesting structural properties allowing the possible incorporation of anions within the interstitial sites. The possible incorporation of water and fluorine into these interstitial sites was investigated for the systems $La_2NiO_{4+\delta}$, $Nd_2NiO_{4+\delta}$, $La_2CuO_{4+\delta}$ and $Sr_3Fe_2O_{7-y}$. Successful fluorination was achieved for each system, leading to a range of new oxide fluoride phases. In the case of water incorporation, the most interesting results were observed in $La_2NiO_{4+\delta}$. For this system, large amounts of water were shown to be incorporated using an indirect method which involved fluorination of the materials followed by ion exchange. This is the first time such a method has been demonstrated.

The work on the perovskite materials ($SrCoO_3$, $SrMnO_3$, $SrFeO_3$ and $CaMnO_3$) focused on doping with various oxyanions (phosphate, silicate and sulphate). It was discovered that small amounts of oxyanion doping could be achieved, which caused a large increase in the conductivity. This increase was correlated either to a phase change on doping or in the case of the $CaMnO_3$ material due to the resultant electron doping. The phase changes were analysed by diffraction techniques which also showed evidence of thermal stability issues for oxyanion doped $SrCoO_3$. This thermal instability could be overcome by codoping with iron, albeit to the detriment of the conductivity.

Electrochemical tests were performed to determine if the materials would be of use as cathode materials in fuel cells. From preliminary tests $CaMnO_3$ was determined to have the most promise as it had the highest onset potential compared to the other materials. Further improvements in this material could be achieved through doping with Ru. *In situ* fuel cell tests were performed which produced encouraging results in terms of the power densities obtained.

iii. Acknowledgements

To begin with I would like to thank my supervisor Peter Slater for all the help and instruction that he has given me throughout the years and for taking me on in the first place. In addition he has expanded my knowledge of music and also whiskey (Although I'm not sure to thank him on that last one).

I would also like to thank past and present members of Pete's research group including Alodia, Felix, Jose, Alaric, Ben (Mr Neutron), Matt and Bastian.

Thanks also to the rest of the 5th floor chemistry group for help with equipment as well as Friday nights at the pub. A special mention to Jackie Deans our 5th floor technician for keeping the floor running.

Many thanks to my supervisor John Varcoe back at Surrey for his input to the project as well as access to the facilities. In addition thanks go to Simon Poynton for teaching me how to use the equipment.

Thanks to Kevin Knight at Isis and Vladimir Pomjakushin at SINQ for their help in the collection of Neutron data. Also thanks to Frank Berry for the performance and analysis of Mossbauer data presented here.

I'd like to thank my family for the support that they have given me throughout the years as well as my housemates Evin and Ying who fed me excellent grub and provided a brilliant atmosphere to live in for the past 2 years.

Finally thanks to the EPSRC for funding this research and Advantage West Midlands for providing funding for the equipment used in this project.

iv. Table of Contents

v. Abbreviations

AAEM	Alkaline Anion Exchange Membrane
AFC	Alkaline Fuel Cell
CGO	Cerium doped with Gadolinium
DTA	Differential Thermal Analysis
EDTA	Ethylenediaminetetraacetic Acid
GSAS	General Structure Analysis System
MCFC	Molten Carbonate Fuel Cell
NASA	National Aeronautics and Space Administration
PAFC	Phosphoric Acid Fuel Cell
PEMFC	Polymer Electrolyte Membrane Fuel Cell
PTFE	Polytetrafluoroethylene
PVDF	Poly(vinylidene Fluoride)
RDE	Rotating Disk Electrode
RRDE	Rotating Ring Disk Electrode
SOFC	Solid Oxide Fuel Cell
TGA-MS	Thermogravimetric Analysis – Mass Spectrometry
XRD	X-Ray Diffraction
YSZ	Yttria stabilised Zirconia

1. Introduction

1.1. The Need for New Energy Production

Currently most electrical energy is produced from the burning of fossil fuels as seen in Figure 1. This is leading to problems in terms of increasing greenhouse gas emissions.

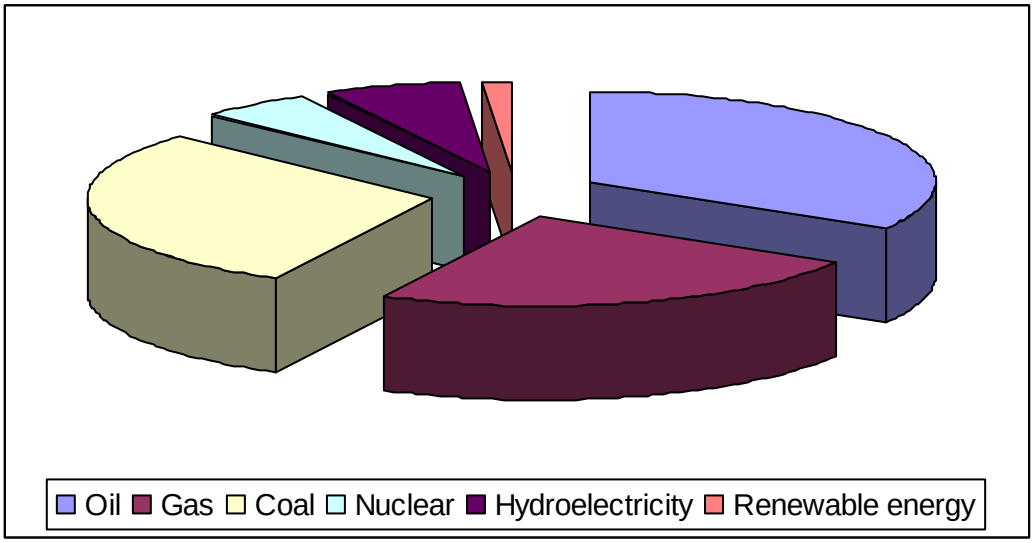

Figure 1: Worlds energy consumption by resources 2010 [1].

Moreover, as supplies of these fossil fuels dwindle and the population increases it is necessary to improve the efficiency of our energy production [2].

Table 1: Population and energy demands [3, 4].

Year	World Population (Billions)	Energy (Million tonnes of oil equivalent)
1965	3.3	3766.9
1970	3.7	4945.3
1975	4	5766.7
1980	4.5	6624.0
1985	4.85	7137.5
1990	5.3	8108.7
1995	5.7	8577.9
1999	6	9151.4
2006	6.5	11087.8
2009	6.8	11363.2

With further research there are many different types of energy technologies that could replace our reliance on fossil fuels. Examples include renewable energies such as solar and wind

farms. Such renewable sources are, however, limited by their intermittency of supply, and so there is still the need for other means of electrical energy generation such as using hydrogen in fuel cells. These fuel cells are highly efficient devices for the conversion of chemical energy into electrical energy and can be adapted to both small and large scale applications.

1.2. History of the Fuel Cell

Despite recent interest in fuel cells, they are not a new technology as they have been around for 200 years [5-7]. Research in this area can be dated back to the 1800s with work by two British scientists Sir Anthony Carlisle and William Nicholson. These two scientists discovered the inverse of the fuel cell process, the decomposition of water into its constituent parts, hydrogen and oxygen using electricity [5, 8].

By 1838 another British scientist named William Grove, who is considered to be the father of the field, created the first fuel cell [5, 6, 9, 10]. He discovered that by immersing two platinum electrodes into sulphuric acid, and with the other ends sealed in a hydrogen and oxygen atmosphere, a constant current would be produced along with a rise in the water level [5, 6, 8]. He realised that the next step of combining pairs of electrodes in series would result in a higher voltage. He called his creation a gas battery, and this was the first fuel cell.

Grove thought the process of his battery occurred at the point of contact between the electrolyte, electrode and gases, but could not explain this further [8]. The processes involved were later explained by Friedrich Wilhelm Ostwald in 1893 and this inspired further research [8].

The next main accomplishment came from Thomas Francis Bacon. In 1933 he had begun his research into alkaline fuel cells using hydrogen and oxygen as fuel and oxidant respectively [8, 9]. In 1939 he managed to produce a fuel cell using a nickel electrode at a high pressure of 200 atm which was used aboard World War II submarines [8]. This research was carried on further to produce expensive but reliable cells, which caught the attention of Pratt and Whitney in 1958. These cells were then used to power the on board electronics for the Apollo space missions [5, 6]. With funding

from Marshall Aerospace, Bacon managed to produce a 5kW fuel cell consisting of 40 cells, operating with 60% efficiency [8].

The development of polytetrafluoroethylene (PTFE) in the 1950s helped developed the aqueous electrolyte fuel cell to its current form and in 1959, a 15kW, 1008 cell system was made for use in a tractor by Harry Ihrig [8, 9]. By the 1960's different fuel cells were being developed using different electrolytes such as molten salts by E. Baur, G. H. J. Broers and J. A. A. Ketelaar, with further developments using ceramic materials by J. Weissbart and R. Ruka [6, 8, 10].

In the past 10 years there has been an increase in public awareness of fuel cells with the first fuel cell cars becoming available (Table 2). Mobile applications such as methanol fuel cells for powering of laptops and mobile phones have also been developed [8, 11]. In addition, natural gas fuelled systems (operating at elevated temperatures >500^{o}C) are also being developed for the household market as replacement for gas boilers.

Table 2: Types of fuel cell cars [8].

Manufacturer	Year	Fuel Cell	Autonomy/Speed
Daimler-Chrysler	2008	Hybrid Fuel Cell and battery	483 km-185 km/h
Fiat-Panda	2007	Nuvera	200 km-130 km/h
Ford HySeries edge	2007	Ballard	491 km-160 km/h
GM Provoq	2008	GM	483 km-160 km/h
Honda FCX Clarity	2007	Honda	570 km-160 km/h
Hyundai I-Blue	2007	Fuel Cell	600 km-165 km/h
Morgan LIFECar	2008	QinetiQ	402 km-137 km/h
Peugeot H2Origin	2008	Intelligen Energy	300 km
Renault Scenic FCV H2	2008	Nissan	240 km-161 km/h
Mitsubishi SX4-FCV	2008	GM	250 km-150 km/h
Toyota FCHV-adv	2008	Hybrid Fuel Cell and Battery	830 km-155 km/h

1.3. How Fuel Cells Work

All types of fuel cell operate in the same way. Fuel cells consist of two electrodes, an anode and cathode that have an electrolyte sandwiched between them. The fuel cell operates in the same way as a battery in that an electrochemical reaction takes place. However the difference between them is that in a fuel cell, the fuel and oxidant are supplied continuously, whereas in the battery

these are stored in limited quantities in the electrodes. Once this supply has been exhausted the battery then needs to be recharged or thrown out. In contrast for fuel cells, operation is continuous as long as the fuel and oxidant are supplied.

In order to explain how a fuel cell operates, the proton conducting polymer electrolyte membrane fuel cell will be used. The fuel, typically hydrogen gas, is supplied at the anode where the hydrogen is oxidised. The electrons pass through an external electrical circuit (producing the power for many different applications) to the cathode. Meanwhile the protons migrate through the electrolyte to the cathode. Once the electrons and protons arrive at the cathode they will combine with the oxygen to produce water. This is demonstrated in Figure 2.

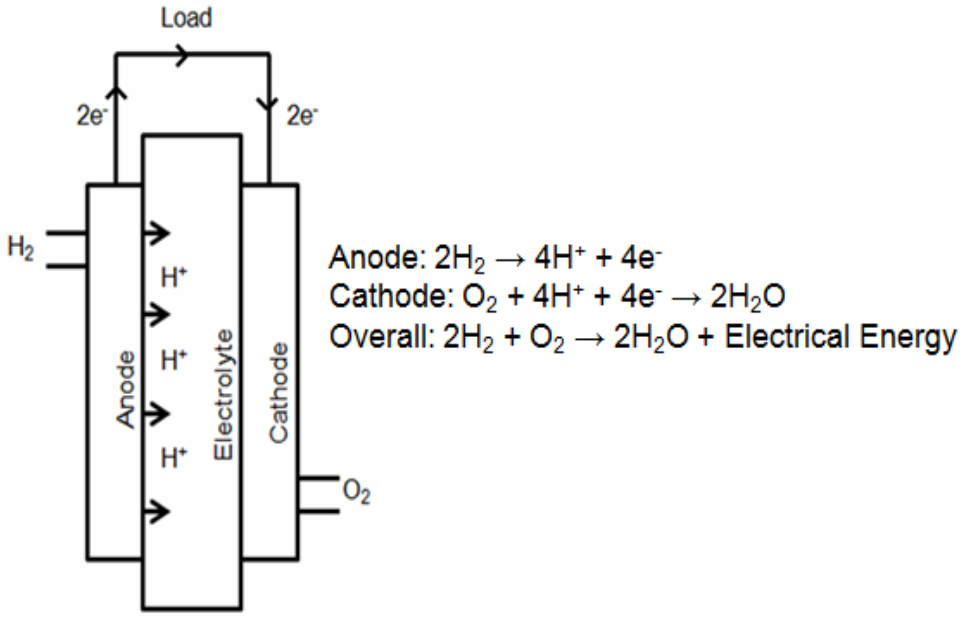

Figure 2: Diagram to show how a fuel cell operates.

1.4. Types of Fuel Cells

There are 5 main types of fuel cell. Fuel cells are classified by the type of electrolyte that they use and each type has different main applications. These 5 fuel cells can be split into high or low temperature classes, which are determined by their temperature of operation. A summary of the 5 types of fuel cell is shown in Figure 3.

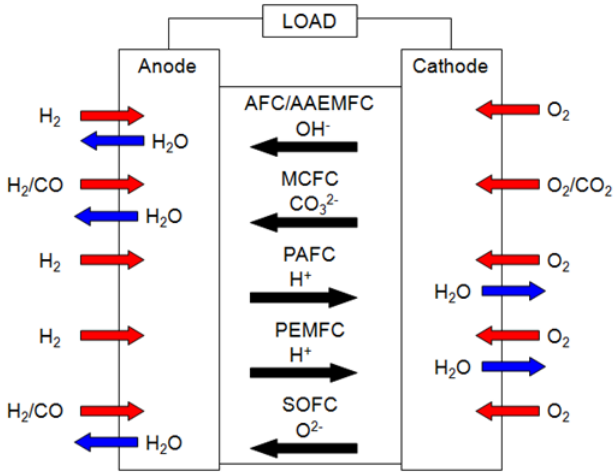

Fuel Cell	Anode	Cathode
AFC/ AAEMFC	$2H_2 + 4OH^- \rightarrow 4H_2O + 4e^-$	$O_2 + 4e^- + 2H_2O \rightarrow 4OH^-$
MCFC	$2H_2 + 2CO_3^{2-} \rightarrow 2H_2O + 2CO_2 + 4e^-$	$O_2 + 2CO_2 + 4e^- \rightarrow 2CO_3^{2-}$
PAFC	$2H_2 \rightarrow 4H^+ + 4e^-$	$O_2 + 4e^- + 4H^+ \rightarrow 2H_2O$
PEMFC	$H_2 \rightarrow 2H^+ + 2e^-$	$0.5O_2 + 2H^+ + 2e^- \rightarrow H_2O$
SOFC	$2H_2 + 2O^{2-} \rightarrow 2H_2O + 4e^-$	$O_2 + 4e^- \rightarrow 2O^{2-}$

Figure 3: Summary of the different fuel cell types.

1.4.1. Alkaline Fuel Cell (AFC)

Francis Thomas Bacon started experimenting with alkaline fuel cells in the 1930's [5]. His first working large scale fuel cell was created in the 1950s and it provided 5kW power using a nickel anode, lithiated nickel oxide cathode and 30 wt% aqueous KOH at 200^{o}C and 5MPa [7]. By the 1960's Pratt and Whitney had licensed Bacon's patents and won the National Aeronautics and Space Administration (NASA) award to power the Apollo spacecraft [5]. Other applications using AFCs included a farm tractor equipped with an Allis Chalmers AFC, and in the 1970's an Austin A40 was operated by Karl Kordesh [12]. However this success was short lived. Even though the system performed well, there was a significant problem with it being commercialised as it is very sensitive to carbon dioxide poisoning, and has since largely been superseded by the development of the PEMFC [12]. However, the AFC was used for many years by the space industry due to its' reliability, but recently NASA has focused on the PEMFC [13].

The electrolyte of this fuel cell is a potassium hydroxide solution, which has typical concentrations of 30% KOH [12]. There are four different types of AFC and some of these have mobile electrolytes [14]. Mobile electrolyte systems pump the electrolyte around the system as seen in Figure 4 [12] and [14].

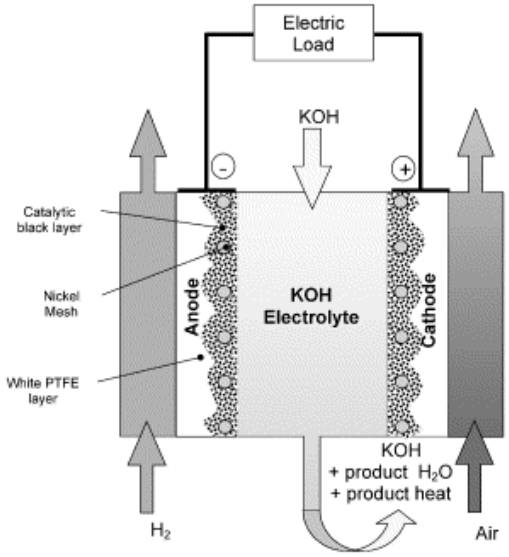

Figure 4: Schematic of the mobile electrolyte system.
According to Ref [12] Elsevier permission.

This system has advantages as the water and heat by product can be removed [12]. It also allows the electrolyte to be easily replaced. The electrolyte has to be removed and changed regularly because if carbon dioxide is introduced into the system from the air intake, it will react with the KOH to produce K_2CO_3 as seen in Equation 1 and 2 [7] and [12].

Equation 1 $CO_2 + 2OH^- \rightarrow (CO_3)^{2-} + H_2O$

Equation 2 $2KOH + CO_2 \rightarrow K_2CO_3 + H_2O$ [7], [12] and [14]

This reaction causes problems as it lowers the amount of OH^- in the electrolyte meaning the conductivity decreases [14]. In addition the carbonate is less soluble so precipitates out, which blocks the pores in the cathode and reduces the surface area, and so in turn the reaction rate decreases [14]. Scrubbers can be used to decrease the amount of carbon dioxide entering the system, but it will never remove all of it. It also means that extra equipment is needed, which will increase costs. The fact that the electrolyte is liquid based means that there are more chances of leaks, while the concentrated KOH electrolyte is also corrosive [14].

The second type adopt a static electrolyte (Figure 5), where the electrolyte is held in a matrix, usually asbestos, which gives it excellent porosity, strength and corrosion resistance. However there are safety issues due to the use of asbestos, and also high cost factors, due to the

need to use pure oxygen, as it is very difficult to remove the electrolyte if it reacts with the carbon dioxide. The water is removed by circulating hydrogen through the electrolyte, but there are still problems with managing the water levels [14].

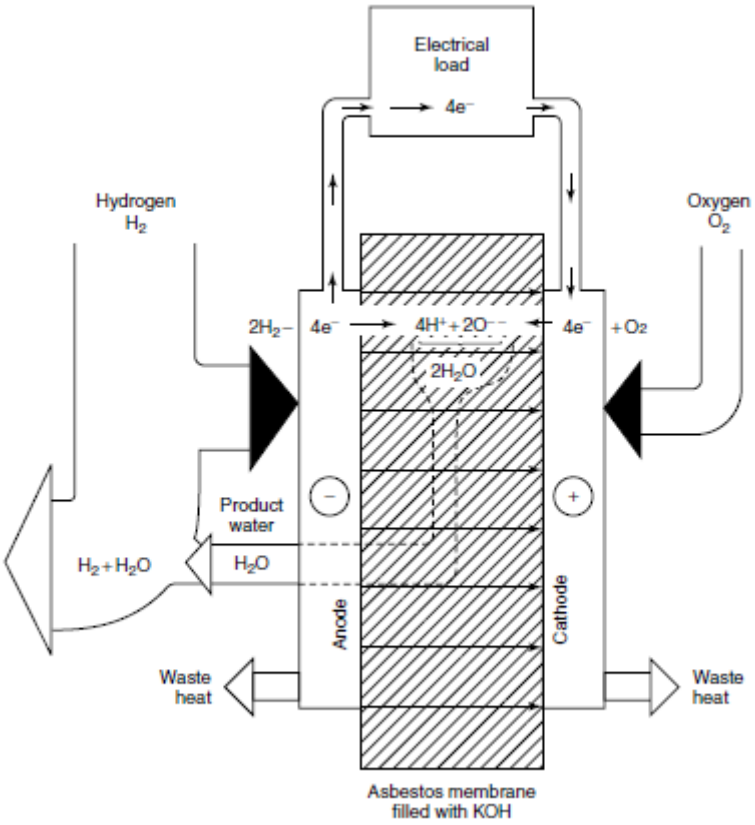

Figure 5: Schematic of an alkaline fuel cell with a static electrolyte [15].

The third type of liquid electrolyte AFC, that uses KOH, is the dissolved fuel alkaline fuel cell (Figure 6). It is one of the easiest to manufacture as there is only one seal between the air cathode and the electrolyte, and the electrolyte is very easy to refill. However the fuel used is similar to hydrazine, and since these compounds can be toxic and explosive, this type of fuel cell is not used for high power generation, but only for demonstrations [14].

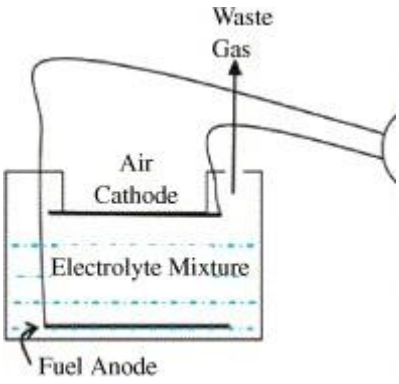

Figure 6: Schematic of a dissolved fuel alkaline fuel cell.
According to Ref [16] Elsevier permission.

The final type of AFC which has recently generated a lot of research is the alkaline anion exchange membrane fuel cell which is analogous to the PEMFC, but with an alkaline rather than acidic polymer electrolyte. The membrane contains positive ionic groups, typically with a quaternary ammonium functional groups, for example poly-$N^{+}Me_3$, with mobile negatively charged hydroxide ions. A membrane which has shown promising results is Surrey University's benzyltrimethyl ammonium containing S80, S50 and S20 radiation grafted AAEM's (Figure 7) which have thermochemical stability up to 80^{o}C, and conductivities that reach 0.06Scm^{-1} at 60^{o}C when fully hydrated (comparable with proton conducting polymers).

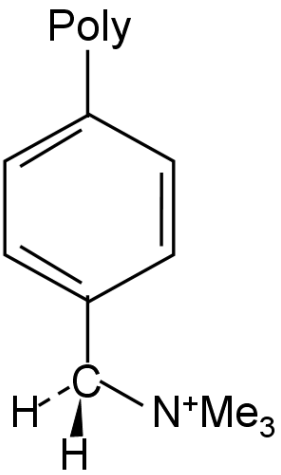

Figure 7: Chemical structure of the Benzyltrimethylammonium.

For AFC's there are many different materials that have been used in the electrodes to get desirable results. At first nickel electrodes were used, and now other metals like copper and platinum have been impregnated into the electrode [7] and [12]. Alloys with platinum have also been investigated and given good results with only small loadings of the platinum (less than $0.3mgcm^{-2}$) [7]. In determining the best material a number of factors need to be considered, particularly the balance between price and performance [17]. There are no standard materials but the most common electrodes are rolled electrodes [14], which are carbon supported catalysts mixed with PTFE and rolled onto a material such as nickel mesh [14].

As already mentioned, the AFC traditionally has been shown to have some disadvantages in that it needs pure oxygen and hydrogen to prevent carbon dioxide poisoning, the electrolyte has to be replenished, and the water has to be removed from the anode [18]. However, with the introduction of polymer electrolytes many of these problems are negated. For example, this negates the use of KOH which means that there is no need to replace the electrolyte as it will not be affected by the carbon dioxide poisoning. This also has the benefit of making the fuel cell entirely solid state meaning that there are no leakages. There are also many advantages to the use of AFCs, due to the fact that the electrodes and electrolyte are generally inexpensive in that they may contain non Pt group metal catalysts for both the anode (e.g. Ni) and cathode (e.g. Ag) [19, 20]. This can be related to the fact that the catalytic processes are more favourable under alkaline conditions (compared to acidic) especially for the oxygen reduction reaction at the cathode [18]. Finally AAEMFCs (Alkaline Anion Exchange Membrane Fuel Cell) are much more tolerant to "dirty H_2". For example, when H_2 is reformed from ammonia it generally contains traces of NH_3 which can poison the PEM compared to the tolerant alkaline membrane [21].

There are many applications that AFC's can be used for. Mostly they are used in low temperature applications with the majority being in the portable and transport area, as stated before.

1.4.2. Polymer Electrolyte Membrane Fuel Cell (PEMFC)

The polymer electrolyte membrane fuel cell was developed in the 1960's by General Electric in the USA for use by NASA in a manned space vehicle, Gemini [2, 17]. The Gemini spacecraft used a 1kW fuel cell stack as an auxiliary power source and it also provided clean drinking water for the astronauts [7]. Unfortunately there were problems with the water management in the electrolyte, a polystyrene sulfonate polymer; which caused NASA to change to alkaline fuel cells instead [2, 7].

In the 1980s and 1990s there were significant advances in PEMFCs by two companies Ballad Power Systems of Vancouver, Canada and Los Alamos National Laboratory in the USA [17]. Today current densities of 850A/ft^2 are achieved at 0.7V per cell with the hydrogen and oxygen at 65psi, while over 500A/ft^2 is obtained using air at the same pressure [17] compared to the 74A/ft^2 at a cell voltage of 0.65V that was produced on the Gemini space craft [22].

The electrolyte used is a solid polymer membrane. The membrane most commonly used is a fluorinated sulfonic acid polymer, called Nafion® which is produced by DuPont; it has a fluorocarbon backbone with sulfonic acid groups attached see Figure 8 [2].

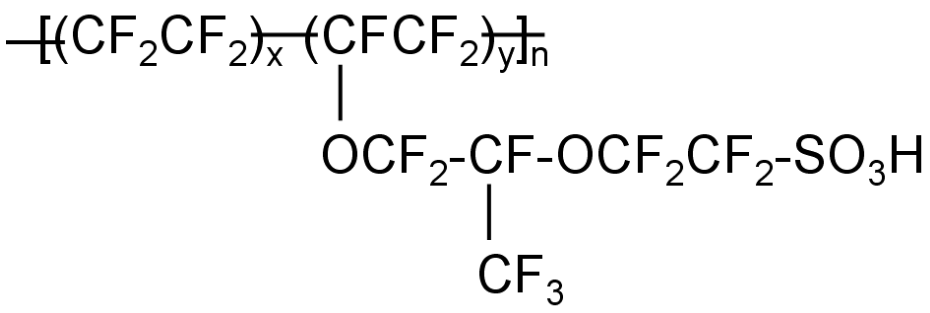

Figure 8: Chemical formula of Nafion® [23].

This ion exchange membrane is an excellent conductor of protons and is an electronic insulator [2]. The acid groups are firmly attached to the polymer but the protons from these groups are free to move through the membrane, provided the membrane is suitably hydrated, which is why it is a good proton conductor [2]. There are other membranes that have been developed by DOW, Aciplex, Gore and Asahi Chemical, but Nafion® is still the most widely used [7].

These membranes are usually saturated with water to keep the conductivity high, as conduction is mainly via H_3O^+. It is a problem to keep the membrane properly hydrated as when each proton is dragged through the membrane it brings with it some water molecules, which dries out the anode and over saturates the cathode [7]. This sensitivity of water management means that the temperature cannot go over 60^{o}C, as otherwise it will cause the electrolyte to dry out. One way of improving the water management is to humidify the gases going into the cell [7].

Both of the electrodes have to be porous to ensure that the reactant gases get to the active zone, which is the three phase boundary between the gas, catalyst and the electrolyte. The best materials for the reaction at the cathode are platinum based catalysts dispersed on carbon [7]. As these catalysts are expensive, other less expensive catalysts have been researched, although Pt remains the dominant material commercially.

The anode also uses platinum based catalysts, but because of potential poisoning from impure hydrogen it cannot use pure platinum. This means usually an alloy of platinum and ruthenium is used, the latter will help to oxidise any carbon monoxide contaminant in the fuel gas at lower temperatures. A way to prevent using alloys and have just platinum is to have a gas clean up system which can be built in-between the fuel supply and the fuel cell [7].

From research into the alloying of platinum and further developments with the Nafion® conducting membrane, the power density has been gradually improved while the loading of platinum has been decreased. In addition by optimising the catalyst and electrode structure the platinum loadings were further decreased from 28mg/cm^2 to 0.2mg/cm^2, while maintaining current densities in excess of 1A/cm^2 at 0.7V [17].

As mentioned, the cost of the platinum is a disadvantage, as well as the poisoning of this catalyst by impurities in the fuel, but progress in mitigating these problems has been made by using the alloyed materials. Water management is also a problem due to the conductivity loss which was explained earlier [18]. There are however many advantages to this type of fuel cell as it has the

highest power density of all fuel cell types, it has good start-stop capabilities and it is a good portable device due to the low temperature operation [18].

The applications are primarily suited for residential/commercial (business) and transport applications [2]. In 1993, the first fuel cell powered bus was demonstrated and since then others have been made which have the same capabilities as a normal bus [17]. Such buses have undergone detailed trials in many cities worldwide.

1.4.3. Solid Oxide Fuel Cell (SOFC)

E. Baur and H. Preis were the first to experiment with solid oxide electrolytes in the 1930s. They experimented with zirconium, yttrium, cerium, lanthanum and tungsten oxide. The first operation of their fuel cell at 1000^{o}C was achieved in 1937 [6]. Unfortunately unwanted chemical reactions occurred between the components [5]. This, however, did not stop progress on solid oxide fuel cells, as in the 1950s research was accelerated at the Central Technical Institute in the Hague, Netherlands [6].

The first commercial demonstration model was operated in the Netherlands in 1998. The demonstration finished in 2000 but in this time 16,612 hours had been accumulated by the 100kW unit built by Siemens Westinghouse [17]. Subsequently a new demonstration fuel cell was built by Siemens Westinghouse. In a year of operation the 220kW SOFC, which ran on natural gas, achieved an efficiency of 60% [6].

The electrolyte of this fuel cell is solid, specifically a hard non porous ceramic compound. Due to the high temperatures (500-1000^{o}C) used in SOFCs, many ceramics are conductive enough to give good overall cell performance. There are three main structure types examined for use as SOFC electrolytes, which include the fluorite, perovskite and more recently the apatite structures (Figure 9).

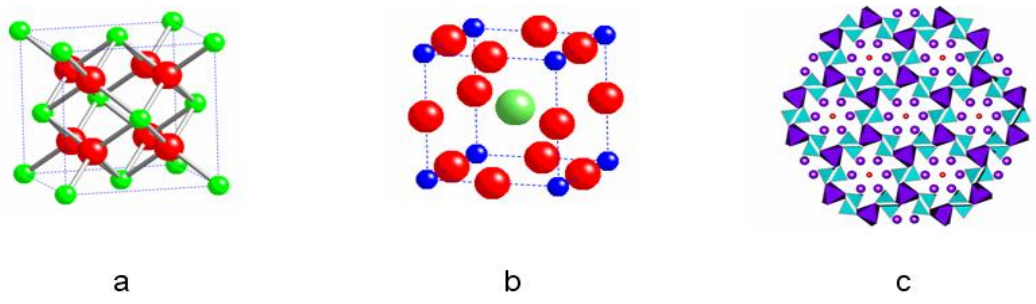

Figure 9: Structures of different electrolytes for solid oxide fuel cell (a=fluorite, b=perovskite and c=apatite).

The most commonly used is the fluorite system with the ionic conductivity due to oxide ions. One of the most favoured materials is yttria stabilised zirconia (Y_2O_3 – stabilised ZrO_2, YSZ) [6]. In ZrO_2 there are 2 oxide ions to every zirconium ion but in Y_2O_3 there are 1.5 oxide ions to each yttrium ion. This means that the introduction of Y in place of Zr leads to vacancies in the structure. These vacancies allow the conduction of oxide ions from the cathode to the anode in the fuel cell system, while the dopant also stabilises the cubic lattice, which further improves conductivity over undoped ZrO_2 [6]. There are other stabilising dopants which can be used which include CaO, MgO, Y_2O_3, Sc_2O_3, Nd_2O_3, Sm_2O_3 and Yb_2O_3 [6]. Other popular fluorite materials include CeO_2 based systems, e.g. $(Ce_{0.85}Sm_{0.15})O_{1.925}$, $(Ce_{0.9}Gd_{0.1})O_{1.95}$, $(Ce_{0.85}Y_{0.15})O_{1.925}$ and $(Ce_{0.88}Ca_{0.12})O_{1.88}$. To a large extent CeO_2 based systems are replacing ZrO_2 as the favoured fluorite electrolyte, due to the higher conductivity of the former. Perovskite materials have also proved popular including $La_{1-x}Sr_xGa_{1-y}Mg_yO_{3-x/2-y/2}$ and $Ba(Ce_{0.95}Yb_{0.05})O_{2.975,}$ and newer systems such as apatite materials have attracted attention. The latter are typically doped lanthanum silicates/germanates, such as $La_{9.8}(SiO_4)_{5.7}(MgO_4)_{0.3}O_{2.4}$, $La_{9.5}(GeO_4)_{5.5}(AlO_4)_{0.5}O_2$ and $La_{10}(SiO_4)_5(GaO_4)O_{2.5}$ [6, 24-28].

SOFC anodes are usually Ni electrolyte cermets. Generally an anode material of NiO/YSZ is used with an electrolyte of YSZ, whereas NiO/SDC (SDC-Cerium oxide doped with samarium) and NiO/GDC (GDC-Cerium oxide doped with gadolinium) anode materials are used with ceria based electrolytes [6]. On exposure to the fuel at the SOFC operating temperature (>500^{o}C), the NiO reduces to Ni metal which provides the required electron conductivity and catalytic performance.

The cathode has to be stable at high temperatures in oxidising atmospheres, so only noble metals or electronically conducting oxides can be used. Perovskites have mainly been investigated in this respect. Lanthanum strontium manganites $La_{1-x}Sr_xMnO_3$ (LSM) and lanthanum calcium manganites $La_{1-x}Ca_xMnO_3$ (LCM) give good thermal expansion match to the electrolyte, and have a good performance at high temperatures [6], although at temperatures below 700^{o}C their performance drops significantly. Consequently for the lower (500-700^{o}C) region, alternative Fe and Co based perovskites have been investigated.

There have been many different SOFC designs to allow the successful production of fuel cell stacks. These different SOFC designs can be split into 2 different types: the supported and the self supported. The supported design uses a substrate to provide the cell with mechanical stability, whereas the self supported design uses one of the electrodes as a support structure for the other components in the cell [7].

One design type is the tubular design (Figure 10) developed by Siemens-Westinghouse. The advantage of the tubular design is that it has a self sealing structure which improves the thermal stability and also means that good sealants are not necessary. Tubular SOFCs can be supported or self supported and the gas flow can be either parallel or perpendicular to the axis of the tube [6, 7].

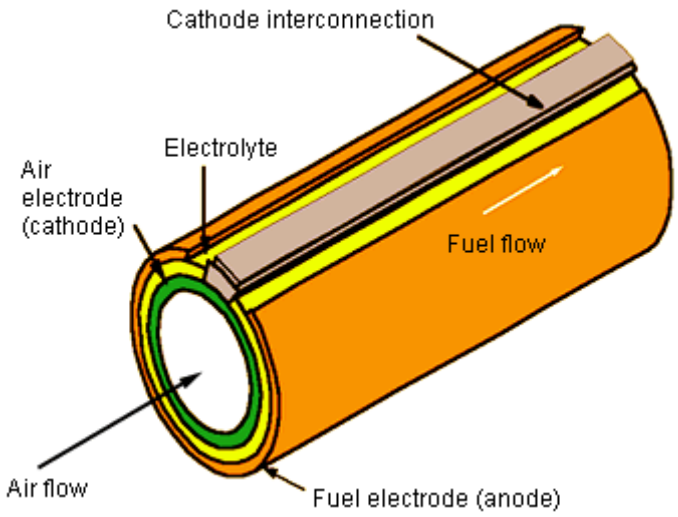

Figure 10: A self supported tubular SOFC design with parallel gas flow [29].

The planar design (Figure 11) is however more efficient and cheaper to produce than the tubular design, as its current path is shorter (leads to lower I R loss) and it is easier to stack. However finding good sealants for such cells is a problem. This design is, however, being developed by a number of companies.

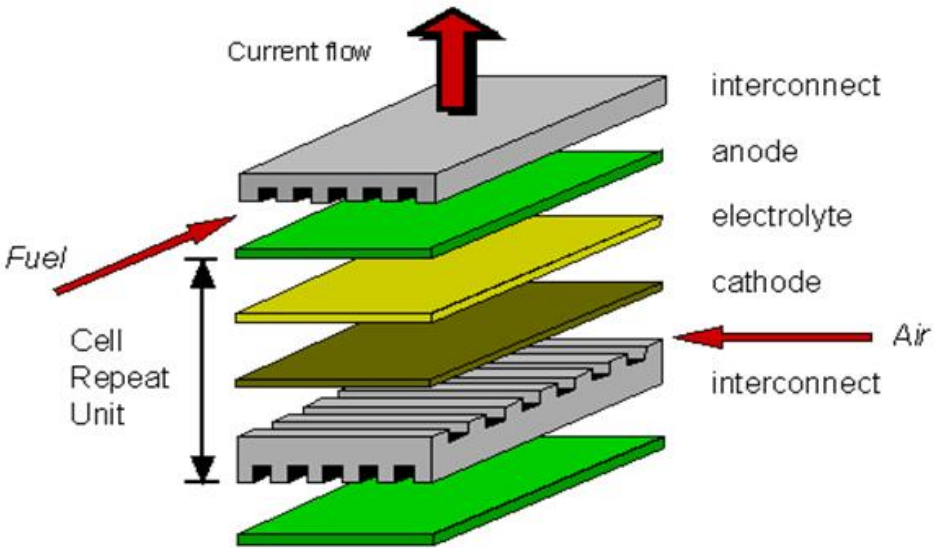

Figure 11: SOFC planar design [30].

A design which combines the advantages of the previous two designs is the long monolithic planar cell (see Figure 12). The cathode and the interconnection material are shaped into a long planar structure with the electrolyte sprayed on, covering the cathode completely, and finally the anode is placed onto the electrolyte film. This gives it a short current path and makes it easier to stack [7].

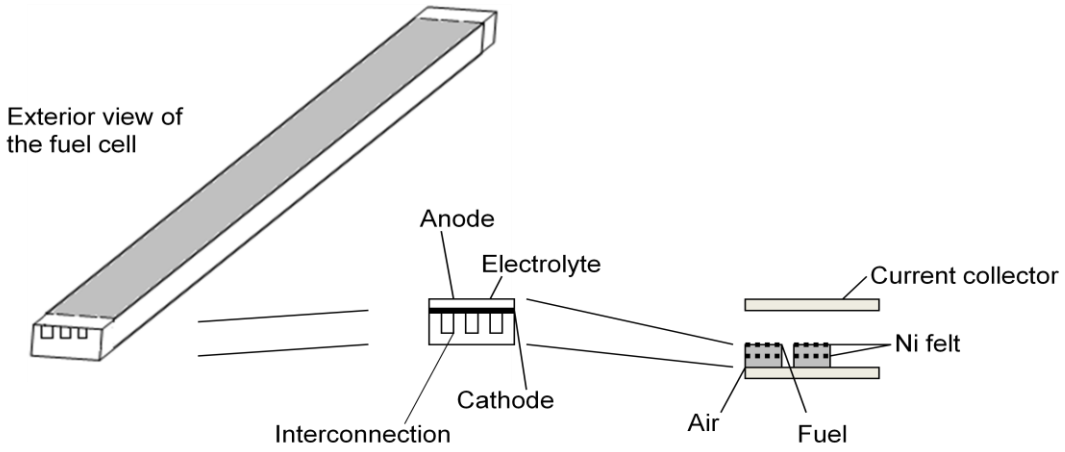

Figure 12: SOFC long monolithic planar cell.
According to Ref [7] Elsevier permission.

There are many advantages and disadvantages of SOFCs. Carbon monoxide and carbon dioxide are not a problem allowing greater fuel flexibility (H_2 or hydrocarbon fuels, e.g. natural gas) in operation. In addition there is no need for expensive catalysts due to the high temperature operation. The main problem is the high temperatures of around 600^{o}C to 1000^{o}C, which causes problems due to materials degradation, cell sealing and the need for good insulation.

There are many applications that SOFCs are used for, e.g. generators for large scale power plants, or smaller scale power plants, or emergency power generators [6]. They are also being developed for transport applications, specifically auxiliary truck power units to provide electric power for on road use, and heating and cooling when the truck has stopped [17]. The main commercial target at present though is the housing market, as combined heat and power systems to replace gas boilers.

1.4.4. Molten Carbonate Fuel Cell (MCFC)

Molten carbonates were used as electrolytes in fuel cells since the mid 20th century [7]. By the 1960s two scientists named G. H. J. Broers and J. A. A. Ketelaar reported to have made a molten carbonate fuel cell which ran for 6 months. At the same time Francis Bacon was also working on developing his molten carbonate fuel cell [5].

Molten carbonate fuel cells have come a long way since then, with the largest demonstration model in Santa Clara. A 2MW unit was run on natural gas from 1996 to 1997; it achieved a maximum output of 1.93MW with an efficiency of 43.6%, and was connected to the grid for 4100 hours [17]. This efficiency can be significantly increased if the waste heat produced by the cell is used for other power generation. In this way the efficiency could be increased to 85% [2]. This fuel cell plant was built by the Energy Research Corporation, and they are now building smaller units of 250kW [17].

Many different fuels can be used for the MCFC, which include hydrogen, carbon monoxide, natural gas, propane, landfill gas, marine diesel and simulated coal gasification products [5].

The electrolyte is a very important component in the MCFC; it provides the ionic transport of the CO_3^{2-}, and it also separates the reactant gas and gives it a perimeter seal formation [31]. In the past the electrolyte was a Li_2CO_3/K_2CO_3 mix. This, however, was too corrosive, as most of the fuel cell components degraded in this melt. The mix, that was used as a replacement, was a Li_2CO_3/Na_2CO_3 melt, which is slightly more alkaline making the dissolution of the anode and the cathode lower [7]. The electrolyte is suspended in an inert matrix, most commonly γ-$LiAlO_2$ [2, 7, 31].

The standard operating temperature of a MCFC is around 600-700^{o}C. It is optimal to work at the higher temperature end, as even a small change of temperature from 650^{o}C to 600^{o}C can cause the cell voltage to drop 15%, due to increased ionic and electrical resistance and a reduction in electrode kinetics [2]. Due to the high temperatures that are needed for this fuel cell, the selection of materials for the fuel cell is important. Important things to consider are the degradation, sealing and thermal expansion. Nickel, cobalt and iron based alloys or chromium/aluminium alloys have been proven to be most stable for the electrodes [7].

Due to the high temperature that occurs within the fuel cell, expensive platinum based metals are not needed, since cheaper non precious metal catalysts have good catalytic activity at these temperatures. The cathode is usually made from NiO [2, 7, 31]. There is a problem with using NiO as its particles grow over time leaching into the electrolyte which may cause short circuiting of

the cell resulting in a fuel loss and also a decrease in the active surface area [7, 31]. To solve this problem small amounts of magnesium can be added to the cathode and the electrolyte to increase stability [7]. The electrolyte matrix could be changed which could decrease the problem or the cathode material could be changed [7]. Alternatives have been found in doped lithium transition metal oxide materials like $LiFeO_2$, $LiMnO_2$ and $LiCoO_2$ and they can also be combined with NiO to form double layered electrodes [7, 31].

Anodes are also made out of nickel but are alloyed with either Al or Cr to stop the Ni leaching out, as it does in the cathode. This combination of the ceramic and the metal helps to avoid the sintering, pore growth and shrinkage of the Ni metal [7]. There is a disadvantage as these materials are expensive to fabricate so a lower cost process is required [7].

As in other fuel cells there are many advantages and disadvantages to this specific fuel cell. The main advantages include the fact that many different fuels can be used, the waste heat can be used for cogeneration applications, and finally that expensive platinum catalysts are not needed [18]. However there are disadvantages which include the corrosiveness of the molten electrolyte, degradation and lifetime issues because of the corrosive materials, the relatively expensive materials (such as the current collectors made from nickel clad on stainless steel) to combat the high temperature of the fuel cell, and finally carbon dioxide recycling has to be implemented from the anode to the cathode [18].

The best application of this type of fuel cell is for stationary continuous use [18], but in the mid 1990's the US Army Mobility Equipment Research and Development Centre tested some MCFC to use in their mobile applications [5]. In general, however MCFCs have been superseded by SOFCs as the favoured high temperature fuel cell.

1.4.5. Phosphoric Acid Fuel Cell (PAFC)

Acid electrolytes have been used for years in fuel cells. Grove himself used sulphuric acid (H_2SO_4) for his "Gas Battery" in 1842. Originally phosphoric acid electrolytes, which are used in fuel cells today, were not that attractive due to the phosphoric acid (H_3PO_4) not being as good a

conductor of electricity as other acids [5]. Now, however, the PAFC is the most widely used liquid acid electrolyte fuel cell and one of the few types of fuel cells that is commercially available [5, 32].

Since the 1970's more than 500 PAFC power plants have been installed around the world. Some of the most important developers include UTC fuel cells, Toshiba and Fuji Electric. One of the largest to be built is a 11MW PAFC power plant for Tokyo Electric Power Co in Japan, which was operated for more than 230, 000 hours for a 6 year period between 1991 and 1997 [17, 32]. The typical efficiencies of these types of fuel cells are around 40% although the efficiency increases to over 70% in combined heat and power applications [5, 18, 32].

The electrolyte used, as already mentioned, is H_3PO_4. The H_3PO_4 is contained in a Teflon bonded silicon carbide matrix to make sure that the reactant gas crossover is minimised, as well as to keep the electrolyte in place, and also provide its mechanical strength [2, 18]. In the past the electrolyte was not pure because otherwise material corrosion would occur, but now due to developments in material synthesis 100% H_3PO_4 can be used [32]. Due to pure H_3PO_4 being used, the temperature of the fuel cell must be above 42^{o}C as otherwise the H_3PO_4 would solidify, while going above 210^{o}C results in an unfavourable phase transition which renders it useless [18]; this means the ideal operating temperature is between 180-210^{o}C [2].

Both the anode and the cathode are platinum based catalysts dispersed on a carbon based support [7]. The cathode has a higher loading of around 0.5mg cm^{-2} compared with the anode which is around 0.1mg cm^{-2} [33]. A hydrophobic backing layer of polytetrafluoroethylene (PTFE) is used to prevent flooding of the electrodes, while ensuring the best degree of gas diffusion [7, 32].

PAFCs have their advantages and disadvantages, as with the other types of fuel cell. The electrolyte is cheap, which is an advantage, but the disadvantage is that the platinum electrodes are expensive. The other advantages of PAFC's include the simple construction, the thermal, chemical and electrochemical stability, low electrolyte volatility [7], reliability and the fact that it is a mature technology [18]. The disadvantages include the corrosive electrolyte and the susceptibility of the Pt catalysts to carbon monoxide poisoning [18].

The applications of this fuel cell are for premium reliable power applications, (e.g. backup power systems) which include banks and hospitals and computing. Most of the PAFC plants are between 50 to 200kW systems [18].

1.5. Materials for Use as Electrode Catalysts in Fuel Cells

1.5.1. Platinum

Platinum so far is the best catalyst for use in low temperature fuel cells. Unfortunately due to the expense of this material it is highly desirable to find a cheaper replacement.

Generally the platinum catalyst is formed of small particles on a surface of a larger substrate, typically a carbon powder which acts as a support. This means that the platinum is highly divided and spread out so there is a high surface area in contact with the reactant. This allows a lower catalyst loading which helps to reduce costs; for example from 28mg/cm^2, when the fuel cells were first being developed, to 0.2mg/cm^2 in the more recent fuel cells [34].

Apart from the control of the particle size, there are other methods to improve the performance of platinum, for example reports have indicated that by tuning the particle shape to hexagonal, there is an enhanced activity for the oxygen reduction reaction [34].

Another method that can be used is alloying the platinum with other elements. This is necessary for the anode electrode, as if carbon monoxide enters the cell it will absorb to the platinum which blocks the sites and reduces the efficiency of the fuel cell. One of the most used elements to combat this problem is ruthenium, and while it improves the efficiency it is also an expensive material [34].

1.5.2. Perovskites

The perovskite structure, named after the Russian mineralogist Lev Aleksevich von Perovski, who discovered $CaTiO_3$, is frequently adopted by materials with the general formula ABO_3.

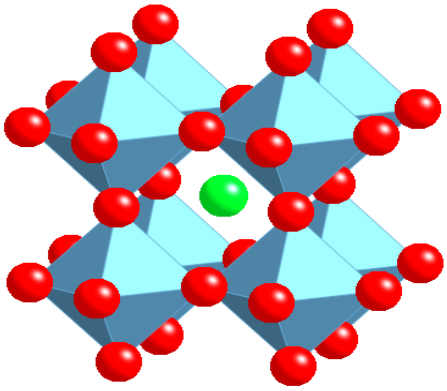

Figure 13: Cubic perovskite structure (Green = A, Blue octahedral = B and Red = Oxygen).

In an ideal cubic perovskite (Figure 13) the larger A cation is co-ordinated to 12 anions and located in the body centre of the unit cell. The smaller B cations are located at the corner of the unit cell and are octahedrally co-ordinated to 6 anions. The oxygen anions are found halfway along the unit cell edges.

To determine whether the perovskite structure is feasible for a particular compound the Goldschmidt tolerance factor (t) can be calculated from the ionic radii (R) of the A, B and O ions as seen in Equation 3 [33, 35-37].

Equation 3 _____

This tolerance factor allows a prediction of the relevant strain within the structure and the consequent symmetry of the system. For a perfect cubic perovskite, the tolerance factor should be close to 1. If the B ion is too large the tolerance factor will decrease resulting in strain relief by in tilting of the octahedron and hence an orthorhombic cell is typically observed where t is in the range $0.8<t<0.9$. However if the size of the B ions are smaller than the A ions it results in a higher tolerance factor $t>1.0$ which, typically gives rise to a hexagonal structure containing face sharing of the octahedra rather than corner sharing as for the ideal perovskite [33, 35-38]. For very low tolerance factors the perovskite structure will not form.

Many perovskites can alter their symmetry when heated. An example of this is $SrCoO_3$ which can exist as three different structures (orthorhombic, hexagonal and cubic) depending on the

temperature (Figure 14) [39, 40]. The origin of these changes, particularly at the high temperature region, is loss of oxygen leading to partial reduction of Co^{4+} to Co^{3+} and a consequent change in B cation site size and hence tolerance factor. The orthorhombic phase is metastable and cannot be obtained by slow cooling but only by quenching the high temperature cubic phase from 1200°C in liquid nitrogen. This brownmillerite-type structure (a perovskite type material with alternating layers of octahedra and tetrahedra due to ordered oxygen defects resulting in a general formula of $A_2B_2O_5$) is stabilised by high spin Co^{3+}. Once heated there is an intake of oxygen and oxidation of Co^{3+} to Co^{4+} to produce the hexagonal phase [39].

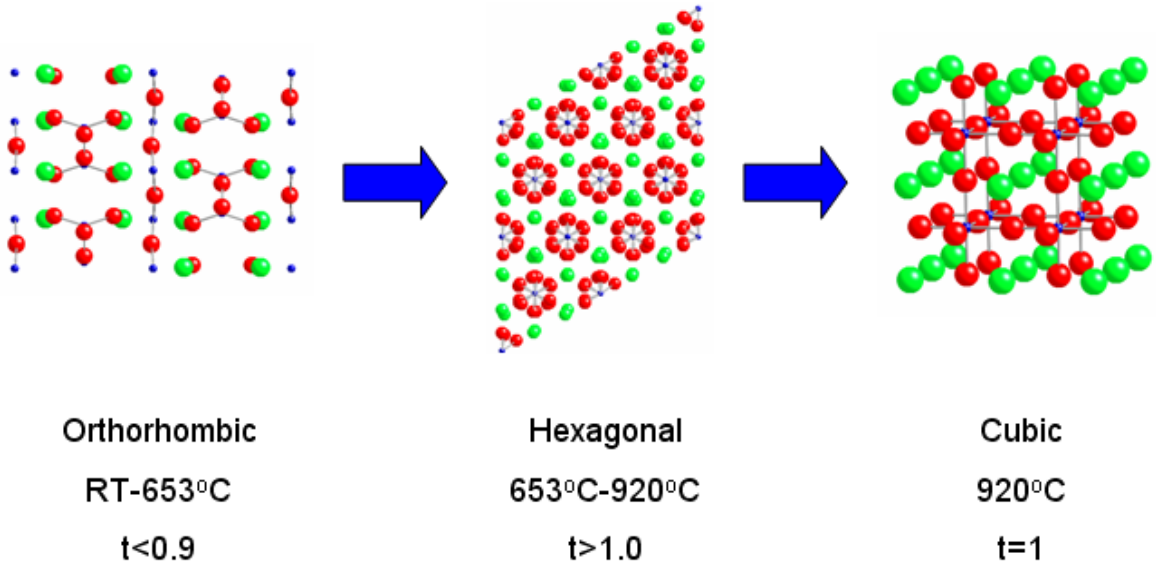

Figure 14: Different structures of perovskite based $SrCoO_3$ at different temperatures.

Perovskites are promising materials for use as solid oxide fuel cell cathodes due to their many advantageous properties. The most relevant of these are their generally high electronic conductivities and catalytic activity towards oxygen reduction [41-45]. One feature that makes perovskites so attractive to researchers is their ability to accommodate a wide variety of cations, which gives a wide range of doping possibilities, which can be explored to optimise the properties.

Perovskites used in solid oxide fuel cells include the lanthanum strontium manganates $(La,Sr)MnO_{3-x}$ (LSM), lanthanum strontium ferrates $(La,Sr)FeO_{3-x}$ (LSF) and lanthanum strontium

cobalt iron oxides (La,Sr)(Co,Fe)O_{3-x} (LSCF) and other Co, Fe and Mn containing systems [17, 41, 42, 46-48]. While most of the research on perovskite systems has focused on cathode applications in SOFCs, there is growing interest in perovskite systems for SOFC anodes for example $La_{0.75}Sr_{0.25}Cr_{0.5}Mn_{0.5}O_3$ [49], $Sr_{1-x}(Y,La)_xTiO_3$ [50, 51], $La_{0.3}Sr_{0.7}Sc_{0.1}Ti_{0.9}O_3$ [52, 53], $La_4Sr_8Ti_{11}Mn_{0.5}Ga_{0.5}O_{37.5}$ [54] and $BaZr_{0.1}Ce_{0.7}Y_{0.1}Yb_{0.1}O_{3-\delta}$ [55, 56]. In addition there has been growing interest in the potential to use perovskite systems in low temperature fuel cells. In particular the improved catalytic activity in alkaline conditions over acidic has promoted interest in their potential application in alkaline fuel cells. In this respect promising preliminary results have been reported for $La_{0.5}Sr_{0.5}CoO_3$, $La_{0.99}Sr_{0.01}NiO_3$ [57], $La_{1-x}A_xCoO_3$ (A=Ca,Sr) [58], $Ca_{0.9}La_{0.3}MnO_3$ [59] and $Pr_{0.6}Ca_{0.4}MnO_3$ and $La_{0.6}Ca_{0.4}CoO_3$ [60, 61].

1.5.3. Ruddlesden Popper Phases

Ruddlesden and Popper were the first to investigate the series of titanates of general formula $Sr_{n+1}Ti_nO_{3n+1}$ [62, 63]. A range of other systems can be prepared with similar structures and this led to the series of compounds with the general formula $A_{n+1}M_nO_{3n+1}$ being known as the Ruddlesden Popper phases. Generally the A cation is either an alkaline earth or rare earth metal ion with B a transition metal. The structure is made of n consecutive perovskite layers $(AMO_3)_n$ alternating with rock salt layers (AO) along the c direction. This formula can be represented as $(AO)(AMO_3)_n$ with n representing the number of connected MO_6 octahedra layers (Figure 15) [33, 64]. The value of n can be increased from 1, which corresponds to the K_2NiF_4 structure, all the way to n=∞ which represents the perovskite structure (Figure 15) [37, 65, 66]. Since the perovskite structure is so stable, the higher the value of n (especially above 3), the more the phase becomes thermodynamically unstable with respect to phase separation to lower order Ruddlesden Popper phases and the perovskite.

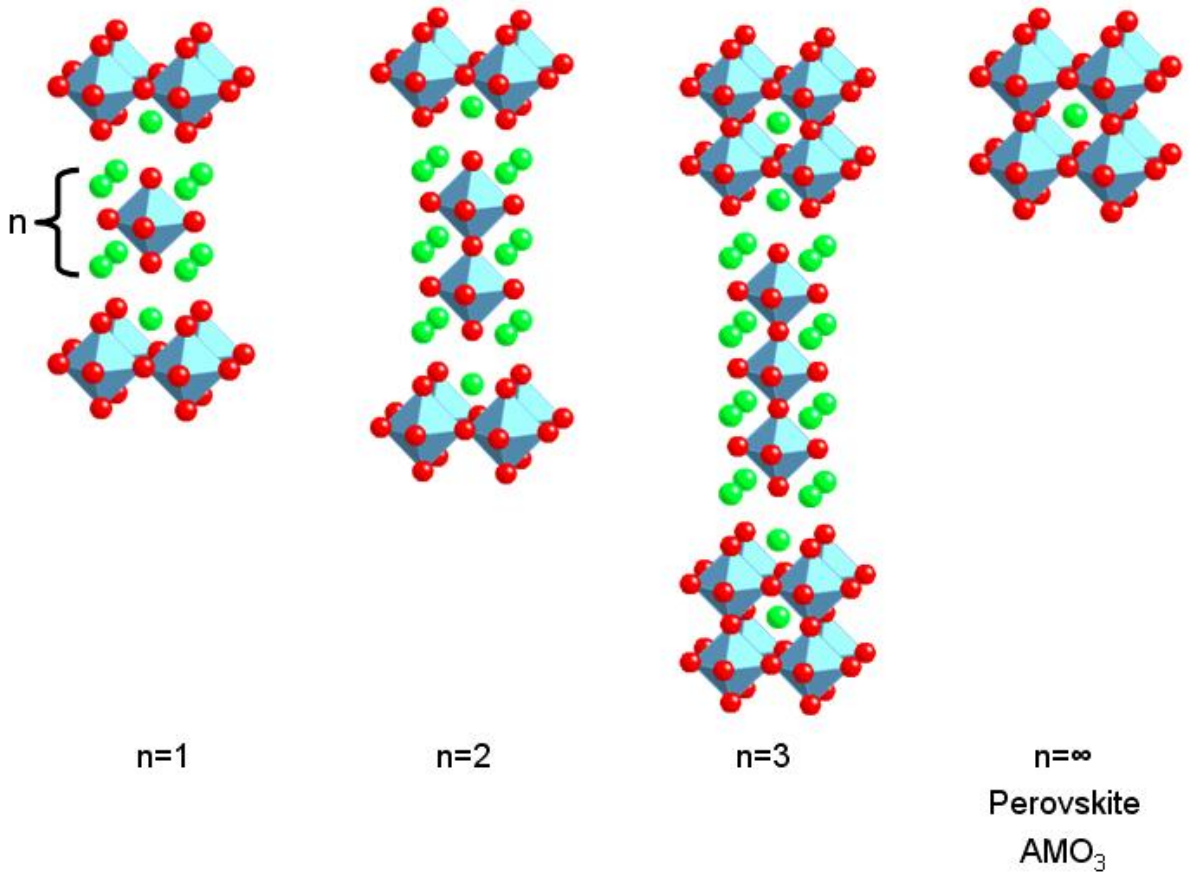

Figure 15: Illustration of the structures of the Ruddlesden Popper phases $A_{n+1}M_nO_{3n+1}$ where n=1 represents the K_2NiF_4 structure and n=∞ the perovskite (Green = A, Blue octahedra = M and Red = O).

These materials can potential show many different interesting properties. The physical properties include superconductivity and ionic/electronic conduction. These physical properties are dependent on the size, n, of the perovskite layer, the nature of the A ion, the M-O bond distance, the M-O-M bond angle, as well as the oxygen content [66].

A feature of great interest within these materials is that they have an open structural framework, because of the rock salt layers, which can allow the incorporation of interstitial anions (Figure 16) [65, 67]. This has a profound effect on the structural and physical properties of the system. The most notable of these properties are the electronic properties, which include superconductivity which can be achieved after the insertion of fluorine ions into the oxygen deficient K_2NiF_4 system Sr_2CuO_3 to give $Sr_2CuO_2F_{2+\delta}$, and also with incorporation of extra oxygen in La_2CuO_4 to give $La_2CuO_{4+\delta}$ [64, 68]. In addition to gaining interesting electronic properties, the introduction of

interstitial anions offers interesting ionic conducting properties. The fast oxygen ion conductivity in oxygen excess $La_2NiO_{4+\delta}$ has resulted in these nickelates being considered for high temperature SOFC cathodes. Many other properties have been displayed in systems with this structure type, including colossal magnetoresistance and a range of interesting magnetic properties [69-72].

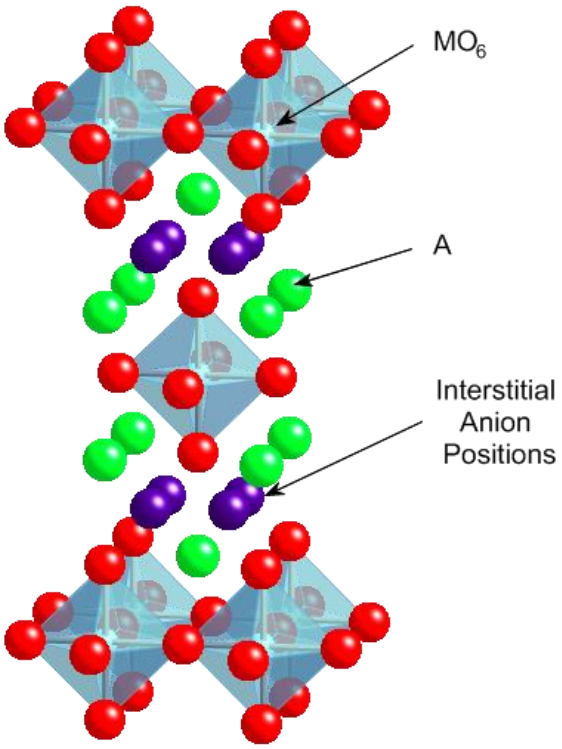

Figure 16: Ruddlesden Popper structure showing the position of interstitial anions.

As noted above, Ruddlesden Popper phases are generating significant interest for use as cathode materials in solid oxide fuel cells. In this respect a lot of research has been performed into IT-SOFC cathodes using materials such as $La_2NiO_{4+\delta}$, $La_{2-x}Sr_xCoO_{4+\delta}$, $La_{2-x}Sr_xNiO_{4+\delta}$ and $La_2Ni_{0.6}Cu_{0.4}O_{4+\delta}$ [65, 70, 73-75].

2. Project Objectives

Perovskite and perovskite related materials (Ruddlesden Popper) have been identified as promising materials for use as cathode electrode materials in SOFCs. The aim of this project was to improve the suitability of these materials for use in such fuel cells, as well as to examine their potential for use in the lower temperature AAEMFC.

To try and improve the properties of Ruddlesden Popper materials, the potential to increase the interstitial anion content of known phases (e.g. $La_2NiO_{4+\delta}$), which have already demonstrated promise for use in fuel cells, has been examined.

In the perovskite area a range of well known materials have been investigated for use in both high and low temperature fuel cells. These studies have included novel oxyanion doping strategies to improve the stabilisation, conductivity and electrochemical properties. In addition fluorination of such materials has been studied to determine the effect this has on the structure and properties.

3. Experimental

3.1. Synthesis Routes

3.1.1. Solid State

The most widely used method in materials chemistry is the solid state synthesis route, sometimes referred to as the "Shake and Bake" technique. In this method the relevant metal oxides/carbonates are ground together in the correct stoichiometric ratio. This mixture is then placed into a crucible and heated at high temperatures in a furnace. The temperature and duration of the synthesis is dependent on the material being synthesised. Generally the temperature is above 800^{o}C and the reaction time longer than 12 hours [44, 76]. The reason for such high temperatures is to provide the reagent materials with enough energy to break their bonds, migrate to reaction sites and form new bonds. In order to speed up the process it is usual to regrind the samples intermittently to give the reagents fresh reaction sites. This regrinding and reheating is repeated until the material becomes single phase. The advantages of this method are that it is easy to perform and usually effective. However it does have some disadvantages, which include the high temperatures and long reaction times. These are due to the long diffusion distances and slow reaction kinetics, which hinder the formation of single phase samples and limit particle size and surface area control.

3.1.2. Sol Gel

In the sol gel method employed in this work the relevant metal nitrates are weighed in the correct stoichiometric ratio and added to deionised water. The metal nitrates are dissolved in the water by gentle heating. Chelating and gelation materials are added to firstly form an organic-polymeric complex between the metal ions and then to facilitate the formation of the polymeric resin [77-79]. The most common materials used are citric acid for the chelating material and this is combined with ethylene glycol as the gelation material. Literature on this subject shows there is not an universal optimum ratio of these materials to the metal nitrates, as some papers report using

ratios of 1:1:1-6 for glycol: citric acid: metal moles [46, 77, 78] with many other variations reported in the literature [42, 80, 81].

Once the chelating and gelation materials are added, they are heated on a hot plate until sufficient water evaporates and the mixture has turned into a gel. This can then be transferred to a furnace and heated to 600^{o}C for 12 hours in order for all the organic material to be burnt off. Once cooled, the product is ground and analysed by XRD to determine if it is pure; if not, it is heated at higher temperatures until a single phase sample is obtained.

This method does have its advantages, which include lower temperatures required compared to the solid state method, and the fact that it can produce smaller more homogeneous particle sizes. It also has the capacity to form films or fibres. However there are disadvantages, which are typically higher reagent costs and longer processing times.

Another method which is very similar to the sol gel method is the sol gel combustion method. This method follows the same procedure as in the sol gel method, but instead of having both a chelating and gelation materials, only one is used. This one material chelates with the metal and is also used as a fuel for combustion. As for the sol gel method, there is more than one material that provides this reaction which include glycine [77, 82-85], urea [86] or alanine [86]. In some cases a chelating material and a fuel for combustion is needed. An example of this is using citric acid and EDTA. Again various ratios can be used with EDTA:Citric acid:metal mole ratios of 1:2:1 [82, 87] and 2:2:1 reported [46, 79, 88]. This method produces small homogeneous particle sizes like the sol gel technique.

3.1.3. Co-Precipitation

This technique is one of the oldest techniques for the preparation of mixed metal oxides. It consists of preparing an aqueous solution of metal cations generally by using metal nitrates. To this mixture a precipitating solution is added; examples of precipitating agents include, ammonia, urea and oxalic acid [77, 89, 90]. Once the two solutions have been mixed together and the precipitated

product is seen, the product can be removed from the solution and thermally decomposed to produce the desired product.

Several parameters must be controlled to get desirable results; these include the pH, mixing rates, temperature and concentration. When these parameters are optimised, good composition control, purity and morphology can be achieved. However due to different rates of precipitation for each compound, it may lead to in homogeneity and agglomerates forming in the subsequent calcination treatments [77, 91].

3.1.4. Hydrothermal

The hydrothermal synthesis of mixed metal oxides can employ many different routes. In general all reactions occur at high pressures and at intermediate temperatures, usually between 100-250^{o}C.

The general method used in this work involved the reaction of metal nitrates or salts with high concentrations of KOH or NaOH solution. Reacting these nitrates or salts at different concentrations of base and with a range of temperatures and durations can give different results. These include having different products as well as the shape and size of the particles being different [92-95].

Other methods can be used to synthesise materials hydrothermally. Recently Walton *et al* have produced lithium niobates via a one step reaction using various concentrations of LiOH and solid Nb_2O_5, and heating them at different temperatures and durations [96].

There are many advantages in using hydrothermal synthesis, the most notable being the lower temperature conditions that are needed compared to other synthesis routes. This method also has the capability to control the particle shape and size, although, this can be sometimes difficult to determine. In most cases there is also no need for a further calcination step, which again means that it is less energy intensive and hence it is more cost effective. Another advantage is that high quality products can be produced from a wide variety of raw materials [91, 97, 98]. A key disadvantage is that not all materials can be prepared by this route.

3.1.5. Fluorination Methods

The high temperature reaction of metal fluoride and oxides cannot usually be used to produce mixed metal oxide fluorides, since these are commonly not thermodynamically stable compared to the starting materials. Consequently, low temperature fluorination of oxide precursors is typically performed to kinetically stabilise these phases.

There are numerous different fluorinating agents used for these low temperature fluorination reactions. Depending on the method used, the fluorination either proceeds by a substitution process ($2F^-$ replace $1O^{2-}$) with no change of oxidation state, or an insertion process where oxidation of one or more of the cations occurs, or a mixture of both these processes. In some cases a process in which $1F^-$ replaces $1O^{2-}$ can occur leading to reduction of the cation oxidation states. Each fluorination method has its own advantages and disadvantages which are discussed here.

One of the methods used is the reaction of the sample with F_2 gas or a F_2/N_2 gas mixture. The temperature used depends on the sample, but generally the reaction temperature does not need to be any higher than 250^{o}C. The extent of fluorination required determines how long the sample is heated, as the longer the reaction times the higher the extent of fluorination. The problem with this technique is that it is difficult to control the level of fluorination throughout the sample, as the surface will typically have higher fluorination levels than the bulk. In addition, at higher temperatures decomposition occurs resulting in AF_2 (A=Alkaline earth) impurity in the case of fluorination of alkaline earth metal containing systems. A final disadvantage of this technique is the handling difficulties associated with the use of toxic fluorine gas. However the advantage of using this fluorine insertion technique is that it can produce novel highly oxidised mixed metal oxide fluoride materials [75, 99-104].

An easier technique to use is the fluorine substitution ($2F^-$ replace $1O^{2-}$) reaction with NH_4F. The NH_4F is ground with the material and then heated at low temperatures between 250^{o}C-350^{o}C for a number of hours with intermittent grinding. The temperature and duration is dependent on the

material being fluorinated, while the level of fluorination can be controlled by the amount of NH_4F used. However, as with F_2 gas, for alkaline earth containing systems there are typically AF_2 impurities, due to the partial decomposition of the sample [99, 100, 105-107].

Another technique that has the same AF_2 impurity problem as the NH_4F technique is the reaction of the materials with XeF_2. This leads typically to a mixture of fluorine insertion and substitution although the reaction is very sensitive to the presence of water. Consequently for the best results, the material and the fluorinating agent must be mixed together in a glove box and sealed in a copper tube, which is then heated to temperatures between 200^{o}C-400^{o}C for a number of hours. The main disadvantage here is the handling problems and the higher cost of XeF_2, which, when considering that the NH_4F technique can give the same quality of data but without the handling difficulties, means that it is not as often used [108].

Fluorination by CuF_2 is another easy technique to use, whereby the CuF_2 is added to the material, ground together and heated at a temperature around 350^{o}C for at least 12 hours. In this technique both insertion and substitution reactions can occur, but at higher temperatures the substitution mechanism will dominate. Again, as with the other techniques examined, there can be a small impurity of AF_2, but typically not as much as with the NH_4F technique. However, there is a large amount of CuO impurity from the CuF_2 reagent. This CuO impurity can be eliminated if the fluorination is performed in an autoclave, as this allows the CuF_2 to be kept separate from the precursor material to be fluorinated [99, 100, 105-107].

The final technique is the reaction with poly(vinylidene fluoride) (PVDF). This technique typically follows the same reaction mechanism as with the NH_4F, the substitution of two fluorine atoms for each oxygen. However due to this being an organic compound, the organic component can be burnt off at around 350^{o}C giving a more or less pure sample with negligible AF_2 impurities at lower amounts of fluorinating agent. The presence of the carbon component can result in a reducing environment, which can lead to $1F^-$ replacing $1O^{2-}$ and accompanying reduction of the metal(s)

oxidation state. For very high fluorination levels AF_2 impurities can be formed due to the increasing instability of the oxide fluoride products at higher F levels [109].

In the work performed in this thesis the CuF_2 and PVDF fluorination techniques were used.

3.1.6. Ion Exchange

Ion exchange reactions can be used to synthesise novel materials, for example various layered perovskites. This can be accomplished by first preparing the parent phase (usually which contains sodium, which will be the element exchanged) in a standard solid state reaction. After this has been prepared it will be reacted in a molten mixture containing the ion to be exchanged. This is left to react at temperatures around 300^{o}C for numerous days [110, 111]. A lower temperature technique by mixing the parent material and ion exchange material in water for a few days around 50^{o}C has also been achieved [112].

Most of the work in this area has focused on cation exchange. In this project the potential of anion exchange was examined, namely the exchange of F^- by OH^- ions. In this way, it was hoped to produce novel metastable hydroxide containing Ruddlesden Popper phases, by exploiting the ready ability of such phases to accommodate high levels of F^- and then exchanging this F^- for OH^-. This was accomplished by placing the fluorinated sample in a hydrothermal bomb. To this a 1M potassium hydroxide solution was added and the closed vessel placed in the oven at 200^{o}C for 48 hours. Once cooled the sample was vacuum filtered and washed with copious amounts of distilled water. The sample was then analysed (by thermogravimetric analysis) to determine the degree of exchange. If further exchange was necessary then the process was repeated.

3.2. Structural Characterisation

Both X-ray and neutron powder diffraction was used in this project to determine the purity and structures of the different materials studied. In the next few pages, the key features of these techniques as well as crystal structures will be discussed.

3.2.1. Crystal Symmetry

A crystalline solid has a regular three dimensional arrangement of atoms/ions. The simplest part of the structure, that can be repeated by translation and still shows the full symmetry of the system, is called the unit cell. The angles and lengths are used to define the size of the unit cell and are known as the unit cell or lattice parameters. As the level of symmetry increases relationships occur between the cell parameters resulting in 7 different crystal classes, which have different shapes depending on their different angles and lengths. Along with the different shaped crystal classes it is common to describe the lattice type. These are derived by replacing each group of units with a point. There are 4 types of lattice, namely primitive (P), body centred (I) and face sharing (F) and (C). These, added to the 7 crystal classes, give rise to 14 Bravais Lattices (Figure 17).

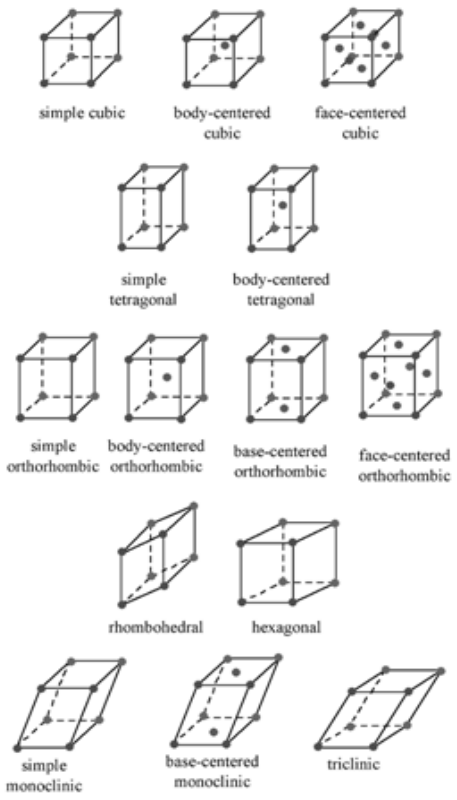

Cubic	a = b = c	α = β = γ = 90°
Tetragonal	a = b ≠ c	α = β = γ = 90°
Orthorhombic	a ≠ b ≠ c	α = β = γ = 90°
Monoclinic	a ≠ b ≠ c	α = γ = 90° β ≠ 90°
Triclinic	a ≠ b ≠ c	α ≠ β ≠ γ ≠ 90°
Hexagonal	a = b ≠ c	α = β = 90° γ = 120°
Trigonal/ Rhombohedral	a = b = c	α = β = γ ≠ 90°

Figure 17: The 14 Bravais Lattices [113].

To fully describe the crystal structure further elements of symmetry need to be considered, leading to a total of 230 different space groups. The space group describes the full symmetry of the crystal system.

To determine where atom positions occur along with the lattice planes, which are essential for diffraction, a description of directions and lengths are necessary. To do this directions are defined from the unit cell origin and the distance from the origin given in fractions of the unit cell lengths (Figure 18). Lattice planes are described in terms of their Miller Indices. These are defined as the inverse of the fractional intercept along (a, b, c). This leads to the assignment of Miller Indices in the form (h k l), examples of which are shown in Figure 19.

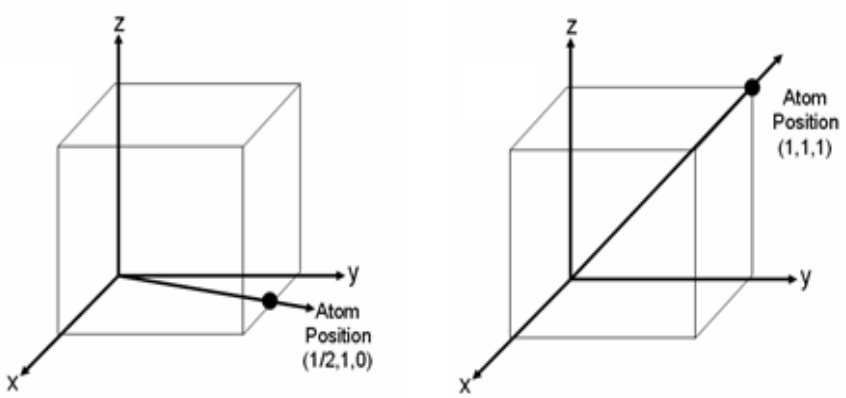

Figure 18: Examples of description of atom positions.

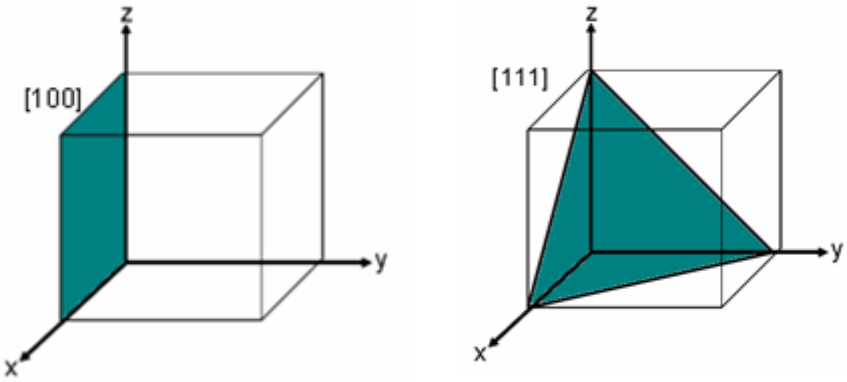

Figure 19: Examples of lattice planes with different Miller indices.

X-ray diffraction analysis can be performed on crystalline materials either as a single crystal or a powder which contains very small crystallites. Diffraction occurs when the X-rays are scattered at different positions in the sample due to interactions with the electrons on the atoms. For a peak to be observed, constructive interference must be observed. This can be explained by considering two parallel X-ray waves being diffracted by different planes. For constructive interference, the

additional distance travelled between the lattice planes must be of an integral number of wavelengths. This depends on a couple of factors including the distance between the lattice plane, as well as the angle of the X-ray incidence (see Figure 20). This relationship can be explained by using the Bragg equation (Equation 4)

Equation 4 Path Difference = BD + DC = $2d_{hkl}\sin\theta = n\lambda$

$\lambda = 2d\sin\theta$ (as usually n is set as 1)

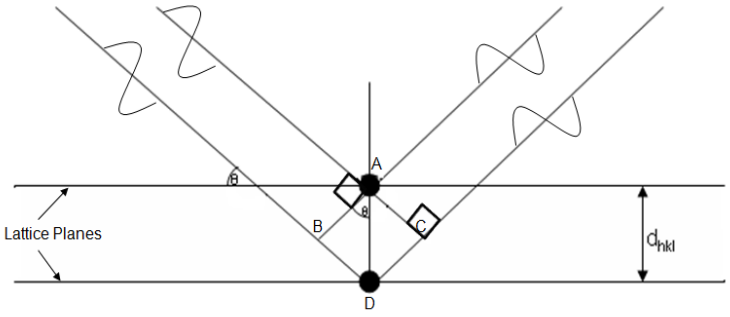

Figure 20: Derivation of Bragg's Law.

As mentioned before, crystalline materials have different crystal systems resulting in an infinite number of lattice planes with different Miller indices and particular d_{hkl} separation. To calculate all the various possible d spacings the Bragg equation can be joined with the crystal classes giving equations as seen in Table 3.

Table 3: Expressions for d spacings in different crystal classes.

Crystal System	Expressions for d_{hkl} in terms of lattice parameters and Miller Indices
Cubic	$\frac{1}{d^2} = \frac{h^2+k^2+l^2}{a^2}$
Tetragonal	$\frac{1}{d^2} = \frac{h^2+k^2}{a^2} + \frac{l^2}{c^2}$
Orthorhombic	$\frac{1}{d^2} = \frac{h^2}{a^2} + \frac{k^2}{b^2} + \frac{l^2}{c^2}$
Hexagonal	$\frac{1}{d^2} = \frac{4}{3}\left(\frac{h^2+hk+k^2}{a^2}\right) + \frac{l^2}{c^2}$
Monoclinic	$\frac{1}{d^2} = \frac{1}{\sin^2\beta}\left(\frac{h^2}{a^2} + \frac{k^2\sin^2\beta}{b^2} + \frac{l^2}{c^2} - \frac{2hl\cos\beta}{ac}\right)$
Triclinic	Complex expression

For powder diffraction, because the crystallites are all in a random orientation, it is necessary to bring the lattice planes into orientation with the Bragg angle. To do this the X-ray beam, detector and sample move relative to one another to perform the analysis. There are two common techniques used in powder diffraction, the reflection (Bragg-Brentano) and transmission (Debye-Scherrer) (Figure 21). In this work the majority of the X-ray data were collected using a Bruker D8 in transmission mode, with a copper X-ray source, using a primary focussing Ge crystal monochromator to give Cu $K\alpha_1$ radiation at a wavelength of 1.5406Å.

Since X-rays are scattered by the electrons in the atom, the intensities are strongly influenced by the positions of the heavy atoms, which can make lighter atoms (e.g. O, F) difficult to locate.

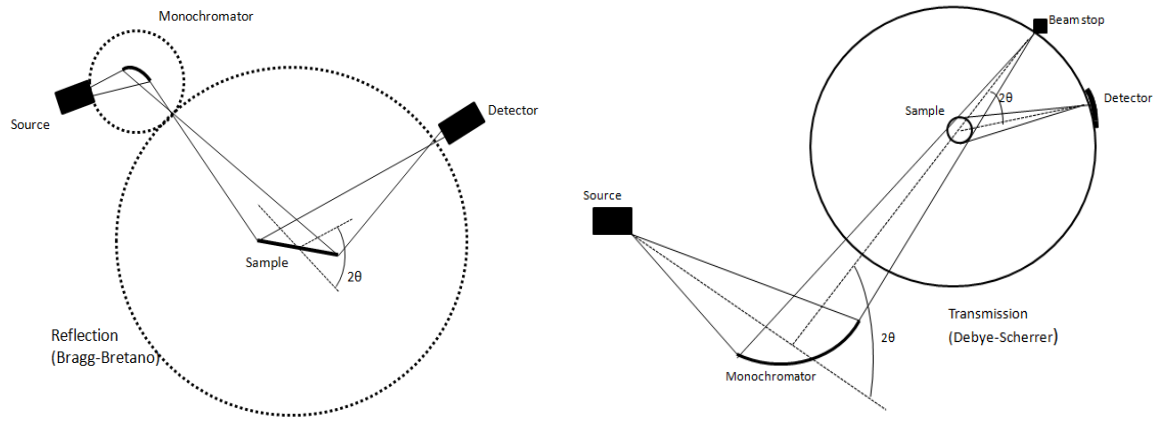

Figure 21: Bragg-Brentano and Debye-Scherrer geometries for X-ray diffraction.

3.2.2. Production of X-rays

X-rays are produced by the filling of an electron hole with electron decay from a high energy orbital, the energy lost given off as X-rays. These holes are caused by an electron beam striking a metal plate, resulting in the ejection of an electron from the metal core orbital.

In this case the metal being bombarded is copper. In addition to X-rays being produced from electron decay, it is also possible for X-rays to be produced from the slowing down of electrons as they enter the metal target leading to a broad background of X-rays (Bremstrahlung). A typical X-ray spectrum of copper is shown in Figure 22, with sharp peaks resulting from the electron transitions. As noticed in the spectrum there are two distinct sets of peaks, which is due to copper having electron decay from two different levels. These levels named Kα and Kβ are due to the 2p → 1s and 3p → 1s transitions respectively. A close inspection shows that these lines are in fact doublets, which is due to the different possible spin states of the electron.

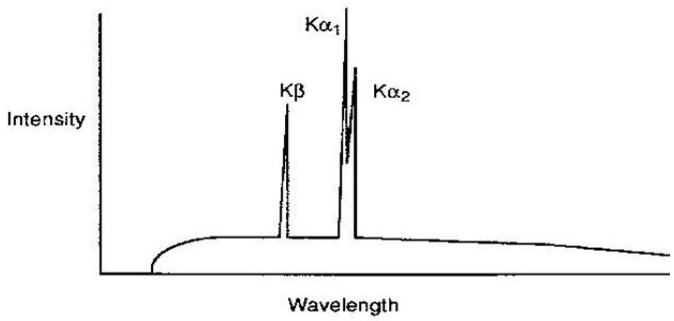

Figure 22: X-ray spectrum from a copper target [114].

For X-ray diffraction experiments to be performed it is necessary to have a single wavelength of X-ray radiation. This is achieved by using a crystal monochromator, where the X-rays generated impact on a single crystal at a fixed orientation, resulting in a single wavelength being diffracted as stated by Bragg's Law. Another way of creating a single wavelength is by using a filter, usually a metal foil with an atomic number lower than the target source, e.g. nickel in the case of CuKα radiation. The transitions in the nickel will require less energy than the copper due to the decreased nuclear charge, resulting in the lower wavelength to be absorbed. The outcome is a single wavelength for diffraction experiments.

3.2.3. Neutron Diffraction

Neutron diffraction is very similar to that of X-ray diffraction; however instead of being scattered by the electrons in the sample, neutrons are scattered by the atom nuclei. This difference gives rise to a lot of advantages. The main advantage is being able to detect lighter atoms that would be difficult to observe by X-ray diffraction, due to the scattering dominance of heavier atoms in X-ray diffraction. Another advantage of this technique is the determination of magnetic structures in the sample. This is due to neutrons having a magnetic moment, which allows the neutrons to interact with unpaired electrons in the sample, giving rise to extra scattering in the diffraction pattern, including potentially extra peaks when there is magnetic ordering and the magnetic super cell is different from the crystallographic unit cell.

A key disadvantage is that production of intense neutron beams cannot be generated in the laboratory and so specific expensive central facilities are used. At these central facilities, there are two strategies for producing the neutron beam, either with a nuclear reactor or a spallation source. Using a nuclear reactor produces a distribution of neutrons of different wavelengths, from which neutrons of a single wavelength can be selected, and the diffraction pattern then plotted in the same way as X-ray data, the intensity against 2θ. For the spallation source a pulsed beam of highly energetic protons is accelerated and impacted on a heavy metal target. Neutrons of different wavelengths are then expelled from the target and timed between the source and the detector (at

fixed θ). The wavelengths can then be used in the Bragg equation to calculate the d spacings which can be plotted against the intensity of the neutrons. Thus in this case θ in Bragg's law is fixed, and λ is effectively varied. One of the key benefits of the spallation source is that typically a higher intensity is possible, and the experiment makes use of all the neutrons produced, rather than selecting a single wavelength, and not using the other neutrons, in the case of a reactor source.

There are different facilities around the world where neutron diffraction can be performed. In this project the data were collected at the ISIS spallation neutron source at the Rutherford Appleton Laboratory in Oxfordshire, England as well as the SINQ spallation neutron source at the Paul Scherrer Institut in Villigen, Switzerland.

3.2.4. Rietveld Analysis

Traditionally the preferred method for the structural determination of crystalline materials was single crystal X-ray diffraction. However the production of single crystals of a suitable size for many materials is a problem, and so another technique had to be developed. This technique was X-ray powder diffraction. Until the early 1960's the only structures that could be determined were simple high symmetry materials, as in these cases the peaks would be well resolved and the integrated intensities could be easily obtained for structure refinement. Structure determination was then accomplished by using the "integrated intensity method". With more complex compounds the overlapping of the peaks became worse, and therefore using the integrated intensity method became practically impossible. It was subsequently realised that by applying the full power of computers to full pattern analysis, much more information can be obtained [115, 116]. It was Rietveld that worked out a computer based analytical procedure, by using every data point instead of an intensity value for each peak using least square refinements until the best fit is obtained from a calculated model to the observed pattern. This is now the technique (termed Rietveld refinement) used to analyse powder X-ray diffraction data and has consequently expanded our understanding of the structures of solids considerably [117].

There are many suites of programs used for the Rietveld refinement of crystal structures using X-ray and neutron diffraction data. These include FULLPROF, TOPAZ and GSAS. GSAS (General Structure Analysis System) [118] is the set of programs that have been used to analyse the data presented in this thesis. GSAS is a versatile suite of programs capable of structure refinement with more than one phase. It is also capable of determining the structures of magnetic systems [119, 120], determining atom positions from FOURIER maps [121] and is capable of providing considerable structural information.

The Rietveld method requires some information for the structural data before starting the refinement. This information includes the space group, cell parameters and starting atom positions, along with the instrumental parameters from the diffractometer. Least square calculations are then performed on the starting parameters which are refined so that the calculated pattern from the structural model fits the observed diffraction pattern. The quantity minimised in the least-squares refinement is the residual, S_y (see Equation 5).

Equation 5

$w_i = 1/y_i$

y_i = observed (gross) intensity at the *i*th step.

y_{ci} = Calculated intensity at the *i*th step.

In addition to the atom positions, other parameters can be varied, for example background, scale factors, peak shapes and atom thermal displacement parameters to gain a better fit.

The best way to determine the quality of the fit is by a visual display. A visual display shows the observed, calculated and difference diffraction profiles (Figure 23) which for a good structural model should ideally show a small difference between the observed and calculated patterns.

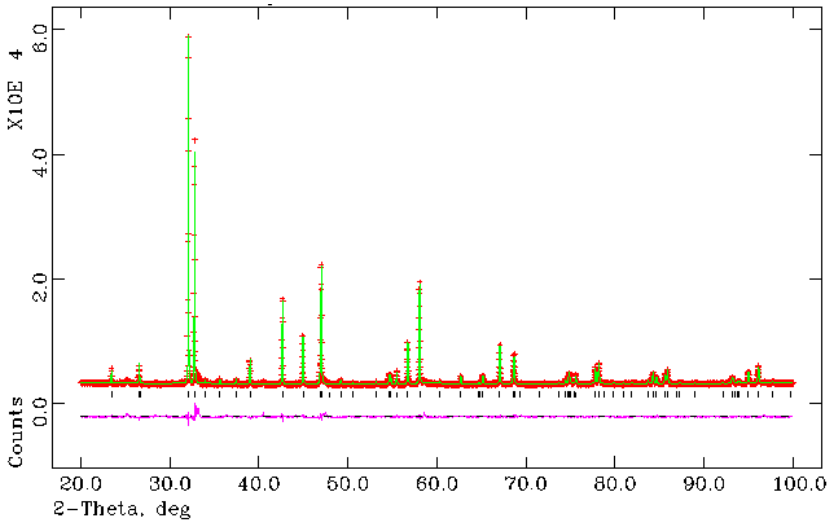

Figure 23: An example GSAS refinement profile. The solid green line is the calculated pattern from the model structure. The dotted red line shows the observed pattern from the data collected. Finally the pink curve at the bottom shows the difference between the two; ideally this should be as flat as possible.

There is another way to determine if the refinement is proceeding well, and this is by using the agreement indices. These are more commonly known as the R factors. There are several R factors that are used, which are defined below:

The R profile:

Equation 6

Y_i (obs) = Intensity observed at point i

Y_i (calc) = Intensity calculated at point i

The R weighted profile:

Equation 7

W_i = weighting

The R_{wp} is the most meaningful of the R factors due to the fact the numerator is the residual being minimised. This same reason is why it is the best R factor that reflects the progress of the refinement. However R_{wp} values can be misleading as they can be seriously inflated by things which do not arise from a good structural model, for example the presence of an impurity phase results in

a strong line in the difference plot which can cause the R_{wp} value to increase significantly. On the other hand the R_{wp} can be misleadingly small if the refined background is high due to the intensity being accounted for by the background function [117, 122].

The expected R factor:

Equation 8

N = number of observations

P = number of parameters varied

The R_{exp} will give an indication of the quality of the data as it will be very small if the data has been collected for a long time, due to the errors not being dominated by counting statistics, or very large if the data has been collected too quickly [117, 122].

A useful number to look at is S, the "goodness of fit":

Equation 9 S =

For a good refinement a χ^2 value of less than 4 is typical. However the χ^2 value is influenced heavily by the R_{exp} so it is important to be mindful of the problems associated with the R_{exp} factor.

The R Bragg factor:

Equation 10

I_k = Intensity

R_B can be used to monitor the improvement in the structural model as it is only dependent on structural parameters not profile parameters.

Structure refinement using the Rietveld method is a powerful technique for structure determination from powder patterns, however a good starting structural model is required in the first instance.

3.3. Thermogravimetric Analysis

In Thermogravimetric Analysis (TGA), a substance is heated to a specific temperature at a specific rate, whilst the mass of the sample is carefully measured. In this technique the sample is placed on a platinum or alumina heating pan on a precision thermobalance. The sample is then subjected to the preset program, which controls the rate and temperature whilst measuring the weight loss or weight gain. This is usually recorded by a computer coupled to the thermal analyser which produces a graph as shown in Figure 24. Most TGA instruments also have the capability for Differential Thermal Analysis (DTA) of the sample. This can be especially useful in determining phase changes in the sample. With this technique the sample is placed in a pan with an identical but empty pan next to it and the difference is measured as a function of temperature. An exothermic event will lead to the sample pan being hotter than the empty pan, while the reverse will be the case for an endothermic event.

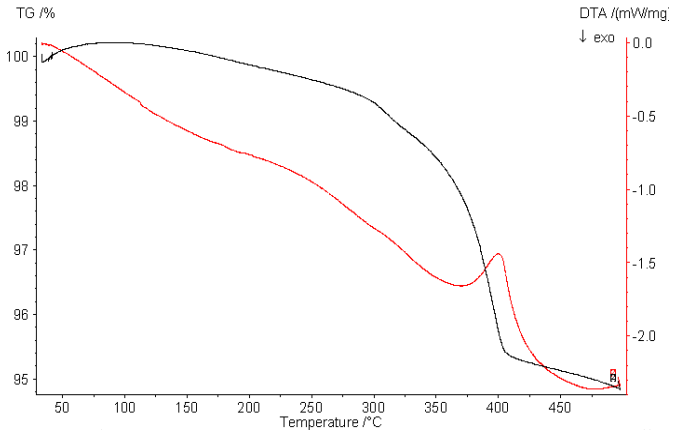

Figure 24: An example of TGA and DTA data. The black line shows the weight difference in % of the sample against the temperature while the red line shows any thermal events exothermic or endothermic taking place.

If the relative molecular mass of the starting material or of the product at a particular stage of the decomposition is known, then the relative molecular mass at each of the plateaus can be determined.

The TGA data can be collected in different atmospheres other than air, such as H_2, N_2, O_2 or Ar depending on what conditions are needed for the experiment. Also some TGA instruments can be

coupled to other analytical devices, for example a mass spectrometer or Infra Red spectrometer. Mass Spectrometers are especially useful as the gases that are given off from the decomposition can be analysed as seen below in Figure 25.

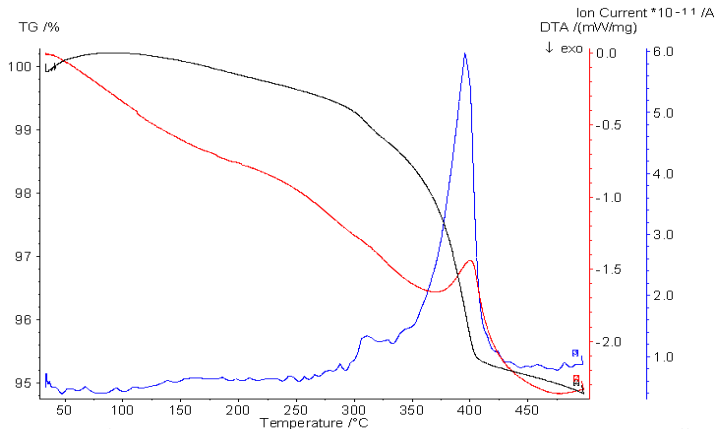

Figure 25: An example of TGA/DTA with Mass Spectrometry data. The black and red lines represent the TG and DTA data respectively while the blue line shows the amount of a specific mass (in this case water) being released against temperature.

In this project the TGA/DTA were used to study the water content, oxidation states and phase changes of the perovskite and Ruddlesden Popper systems investigated.

3.4. Raman Spectroscopy

Raman spectroscopy is a technique that is used to determine the information concerning the bonding in a material. This technique is complimentary to Infrared spectroscopy due to there being different selection rules between the two. Infrared spectroscopy requires a dipole moment change through the vibration of bonds, compared to Raman spectroscopy which requires a change in polarisability.

Raman spectroscopy is an informative technique as it can provide qualitative data from the sharp bands seen in the spectra which are characteristic of specific groups in the material. In addition quantitative analysis can be performed as the intensity of the peaks are proportional to the concentration of the components. Coupled with the amount of data available from Raman analysis, the ease of collecting data makes Raman spectroscopy a popular technique [123].

In Raman spectroscopy, the sample is subjected to a monochromatic beam of light. A photon raises the energy of the molecule to a "virtual state" which is a distortion of the electron distribution of a covalent bond. This molecule relaxes immediately to its original electronic state by emitting a photon. If it relaxes back to the vibrational energy from where it began the photon has the same energy and so the same wavelength as the incoming radiation. This is called Rayleigh or elastic scattering. However if the photon returns to a higher vibrational energy the photon has less energy and so a longer wavelength is observed than the original. This is Stokes Raman scattering. The final possibility is that the photon returns to a lower vibrational energy giving the photon more energy and a shorter wavelength. This is Anti-Stokes scattering. This is shown pictorially in Figure 26.

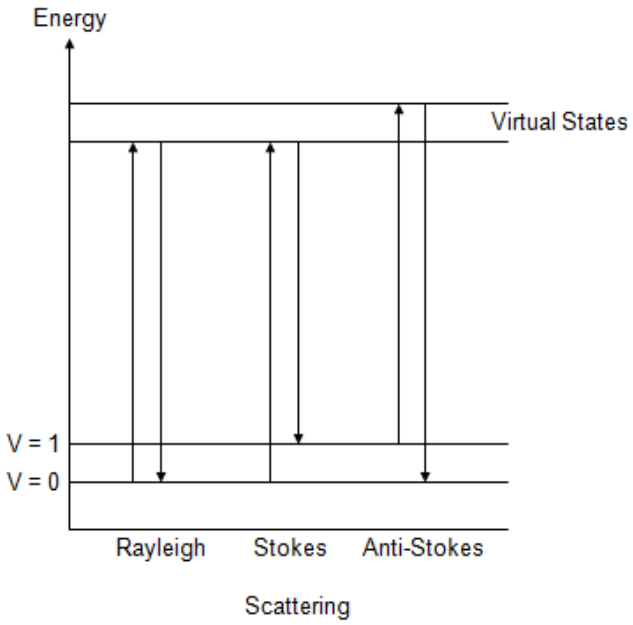

Figure 26: Energy level diagram showing the states involved in Raman Spectroscopy.

The vast majority of scattering is from Rayleigh scattering. The Stokes and Anti-Stokes intensity is proportional to the number of molecules occupied in the original vibrational energy [123, 124].

Raman spectra in this work were collected using a Renishaw InVia Raman microscope using an ion laser at wavelengths of 532 nm and 633 nm on powdered samples. The Renishaw InVia Raman microscope (Figure 27) works by the monochromatic beam of light produced from the laser

being directed to the microscope by beam steering optics. The microscope can be focused on the sample to allow specific areas to be analysed selectively. The photons are then collected and directed to the spectrometer. To stop the weak Raman signal from being overwhelmed, the reflected and Rayleigh scattered photons are removed by a holographic notch filter. Once removed the remaining Raman photons are sorted spatially by a diffraction grating and detected by a CCD camera producing a Raman spectra [125].

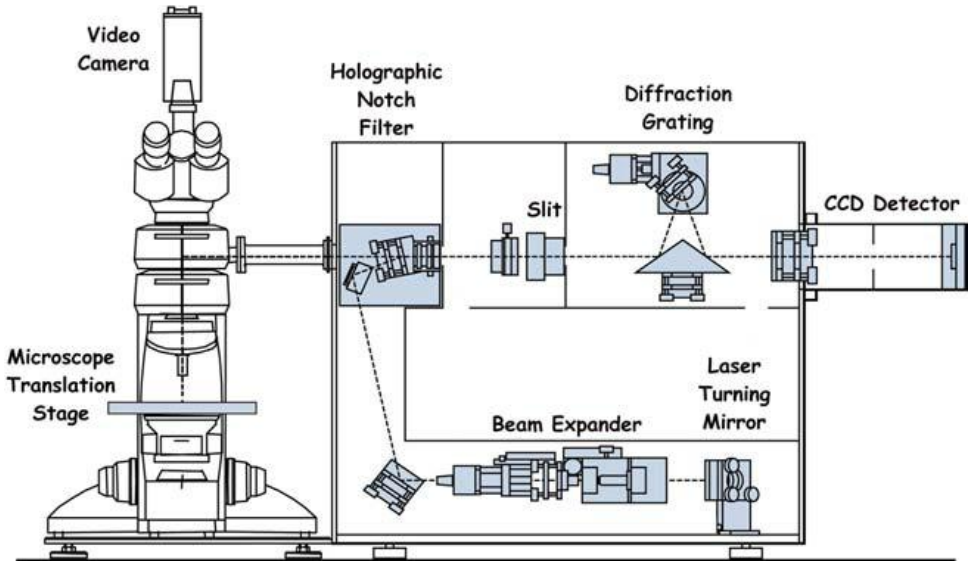

Figure 27: Schematic of a research-grade dispersive Raman microscope.
According to Ref [125] Elsevier permission.

3.5. Mössbauer Spectroscopy

Mössbauer spectroscopy is a versatile technique used in many different scientific areas. It can provide very precise information about the chemical, structural and magnetic properties of a material, such as valency state, ligand bonding states, electron shielding and electron drawing power [48, 110, 111, 126] .

The Mössbauer effect is the emission and resonant absorption of nuclear gamma rays. This technique has to be performed on solid samples held in a rigid crystal lattice, so that when the gamma ray energy is small enough the recoil of the nucleus is too low to be transmitted as a phonon. This means that the whole system recoils making the recoil energy effectively zero, and thus giving a recoil free event.

As resonance only occurs when the emitting and absorption nucleus match exactly, the effect is isotope specific. Table 4 shows some nuclei that can be observed.

Table 4: Example Mossbauer isotopes [48].

Nucleus Observed	Natural abundance %	Ground Spin State	Excited Spin State	Radioisotope source
57Fe	2.2	½	3/2	57Co
119Sn	8.6	½	3/2	119mSn
99Ru	12.7	3/2	5/2	99Rh
197Au	100	3/2	1/2	197mPt

When the emitting and absorbing nuclei are in identical environments there is a single line in the Mössbauer spectrum. However it is not likely that the nuclei studied in the system will be identical to the source so it is necessary to change the energy of the gamma rays. To do this the gamma source is moved closer and further away from the absorber to modify the energy by the Doppler effect. This is achieved by using an oscillator. The spectrum intensity is then recorded against the velocity. When the modulated gamma ray energy matches the absorber nuclear transitions energy the gamma rays are absorbed and a peak is recorded on the spectrum. An example of a Mössbauer spectrum is shown in Figure 28.

The parameters of greatest interest are the magnitude of resonance effect (ε), line width (Γ), isomer shift (IS), quadrupole splitting (QS), magnetic hyperfine structure (mhfs), line asymmetry and temperature coefficient [127].

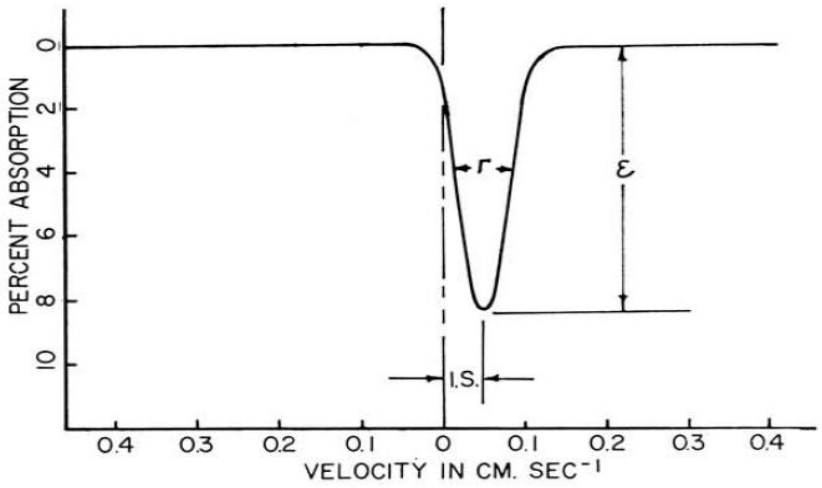

Figure 28: An example of a Mössbauer Spectrum.
According to Ref [127] Elsevier permission.

The magnitude of the resonance effect, if measured at various absorber temperatures, can be used to calculate the Debye temperature for the absorber. In addition, the relative values can give a qualitative estimate of the proportion of various chemical environments in a system. The line width gives the most reliable measure of the quality of the Mössbauer source. The most important information can be gathered from the isomer shift and quadrupole splitting. These can give information about the oxidation state and chemical environment as stated earlier. Further information is also gathered from the splitting of peaks when exposed to a magnetic field or asymmetrical electrical field [110, 126, 127]. This can give information on the presence of any magnetic ordering in the sample.

The Mössbauer spectroscopy performed in this project was carried out by Professor Frank Berry and researchers from the Instituto de Quimica Fisica, Madrid.

3.6. 4 Probe DC Conductivity Measurements

There are two different types of techniques to measure the conductivity of a material. The decision of which one to use depends on how good a conductor it is. If the material has a relatively high resistivity, for example the electrolytes in solid oxide fuel cells (10^1 to 10^4 Ωcm), then A C impedance spectroscopy is preferred. However if the resistivity is low (10^{-1} to 10^{-3} Ωcm), as is the case for fuel cell electrode materials, then the 4 probe DC technique is used.

There are two different types of DC conductivity methods namely the Van de Pauw and the 4 probe DC method.

For the Van de Pauw method, 4 Platinum wires are attached at 90^{o} angles on the pellet (either circular or square). The resistance (R) is then measured at least twice as shown in Figure 29 below [128, 129].

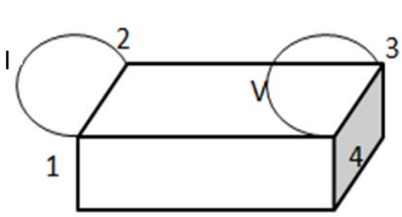

$R_A = V_{43} / I_{12}$

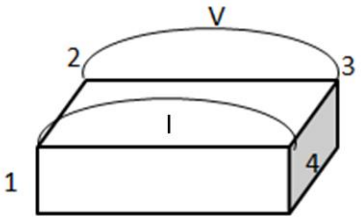

$R_B = V_{23} / I_{14}$

Figure 29: Van de Pauw method of 4 probe conductivity.

The conductivity of the sample can then be calculated by using Equation 11 below [128-130].

Equation 11 $\sigma = \frac{d}{R_A \pi} f(r)$

Where d = thickness of the sample and f(r) depends on the ratio of $r=R_A/R_B$

Reversing the current and voltage contacts would also define RC and RD, which should be equal to RA and RB for symmetry reasons.

The other 4 probe method also attaches 4 platinum contacts to the pellet, but in a different configuration as seen below in Figure 30.

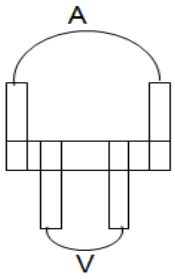

Figure 30: 4 probe DC conductivity method.

The conductivity of the sample can then be calculated using Equation 12.

Equation 12 Conductivity = (Length between wires/(Cross sectional area)) * I/V

For both techniques the sample was attached to Pt wires in an alumina measurement rig and put in a furnace with the conductivity measured at varying temperature.

A graph can then be plotted to show how the conductivity varies over temperature. To determine which method was the best, the two techniques were performed in the lab on a pressed pellet of LSM giving the graph shown below in Figure 31 [131]:

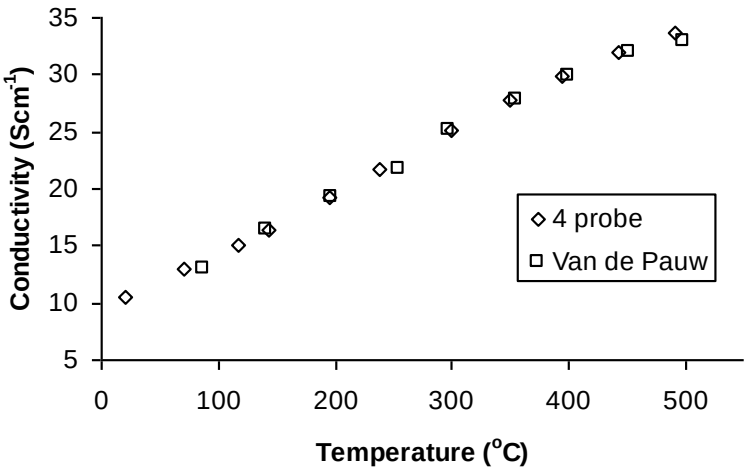

Figure 31: Graph showing the conductivity of the two different 4 probe methods on LSM.

As can be seen in the graph there was not much difference between the two methods. In this thesis the 4 probe D C technique was used, due to the greater ease of this method.

3.7. Electrochemistry

3.7.1. Cyclic Voltammetry

Cyclic voltammetry is a popular method used in many areas of chemistry. It is used for the study of redox processes, electrode mechanisms, the study of intermediate reactions and for obtaining information on the stability of reaction products [132-134]. In the case of this work, cyclic voltammetry was used to determine the onset potential of the various materials for potential use as cathodes (oxygen reducing electrodes) in alkaline fuel cells.

Cyclic voltammetry consists of cycling the potential of the working electrode and measuring the resulting current. The working electrode potential is controlled relative to a reference electrode,

generally either a saturated calomel electrode (SCE) or a silver/silver chloride electrode (Ag/AgCl) [132, 135]. There is a final Pt electrode needed to avoid passing current through the reference electrode, which would alter its potential [21, 135]. The setup of these electrodes is shown in Figure 32.

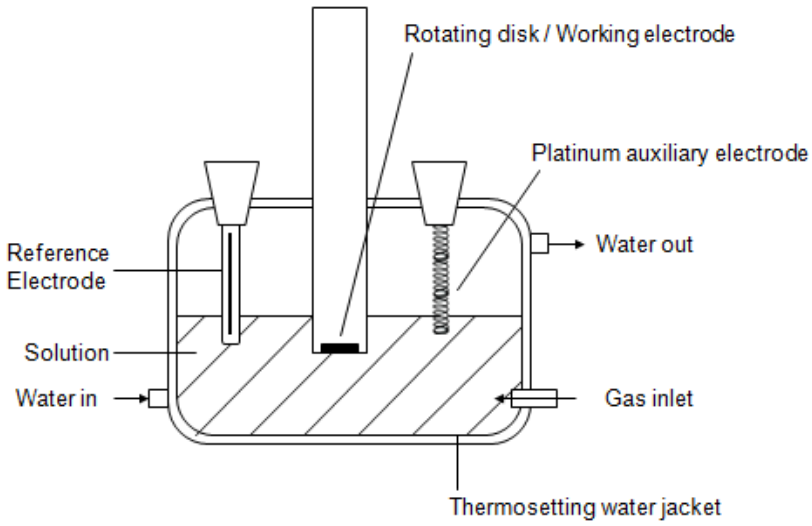

Figure 32: Potentiostat diagram.

The voltage applied to the working electrode is scanned from an initial value E_1 to a predetermined limit E_2, and then the direction is reversed. A typical cyclic voltammogram for a reversible reaction can be seen in Figure 33.

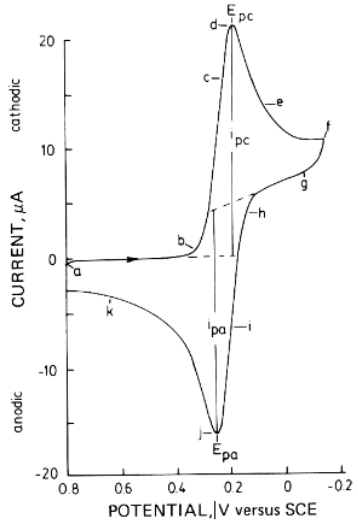

Figure 33: A typical Cyclic Voltammogram diagram for a reversible reaction.
According to Ref [132] Elsevier permission.

Not only can the onset potential of the material be measured, which gives an indication of how easily the oxygen reduction reaction occurs with the more positive onset potential [136], but also other information, such as the number of electrons transferred, is obtained. This information comes from Equation 13 and 14:

Equation 13 $I_{pc} = -2.69 * 10^5 n^{3/2} A D_o^{1/2} C V^{1/2}$

Equation 14 $Ep^{ox} - Ep^{red} = 2.2RT/nF$

I_{pc}=Peak Current (A)

n=Number of Electrons

A=Electrode area (cm^2)

D=Diffusion Coefficient (cm^2/s)

C=Concentration (mol/cm^3)

V=Scan rate (V/s)

R=Universal gas constant

T=Temperature (K)

F=Faraday constant ($96500 C mol^{-1}$)

$E_p^{ox} - E_p^{red}$=Peak Separation

The shape of the voltamograms also gives a lot of information. As already described with the reversible system, the onset potential can give a rough idea of how well the material is going to perform. In addition the distance between the two peaks can show the irreversibility of the systems, the irreversibility increases as the distance between the peaks increase [137].

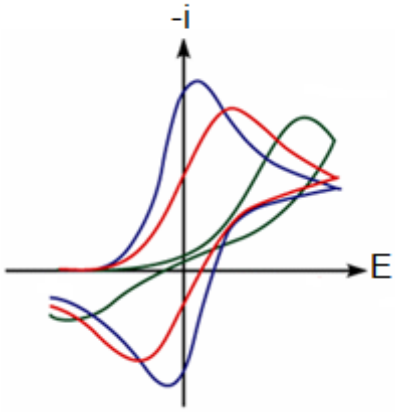

Figure 34: Voltammograms showing different types of systems, Green = irreversible, Blue = reversible and Red = quasi reversible [138].

There are, however, problems with using cyclic voltammograms, as reproducible results can be highly dependent on electrolyte purity, identity of electrode material, choice of turnaround potential and the rate of change of the potential (as at slower rates there is a perceptible deactivation of the electrode surface). The most significant problem however is the possible dissolution of the counter electrode [21].

3.7.2. Rotating Disk Electrode (RDE) Measurements

Performing rotating disk electrode measurements can give a lot of information about the properties of the materials. One of the most important pieces of information is which electron pathway does the material take, e.g. is the oxygen reduction through a 2 or 4 electron pathway. It is highly desirable to reduce oxygen via the $4e^-$ pathway as it is more efficient, obtaining the maximum energy capacity, and it does not produce peroxide intermediates which can damage a fuel cell membrane. The general mechanism is shown below in Figure 35.

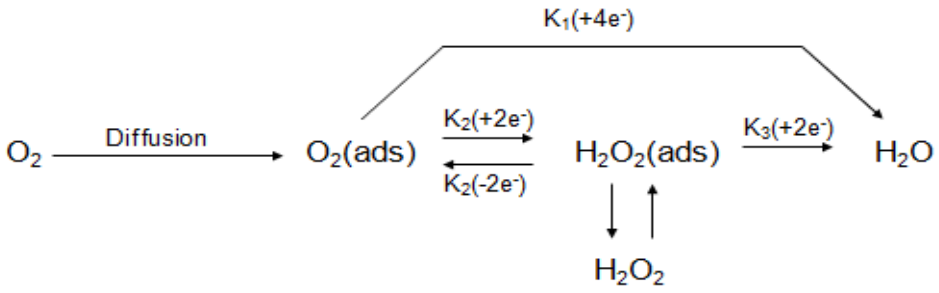

Figure 35: General mechanism of different electron pathways, where k_i represents the various rate constants [45].

The electrode material is placed on the working electrode and spun at different rotation rates while supplying a potential and recording the current. This is then plotted as polarisation curves, as shown in Figure 36.

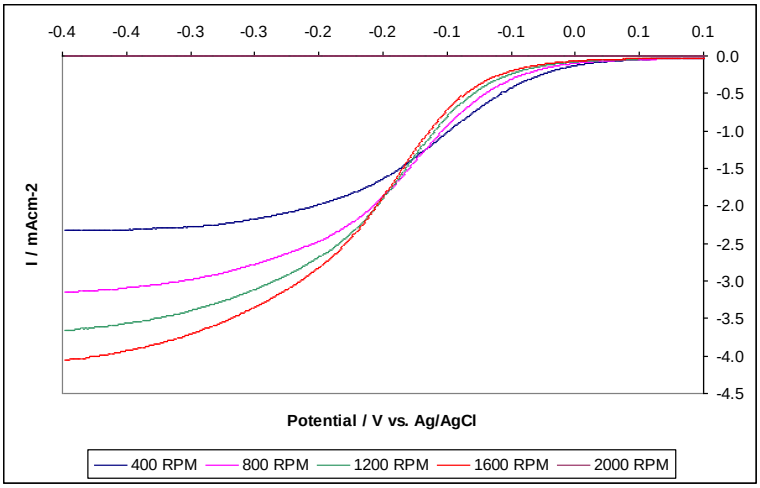

Figure 36: Polarisation curve for the oxygen reduction reaction on platinum at various rotation rates.

As with the cyclic voltammograms, the onset potential of the system can be seen from the intercept on the x axis. From the figure it can be seen that the limiting diffusion current has a higher magnitude at higher rotation speeds. This is due to the velocity of the solution being increased, which leads to a higher convective transport of electroactive material, and a shrinking of the diffusion layer thickness [138] as described by Equation 15 and 16.

Equation 15 $\delta_d = 1.61 D_B^{1/3} v^{1/6} w^{-1/2}$ [137, 138]

Equation 16 $J_L = D_B[B]bulk/\delta_d$

δ_d = Diffusion layer thickness (m) W = angular velocity of rotation (s^{-1})

D_B = Diffusion coefficient (m^2s^{-1}) J_L = Transport limited current (Am^2)

V = Kinematic viscosity of solution (m^2s^{-1}) [B] = Concentration of solution

Another important equation is the Koutecky-Levich equation which states:

Equation 17 $I_L = 0.62nFAD^{2/3}v^{-1/6}C_\infty w^{1/2}$ [21, 138-141]

I_L=Limiting current density (Acm^2) D=O_2 diffusion coefficient (cm^2s^{-1})

N=Number of electrons transferred per oxygen molecule V=Kinematic viscosity (cm^2s^{-1})

F=Faraday constant ($96500Cmol^{-1}$) C=Concentration of O_2 ($mol\ cm^{-3}$)

A=Area of the electrode (cm^2) W=Rotation rate (Radians)

By using Equation 17 we can determine how many electrons are transported by plotting $1/I_L$ vs $1/w^{1/2}$ at fixed potential. Once plotted (Figure 37) the gradient of the slope will give the electron exchange number. These Koutecky-Levich plots can also show if the electrode reaction is mass transport or kinetically controlled. If the intersection of $I/w^{1/2}$ is zero then it is mass transport controlled, otherwise it has a kinetically controlled component [142].

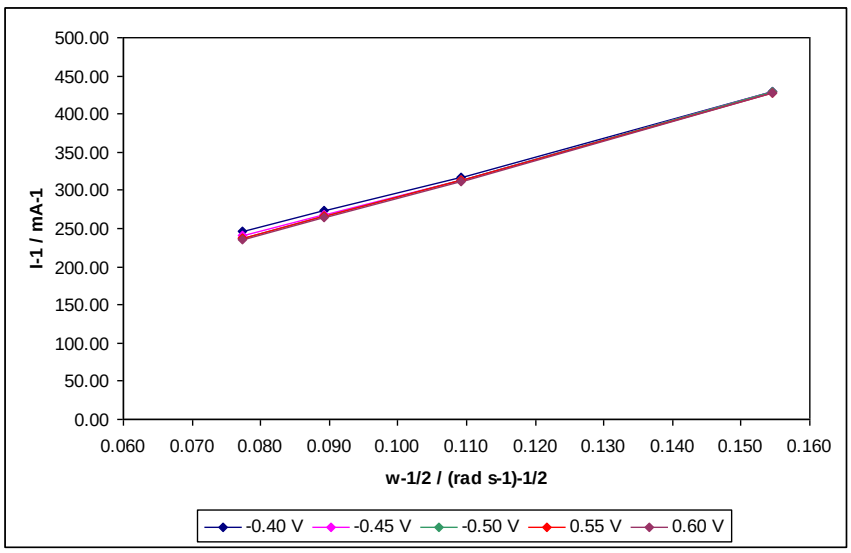

Figure 37: Koutecky-Levich plot for the oxygen reduction reaction on platinum at various fixed potentials.

The final information that can be derived from the RDE data is a Tafel plot. Tafel plots are derived from polarisation curves with a specific rotation rate, and plot Log I_k ($mAcm^{-2}$) vs the

electrode potential. These Tafel plots can compare the catalytic performance of each material [45, 141].

Despite the many benefits of using RDE measurement there is a disadvantage for some materials. This is because the area of the electrode material needs to be known. The problem with the materials examined in this study was that they could not be immersed properly due to them being too heavy, and therefore the results gathered could not be used to determine the number of electrons transferred. To discover which electron transfer is occurring it is necessary to use a rotating ring disk electrode which can detect the presence of hydrogen peroxide which could verify if this was a 2 or 4 electron process [143].

Other general problems include vortex formation and turbulence at high rotation rates in addition to the depletion of electroactive species, and the build up of unwanted products and intermediates.

3.7.3. Rotating Ring Disc Electrode (RRDE) Measurements

As already seen, the RDE experiment can be used to measure electrochemical rate constants. However to determine what happens after electron transfer, and if any intermediates are produced, it is necessary to use multiple electrode arrangements, in this case the ring disk configuration.

As with the RDE, the electrode is rotated and as this happens the solution in contact with the electrode is pushed to the side, crossing the ring and back into the bulk solution. If the flow is laminar, which is provided if R_e doesn't exceed $1*10^5$ as shown in Figure 38 and Equation 18, then the solution is brought into contact with the disk and the ring in a very controlled manner, resulting in any changes occurring during transport being monitored [21].

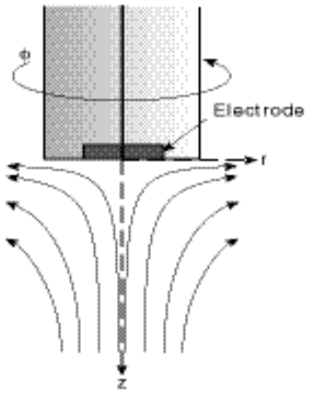

Figure 38: Laminar flow from a RDE/RRDE [144].

Equation 18 $R_e = wr_c^2 / v$

R_c=radius of cylinder (cm) V=viscosity of solution (cm^2s^{-1})

W=rotation rate (hertz)

As in RDE measurements the number of electrons detected at the ring can be calculated but the equation (Equation 19) is different due to the more complex geometry of the ring disk electrode [21].

Equation 19 $\delta_N = 1.61D^{1/3}v^{1/6}w^{-1/2} (r_3^3-r_2^3)^{1/3} / r \quad r_2 \leq r \leq r_3$

δ_N= Diffusion length (cm)

D= Diffusion coefficient of O_2 (cm^2s^{-1})

V= Kinematic viscosity (cm^2s^{-1})

W= Rotation rate (radians)

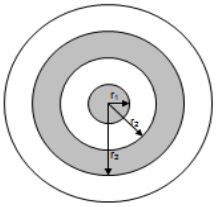

An example of data recorded from RRDE measurements can be seen in Figure 39. The two graphs show polarisation curves from the ring and the disk. For the FePc/C (carbon supported Fe-phthalocyanine) and Pt/C (carbon supported platinum) there was no significant ring current observed starting at the ORR onset potential of the disk electrode, meaning a negligible amount of H_2O_2 was produced. In comparison there was a significant ring current detected for the CoPc/C (carbon supported Co-phthalocyanine) electrode meaning significant H_2O_2 was produced. This in

turn means that for the first 2 catalysts a $4e^-$ procedure occurred compared to a $2e^-$ procedure for the CoPc/C catalyst [21, 141].

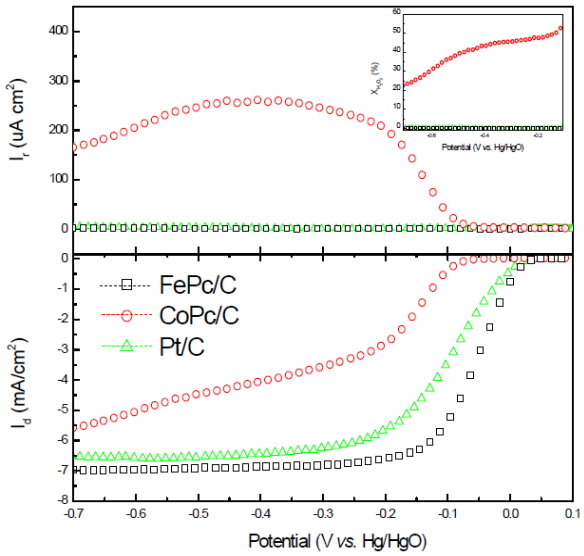

Figure 39: RRDE plot showing the current observed at the disk and the ring for carbon supported iron and cobalt phthalocyanine as well as platinum.
According to Ref [141] Elsevier permission.

3.7.4. Fuel Cell Testing

There are many different techniques that can be used to characterise the components of the fuel cell. However while individual materials testing can provide useful information, ultimately it is necessary to perform *in situ* testing of a complete fuel cell as performance cannot be determined solely by the individual properties of the components, but also the interaction between the components can cause decreased performance. *In situ* testing is performed by fuel cell test stations, a schematic of which is shown in Figure 40 [18, 145].

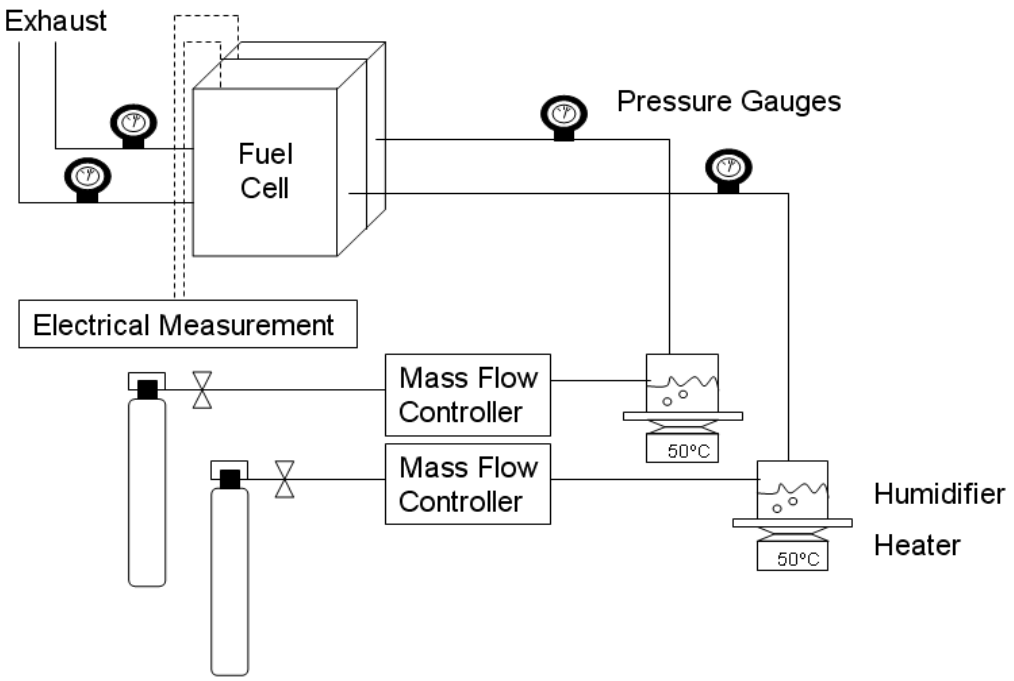

Figure 40: Schematic of a fuel cell test station.

The test conditions are extremely important as they can dramatically affect the fuel cell performance. The temperatures, pressures, flow rates and compression force, gas and humidity all must be taken into account and kept identical to determine the relative performance differences between two fuel cells. In addition, before testing begins, the cell must be conditioned so that the fuel cell environment is stable.

The most common fuel cell measurement used is the fuel cell polarisation (I-V) curve. For this experiment a potentiostat/galvanostat draws a fixed current from the fuel cell and then measures the fuel cell output voltage. The load (current) of the potentiostat/galvanostat is slowly increased with the voltage response recorded. This voltage drop is not instantaneous and can sometimes take hours for the voltage to stabilise especially with the larger fuel cells. This is due to subtle changes in the cell such as temperature and flow rates. An example of the I-V curve is shown in Figure 41. As seen from the figure the voltage decreases as more current is drawn from the cell. There are three regions of fuel cell loss which give the shape of the I-V curve [18, 145]:

1. Activation losses due to the electrochemical reactions.

2. Ohmic losses due to ionic and electronic conduction.

3. Concentration losses due to mass transport.

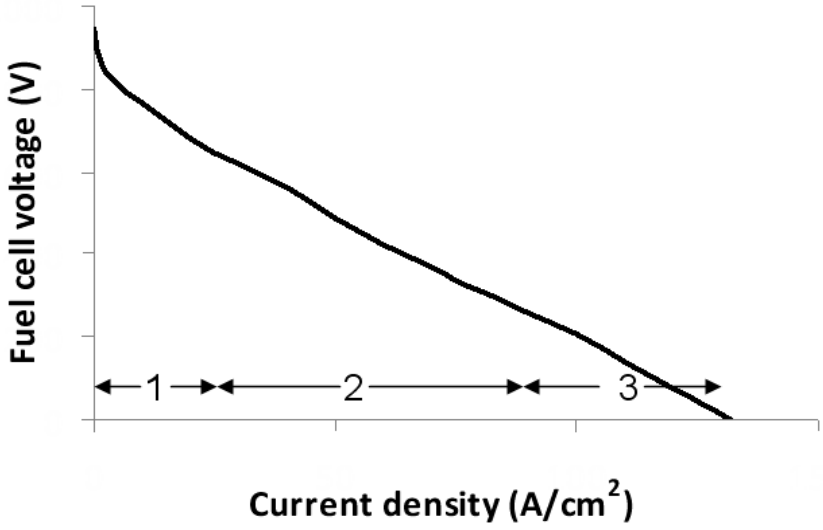

Figure 41: Polarisation curve showing the different regions of voltage loss (1=Activation losses, 2=Ohmic losses and 3=Concentration losses).

From the I-V curve, a power density curve, which shows the power density delivered by the fuel cell as a function of current density, can be plotted. The power density can be calculated by multiplying the current density normalised by the fuel cell area with the voltage. Published data usually show a combined fuel cell I-V and power density curve (Figure 42) [18, 145].

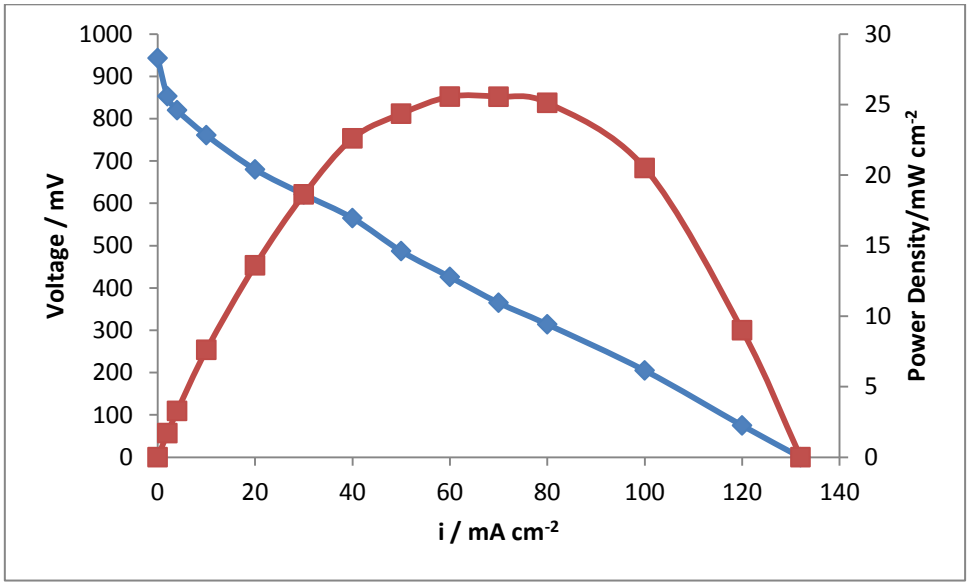

Figure 42: An example of fuel cell performance with the blue line showing the polarisation curve (mV) and the red showing the power density of the cell.

The fuel cell testing performed in this project was carried out by Dr Simon Poynton at the University of Surrey.

4. Anion Interstitial Incorporation/Exchange in Ruddlesden Popper Systems

4.1. Synthesis and Analysis of $La_2NiO_{4+\delta}$ Systems

4.1.1. Introduction

One interesting material that has the K_2NiF_4 structure is $La_2NiO_{4+\delta}$. The structure consists of alternating layers of perovskite, $LaNiO_3$, and rock salt, LaO, along the c axis as seen in Figure 43 [66, 68, 70, 73, 146, 147]. As can be seen from the formula, this phase (like many other K_2NiF_4 systems) has the ability to accommodate excess anions, due to the presence of available space in the rock salt layer to incorporate such extra anions into the structure [65, 66, 70, 73, 146-148]. In $La_2NiO_{4+\delta}$ the excess O^{2-} is charge compensated by Ni^{3+} ions (holes) leading to an enhancement in the electronic conductivity. Moreover the presence of these excess oxide ions has also been reported to enhance the oxide ion conductivity, leading to a large amount of interest in this material as a SOFC cathode [66, 70, 73, 146].

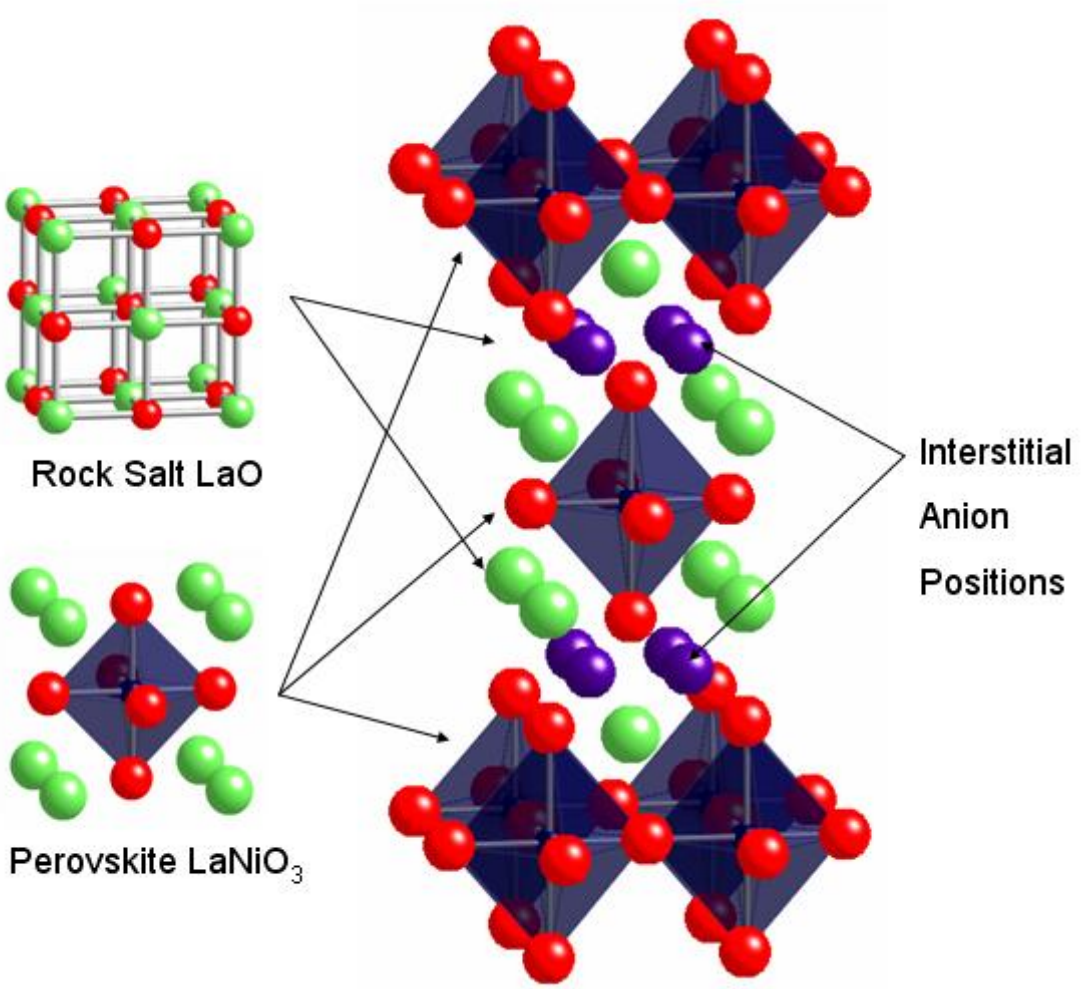

Figure 43: Structure of $La_2NiO_{4+\delta}$.

The presence of these interstitial anions can affect the structural symmetry of the material. Thus $La_2NiO_{4+\delta}$ material has a range of potential oxygen hyperstoichiometry dependant on the method of synthesis. The additional oxygen anions are incorporated into the rock salt layers and depending on the level of oxygen excess different symmetries result as seen in Figure 44 [66, 70, 71, 146-148]. Since the oxygen hyperstoichiometry is most favoured at low temperatures structural changes can also be observed by heating the material, with the high oxygen excess orthorhombic (Fmmm) phase undergoing a phase change to a lower oxygen content tetragonal phase on heating due to the loss of oxygen [70, 71, 146, 148, 149].

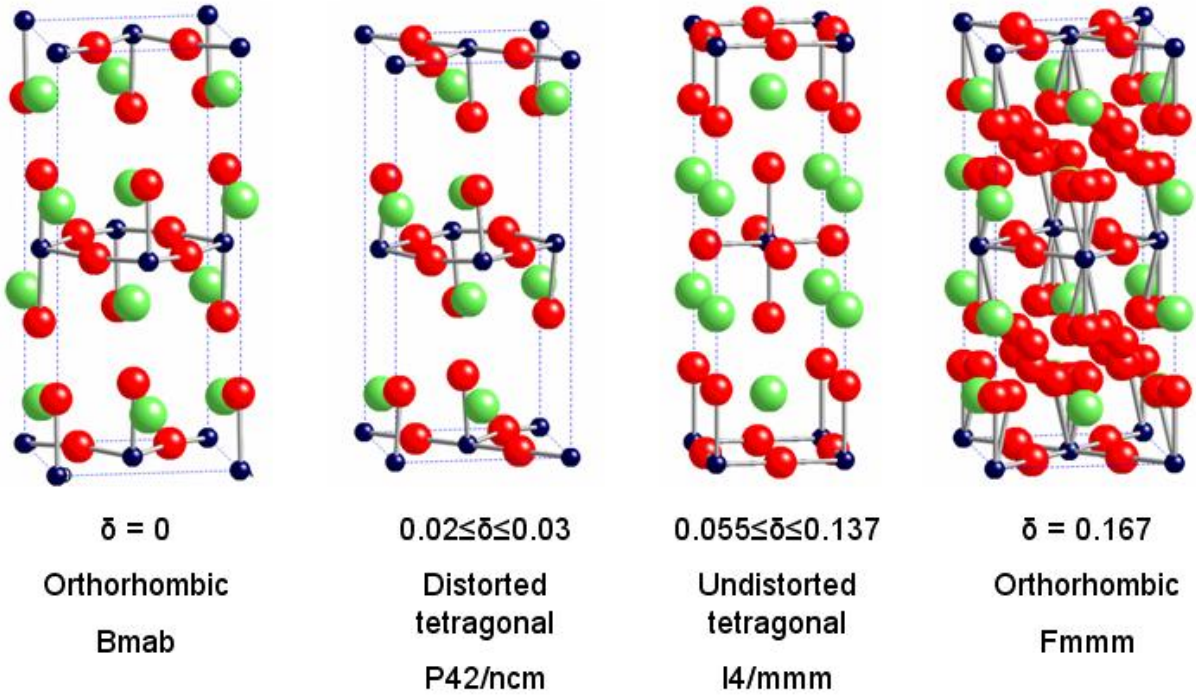

Figure 44: Different symmetries for a range of oxygen excess $La_2NiO_{4+\delta}$.

The $La_2NiO_{4+\delta}$ system has attracted significant interest in its properties. Due to its similar structure with the high temperature cuprate superconductor $La_2CuO_{4+\delta}$, it was widely researched for possible superconductivity [66, 69, 150, 151]. However while traces of superconductivity were initially reported in highly acceptor doped nickelates [68], such results have not been found to be reproducible. More recently this system has found applications as a cathode material in solid oxide fuel cells. In this respect this material shows good mixed ionic and electronic conductivity with fast oxide ion conductivity over a wide range of temperatures [70, 71, 73, 147, 150, 152]. The catalytic properties of this material are also beneficial for such cathode applications [150, 151]. In addition, for use in fuel cells, the material must be stable in conjunction with the electrolyte, and $La_2NiO_{4+\delta}$ is also competitive with existing perovskite materials in this area [70]. Along with the competitive chemical stability of these materials, they have good thermal expansion match with conventional electrolytes [66, 69, 70]. While there has been detailed research of this system for SOFC applications, potential applications in lower temperature fuel cells have not been performed. Therefore in this study the potential for use of $La_2NiO_{4+\delta}$ in low temperature fuel cells was examined

with a view to investigating the effect of interstitial anion content on the performance. The ability to accommodate water into $La_2NiO_{4+\delta}$ was studied via both direct and an indirect route. The direct route involved heating in wet atmospheres, while the indirect route involved preparation of an oxide fluoride followed by ion exchange of OH^- for F^-.

4.1.2. Experimental

High purity La_2O_3 and NiO were used to prepare the $La_2NiO_{4+\delta}$ sample. The starting materials were ground together in the correct stoichiometric ratio and heated to 1100^{o}C for 12 hours. The samples were then reground and further heated to 1300^{o}C for another 12 hours.

Powder X-ray diffraction experiments using a Bruker D8 transmission diffractometer with Cu $K\alpha_1$ radiation were used to determine phase purity and the GSAS suite of programs was used for the refinements of the structure.

4.1.3. Structural Determination of $La_2NiO_{4+\delta}$

As previously mentioned in the introduction, the structure depends on the synthesis method due to resultant variations in the amount of oxygen incorporated into the interstitial sites. For the samples in this thesis the space group assigned from the XRD data was Fmmm. A Rietveld refinement was performed, which resulted in a good fit to the data as seen in Figure 45. The resultant structural parameters are given in Table 5 and 6. The interstitial site (O2) is found at 0.25, 0.25, 0.23 (1) and the occupancy was allowed to vary resulting in the formula $La_2NiO_{4.32}$. Due to this insertion of additional oxygen atoms into the lattice a displacement of the apical O3 oxygen occurs. This incorporation forces the O3 apical oxygen into 2 split positions (Here O3 and O4) [148, 153, 154]. Figure 46 shows the positions of the oxygen in $La_2NiO_{4+\delta}$. For the refinement, the atomic displacement parameters for the anion sites were all constrained to be equal and then allowed to refine. In addition the O3 and the O4 occupancies were constrained together for the refined total occupancy to equal 2. In addition the O2 occupancy was constrained to be 4 times smaller than the O4 occupancy in agreement with prior studies [153]. The results show that the oxygen content is larger than δ=0.167 (In this case δ = 0.32), previously reported for the orthorhombic phase which

may be related to issues with using XRD data rather than ND data. X-ray diffraction is less sensitive to lighter oxygen than neutron diffraction, so this is probably leading to issues, which may then result in an overestimation of oxygen content.

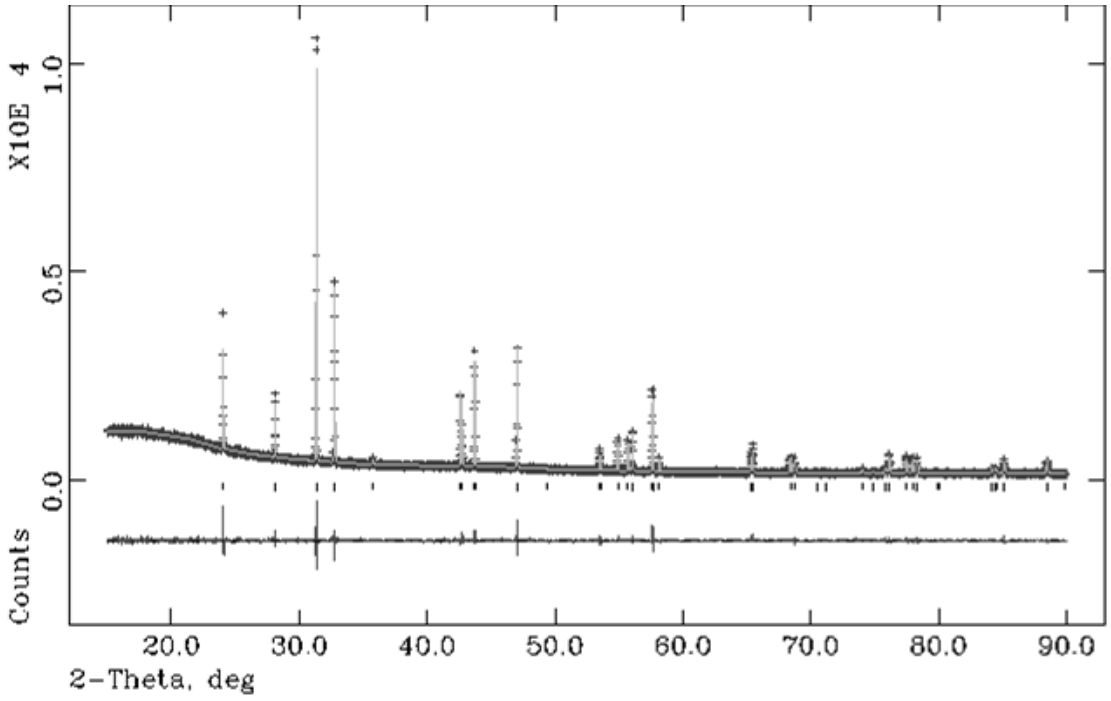

Figure 45: Observed, calculated and difference x ray diffraction profiles for $La_2NiO_{4+\delta}$.

Table 5: Structural parameters for $La_2NiO_{4+\delta}$.

Atom	Multiplicity	X	Y	Z	Uiso	Occupancy
La1	8	0	0	0.36111 (8)	0.75 (5)	1
Ni1	4	0	0	0	1.3 (1)	1
O1	8	0.25	0.25	0	1.9 (3)	1
O2	16	0.25	0.25	0.225 (9)	1.9 (3)	0.08 (2)
O3	8	0	0	0.174 (6)	1.9 (3)	0.4 (1)
O4	32	-0.07 (1)	-0.06 (1)	0.171 (5)	1.9 (3)	0.15 (3)
Fmmm, a=5.45265(4), b=5.45859(4),c=12.66989(9), χ^2= 1.589, Rwp=6.29%						

Table 6: Bond distances for $La_2NiO_{4+\delta}$.

Bond	Bond Length
La1-O1	2.6109 (7) x4
La1-O2	2.58 (8) x4
	2.22 (6) x4
La1-O3	2.37 (8) x1
	2.766 (13) x2
	2.763 (13) x2
La1-O4	2.46 (7) x4
	3.09 (7) x4
	2.48 (6) x4
	2.39 (6) x4
Ni1-O1	1.92885 (1) x4
Ni1-O3	2.21 (8) x2
Ni1-O4	2.22 (7) x8

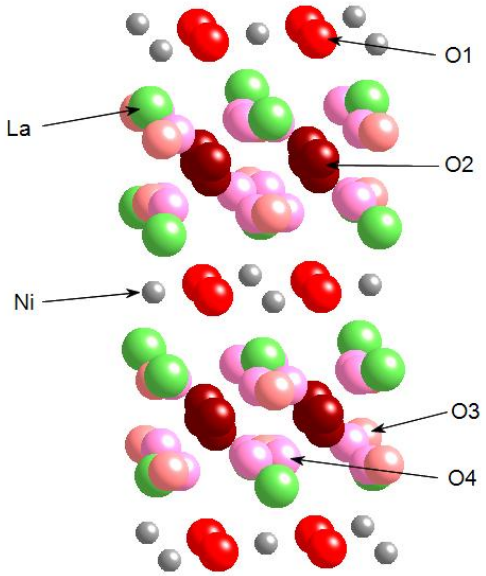

Figure 46: Structure of $La_2NiO_{4+\delta}$ showing positions of the different oxygens.

While $La_2NiO_{4+\delta}$ has attracted significant interest as a SOFC cathode, there have been no prior studies of this material for use in low temperature alkaline fuel cells (AFC). In this respect a first experiment was to determine the stability in the fuel cell environment. For use in an AFC the $La_2NiO_{4+\delta}$ has to be resistant to alkaline conditions as well as H_2O_2 which could be produced if carbon electrode supports are used, as well as if incomplete reduction of oxygen at the cathode catalyst occurs.

The stability of the material was determined by analysing by X-ray diffraction both before and after placing the material in a hydrothermal bomb with 1M KOH and 10% H_2O_2 and heating at 200^{o}C for 2 days. These are quite extreme conditions, far greater than would typically be observed, but were chosen to partially mimic the effects of long term usage at lower temperatures. Any difference in the XRD patterns (Figure 47) and cell parameters (Table 7) should show if degradation has occurred.

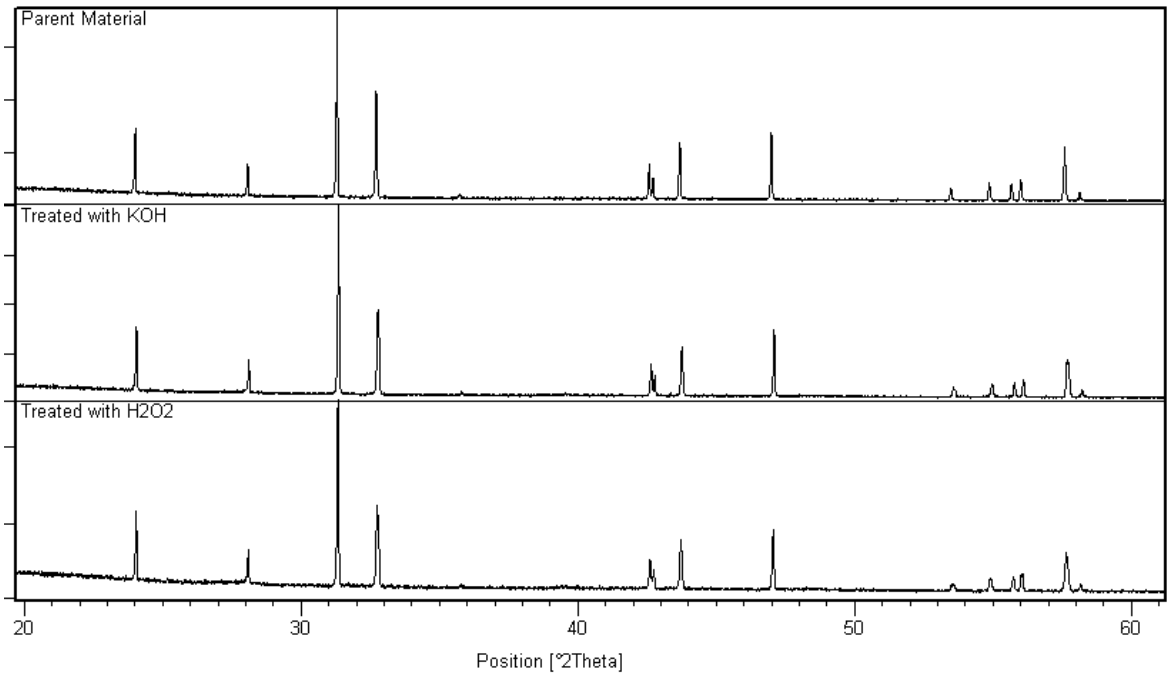

Figure 47: Powder X-ray diffraction patterns for stability tested $La_2NiO_{4+\delta}$.

Table 7: Cell parameters for stability tested $La_2NiO_{4+\delta}$.

Sample	a (Å)	b (Å)	c (Å)	Cell Volume (Å^3)
Parent	5.4602 (5)	5.4572 (5)	12.6731 (6)	377.62 (4)
KOH Treated	5.4453 (3)	5.4474 (3)	12.6509 (6)	375.26 (3)
H_2O_2 Treated	5.4475 (4)	5.4544 (4)	12.6656 (6)	376.33 (3)

The X-ray diffraction data show no impurity phases, which suggests that this material shows generally good stability in alkaline conditions. There were some small changes in cell parameters which may reflect some changes in oxygen content or water content.

4.1.4. Water Incorporation Studies

For application as electrode materials in alkaline fuel cells the ability to accommodate H_2O and hence introduce OH^- ions was also examined i.e.

$$La_2NiO_4 + xH_2O \leftrightarrow La_2NiO_{4-x}(OH)_{2x} \text{ or}$$

$$La_2NiO_4 + x/2O_2 + xH_2O \leftrightarrow La_2NiO_4(OH)_{2x}.$$

4.1.4.1. Experimental

Two methods were examined to investigate the incorporation of water in $La_2NiO_{4+\delta}$. In the first method the parent material was placed in a tube furnace and exposed to a variety of different atmospheres. The sample was exposed to both wet oxygen and nitrogen atmospheres for 16 hours at 350^{o}C with ramping rates of 3.33^{o}C per minute.

Characterisation was achieved using powder X-ray diffraction experiments with a Bruker D8 transmission diffractometer as well as a variable temperature Bruker D8 reflection instrument with a MRI heating stage. Both diffractometers use Cu $K\alpha_1$ radiation. The GSAS suite of programs was used for structure refinements and the Unit Cell program to determine cell parameters.

Water contents were determined using thermogravimetric analysis (Netzsch STA 449 F1 Jupiter Thermal Analyser). The samples were heated to 500^{o}C at 10^{o}C per minute to eliminate any water present.

4.1.4.2. Results and Discussion

When subjecting the $La_2NiO_{4+\delta}$ material to different atmospheres there was no significant change in the XRD pattern as shown in Figure 48, although small changes in cell parameters were observed (Table 8).

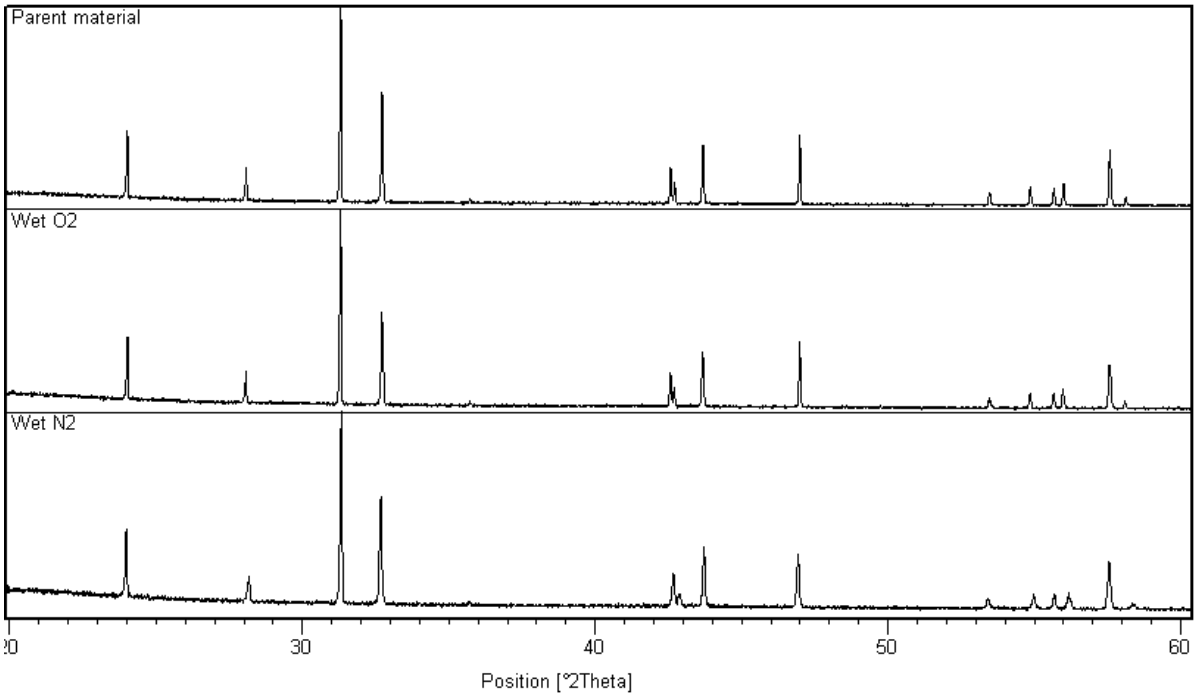

Figure 48: X-ray diffraction patterns for $La_2NiO_{4+\delta}$ exposed to different atmospheres.

Table 8: Cell parameters for $La_2NiO_{4+\delta}$ exposed to different atmospheres.

Sample	a (Å)	b (Å)	c (Å)	Cell Volume (Å^3)
Parent Material	5.4651 (4)	5.4633 (4)	12.6752 (6)	378.45 (3)
Wet N_2	5.4592 (4)	5.4579 (4)	12.6141 (6)	375.84 (3)
Wet O_2	5.4591 (4)	5.4595 (4)	12.6780 (6)	377.85 (3)

The results show slight changes in cell parameters with the various heat treatments, however some of these could be due to changes in oxygen content, rather than water incorporation. In order to determine if water has been incorporated into the interstitial sites, thermogravimetric analysis of the samples was performed, along with mass spectrometry of the components being lost on heating. As shown in Figure 49 there was no decrease in the weight % of the samples suggesting that no water has been incorporated into the material that can be detected by TGA-MS.

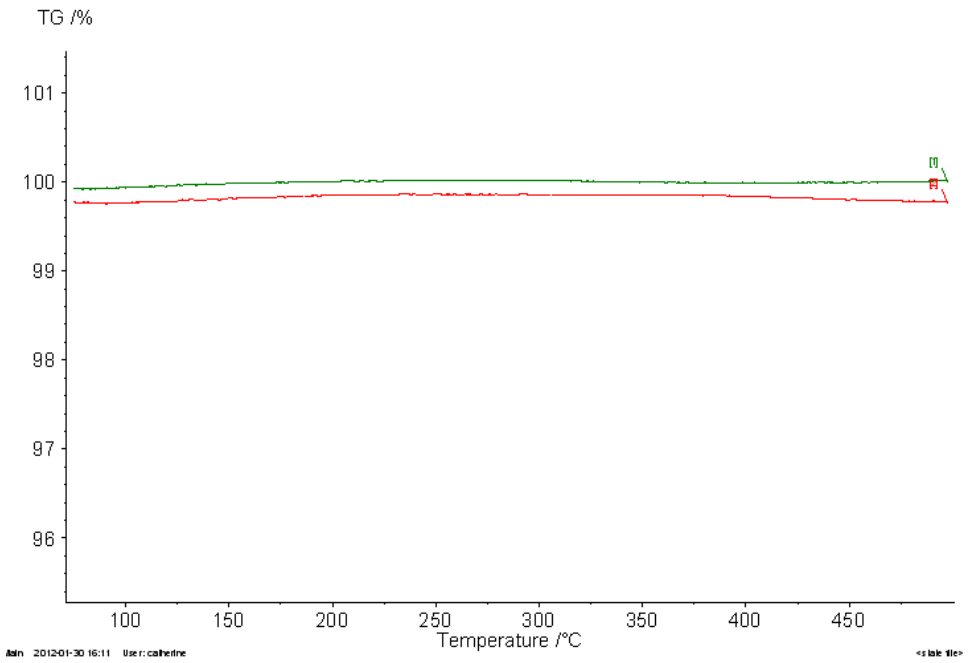

Figure 49: Weight losses of $La_2NiO_{4+\delta}$ after being exposed to different atmospheres (wet O_2 = red and wet N_2 = green).

The initial results from this work therefore suggested that there is no water incorporation in $La_2NiO_{4+\delta}$, unlike the related K_2NiF_4 systems such as Ba_2MO_4 (M=Zr and Sn) where up to 2 moles of H_2O per formula unit is observed [155].

Following these not very promising initial results, further experiments were performed under more extreme conditions, namely heating in different solutions hydrothermally at 200°C. Under such conditions there were small changes in the XRD patterns (Figure 50) with the (020)/(200) peak showing greater splitting after the heat treatments in $KMnO_4$ and H_2O_2 solutions while shoulders on the peaks were seen in the KOH and H_2O samples. The cell parameters are shown in Table 9 which show only small changes between samples. However the incorporation of water in these systems was confirmed from TGA analysis (Table 9). The level of water incorporation was still, however, lower than observed in other K_2NiF_4 systems e.g. $Ba_2(Sn/Zr)O_4$. Therefore in order to achieve greater water incorporation an indirect method was examined, namely ion exchange of a fluorinated material (see next section).

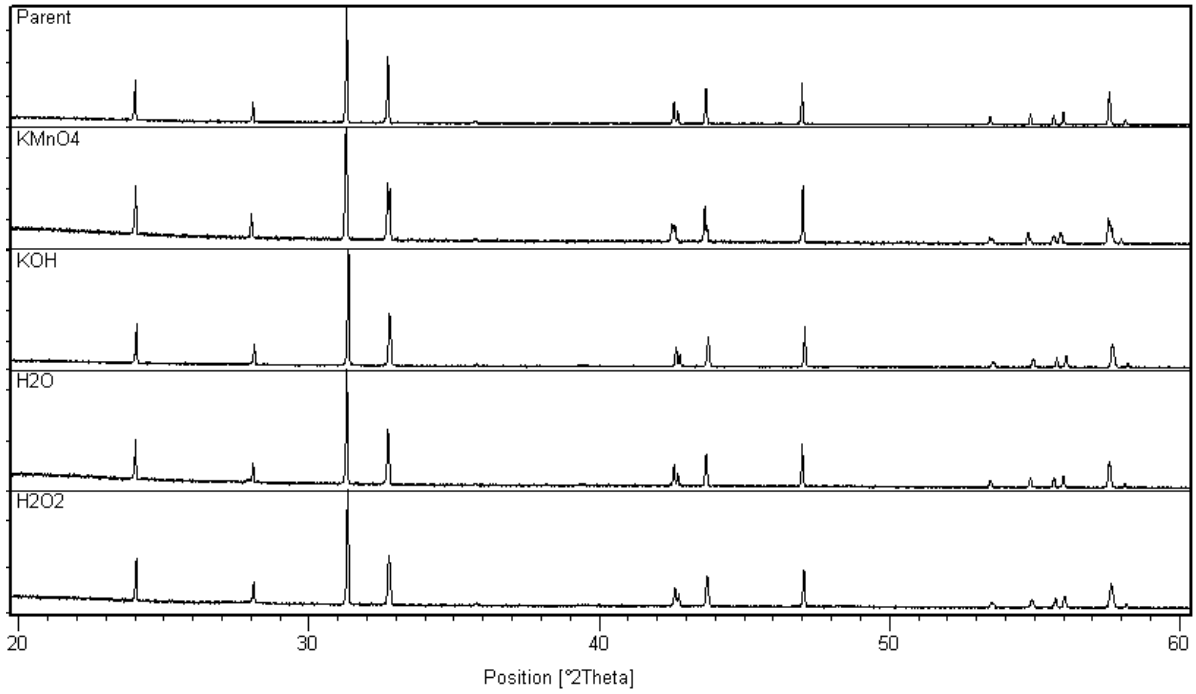

Figure 50: Powder X-ray patterns of $La_2NiO_{4+\delta}$ immersed in different solutions heated hydrothermally at 200°C for 48 hours.

Table 9: Cell parameters and water contents for $La_2NiO_{4+\delta}$ heated hydrothermally at 200°C for 48 hours in different solutions.

Material	a (Å)	b (Å)	c (Å)	Cell volume (Å^3)	Water Content (moles per formula unit)
Parent	5.4572 (5)	5.4602 (5)	12.6731 (6)	377.62 (4)	-
0.1M $KMnO_4$	5.4507 (3)	5.4570 (3)	12.6976 (6)	377.68 (3)	0.16
1M KOH	5.4453 (3)	5.4474 (3)	12.6509 (6)	375.26 (3)	0.18
H_2O	5.4558 (4)	5.4571 (4)	12.6731 (6)	377.31 (3)	0.19
1M H_2O_2	5.4475 (4)	5.4544 (4)	12.6656 (6)	376.33 (3)	0.26

4.1.5. Incorporation of Extra Anions via Fluorination

The initial experiments suggested only a small amount of water incorporation in $La_2NiO_{4+\delta}$. Therefore an alternative strategy for greater H_2O incorporation was examined involving the initial synthesis of a fluorinated analogue followed by OH-/F- ion exchange. The successful fluorination of $La_2CuO_{4+\delta}$ and $La_2NiO_{4+\delta}$ has been reported previously via the low temperature reaction of the parent oxide with a fluorinating agent, in these studies fluorine gas was used as the fluorinating agent [103].

In this work two different methods were examined to fluorinate this material, namely reaction with PVDF and CuF_2.

4.1.5.1. Experimental

The parent material $La_2NiO_{4+\delta}$ was ground with PVDF/CuF_2 in the correct molar ratios of La_2NiO_4:PVDF/CuF_2 to achieve the required F content. For PVDF the ratio was based on the monomer equivalent i.e. CH_2CF_2. These samples were then placed in a furnace in a fume cupboard with a slow heating rate to 350°C for 24hrs with an intermediate regrind. The ion exchange was performed by immersing the fluorinated material in 1M KOH in a hydrothermal vessel and heating for 2 days at 200°C. This exchange was then repeated until the material was fully exchanged.

4.1.5.2. Results and Discussion

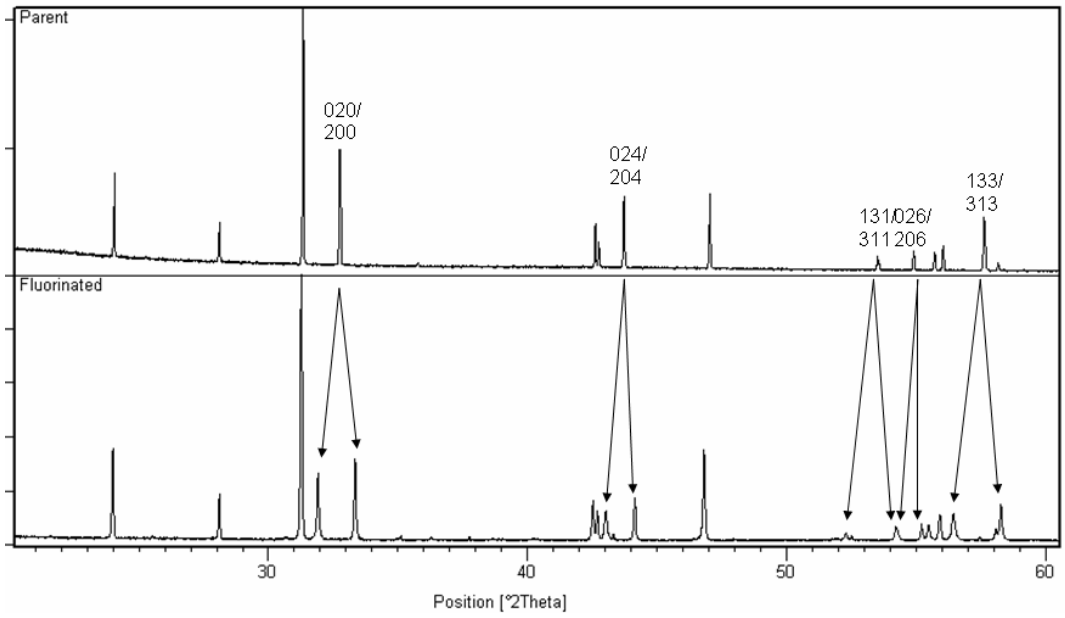

Figure 51: X-ray diffraction pattern of the parent and fluorinated $La_2NiO_{4+\delta}$ material.

Both fluorination methods were successful, with X-ray diffraction of the fluorinated systems showing a significant change compared to the parent material. However in the case of reaction with CuF_2, a CuO impurity is obtained, a known problem with this method. In contrast the samples fluorinated with PVDF were shown to be pure and so further work focused on samples prepared by this method. The successful fluorination with PVDF is shown in Figure 51, which shows a large

splitting of (020)/(200), (024)/(204), (026)/(206) and (133)/(313) peaks indicating a large increase in the orthorhombic splitting. On increasing the fluorination levels to higher amounts there is no longer a single phase, but rather extra peaks are seen, which are believed to be due to higher fluorinated $La_2NiO_{4+\delta}$ (Figure 52). Attempts to prepare a pure sample of this higher content phase were unsuccessful, with higher levels of PVDF leading to large LaF_3 impurities.

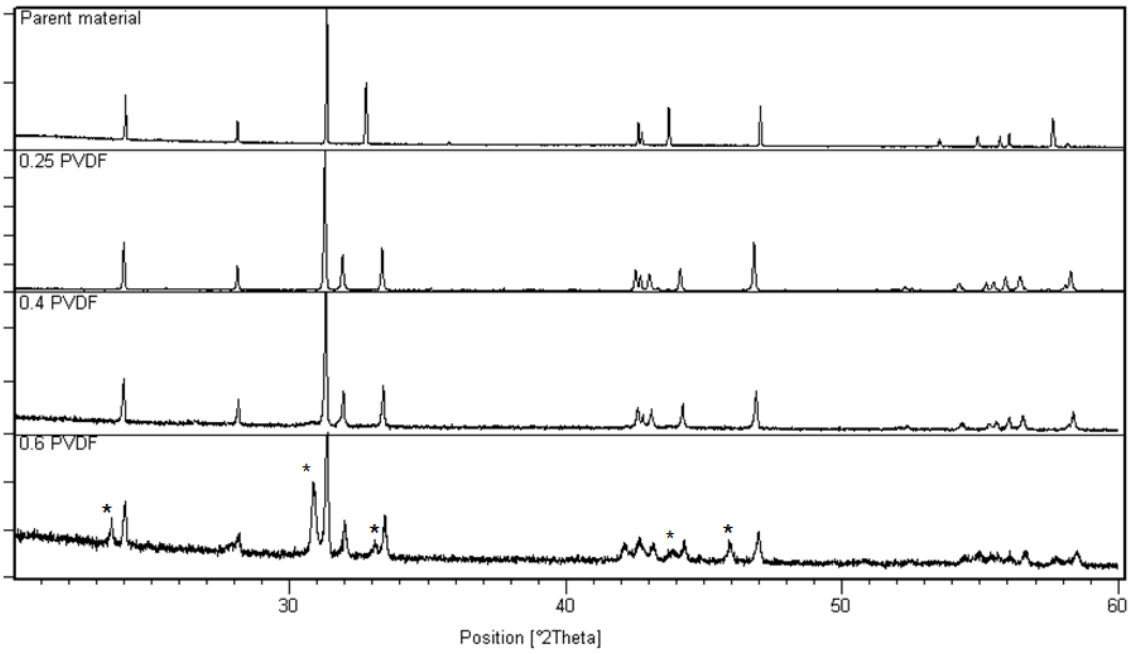

Figure 52: X-ray diffraction patterns of $La_2NiO_{4+\delta}$ samples fluorinated with different amounts of PVDF. At the higher levels (ratio 1 La_2NiO_4 : 0.6 PVDF) extra peaks are seen (marked *) which are believed to be from a higher F content phase.

The structure of the single phase sample fluorinated using 0.25 PVDF was examined using Rietveld refinement. The observed, calculated and difference profiles are shown in Figure 53 while the structural parameters are shown in Table 10 and 11.

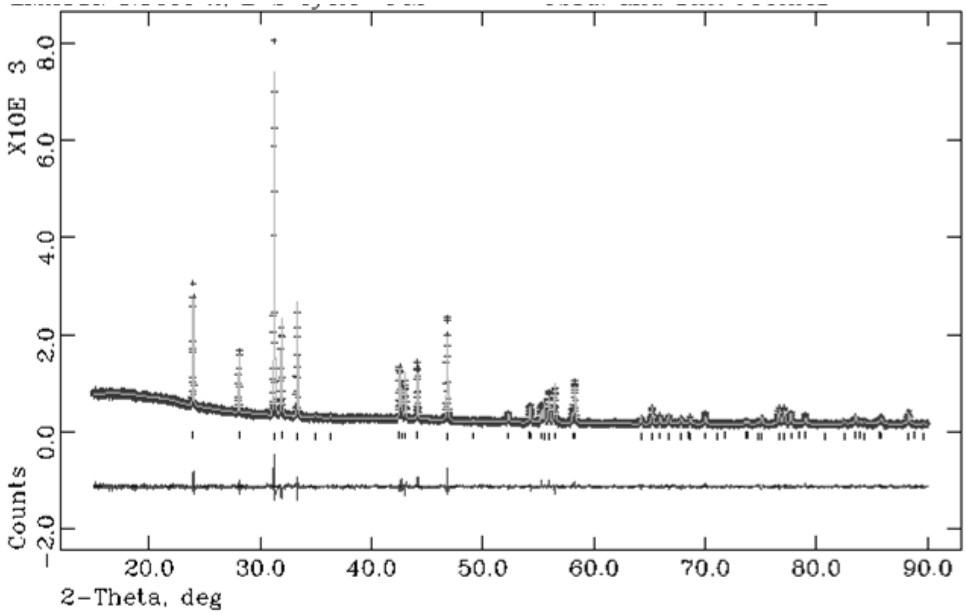

Figure 53: Observed, calculated and difference neutron diffraction profiles for La_2NiO_4 : 0.25 PVDF.

Table 10: Structural parameters for La_2NiO_4 : 0.25 PVDF. F is believed to be located on the O2 and O3/O4 sites.

Atom	Multiplicity	X	Y	Z	Uiso	Occupancy
La1	8	0	0	0.36103 (9)	1.52 (5)	1
Ni1	4	0	0	0	1.2 (1)	1
O1	8	0.25	0.25	0	2.2 (4)	1
O2	16	0.25	0.25	0.225 (7)	2.2 (4)	0.12 (2)
O3	8	0	0	0.17 (3)	2.2 (4)	0.1 (1)
O4	32	-0.060 (7)	-0.062 (7)	0.171 (4)	2.2 (4)	0.23 (3)
Fmmm, a=5.36781(7), b=5.60196(8),c=12.6887(2), χ^2= 1.616, Rwp=6.87%						

Table 11: Bond distances for fluorinated La_2NiO_4 : 0.25 PVDF.

Bond	Bond Length
La1-O1	2.6214 (8) x4
La1-O2	2.59 (6) x4
	2.23 (4) x4
La1-O3	2.4 (4) x1
	2.84 (6) x2
	2.72 (6) x2
La1-O4	2.46 (5) x4
	2.51 (4) x4
	2.422 (34) x4
	3.05 (4) x4
Ni1-O1	1.93964 (2) x4
Ni1-O3	2.2 (4) x2
Ni1-O4	2.22 (5) x8

The same refinement parameters from the parent material were used for the refinement of the fluorinated material. The fluorine incorporation was assumed to increase the occupancy of the interstitial site at the O2 position. The occupancy of this site was allowed to refine and increased on fluorination consistent with the incorporation of additional anions as expected from the partial replacement of 1 O^{2-} by 2 F^-. This F incorporation is also confirmed by the expansion of the unit cell resulting from the extra anions within the structure. Apart from the increase in anion interstitial content the main other structural changes are changes in the bond distances between the nickel and anion sites, in particular an increase in the Ni-O1 distance. Although we are unable to determine by X-ray diffraction the exact location of F (due to the similar scattering factor with O) we presume the F is located in the interstitial sites and/or the apical sites as predicted by modelling studies for structurally related $Sr_2CuO_2F_{2+\delta}$ [156].

In order to produce a metastable hydrated $La_2NiO_{4+\delta}$, ion exchange (OH^- for F^-) of the fluorinated material was attempted. After the first exchange experiment XRD analysis was performed to determine if any change had occurred. As can be seen from the XRD patterns (Figure 54) there appeared to be no major change, with the cell parameters (Table 12) increasing slightly after the exchange. In order to determine whether there had indeed been any OH^-/F^- exchange TGA experiments were performed. The TGA (Figure 55) experiments showed a mass loss consistent with 0.1313 moles of water being lost on heating. Moreover, after the TGA measurement, XRD was performed on the sample which showed a small decrease in cell volume. Both results are consistent with a partial F^-/OH^- exchange and subsequent loss of the OH^-as H_2O in the TGA experiments.

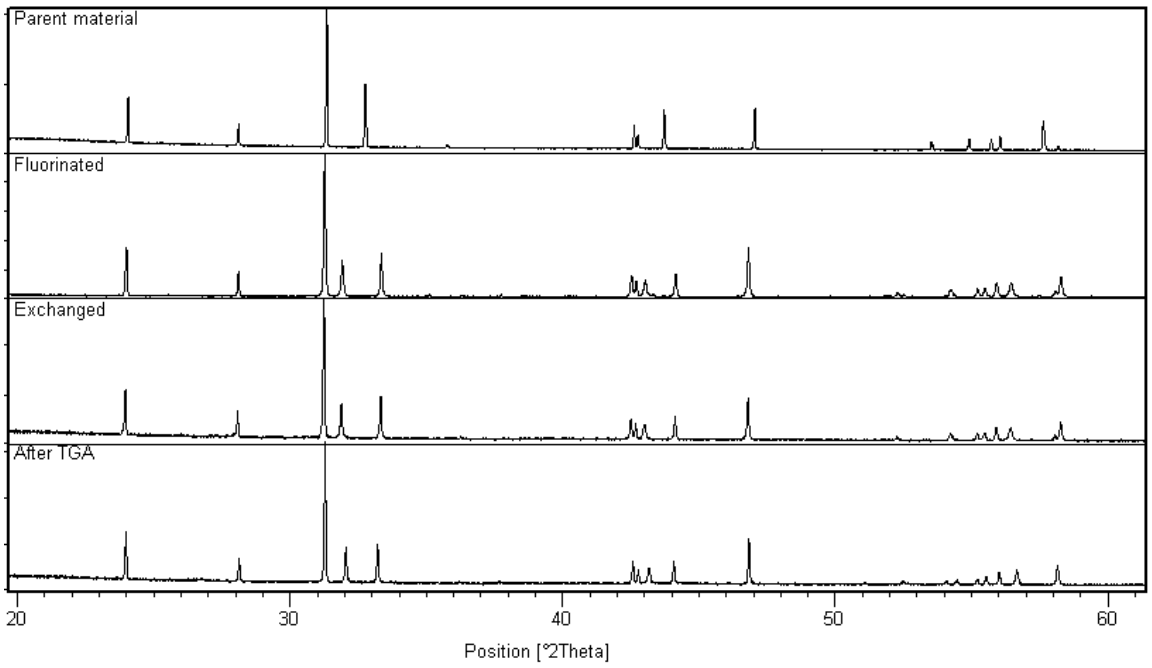

Figure 54: Powder X-ray diffraction patterns for $La_2NiO_{4+\delta}$ throughout the exchange process.

Table 12: Cell parameters for $La_2NiO_{4+\delta}$ throughout the exchange process and subsequent analysis by TGA .

	a (Å)	b (Å)	c (Å)	Cell Volume (Å^3)
Parent	5.45265 (4)	5.45859 (4)	12.66989 (9)	377.104 (7)
Fluorinated	5.36780 (7)	5.60196 (8)	12.6887 (2)	381.55 (1)
Exchanged	5.37093 (10)	5.6061 (1)	12.6959 (2)	382.27 (2)
After TGA	5.38727 (9)	5.57711 (9)	12.6690 (2)	380.65 (1)

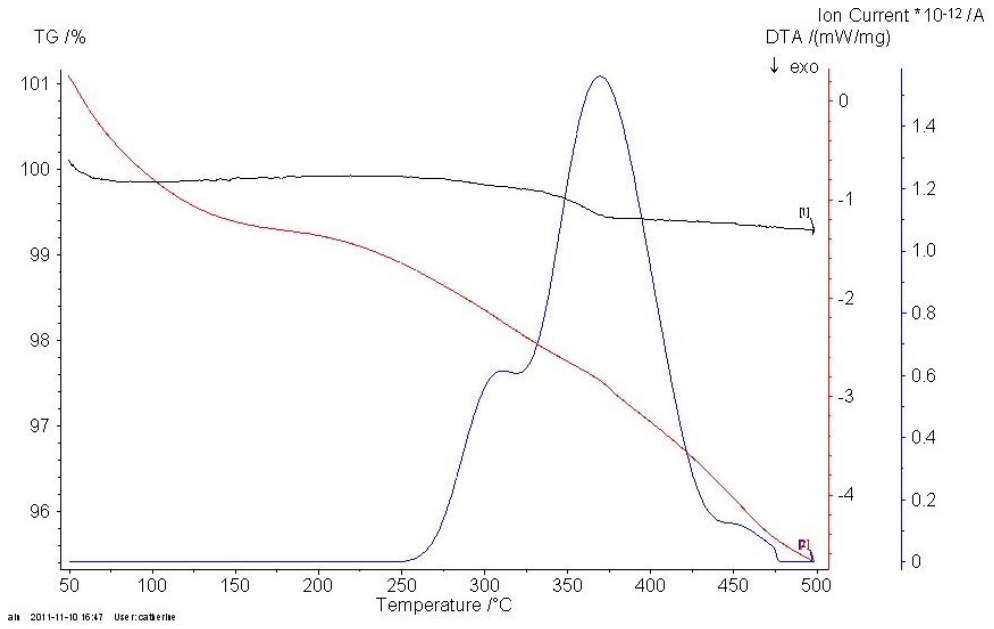

Figure 55: TGA of exchanged $La_2NiO_{4+\delta}$ showing weight loss in black, DTA in red and H_2O release in blue.

The results therefore showed that, when comparing the first exchanged material with the fluorinated material, there is a significant change. Further confirmation is provided by TGA experiments of the as prepared fluorinated sample, (Figure 56) which showed no weight loss occurring in the fluorinated material.

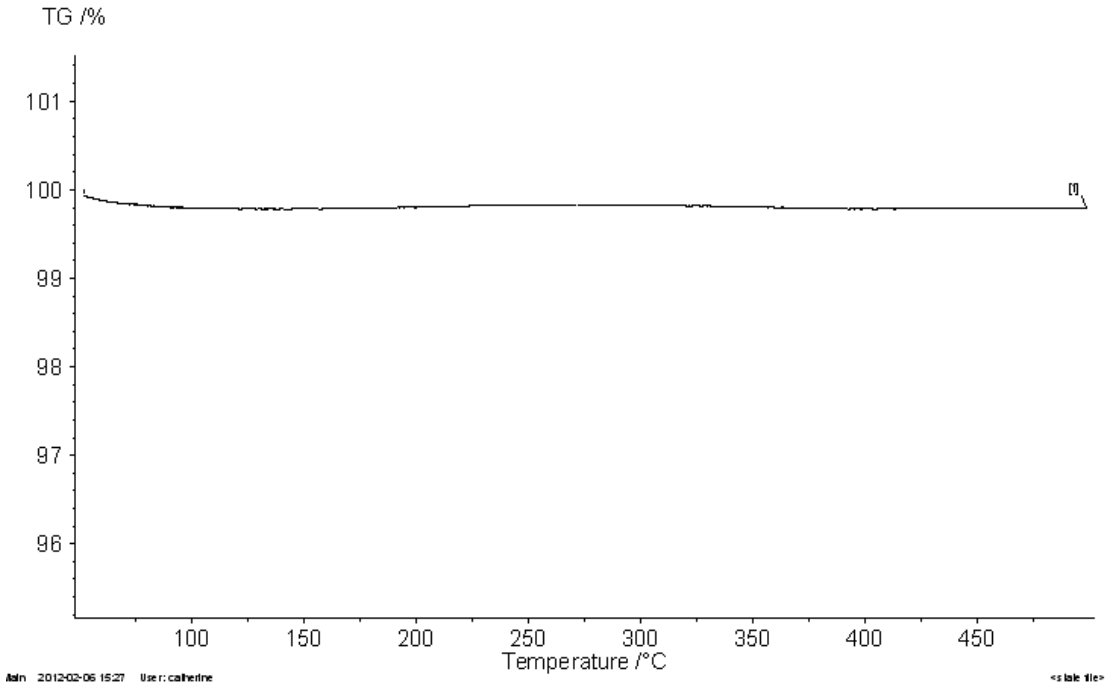

Figure 56: TGA of Fluorinated $La_2NiO_{4+\delta}$.

The initial results were therefore positive, but suggested that a single exchange was insufficient to completely replace all the F^- by OH^-. The exchange process was therefore repeated several times. The material was deduced to be fully exchanged when after performing the TGA studies the XRD showed a pattern similar to the parent material along with similar cell parameters. This showed that the material is fully exchanged after performing the ion exchange 7 times. After this number of exchanges, the TGA results indicated a water content of 0.64 moles per formula unit for this phase. However there was evidence of small amounts of $La(OH)_3$ being present after the exchange which would explain why the water incorporation was higher than that expected from the ion exchange. Figure 57 shows the X-ray patterns of the progression of the material after fluorination, exchange and TGA, along with the cell parameters in Table 13. The XRD patterns show that after heat treatment the exchanged product gives an XRD pattern very similar to that of the parent sample. However the cell parameters of these two phases do show some small differences, which might suggest that there is still a small amount of F in the sample.

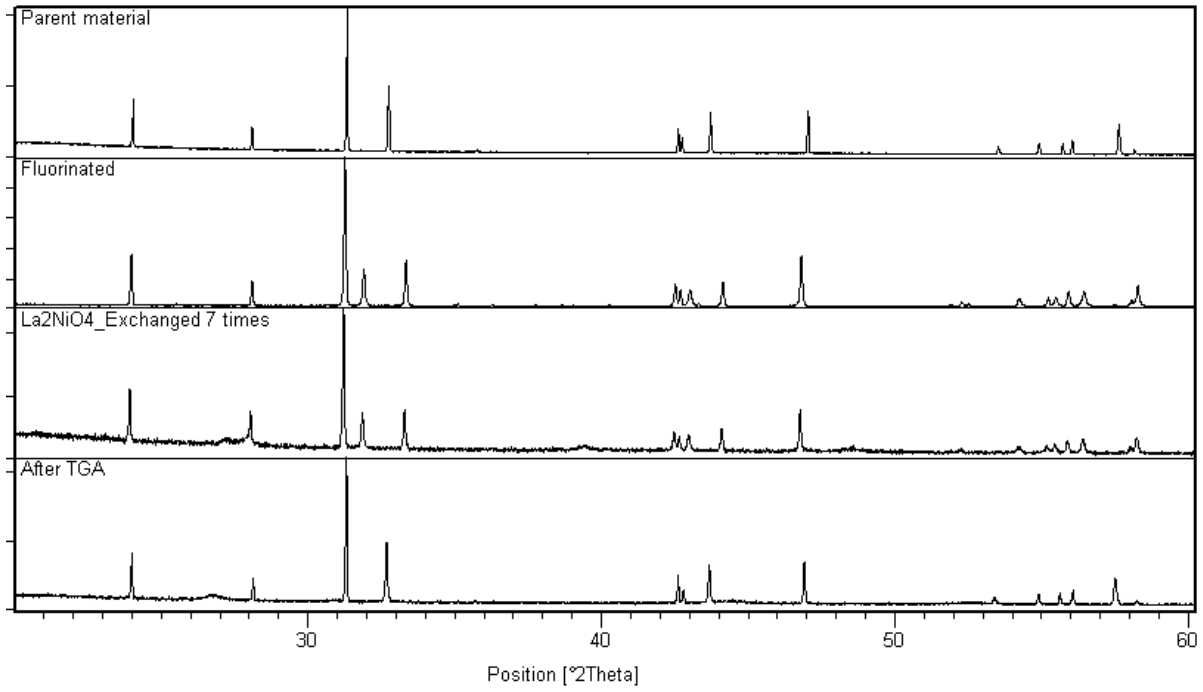

Figure 57: Powder X-ray diffraction patterns of $La_2NiO_{4+\delta}$ throughout the completed exchange.

Table 13: Cell parameters of $La_2NiO_{4+\delta}$ throughout the completed exchange.

	a (Å)	b (Å)	c (Å)	Cell Volume (Å^3)
Parent	5.45265 (4)	5.45859 (4)	12.66989 (9)	377.104 (7)
Fluorinated	5.36780 (7)	5.60196 (8)	12.6887 (2)	381.55 (1)
Exchanged 7 times	5.3699 (2)	5.6047 (2)	12.6939 (4)	382.04 (3)
After TGA	5.4649 (1)	5.4716 (1)	12.6559 (2)	378.44 (2)

The final exchanged sample was analysed further by variable temperature XRD (Figure 59) and these data were compared with the TGA-MS data (Figure 58). The TGA data shows a mass loss around 300°C equivalent to 0.64 moles of water being lost. The high temperature of this mass loss is consistent with lattice water rather than surface water for which the loss should have occurred around 100°C. The variable temperature XRD shows significant changes on heating. At 300°C there is an intermediate phase which shows both the parent and the exchanged material. However at the next temperature examined (400°C) there is only 1 phase due to the complete loss of water from the lattice, resulting in conversion back to the non-hydrated parent material.

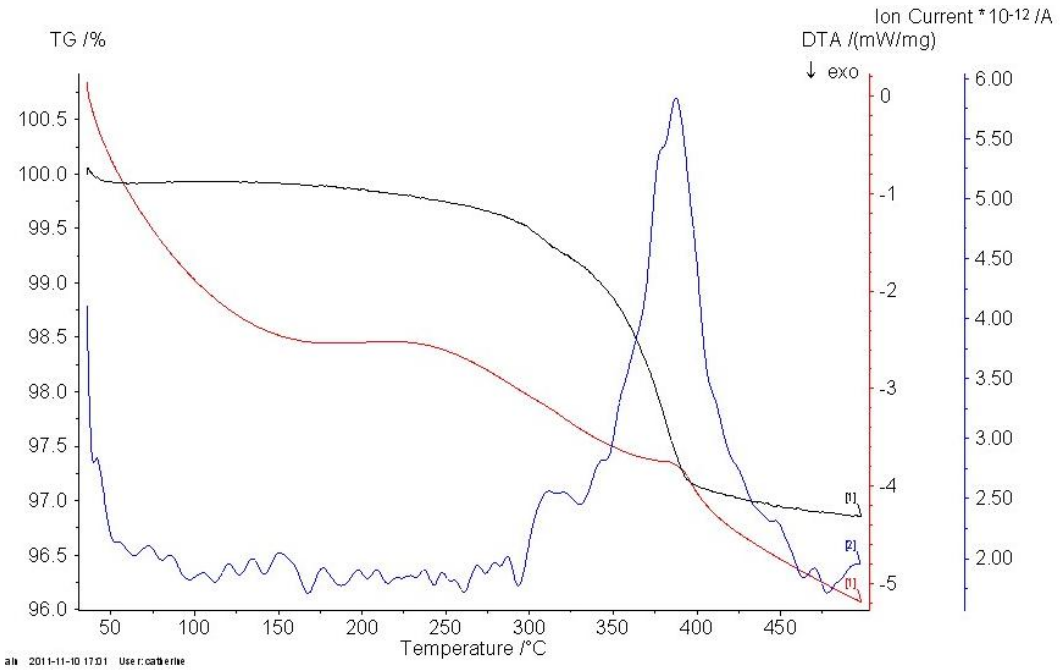

Figure 58: TGA of the final exchanged $La_2NiO_{4+\delta}$ showing weight loss in black, DTA in red and water release in blue.

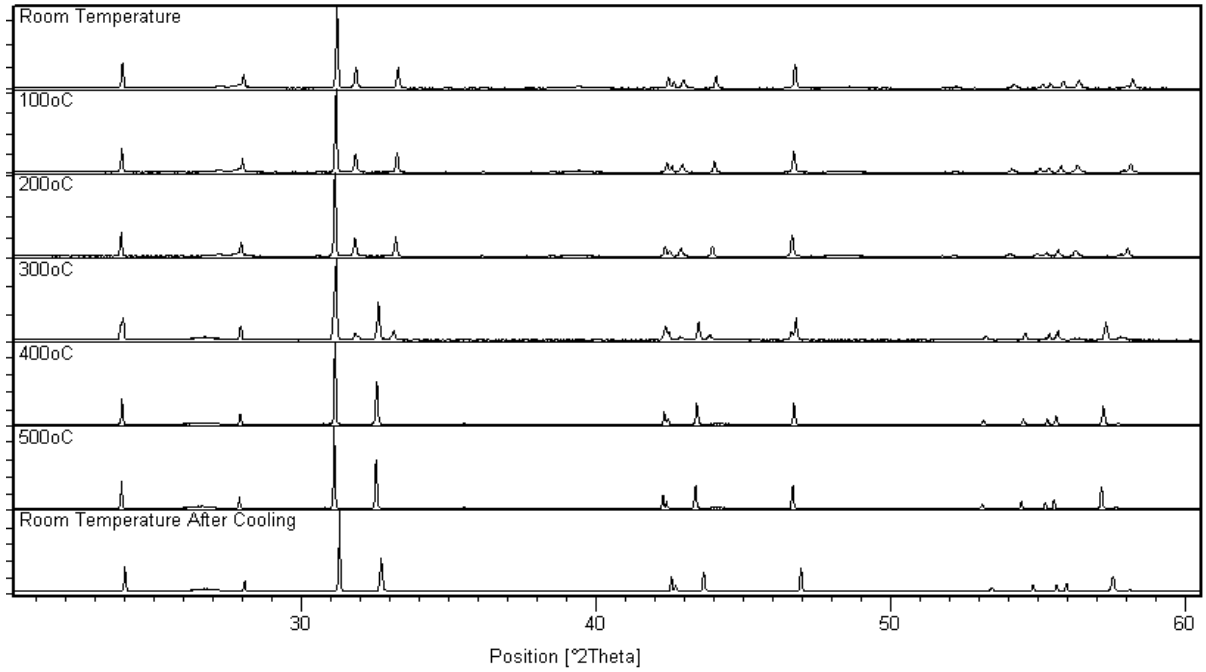

Figure 59: Variable temperature XRD patterns of exchanged La_2NiO_4/F showing the changes on loss of H_2O on heating.

To determine whether the incorporation of water within the interstitial sites would be beneficial for use as cathode catalysts in low temperature fuel cells preliminary electrochemical tests were performed to determine the effectiveness of the oxygen reduction reaction. The preliminary cyclic voltammetry results showed no increase in the onset potential with incorporation of water with the onset potential remaining around -0.25V.

4.1.6. Conclusions

In this work the stability of the Ruddlesden Popper phase $La_2NiO_{4+\delta}$ in alkaline conditions was examined, with the results suggesting good stability. In addition, the amount of water incorporation in this material was analysed by both direct and indirect methods. Direct methods led to low water incorporation levels, with the highest levels (~ 0.1 moles per formula unit) observed for hydrothermally treated samples. In contrast, higher levels of water incorporation could be achieved via indirect methods. The latter involved the initial synthesis of a fluorinated precursor followed by OH-/F- exchange, and led to high levels of H_2O incorporation (0.64 moles per formula unit). The

success of this work highlights the potential of anion exchange as a novel route of preparing new metastable Ruddlesden Popper phases.

4.2. Synthesis and Analysis of $Nd_2NiO_{4+\delta}$ Systems

4.2.1. Introduction

The thermodynamic stability of the K_2NiF_4 oxides are dependent on the size of the ionic radius of the lanthanide cation. This means that according to the Goldschmidt tolerance factor (Equation 20) [66, 157], Nd is the smallest lanthanide that can form $Ln_2NiO_{4+\delta}$ (Ln = Lanthanide) see Table 14 .

Equation 20: $t = (R_{Ln} + R_O) / \sqrt{2}(R_{Ni} + R_O)$ $0.866<t<1.00$ ideal structure

Table 14: Tolerance factors for $Ln_2NiO_{4+\delta}$ materials.

Material	Tolerance Factor
$La_2NiO_{4+\delta}$	0.8851
$Nd_2NiO_{4+\delta}$	0.8671

$Nd_2NiO_{4+\delta}$ has the same structure as $La_2NiO_{4+\delta}$ (Figure 43) as well as the ability to incorporate additional interstitial anions within its structure. As with the $La_2NiO_{4+\delta}$ this ability to incorporate extra anions results in a degree of hyperstoichiometry resulting in different symmetries. The stoichiometries below δ=0.13 generally result in an orthorhombic Bmab system [157-159], while above this an orthorhombic Fmmm system is preferred [158, 160].

As with $La_2NiO_{4+\delta}$, $Nd_2NiO_{4+\delta}$ has attracted significant attention for use as cathode materials in solid oxide fuel cells due to its high ionic and electronic conductivity, thermal expansion coefficients and good electrocatalytic properties, such as its high surface exchange and oxygen diffusion coefficients [66, 161, 162]. In this work, we examined the potential to incorporate water into this system, to compare with results from $La_2NiO_{4+\delta}$.

4.2.2. Experimental

High purity Nd_2O_3 and NiO were used to prepare the $Nd_2NiO_{4+\delta}$ sample. The starting materials were ground together in the correct stoichiometric ratio and heated to 1100^{o}C for 12 hours. The samples were then reground and heated to 1300^{o}C for another 12 hours.

Powder X-ray diffraction experiments, using a Bruker D8 transmission diffractometer with Cu $K\alpha_1$ radiation, were used to determine phase purity, and the GSAS suite of programs was used for the structural refinements of the system.

4.2.3. Structural Determination of $Nd_2NiO_{4+\delta}$

The structure refinement of this system was performed in a similar way as for the previous nickelate system, as in both cases the additional oxygen in the interstitial sites results in a Fmmm space group. The same constraints that were used to refine the $La_2NiO_{4+\delta}$ system were used in this refinement. The structural parameters are shown in Table 15 and 16 along with the structural fit, which is seen in Figure 60.

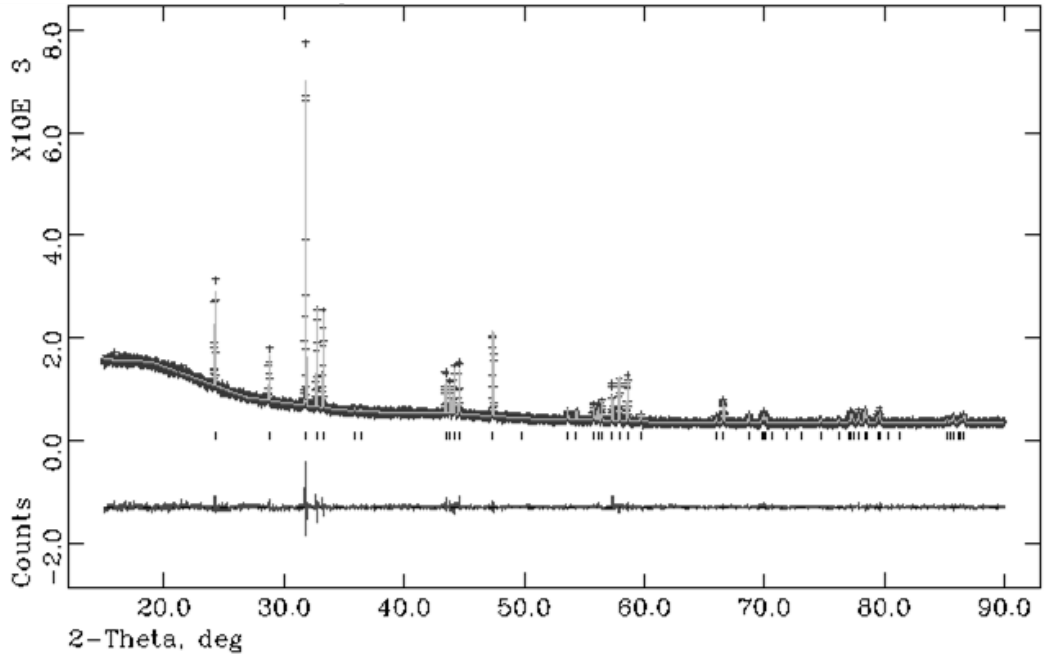

Figure 60: Observed, calculated and difference x ray diffraction profiles for $Nd_2NiO_{4+\delta}$.

Table 15: Structural parameters for $Nd_2NiO_{4+\delta}$

Atom	Multiplicity	X	Y	Z	Uiso	Occupancy
Nd1	8	0	0	0.3587 (1)	0.70 (7)	1
Ni1	4	0	0	0	0.8 (2)	1
O1	8	0.25	0.25	0	1.5 (5)	1
O2	16	0.25	0.25	0.214 (7)	1.5 (5)	0.103 (6)
O3	8	0	0	0.18 (2)	1.5 (5)	0.18 (4)
O4	32	-0.065 (4)	-0.071 (4)	0.164 (4)	1.5 (5)	0.2 (1)
Fmmm, a=5.36529(7), b=5.45129(7),c=12.3575(2), χ^2= 1.563, Rwp=5%						

Table 16: Bond distances for $Nd_2NiO_{4+\delta}$.

Bond	Bond Length
Nd1-O1	2.5897 (11) x4
Nd1-O2	2.62 (6) x4
	2.113 (34) x4
Nd1-O3	2.25 (19) x1
	2.760 (31) x2
	2.718 (31) x2
Nd1-O4	2.47 (5) x4
	2.378 (22) x4
	2.382 (24) x4
	3.069 (26) x4
Ni1-O1	1.91218 (2) x4
Ni1-O3	2.18 (19) x2
Ni1-O4	2.09 (5) x8

The occupancy of the interstitial oxygen site (O2) was refined resulting in the formula $Nd_2NiO_{4.526}$ which is consistent with a Fmmm system. The refined interstitial occupancy is high, which may be due to the fact that X-ray diffraction is not that sensitive to light atoms, and so such issues may be resulting in an overestimation of the oxygen content.

4.2.4. Water Incorporation

The examination of water incorporation into the interstitial sites of $Nd_2NiO_{4+\delta}$ was investigated as for the $La_2NiO_{4+\delta}$ system. Due to the ion exchange of the fluorinated system giving the greatest incorporation of water this was the only method used for the water incorporation studies in $Nd_2NiO_{4+\delta}$.

4.2.4.1. Experimental

The parent material $Nd_2NiO_{4+\delta}$ was ground with PVDF in the correct molar ratios of La_2NiO_4:PVDF (CH_2CF_2 monomer unit). These samples were then placed in a furnace with a slow heating rate (1^{o}C per min) to 350^{o}C for 24hrs with an intermediate regrind. The ion exchange was performed by heating the fluorinated material in 1M KOH in a hydrothermal vessel for 2 days at 200^{o}C. This exchange was then repeated until the analysis concluded that the material was fully exchanged.

4.2.4.2. Results and Discussion

On fluorination of $Nd_2NiO_{4+\delta}$ there is a significant change in the cell parameters as well as a noticeable change in the XRD pattern (Figure 61) with a further splitting of the (020)/(200) peaks. Unlike the fluorination of $La_2NiO_{4+\delta}$, small impurities (NdF_3 and $NdNi(O/F)_3$) were observed at low level fluorination of $Nd_2NiO_{4+\delta}$.

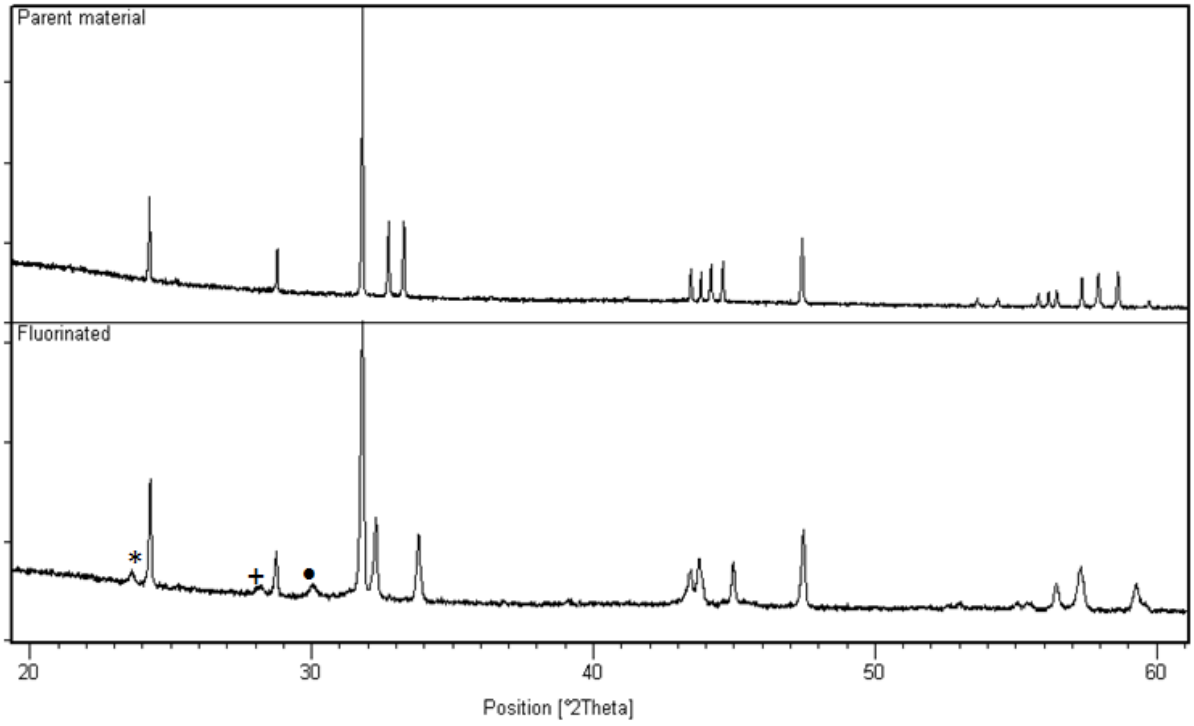

Figure 61: X-ray diffraction patterns of the parent and Nd_2NiO_4:0.25 PVDF material (+ = NdF_3 phase, * = $NdNi(O/F)_3$ and • = Higher F content phase).

Structure refinement for the fluorinated sample was performed with the fluorine assumed to increase the occupancy of the interstitial site. The fluorine incorporation can be confirmed from the refinement by the increase in the cell parameters due to the additional anions within the structure. In addition to the increase in the cell parameters the occupancy of the interstitial site increases due to the replacement of 1 O^{2-} by 2 F^- and this is accompanied by an increase in the Ni-O1 distance. The structural parameters are given in Table 17 and Table 18 and the observed, calculated and difference profiles in Figure 62.

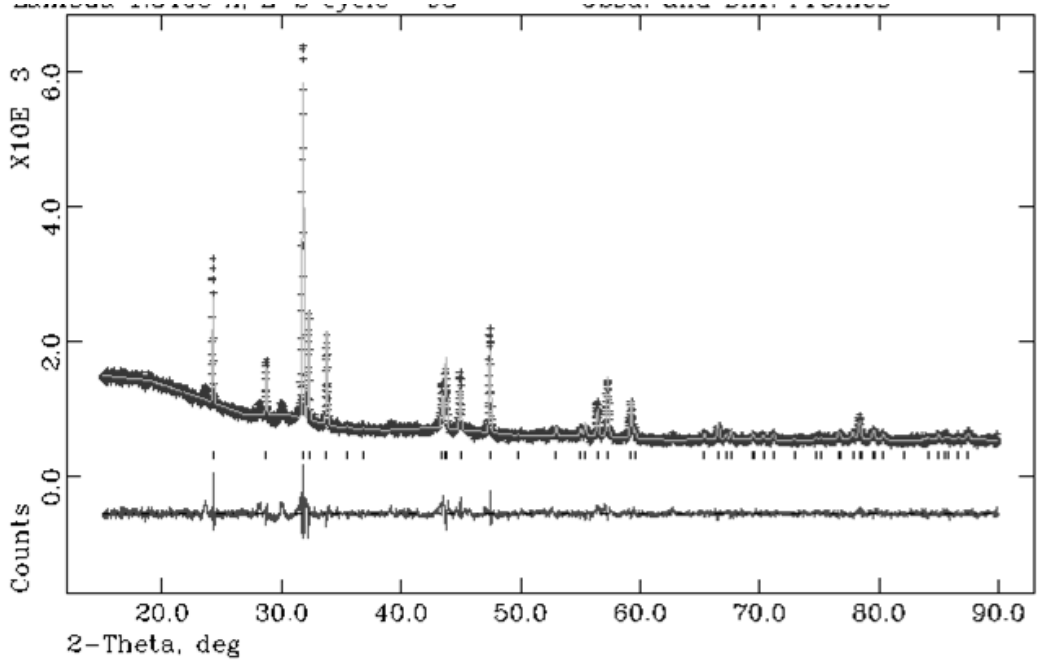

Figure 62: Observed, calculated and difference x-ray diffraction profiles for fluorinated $Nd_2NiO_{4+\delta}$.

Table 17: Structural parameters for fluorinated $Nd_2NiO_{4+\delta}$. It is presumed that F is located in the interstitial O2 and apical O3/O4 positions.

Atom	Multiplicity	X	Y	Z	Uiso	Occupancy
Nd1	8	0	0	0.3593 (2)	2.68 (9)	1
Ni1	4	0	0	0	0.9 (3)	1
O1	8	0.25	0.25	0	1.9 (5)	1
O2	16	0.25	0.25	0.23 (1)	1.9 (5)	0.106 (6)
O3	8	0	0	0.17 (2)	1.9 (5)	0.15 (5)
O4	32	-0.070 (4)	-0.074(5)	0.164 (5)	1.9 (5)	0.21 (1)
Fmmm, a=5.2887(2), b=5.5302(2),c=12.3851(5), χ^2= 2.275, Rwp=5.41%						

Table 18: Bond distances for fluorinated $Nd_2NiO_{4+\delta}$.

Bond	Bond Length
Nd1-O1	2.5874 (14) x4
Nd1-O2	2.33 (29) x1
	2.79 (4) x2
	2.67 (4) x2
Nd1-O3	2.47 (9) x4
	2.23 (8) x4
Nd1-O4	2.48 (6) x4
	2.404 (24) x4
	2.330 (23) x4
	3.054 (24) x4
Ni1-O1	1.91301 (5) x4
Ni1-O3	2.13 (29) x2
Ni1-O4	2.10 (6) x8

In this case, it proved to be difficult to fully exchange the material, with no changes in water content between the 1st and 2nd exchanges. In both cases a water content of ~0.22 moles per formula unit was determined and the cell parameters after dehydration of the exchanged products showed significant differences from the parent phase consistent suggesting that a large amount of F was still present (Table 19). As a result of the problems achieving full exchange, no further work was therefore performed on this system.

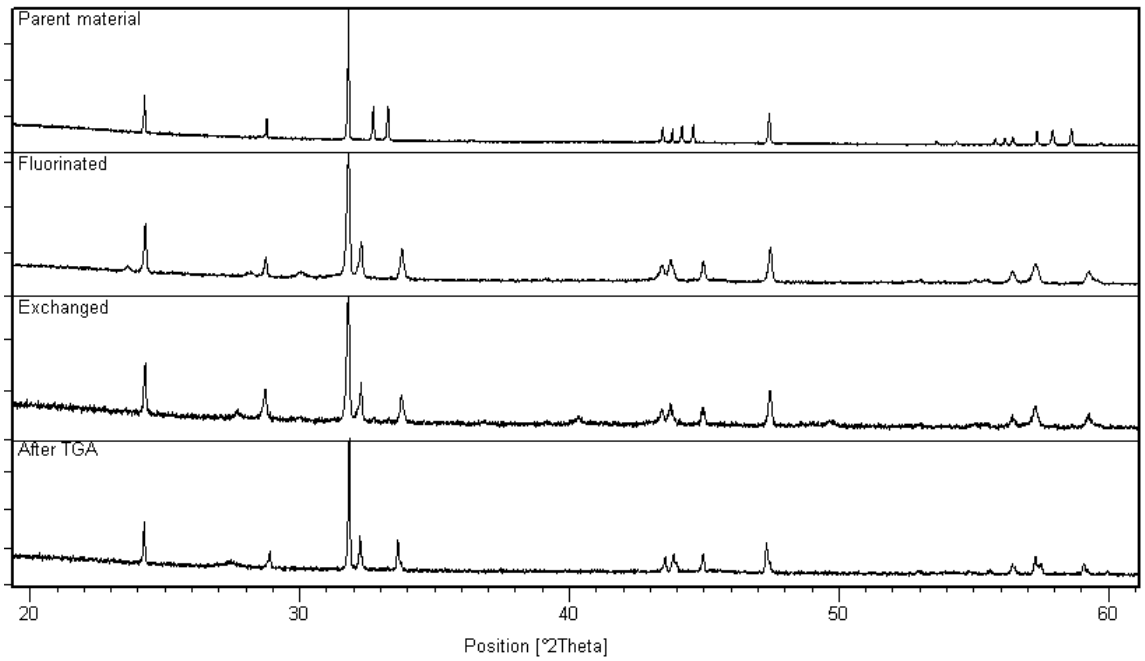

Figure 63: Powder X-ray diffraction patterns for $Nd_2NiO_{4+\delta}$ throughout the exchange process.

Table 19: Cell parameters for $Nd_2NiO_{4+\delta}$ throughout the exchange process.

	a (Å)	b (Å)	c (Å)	Cell Volume (Å^3)
Parent	5.36527 (6)	5.45130 (6)	12.3574 (2)	361.43 (1)
Fluorinated	5.2918 (2)	5.5329 (2)	12.3917 (4)	362.82 (3)
Exchanged	5.2898 (4)	5.5243 (8)	12.3819 (6)	361.83 (5)
After TGA	5.3138 (6)	5.55395 (7)	12.318 (1)	362.57 (5)

4.2.5. Conclusions

The work on $Nd_2NiO_{4+\delta}$ complements the work on $La_2NiO_{4+\delta}$. As seen with $La_2NiO_{4+\delta}$, it is possible to incorporate water into $Nd_2NiO_{4+\delta}$ by indirect methods. However the level of water incorporation achieved in the Nd system was around 3 times lower than the La system. This is due to

the fact that it was not possible to fully OH^-/F^- exchange the fluorinated $La_2NiO_{4+\delta}$. The exact reason behind this behaviour is not known, and warrants further study.

4.3. Synthesis and Analysis of $La_2CuO_{4+\delta}$

4.3.1. Introduction

$La_2CuO_{4+\delta}$ is one of the best known materials to have the K_2NiF_4 structure (Figure 43). This material has interesting properties, with superconductivity with a max Tc of 40K observed on introduction of extra oxygen or by partially replacing the La with an alkaline earth metal (Ba, Sr and Ca) [163, 164]. Similarly superconductivity can be achieved through fluorination [103, 164-166]. Due to the high electronic conductivity, and the ability to accommodate oxygen excess, this material, is a potential candidate for a cathode material in SOFCs [167].

4.3.2. Experimental

High purity La_2O_3 and CuO were used to prepare the $La_2CuO_{4+\delta}$ sample. The starting materials were ground together in the correct stoichiometric ratio and heated to 1000^{o}C for 12 hours. The samples were then reground and further heated to 1100^{o}C for another 12 hours.

Similar methods were examined to incorporate water as for $La_2NiO_{4+\delta}$.

Characterisation was achieved using powder X-ray diffraction experiments with a Bruker D8 transmission diffractometer. The diffractometer uses Cu $K\alpha_1$ radiation. The GSAS suite of programs was used for refinements and the Unit Cell program to determine cell parameters.

Water contents were determined using thermogravimetric analysis (Netzsch STA 449 F1 Jupiter Thermal Analyser). The samples were heated to 500^{o}C at 10^{o}C per minute.

4.3.3. Structural determination of $La_2CuO_{4+\delta}$

As with $La_2NiO_{4+\delta}$ the symmetry of the $La_2CuO_{4+\delta}$ structure is dependent on the amount of oxygen in the interstitial positions as well as the temperature at which the measurement is performed. At lower temperature the two most common structures are based on the Bmab and the Fmmm space groups. For stoichiometric La_2CuO_4, Bmab is used, whereas Fmmm is used when interstitial oxygen is incorporated into the structure, which is the case in this thesis. After heating to around 410K there is a phase change to the tetragonal I4/mmm structure.

A Rietveld refinement was performed which resulted in a good fit to the data, as seen in Figure 64. The structural parameters are shown in Table 20 and 21. The interstitial site was located at 0.25, 0.25, 0.12 (4) between the adjacent LaO layers. This insertion of an additional oxygen position causes the O3 apical oxygen to split. In this refinement all the oxygen thermal parameters were constrained to be the same and then refined. The occupancy of the oxygen sites were refined with the same method as the $La_2NiO_{4+\delta}$ system, giving a composition of $La_2CuO_{4.154}$.

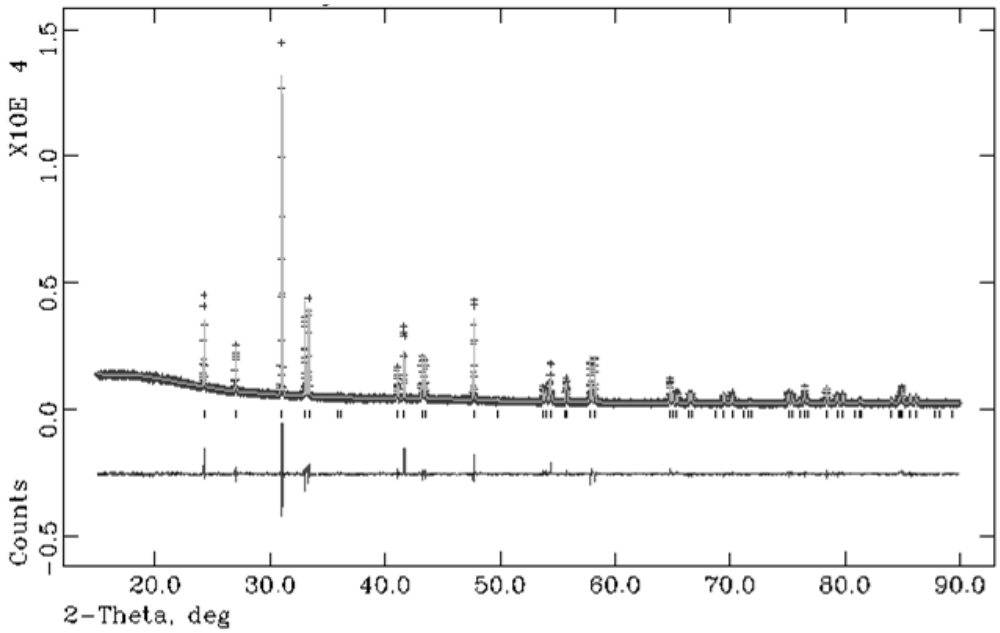

Figure 64: Observed, calculated and difference X-ray diffraction profiles for $La_2CuO_{4+\delta}$.

Table 20: Structural parameters for $La_2CuO_{4+\delta}$.

Atom	Multiplicity	X	Y	Z	Uiso	Occupancy
La1	8	0	0	0.3620 (1)	0.80 (5)	1
Cu1	4	0	0	0	0.8 (1)	1
O1	8	0.25	0.25	0	1.5 (4)	1
O2	16	0.25	0.25	0.12 (4)	1.5 (4)	0.029 (2)
O3	8	0	0	0.062 (6)	1.5 (4)	0.05 (2)
O4	32	-0.040 (3)	0.060 (4)	0.193 (1)	1.5 (4)	0.237 (4)
Fmmm, a=5.35105(5), b=5.39912(5),c=13.1371(1), χ^2= 3.156, Rwp=7.6%						

Table 21: Bond distances for $La_2CuO_{4+\delta}$.

Bond	Bond Length
La1-O1	2.6265 (9) x4
La1-O2	1.92 (8) x4
La1-O3	2.879 (26) x2
	2.856 (26) x2
La1-O4	2.259 (18) x4
	2.493 (20) x4
	3.112 (20) x4
	2.582 (18) x4
	2.996 (18) x4
Cu1-O1	1.90040 (1) x4
Cu1-O2	2.44 (33) x8
Cu1-O3	0.81 (7) x2
Cu1-O4	2.560 (19) x8

Materials with the K_2NiF_4 structure have generated interest for use in IT-SOFCs. However as with the $La_2NiO_{4+\delta}$ material there have been no studies of using $La_2CuO_{4+\delta}$ in low temperature alkaline fuel cells. To determine whether this material could be used a stability test was performed. XRD was performed on the sample before heating it with 1M KOH in a hydrothermal bomb at 200^{o}C for 2 days. After filtering and washing the sample was analysed by XRD. The results can be seen in Figure 65. As can be seen, the X-ray diffraction pattern of the material after this heat treatment shows decomposition of the sample into $La(OH)_3$ and CuO. Admittedly these are extreme conditions, but it does raise questions concerning the long term usage of this material in alkaline conditions at lower temperature. Overall, therefore these results show that $La_2CuO_{4+\delta}$ does not have as good stability in alkaline conditions as the corresponding nickelate.

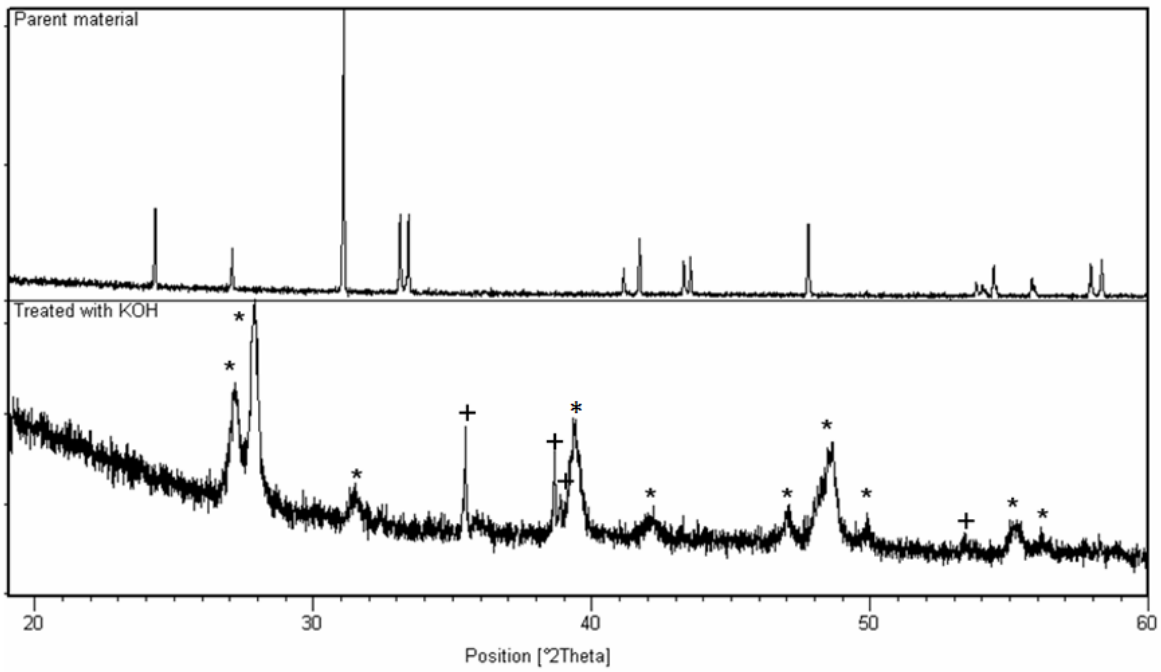

Figure 65: Powder X-ray diffraction patterns for stability tested $La_2CuO_{4+\delta}$ (* = $La(OH)_3$ and + = CuO).

4.3.4. Water Incorporation

Potential water incorporation was still examined for this compound. As seen previously for $La_2NiO_{4+\delta}$ there is not a significant change in the X-ray diffraction pattern of $La_2CuO_{4+\delta}$ after heating in different atmospheres at 350°C as seen in Figure 66 and Table 22.

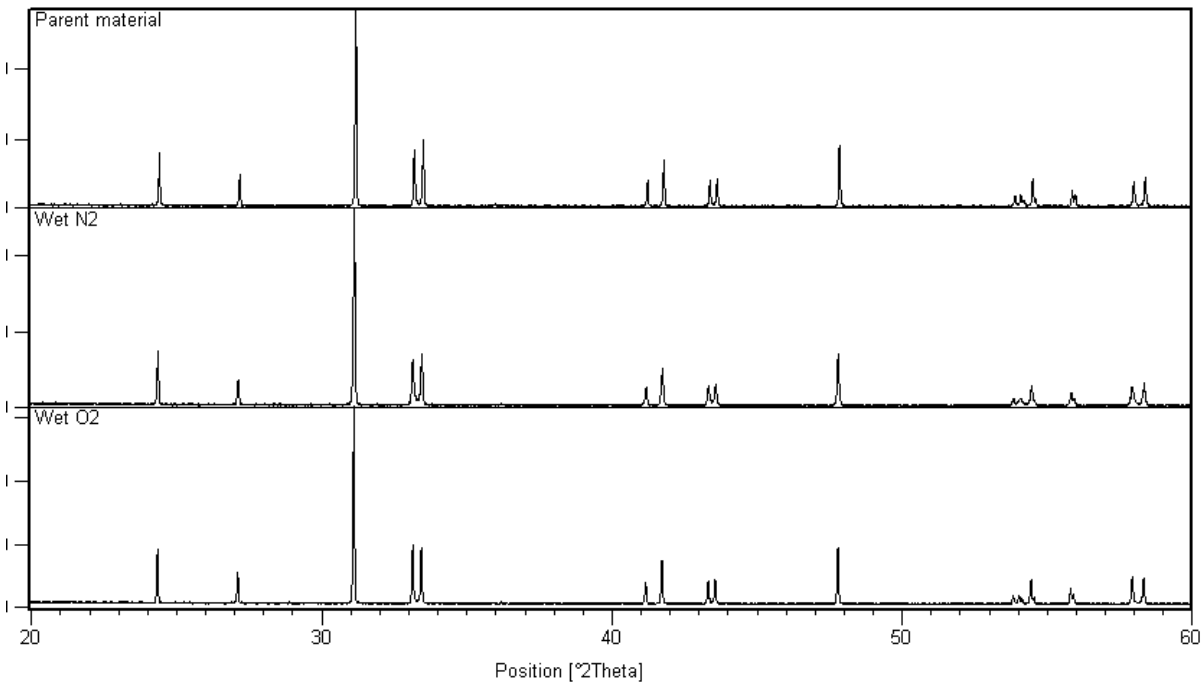

Figure 66: X-ray diffraction patterns for $La_2CuO_{4+\delta}$ heated at 350°C in different atmospheres.

Table 22: Cell parameters for $La_2CuO_{4+\delta}$ heated in different atmospheres at 350°C.

	a (Å)	b (Å)	c (Å)	Cell Volume (Å^3)	Water Content (Moles per formula unit)
Parent	5.3563 (3)	5.4042 (3)	13.1465 (6)	380.54 (3)	-
Wet N_2	5.3542 (3)	5.4061 (4)	13.1416 (6)	380.39 (3)	0.1081
Wet O_2	5.3552 (3)	5.4035 (3)	13.1493 (6)	380.50 (3)	0.0833

However even though the XRD data did not show any major changes, the TGA analysis suggested that there was a significant mass loss at temperatures above 100°C (Figure 67). This mass loss was determined to be water by mass spectrometry, and due to the temperature being above 100°C the water is thought to be from the interstitial sites. This suggests that water incorporation from humid atmospheres is possible in this system unlike in $La_2NiO_{4+\delta}$.

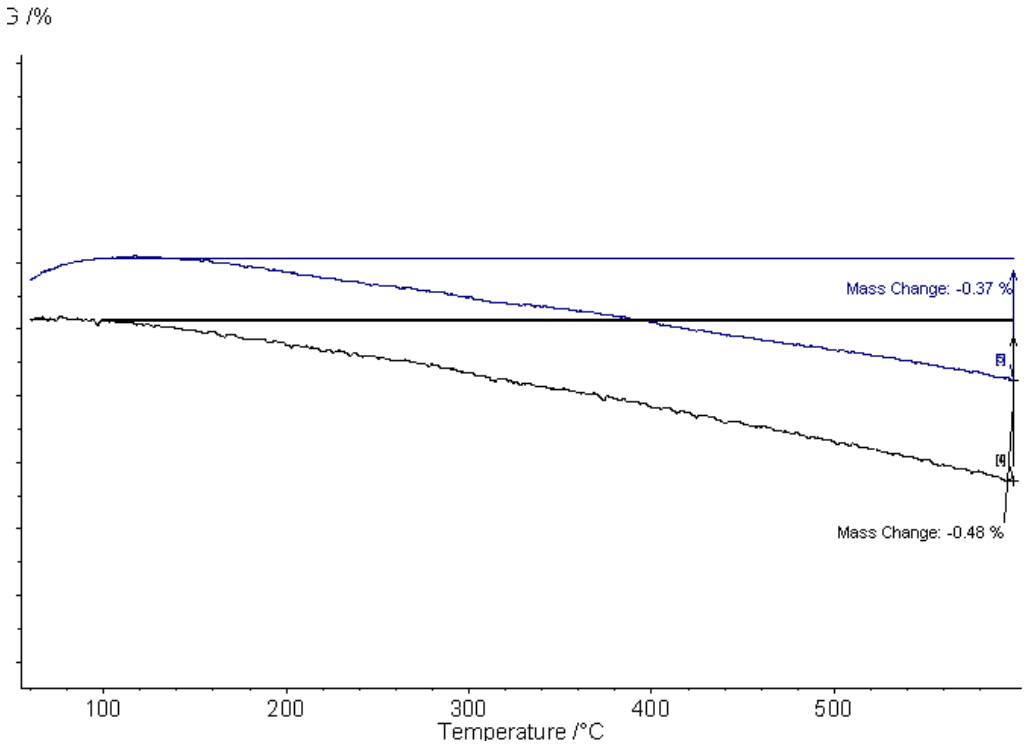

Figure 67: Weight losses after being exposed to different atmospheres (Black = wet N_2, blue = wet O_2).

In the previous work on $La_2NiO_{4+\delta}$ water incorporation was achieved by heating the samples in different solutions for 2 days at temperature of 200°C. However, as seen earlier in stability experiments, the $La_2CuO_{4+\delta}$ material decomposed when heated to this temperature in 1M KOH. This also occurred when heated in water. Due to this instability towards water under these hydrothermal conditions it was not possible to perform ion exchange of a fluorinated sample of $La_2CuO_{4+\delta}$ to increase the water content, despite the fact that fluorination was successful as shown in the next section.

4.3.5. Incorporation of Extra Anions via Fluorination

The results show that fluorination of $La_2CuO_{4+\delta}$ via the PVDF method is successful. The XRD patterns (Figure 68) show that there is an increase in the splitting of (020)/(200) peaks as there was in the $La_2NiO_{4+\delta}$ fluorinated system due to an increase in orthorhombic distortion. For the sample fluorinated with 0.25 PVDF there appeared to be a mixture of fluorinated phases in the sample as indicated by the shoulders on the peaks. As the amount of PVDF was increased, there is a further

increase in the cell parameters (Table 23) which indicates that more fluorine is being incorporated into the interstitial sites, although for these high F content samples there is an increase in LaOF impurities until when 2 moles of PVDF are used, no peaks of the fluorinated parent material can be seen.

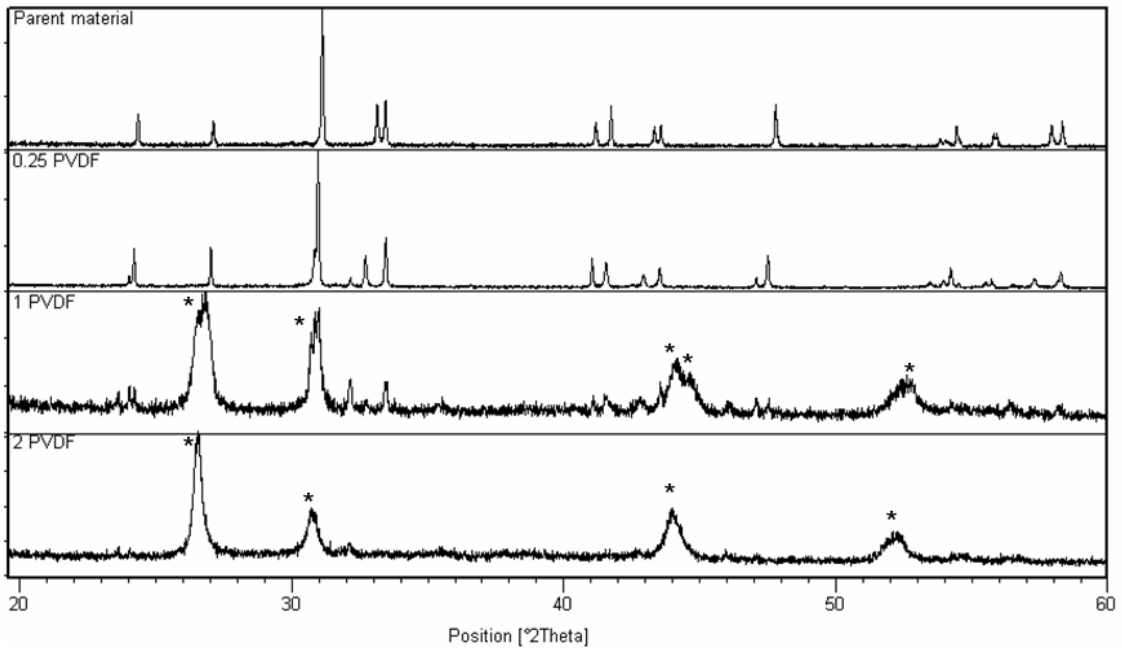

Figure 68: X-ray diffraction patterns of fluorinated $La_2CuO_{4+\delta}$ (* = LaOF).

Table 23: Cell parameters of fluorinated $La_2CuO_{4+\delta}$.

	a (Å)	b (Å)	c (Å)	Cell Volume (Å^3)
Parent	5.3560 (3)	5.4020 (3)	13.1445 (6)	380.31 (3)
0.25 PVDF	5.3496 (4)	5.4700 (4)	13.1819 (6)	385.73 (3)
1 PVDF	5.3560 (4)	5.5758 (5)	13.184 (1)	393.74 (5)

Considering the previous results which indicated the instability of this system under hydrothermal conditions, no further work on attempting to ion exchange these fluorinated phases was performed.

4.3.6. Conclusions

The work undertaken on $La_2CuO_{4+\delta}$ shows that it would not be suitable for use in AFC due to the degradation in alkaline conditions. However water incorporation into this material was demonstrated by heat treatment in wet N_2/O_2. Considering the interest in this system as a high

temperature superconductor, further work is warranted to investigate the effect of water incorporation on the superconducting properties of $La_{2-x}A_xCuO_{4+\delta}$ (A=Sr, Ba and Ca).

5. Synthesis and Characterisation of Novel Perovskite Systems

Materials with the perovskite structure have generated a lot of interest for use as electrode materials in fuel cells. This interest has been due to them commonly displaying high electronic conductivity when the B site cation is a transition metal. In order to optimise the properties, a range of doping strategies on the A or B site can be exploited. Traditional doping strategies focus on doping cations of similar size, for example Sr for La [24, 27, 168]. In this work we have focused on an alternative strategy, doping with the much smaller P^{5+}, S^{6+} and Si^{4+}, which would be expected to be accommodated as phosphate, sulphate and silicate groups respectively. Previous literature work demonstrated the successful incorporation of borate, carbonate, phosphate and sulphate oxyanions into perovskite cuprate superconductors. The work performed on these structures showed that incorporation of significant amounts of oxyanions gave interesting results [169-172]. It was found that the incorporation of these oxyanions resulted in the stabilization of some materials which would not have been possible without this doping. For example 50% $(CO_3)^{2-}$ substitution in "$YSr_2Cu_3O_7$" results in the formation of the new superconductor $YSr_2Cu_{2.5}(CO_3)_{0.5}O_{5.5}$ [169, 172]. This work has been recently extended further to incorporate oxyanions into SOFC electrolyte materials by our research group. It was discovered that doping on the In site in $Ba_2In_2O_5$ with oxyanions resulted in disorder on the oxygen sublattice and an increase in the cell symmetry from orthorhombic to cubic. This symmetry change resulted in an increase of the conductivity due to the resultant disorder on the oxygen sublattice [173-175]. In this thesis the work has been extended to investigate the possible incorporation of oxyanions into perovskites with potential for use as cathode materials for fuel cells (both SOFC and APEMFC systems).

5.1. $SrCo_{1-x}Z_xO_{3-y}$ (Z=P, S, Si)

A material that has generated a lot of interest in the literature for use as a SOFC cathode material is $SrCoO_{3-y}$. This interest is due to its high electrical conductivities and oxygen permeation flux, when it is suitably doped. Undoped $SrCoO_{3-y}$ is a hexagonal perovskite at temperatures below 900^{o}C, resulting in low conductivities. Furthermore, it has been reported that at low temperatures

the $SrCoO_{3-y}$ actually phase separates into $Sr_6Co_5O_{15}$ and Co_3O_4 [36, 176-180]. However it has since been shown that doping $SrCoO_{3-y}$ on the Co site with a range of different cations, such as Sb, Nb and Zr, stabilizes the "cubic" perovskite phase. This results in an substantial increase in the conductivity, (Table 24) due to the change to corner linked octahedra, compared to the face sharing of octahedra in the poorly conducting hexagonal phase [40, 178, 179, 181-184]. This stabilization has also been studied through doping on the Sr site, which has given similar results [176, 185]. In this work we investigated the possible stabilisation of the cubic perovskite by doping with oxyanions.

Table 24: Literature conductivity values of doped $SrCoO_{3-y}$ at 400 and 800°C [40, 178].

Compound	Conductivity in Scm^{-1} at 400°C	Conductivity in Scm^{-1} 800°C
$SrCoO_{3-y}$	8	19
$SrCo_{0.95}Sb_{0.05}O_{3-y}$	505	175
$SrCo_{0.95}Nb_{0.05}O_{3-y}$	370	185

5.1.1. Experimental

High purity $SrCO_3$, Co_3O_4, Fe_2O_3, SiO_2, $(NH_4)_2SO_4$ and $NH_4H_2PO_4$ were used to prepare a range of $SrCo_{1-x}Z_xO_{3-y}$ and $SrCo_{0.9-x}Fe_{0.1}Z_xO_{3-y}$ samples (Z=P, S and Si). These starting materials were ground together in the correct stoichiometric ratios and heated to a temperature of 1100°C for 12 hours. The samples were then ball-milled (350 rpm for 1 hour, Fritsch Pulverisette 7 planetary ballmill) and further heated to 1200°C (Z=P, S) and 1300°C (Z=Si) for another 12 hours. The samples were then furnace cooled to 350°C and held at this temperature for 12 hours to ensure full oxygenation.

Powder X-ray diffraction experiments, using a Bruker D8 transmission diffractometer with Cu $K\alpha_1$ radiation, were employed to determine phase purity, and the GSAS suite of programs used for the preliminary structure refinements of these systems. In order to obtain further details regarding the structures of these doped phases, neutron diffraction data were collected on the HRPT diffractometer at SINQ (Paul Scherrer Institute, Villigen, Switzerland).

Oxygen contents were estimated from thermogravimetric analysis (Netzsch STA 449 F1 Jupiter Thermal Analyser). The samples were heated to a temperature of 1200°C in N_2 at a rate of

10^{o}C/min and held for 30 minutes. This reduces the transitional metal state to 3+ allowing the original oxygen content to be determined from the mass loss observed.

Pellets for conductivity measurements were prepared by ball milling the samples for an hour, and adding a small amount of polyvinyl alcohol binder before pressing as pellets and sintering at 1250^{o}C (Z=P, S) and 1350^{o}C (Z=Si). The conductivity was then measured using the 4 probe d c method. The 4 platinum electrodes were attached to the pellet using platinum paste and then fired to 1000^{o}C for an hour to ensure bonding before lowering the temperature to 350^{o}C for 12 hours to ensure oxygenation.

For potential applications as SOFC cathodes, it is important to examine the chemical compatibility with SOFC electrolytes. These compatibility studies were performed on 0.5g of the sample mixed thoroughly with 0.5g of the electrolyte (YSZ and CGO electrolytes were examined). XRD analysis was performed on the mixture both before being placed in a furnace at 1000^{o}C for 48 hours, as well as afterwards to determine whether there were any changes.

In addition to the above experiments targeting their potential as SOFC cathodes, the materials were also subjected to preliminary experiments to determine their potential for use in low temperature alkaline fuel cells. For these electrochemical measurements electrode inks were made by ballmilling 0.3g of the samples with 2ml of propanol for 2 hours. After ballmilling another 6ml of propanol was added along with 0.1g of polytetrafluoroethylene (60 wt% dispersion in water). The inks were deposited and dried on a glassy carbon electrode and then examined by cyclic voltammetry and rotating disk measurements in oxygen saturated 0.1M KOH, with a variety of rotation rates (400, 800, 1200,1600 and 2000 rpm), using the Invium Stat, Invium A07026 model 636 equipment.

5.1.2. Results and Discussion

5.1.2.1. Structural Studies

The X-ray diffraction data show that on doping with small amounts of phosphate, silicate or sulphate there is a change from a hexagonal to a cubic perovskite (Figure 69, 70 and 71). The

undoped sample was shown to be the hexagonal $Sr_6Co_5O_{15}$ perovskite along with small Co_3O_4 impurities, as has been previously reported. Doping with 3-7% oxyanion resulted in a single phase cubic perovskite (according to XRD measurements) with small concentrations of $Sr_{10}(PO_4)_6(OH)_2$, $SrSO_4$ or Sr_2SiO_4 being seen above these doping levels.

The stabilization of the perovskite can be correlated with the partial reduction of Co^{4+} to Co^{3+}. This reduction is due to the creation of oxygen vacancies which are needed to convert the co-ordination from octahedral (for Co) to tetrahedral for PO_4^{3-}, and SO_4^{2-}, SiO_4^{4-}, along with the introduction of higher valent P^{5+}, S^{6+} in place of Co^{4+} for the phosphate and sulphate doping. The Co oxidation states, as determined by TGA measurements, can be seen in Table 25, 26 and 27. This reduction of Co oxidation state also explains the increase in the unit cell volume, as the reduction of Co^{4+} to the larger Co^{3+} counters the effect of the smaller P^{5+}/S^{6+} being added. These effects can be described by defect equations for incorporation of PO_4^{3-} and SO_4^{2-} (Equation 21 and 22 respectively). In contrast to the expansion of the unit cell on increasing phosphate and sulphate doping, the cell parameter data for the Si doped system show a small decrease in the cell volume on increasing the Si content between 3 and 7%. This can be explained by the smaller radius of the Si^{4+} compared to the Co^{3+}/Co^{4+} ions, while the Co oxidation state and oxygen content remain approximately constant from the TGA analysis. Somewhat surprisingly for low levels (3%) of dopant the greatest reduction is on silicate doping despite the defect equation (Equation 23) in this case implying the lowest level of Co reduction. It should be noted, however, that the TGA data imply overall greater reduction than simply shown from the defect equation, indicating that as soon as the cubic perovskite is formed, additional oxygen loss can occur.

Equation 21 $NH_4H_2PO_4 + 4Co_{Co} + O_O \rightarrow P_{Co}^{\bullet} + 3Co_{Co}' + V_O^{\bullet\bullet} + 3/4O_2 + 3/2H_2O + CoO_2 + NH_3$

Equation 22 $(NH_4)_2SO_4 + 5Co_{Co} + O_O \rightarrow S_{Co}^{\bullet\bullet} + 4Co_{Co}' + V_O^{\bullet\bullet} + O_2 + 2NH_3 + H_2O + CoO_2$

Equation 23 $SiO_2 + 3Co_{Co} + O_O \rightarrow Si_{Co} + 2Co_{Co}' + V_O^{\bullet\bullet} + 1/2O_2 + CoO_2$

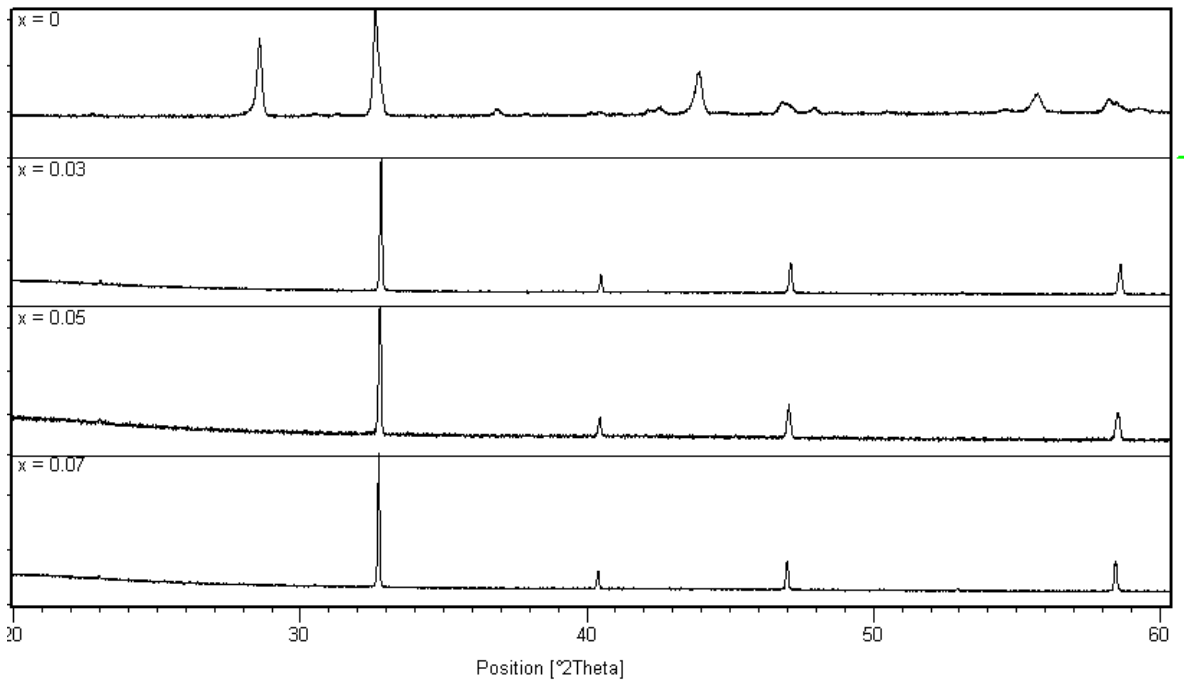

Figure 69: Powder X-ray diffraction patterns for $SrCo_{1-x}P_xO_{3-y}$ showing a phase change from hexagonal to cubic on doping.

Table 25: Cell parameters, oxygen deficiencies from TGA measurements (y), and cobalt oxidation states for $SrCo_{1-x}P_xO_{3-y}$.

P content (x)	Oxygen deficiency (y)	a/ Å	Co oxidation state
0.03	0.10	3.8527 (2)	3.74
0.05	0.14	3.8617 (2)	3.59
0.07	0.16	3.8621 (2)	3.51

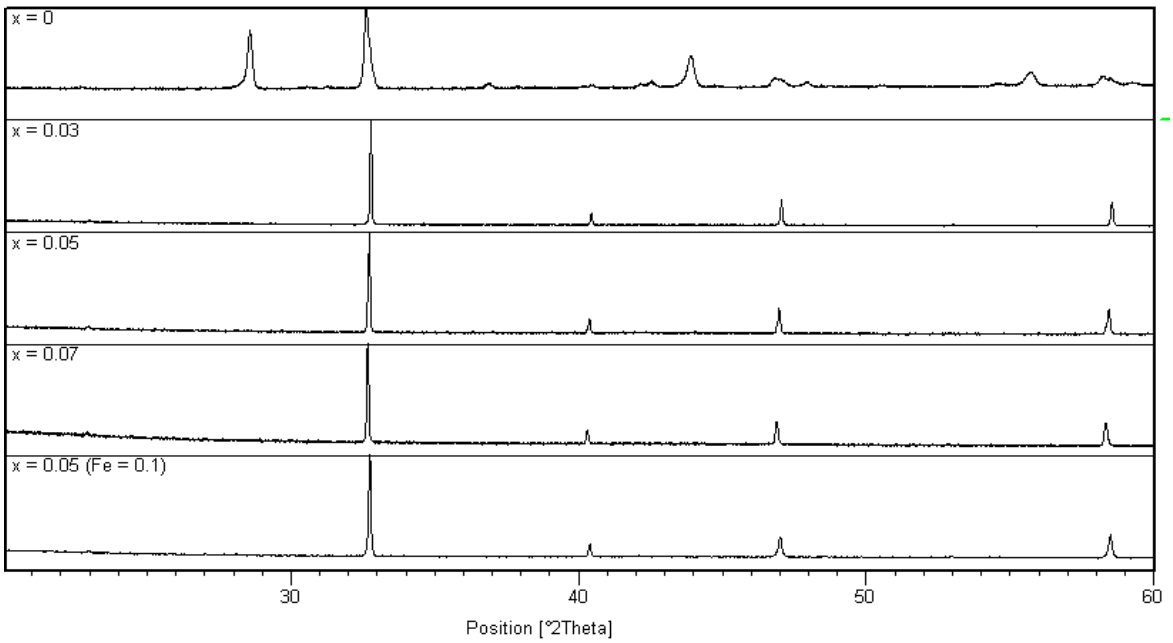

Figure 70: Powder X-ray diffraction patterns for $SrCo_{1-x}S_xO_{3-y}$ and $SrCo_{0.85}Fe_{0.1}S_{0.05}O_{3-y}$ showing a phase change from hexagonal to cubic on doping.

Table 26: Cell parameters, oxygen deficiencies (y) and oxidation states for $SrCo_{1-x}S_xO_{3-y}$ and $SrCo_{0.85}Fe_{0.1}S_{0.05}O_{3-y}$.

S content (x)	Oxygen deficiency (y)	a/ Å	Co oxidation state
0.03	0.09	3.8522 (2)	3.76
0.05	0.07	3.8640 (2)	3.76
0.07	0.04	3.8714 (2)	3.75
0.05 (Fe=0.1)	0.11	3.8610 (2)	3.74

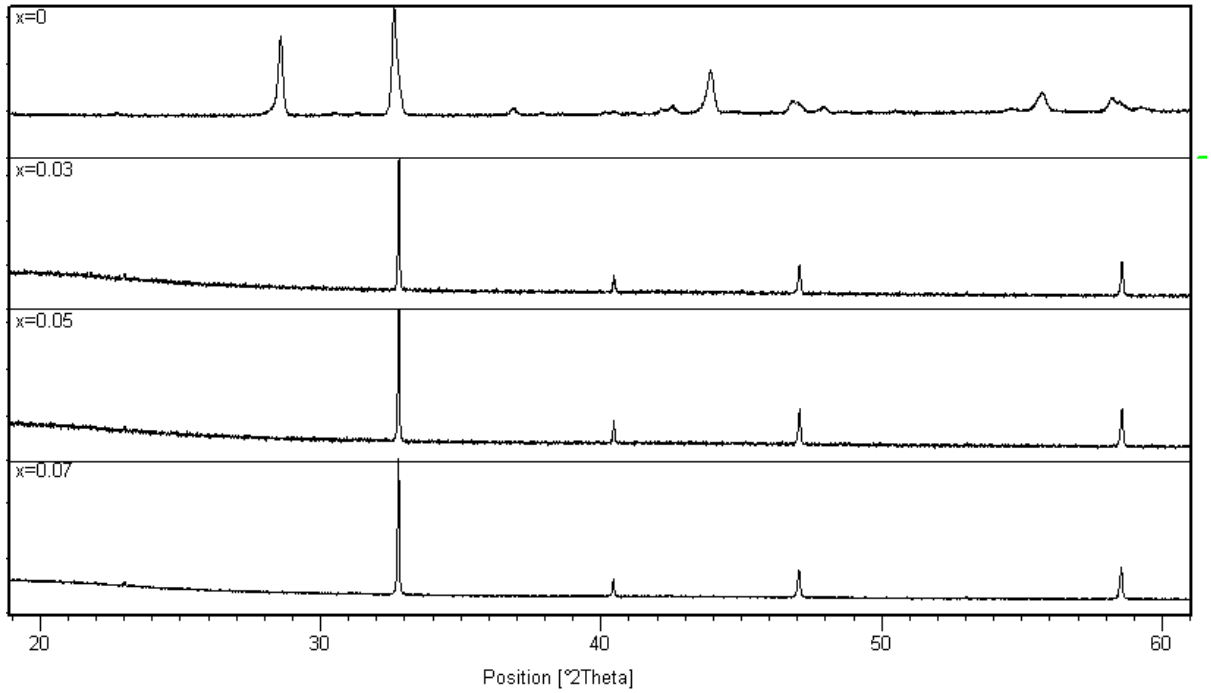

Figure 71: Powder X-ray diffraction patterns for $SrCo_{1-x}Si_xO_{3-y}$ showing a phase change from hexagonal to cubic on doping.

Table 27: Cell parameters, oxygen deficiencies (y) and oxidation states for $SrCo_{1-x}Si_xO_{3-y}$.

Si content (x)	Oxygen deficiency (y)	a/ Å	Co oxidation state
0.03	0.18	3.8549 (2)	3.62
0.05	0.21	3.8537 (2)	3.56
0.07	0.20	3.8522 (2)	3.57

The structures of the $SrCo_{1-x}Z_xO_{3-y}$ (Z=P=0.03, 0.07 and Z=Si=0.03) samples were examined by neutron diffraction. These neutron diffraction measurements showed the presence of extra peaks, which were not seen in the X-ray data. These extra peaks were indexed to an expanded tetragonal P4/mmm cell, which was correlated with a degree of oxygen vacancy ordering. The refined structural data and bond lengths are shown in Table 28, 29, 30, 31, 32 and 33 with the profiles showing observed, calculated and difference plots in Figure 72, 73 and 74. For these refinements, the atomic displacement parameters for the oxygen sites were constrained to be equal, as were those for the two cobalt sites.

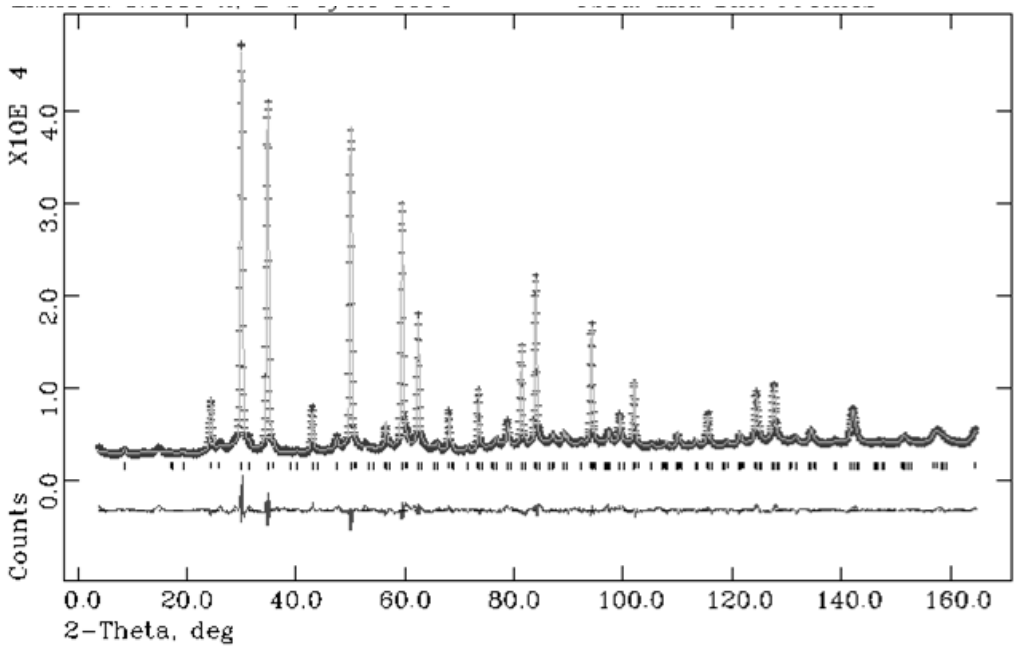

Figure 72: Observed, calculated and difference neutron diffraction profiles for $SrCo_{0.97}P_{0.03}O_{3-y}$.

Table 28: Structural parameters for $SrCo_{0.97}P_{0.03}O_{3-y}$.

Atom	Multiplicity	X	Y	Z	Uiso	Occupancy
Co1	1	0	0	0	1.28 (4)	1
Co2	1	0	0	0.5	1.28 (4)	0.94 (3)
Sr1	2	0.5	0.5	0.2354 (2)	1.19 (3)	1
O1	2	0.5	0	0	2.54 (2)	1
O2	2	0	0	0.2547 (3)	2.54 (2)	0.83 (2)
O3	2	0.5	0	0.5	2.54 (2)	0.79 (1)
P1	1	0	0	0	1.28 (4)	0
P2	1	0	0	0.5	1.28 (4)	0.06 (3)
Space Group P4/mmm, a=3.86123(9) Å, c=7.7330(5) Å, χ^2=7.063, Rwp=3.8%						

Table 29: Bond distances for $SrCo_{0.97}P_{0.03}O_{3-y}$.

Bond	Bond Length (Å)
Co1–O1	1.93061 (4) x4
Co1–O2	1.9695 (27) x2
Co2/P2–O2	1.8970 (27) x2
Co2/P2–O3	1.93061 (4) x4
Sr1–O1	2.6535 (11) x4
Sr1–O2	2.73437 (15) x4
Sr1–O3	2.8132 (12) x4

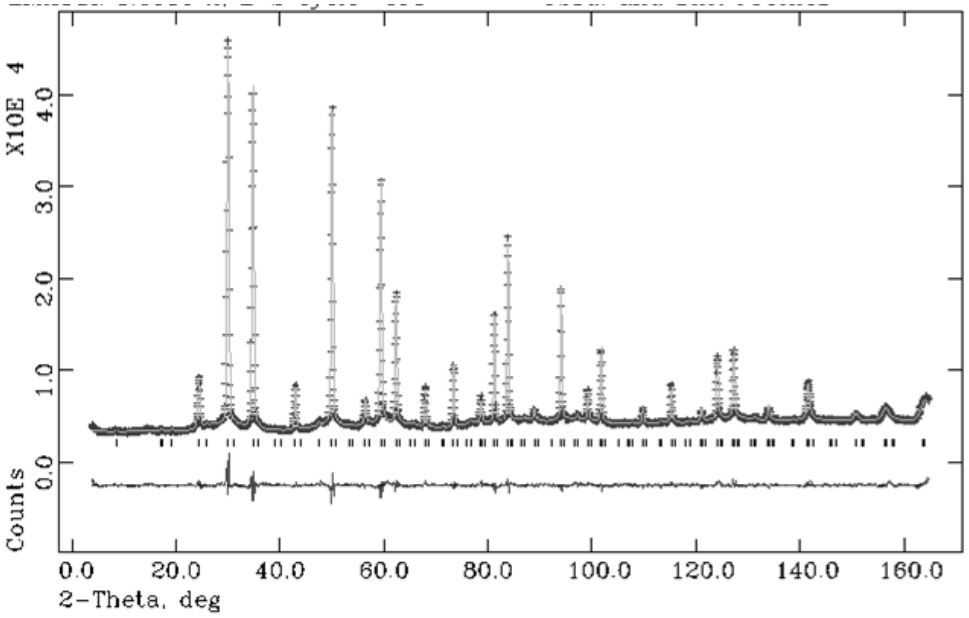

Figure 73: Observed, calculated and difference neutron diffraction profiles for $SrCo_{0.93}P_{0.07}O_{3-y}$.

Table 30: Structural parameters for $SrCo_{0.93}P_{0.07}O_{3-y}$.

Atom	Multiplicity	X	Y	Z	Uiso	Occupancy
Co1	1	0	0	0	1.49 (3)	1
Co2	1	0	0	0.5	1.49 (3)	0.83 (2)
Sr1	2	0.5	0.5	0.2420 (3)	1.51 (2)	1
O1	2	0.5	0	0	2.44 (2)	1
O2	2	0	0	0.2539 (5)	2.44 (2)	0.77 (1)
O3	2	0.5	0	0.5	2.44 (2)	0.80 (1)
P1	1	0	0	0	1.49 (3)	0
P2	1	0	0	0.5	1.49 (3)	0.17 (2)
Space Group P4/mmm, a=3.8680(1) Å, c=7.7393(7) Å, χ^2=4.354, Rwp=2.87%						

Table 31: Bond distances for $SrCo_{0.93}P_{0.07}O_{3-y}$.

Bond	Bond Length (Å)
Co1–O1	1.93402 (7) x4
Co1–O2	1.965 (4) x2
Co2/P2–O2	1.904 (4) x2
Co2/P2–O3	1.93402 (7) x4
Sr1–O1	2.6922 (15) x4
Sr1–O2	2.73669 (16) x4
Sr1–O3	2.7798 (15) x4

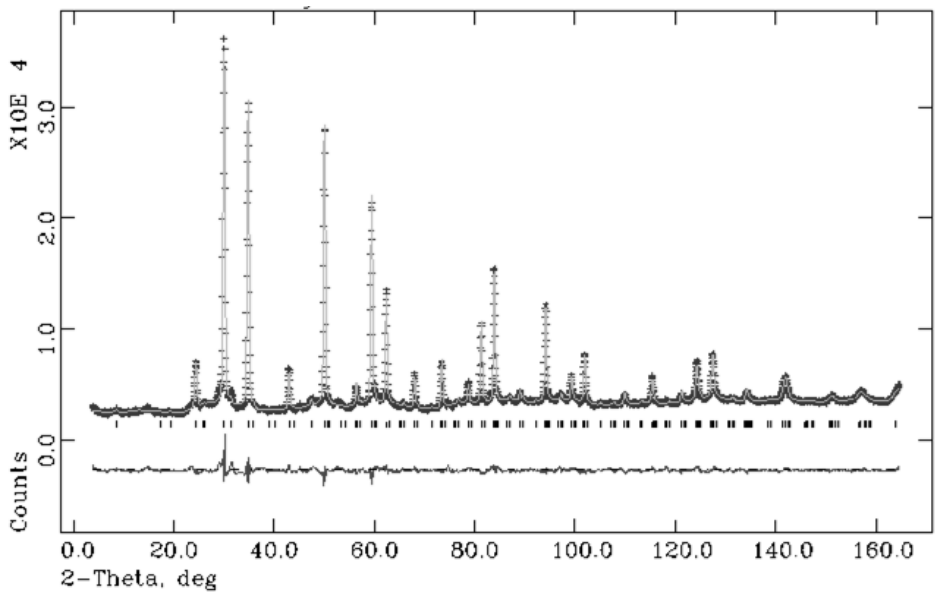

Figure 74: Observed, calculated and difference neutron diffraction profiles for $SrCo_{0.97}Si_{0.03}O_{3-y}$.

Table 32: Structural parameters for $SrCo_{0.97}Si_{0.03}O_{3-y}$.

Atom	Multiplicity	X	Y	Z	Uiso	Occupancy
Co1	1	0	0	0	1.37 (4)	1
Co2	1	0	0	0.5	1.37 (4)	0.89 (4)
Sr1	2	0.5	0.5	0.2384 (3)	1.33 (2)	1
O1	2	0.5	0	0	2.72 (2)	1
O2	2	0	0	0.2534 (5)	2.72 (2)	0.85 (2)
O3	2	0.5	0	0.5	2.72 (2)	0.78 (1)
Si1	1	0	0	0	1.37 (4)	0
Si2	1	0	0	0.5	1.37 (4)	0.11 (4)
Space Group P4/mmm, a=3.86351(8)Å, c=7.7406(4) Å, χ^2=5.462, Rwp=3.66%						

Table 33: Bond distances for $SrCo_{0.97}Si_{0.03}O_{3-y}$.

Bond	Bond Length (Å)
Co1/Si1–O1	1.93175 (4) x4
Co1/Si1–O2	1.961 (4) x2
Co2/Si2–O2	1.909 (4) x2
Co2/Si2–O3	1.93175 (4) x4
Sr1–O1	2.6714 (14) x4
Sr1–O2	2.73438 (16) x4
Sr1–O3	2.7987 (15) x4

The observed expanded cell results in two Co sites, with the P/Si preferentially occupying the Co2 site (meaning that the silicon orders in alternating layers), the site surrounded by the oxide ion

vacancies. These two Co sites show different bond lengths, with the Co2 site having shorter bond lengths than that of the Co1 octahedra consistent with the presence of phosphate/silicate dopant on this site. High atomic displacement parameters were found for the oxide ion sites, which are partly due to the tilting of the octahedra (which has been reported previously [176]). A second contribution to the high atomic displacement, in this case, is the local distortions caused by the presence of phosphate/silicate groups on the Co2 site; to achieve the tetrahedral symmetry for the phosphate/silicate group, the oxide ions will be displaced from the ideal sites resulting in further atomic displacement.

5.1.2.2. Conductivity Measurements

After the observation of a phase change from a hexagonal perovskite to a "cubic" perovskite on oxyanion doping, the conductivities of the samples were measured. There was a substantial increase in the conductivity on doping with oxyanions, with a very low conductivity of 2 Scm^{-1} recorded at room temperature for the undoped sample, compared to conductivities between 250-350 Scm^{-1} on oxyanion doping. This large increase in conductivity is due to the change from edge sharing of the octahedra in the hexagonal perovskite to the corner sharing seen in the "cubic" perovskite. As seen in Figure 75, 76 and 77, the highest conductivity is generally for the lowest doped samples (to convert to the "cubic" perovskite), with the conductivity decreasing on higher dopant levels most likely due to the oxyanions partially disrupting the Co-O network. The one exception was for the phosphate doped system, where the x=0.05 sample had higher conductivity than the x=0.03 sample, despite both samples showing a "cubic" perovskite by XRD.

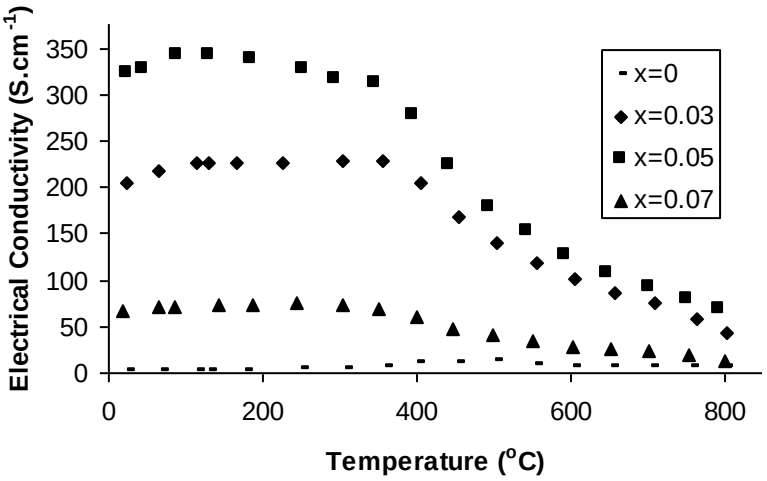

Figure 75: Temperature dependence of the electronic conductivity data for $SrCo_{1-x}P_xO_{3-y}$.

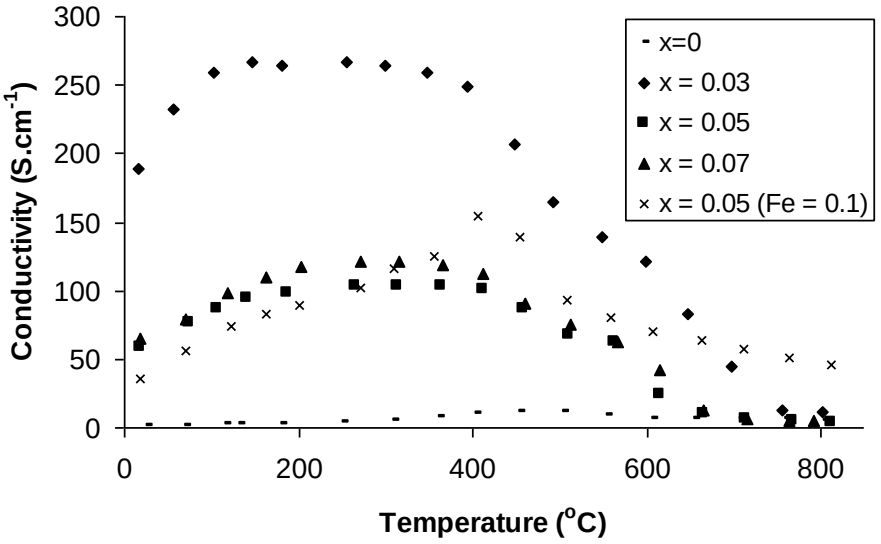

Figure 76: Temperature dependence of the electronic conductivity data for $SrCo_{1-x}S_xO_{3-y}$ and $SrCo_{0.85}Fe_{0.1}S_{0.05}O_{3-y}$.

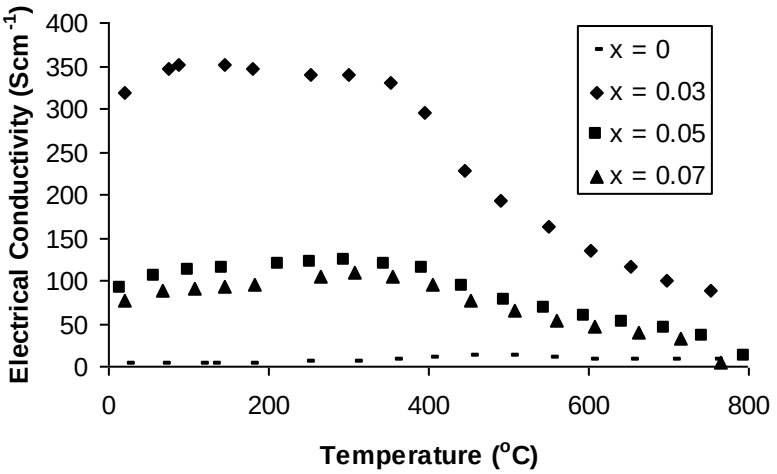

Figure 77: Temperature dependence of the electronic conductivity data for $SrCo_{1-x}Si_xO_{3-y}$.

All the samples show a decrease in conductivity on increasing temperature above ~400°C. This is due to oxygen from the lattice being lost at higher temperatures reducing the Co oxidation state, which was verified by TGA-MS analysis (Figure 78).

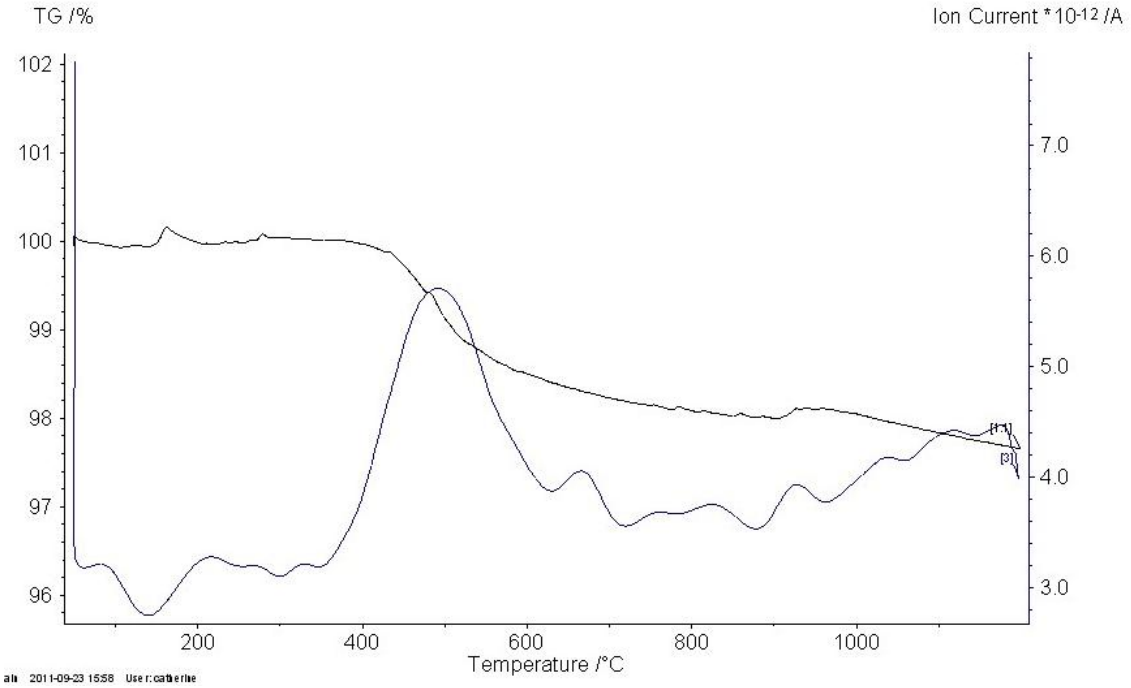

Figure 78: TGA-MS trace for $SrCo_{0.95}P_{0.05}O_{3-y}$ showing the weight loss (black) above 400°C along with the release of oxygen (blue).

5.1.2.3. Thermal Stability

Despite the very promising initial results showing a large conductivity enhancement it was noticed that the conductivity decreased on slow cooling the sample (Figure 79), and after annealing overnight at a temperature of 750°C, the conductivity decreased further.

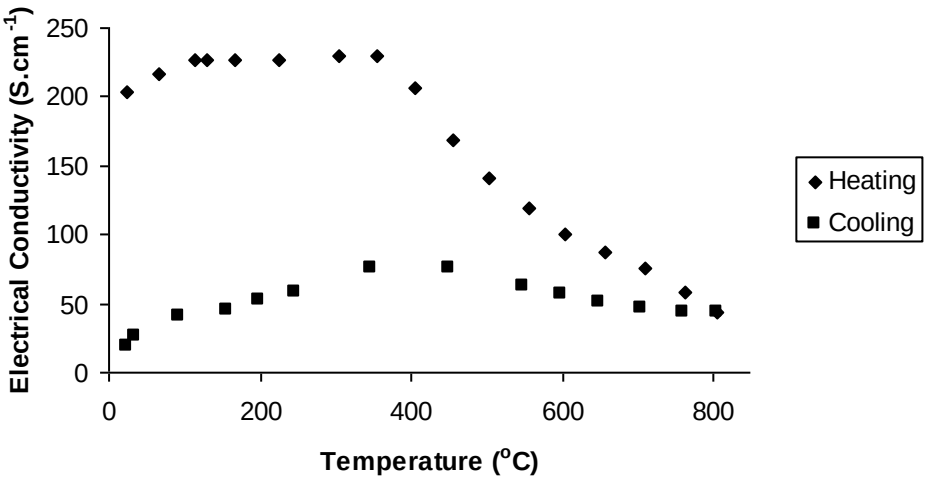

Figure 79: Temperature dependence of the electronic conductivity data for $SrCo_{0.97}P_{0.03}O_{3-y}$ on heating and slow cooling.

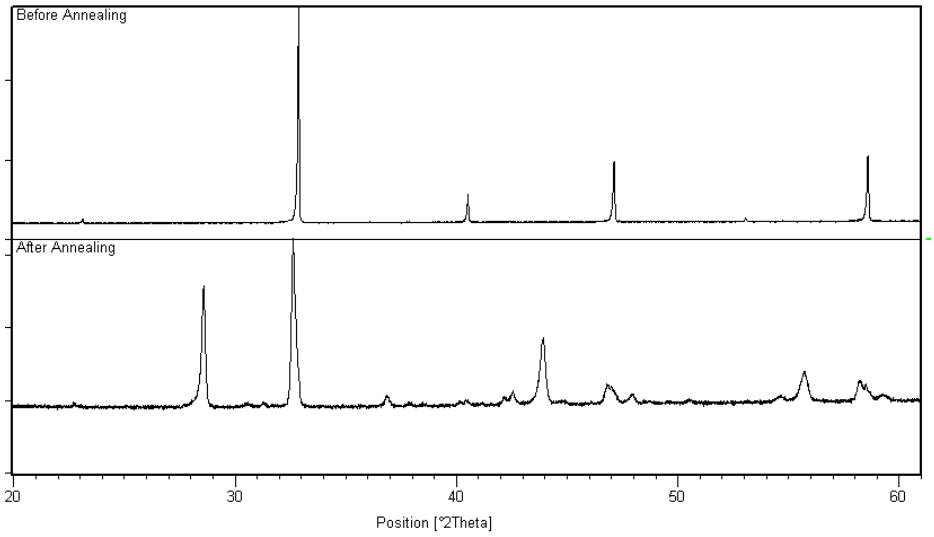

Figure 80: Powder X-ray diffraction patterns for $SrCo_{0.97}P_{0.03}O_{3-y}$ before and after annealing overnight at 750°C.

After performing X-ray diffraction measurements on the annealed sample it was observed that the "cubic" phase converted back to the hexagonal perovskite (Figure 80). This indicates that the material is metastable and could explain why the 3% phosphate doped sample has a lower

conductivity than the 5% phosphate doped sample, due to local regions of hexagonal perovskite in the former.

In order to try to stabilize these “cubic” perovskite samples, iron was co-doped onto the Co site. For the phosphate doped samples the amount of oxyanion was varied with the Fe content remaining constant (at 10%). For the silicate doped samples the oxyanion content was kept constant (at 5%) with the amount of iron being varied. The Fe doping was shown to result in greatly improved stability, with X-ray diffraction experiments (Figure 81, and 82, Table 34 and 35) showing no evidence of conversion back into the hexagonal phase after annealing overnight at 750^{o}C.

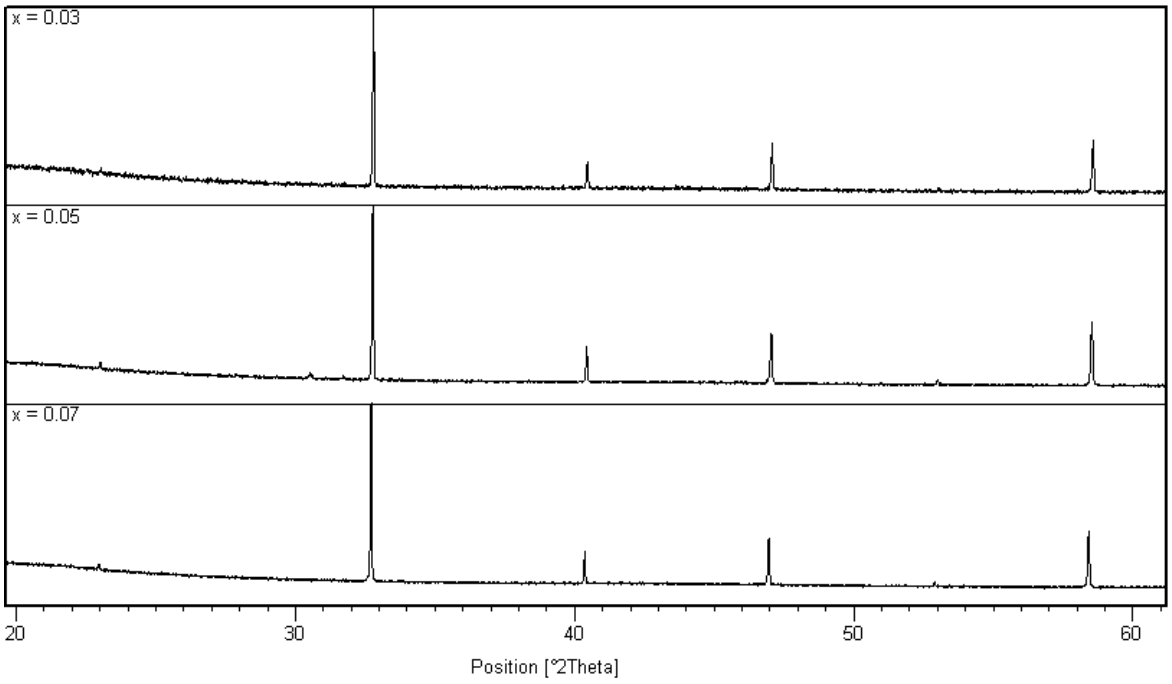

Figure 81: Powder X-ray diffraction patterns for $SrCo_{0.9-x}Fe_{0.1}P_xO_{3-y}$ after annealing at 750^{o}C.

Table 34: Cell parameters, oxygen deficiencies (y) and oxidation states for $SrCo_{0.9-x}Fe_{0.1}P_xO_{3-y}$.

P content (x)	Oxygen deficiency (y)	a/ Å	Co/Fe oxidation state
0.03	0.08	3.8582 (1)	3.90
0.05	0.07	3.8567 (2)	3.89
0.07	0.11	3.8655 (2)	3.78

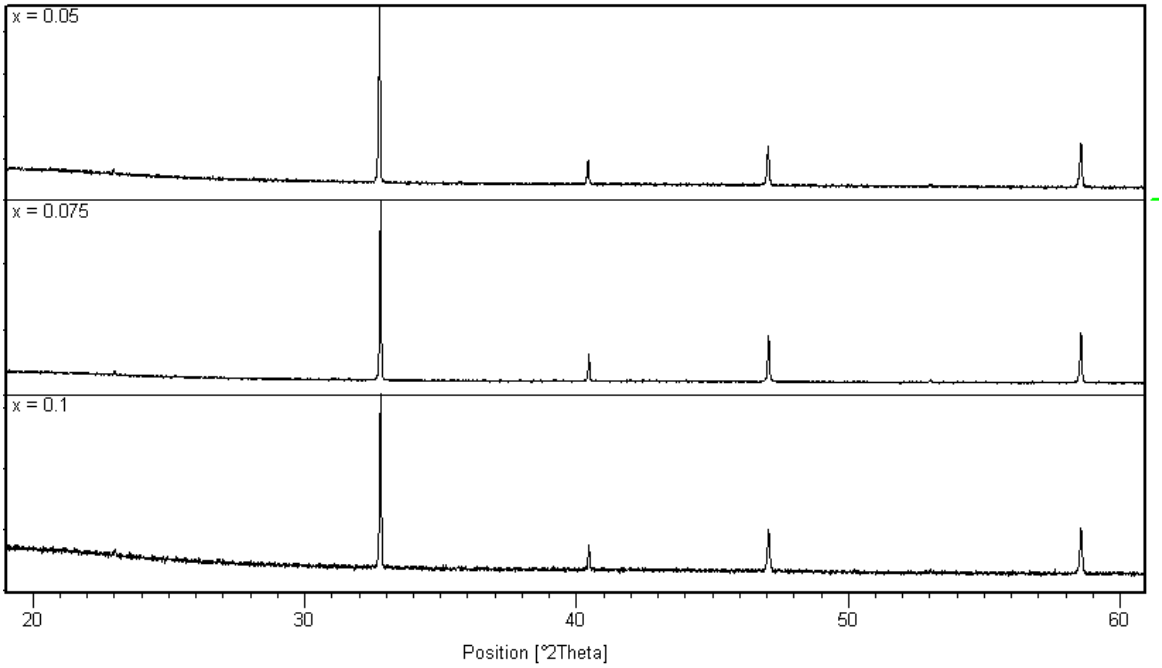

Figure 82: Powder X-ray diffraction patterns for $SrCo_{0.95-x}Fe_xSi_{0.05}O_{3-y}$ after annealing at 750°C.

Table 35: Cell parameters, oxygen deficiencies (y) and oxidation states for $SrCo_{0.95-x}Fe_xSi_{0.05}O_{3-y}$.

Fe content (x)	Oxygen deficiency (y)	a/ Å	Co/Fe oxidation state
0.05	0.11	3.8530 (1)	3.80
0.075	0.10	3.8578 (1)	3.85
0.1	0.15	3.8551 (2)	3.75

The structure of one of these Fe doped phases, $SrCo_{0.83}Fe_{0.1}P_{0.07}O_{3-y}$, was examined using neutron diffraction. As for the $SrCo_{1-x}P_xO_{3-y}$ systems, extra weak peaks were observed indicating tetragonal symmetry consistent with oxygen vacancy ordering. The refinements were carried out as before, with the atomic displacement parameters for the oxygen ion sites, as well as the parameters for the cobalt sites being constrained equally. Due to there being too many variables, the occupancies of the Co, Fe and P could not be refined independently. In this case therefore the P content was fixed at the value expected and located on the Co2 site as observed for the $SrCo_{1-x}P_xO_{3-y}$ samples. The Co and Fe occupancies were then allowed to vary. The results suggested that the iron had a preference for the Co1 site. The final structural data and difference plots can be found in Table 36 and 37, and Figure 83 respectively.

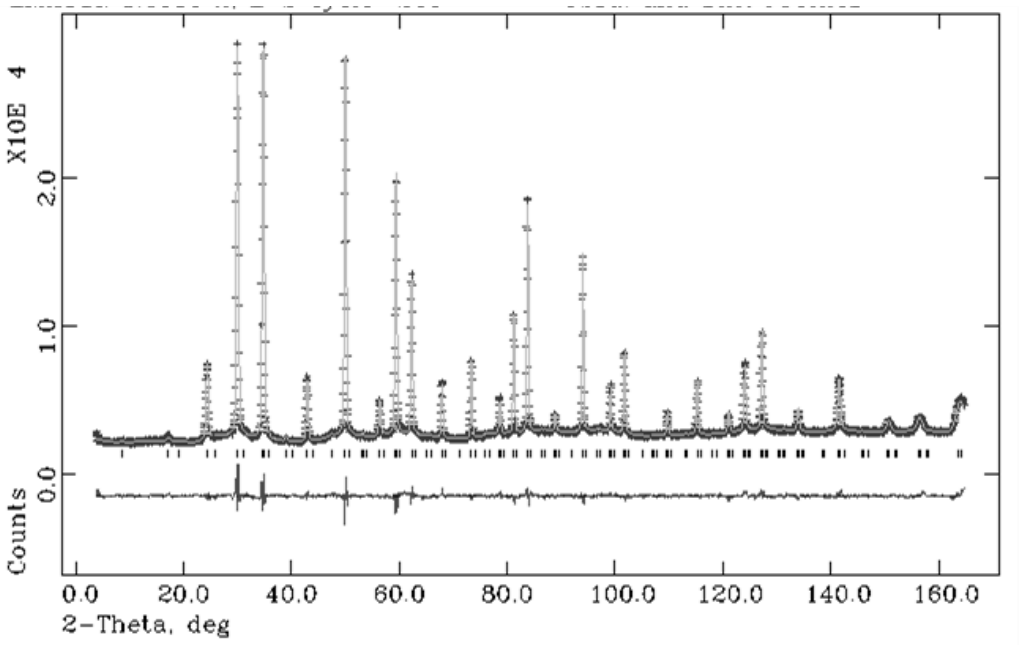

Figure 83: Observed, calculated and difference neutron diffraction profiles for $SrCo_{0.83}Fe_{0.1}P_{0.07}O_{3-y.}$

Table 36: Structural parameters for $SrCo_{0.83}Fe_{0.1}P_{0.07}O_{3-y.}$

Atom	Multiplicity	X	Y	Z	Uiso	Occupancy
Co1	1	0	0	0	1.04 (4)	0.90 (1)
Co2	1	0	0	0.5	1.04 (4)	0.82 (1)
Sr1	2	0.5	0.5	0.2446 (4)	1.60 (2)	1
O1	2	0.5	0	0	2.26 (2)	1
O2	2	0	0	0.2533 (8)	2.26 (2)	0.69 (1)
O3	2	0.5	0	0.5	2.26 (2)	0.82 (1)
Fe1	1	0	0	0	1.04 (4)	0.10 (1)
Fe2	1	0	0	0.5	1.04 (4)	0.04 (1)
P1	1	0	0	0	1.04 (4)	0
P2	1	0	0	0.5	1.04 (4)	0.14
Space Group P4/mmm, a=3.8675(1)Å, c=7.7411(5) Å, χ^2=3.362, Rwp=3.12%						

Table 37: Bond distances for $SrCo_{0.83}Fe_{0.1}P_{0.07}O_{3-y.}$

Bond	Bond Length (Å)
Co1/Fe1–O1	1.93377 (5) x4
Co1/Fe1–O2)	1.961 (6) x2
Co2/P2/Fe2–O2	1.909 (6) x2
Co2/P2/Fe2–O3	1.93377 (5) x4
Sr1–O1	2.7067 (21) x4
Sr1–O2	2.73559 (15) x4
Sr1–O3	2.7653 (22) x4

While the results above showed that Fe doping was beneficial in improving the thermal stability of the system, it was important to analyse the effect on the conductivity. The conductivity of the iron doped samples show a great improvement over the parent undoped sample $SrCoO_{3-y}$ with a conductivity of 254 Scm^{-1} for the x=0.03 phosphate doped sample at room temperature, compared to 2 Scm^{-1} for the parent material (Figure 84). As before the conductivity was highest for systems with the lower levels of oxyanion dopants. In addition, the conductivity was shown to decrease on increasing the Fe content (Figure 85) which may again be due to the partial disruption of the electronic conduction pathway (Figure 85). Overall, however, the high conductivity and improved stability of these Fe doped systems suggests promise for use as cathode materials for intermediate temperature SOFC.

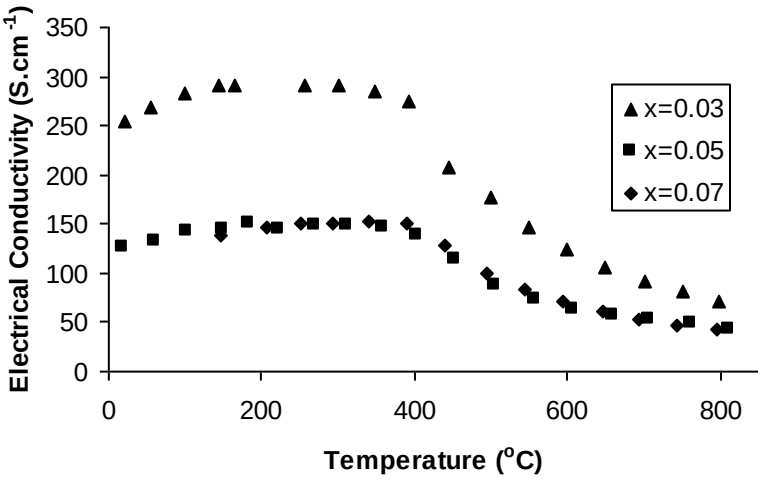

Figure 84: Temperature dependence of the electronic conductivity data for $SrCo_{0.9-x}Fe_{0.1}P_xO_{3-y}$.

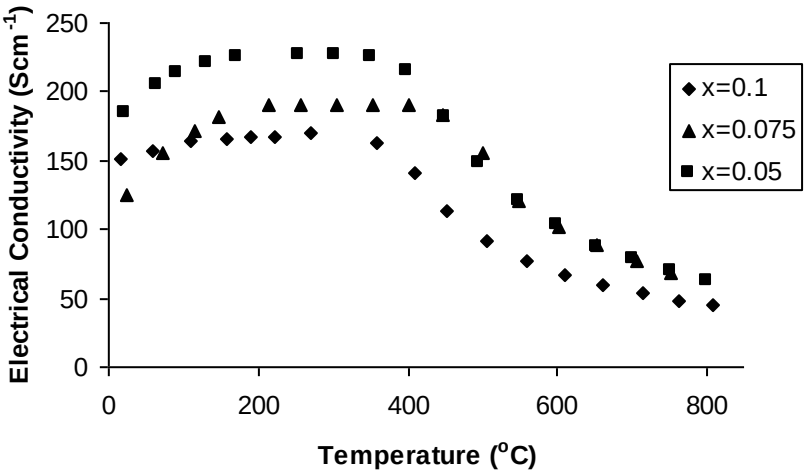

Figure 85: Temperature dependence of the electronic conductivity data for $SrCo_{0.95-x}Fe_xSi_{0.05}O_{3-y}$.

5.1.2.4. Chemical Compatibility with Electrolyte Materials

The above conductivity results suggested promise for these materials as SOFC cathodes. In order to examine this potential further, compatibility studies were performed on the $SrCo_{0.85}Fe_{0.1}(P/Si)_{0.05}O_{3-y}$ and $SrCo_{0.95}Si_{0.05}O_3$ samples. The compatibility results for these materials with a YSZ electrolyte were not promising, with the XRD patterns showing the formation of insulating $SrZrO_3$ and cobalt oxides, thus indicating low chemical compatibility with YSZ. The compatibility with the CGO electrolyte showed more promise with only small amounts of $(Sr/Gd)_2CoO_4$ being apparent after heating (Figure 86, 87 and 88). Moreover this impurity phase would be expected to still display high conductivity, and so may be less of a problem than formation of $SrZrO_3$. Further work is required therefore to investigate the cathode performance of these systems in SOFCs.

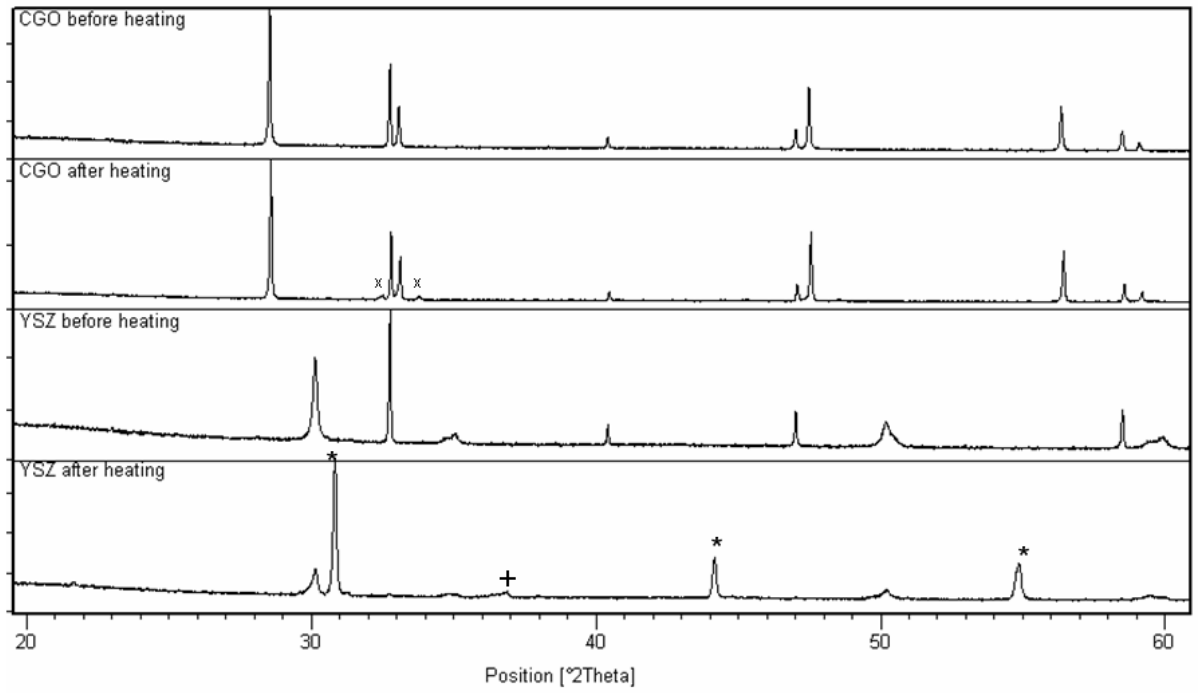

Figure 86: Powder X-ray diffraction patterns for compatibility studies between $SrCo_{0.85}Fe_{0.1}P_{0.05}O_{3-y}$ and electrolytes CGO and YSZ before and after heating at 100°C for 2 days * = $SrZrO_3$ + = Co_3O_4 x = $(Gd/Sr)_2(CoO_4)$.

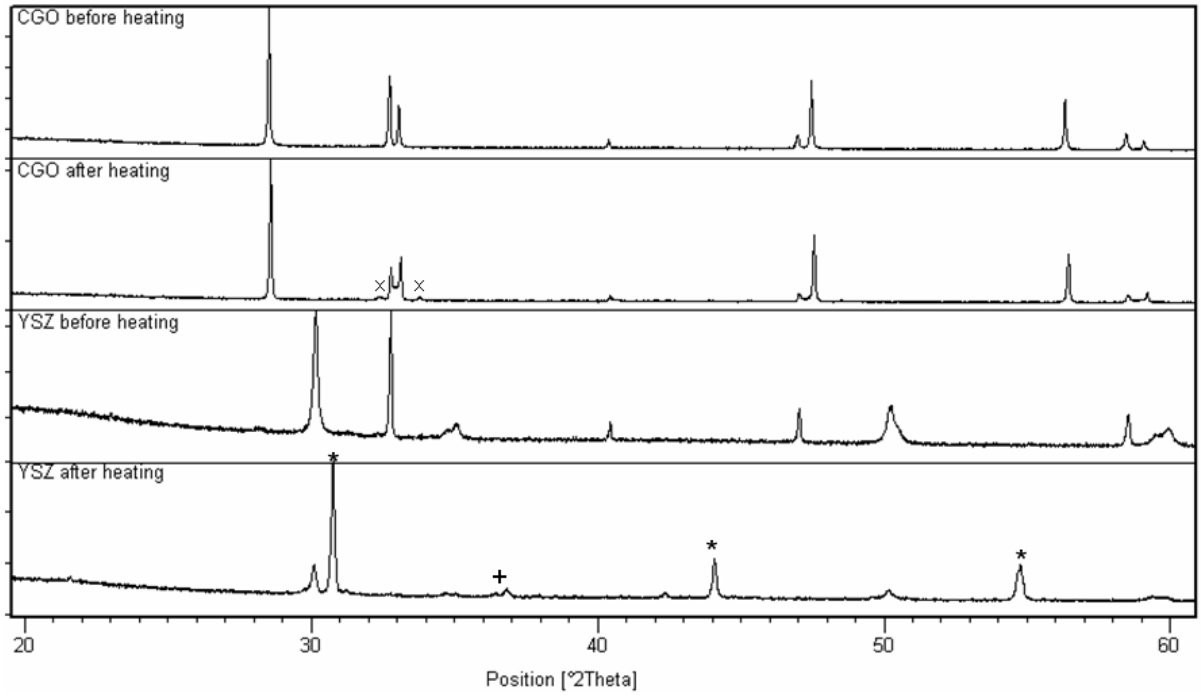

Figure 87: Powder X-ray diffraction patterns for compatibility studies between $SrCo_{0.95}Si_{0.05}O_{3-y}$ and electrolytes CGO and YSZ before and after heating at 1000°C for 2 days * = $SrZrO_3$ + = Co_3O_4 x = $(Gd/Sr)_2(CoO_4)$.

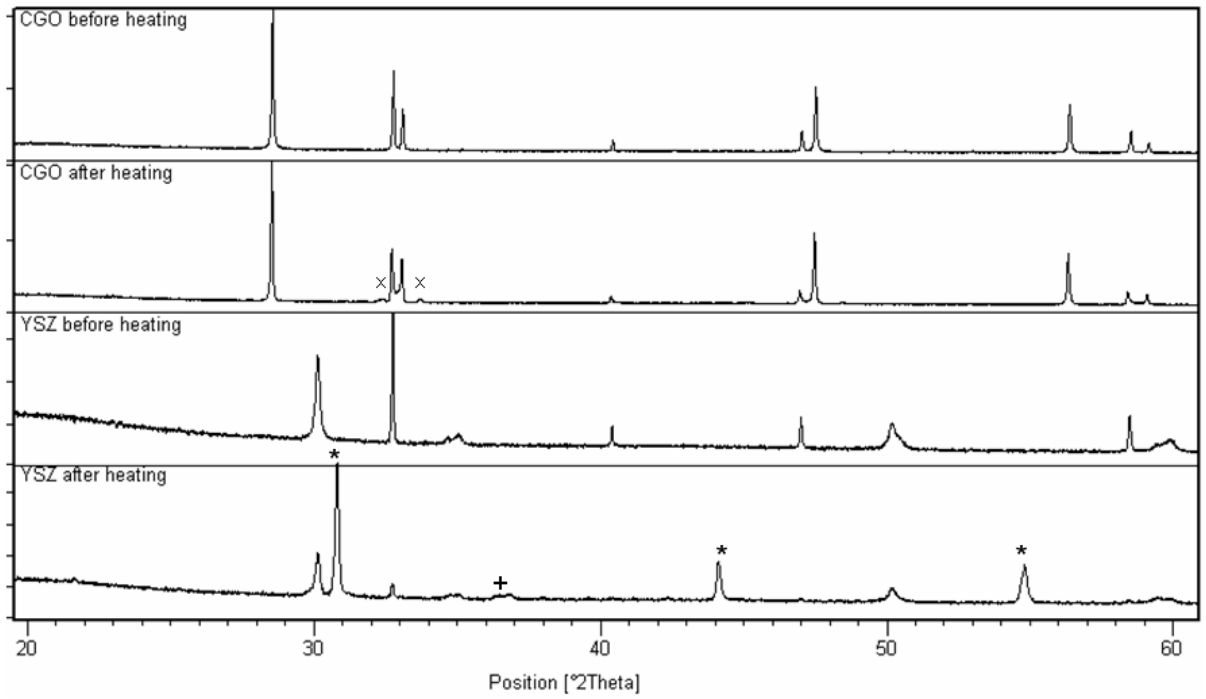

Figure 88: Powder X-ray diffraction patterns for compatibility studies between $SrCo_{0.85}Fe_{0.1}Si_{0.05}O_{3-y}$ and electrolytes CGO and YSZ before and after heating at 1000°C for 2 days * = $SrZrO_3$ + = Co_3O_4 x = $(Gd/Sr)_2(CoO_4)$.

5.1.2.5. Electrochemical Measurements

In order to examine the potential of these materials as cathode catalysts for low temperature alkaline fuel cells, cyclic voltammetry measurements were performed at room temperature on the undoped sample and $SrCo_{0.97}P_{0.03}O_{3-y}$ sample, both with and without iron and cobalt doping. As can be seen in the voltammogram (Figure 89) there is no significant improvement in the onset potential on phosphate doping, indicating no improvement to the oxygen reduction reaction. Moreover the onset potentials are relatively low at -0.23. Therefore, due to this poor result, no further low temperature electrochemical results were performed on these samples.

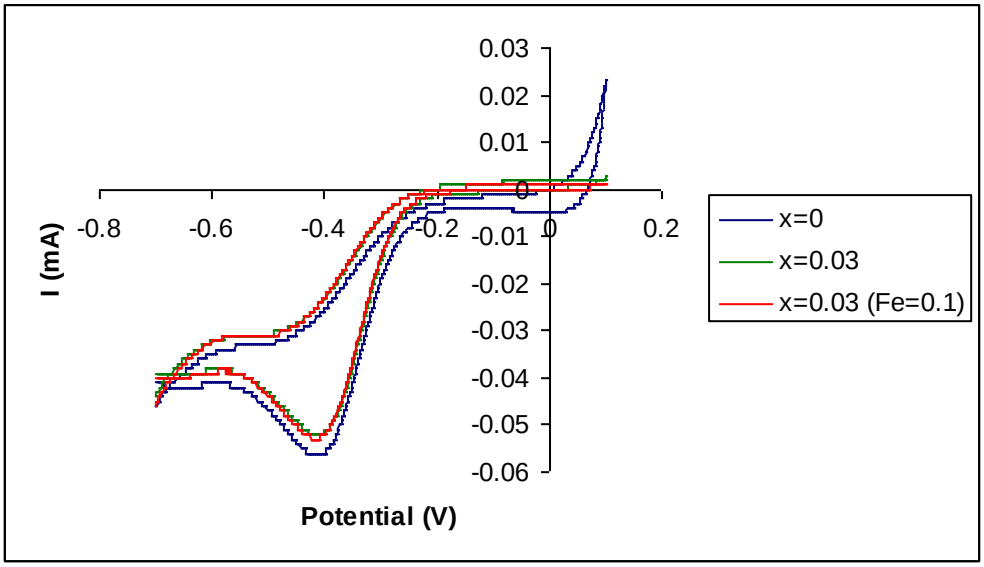

Figure 89: Cyclic voltammograms of $SrCo_{1-x}P_xO_{3-y}$ and $SrCo_{0.9-x}Fe_{0.1}P_xO_{3-y}$.

As for the phosphate doped samples the electrochemical tests at room temperature performed on the $SrCo_{0.95}Si_{0.05}O_{3-y}$ material, also showed no significant change in the onset potential as seen in the cyclic voltammogram in Figure 90. This means that there is no improvement for the oxygen reduction reaction on Si doping, and as noted above, the observed onset potential is significantly lower than observed for platinum, the current favoured low temperature fuel cell catalyst.

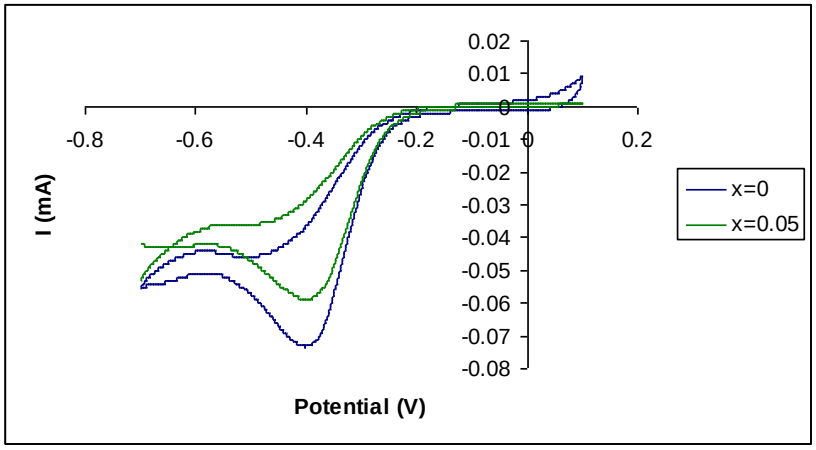

Figure 90: Cyclic voltammograms of $SrCo_{1-x}Si_xO_{3-y}$.

5.1.3. Conclusions

In this work it has been shown that oxyanions (phosphate, silicate and sulphate) can be successfully incorporated into the perovskite system $SrCoO_{3-y}$. This oxyanion incorporation leads to an enhancement in the conductivity due to the change from a hexagonal perovskite with face sharing of octrahedra to a "cubic" perovskite with corner sharing of octahedra. However these doped phases were discovered to be metastable converting back to a hexagonal perovskite on annealing at intermediate temperatures. The thermal stability could be improved by co-doping with a small amount of Fe, although this gave a small reduction in conductivity compared to the corresponding samples without Fe.

Further experiments were performed to determine the potential for use in both high temperature SOFC and low temperature alkaline fuel cells. In terms of the former preliminary chemical compatibility studies showed poor compatibility with YSZ electrolytes, with better results observed for CGO electrolytes. Further work needs to be done to investigate the cathodes performance of these materials in SOFCs. In terms of low temperature fuel cell applications, preliminary electrode measurements were performed, with these initial results giving poor onset potentials for both doped and undoped materials, suggesting that these systems are not viable alkaline fuel cell cathode catalysts.

5.2. $SrZ_{1-x}Si_xO_{3-y}$ (Z=Mn, Fe)

The related manganate system, $SrMnO_{3-y}$, is another interesting potential cathode material. As with the $SrCoO_{3-y}$ system, undoped $SrMnO_{3-y}$ is hexagonal resulting in low conductivities [186, 187]. However on doping with elements such as La the structure can be stabilized as a "cubic" perovskite resulting in improvements in the conductivity and good cathode performance [45, 187-190]. This has led to considerable work on $La_{1-x}Sr_xMnO_3$ as a SOFC cathode material. In this work we examined whether similar improvements in performance could be achieved through oxyanion doping, with the focus on Si doping.

The perovskite $SrFeO_{3-y}$ was also investigated. Unlike its undoped Co/Mn counterparts which contain face sharing of octahedra, undoped $SrFeO_{3-y}$ contains corner linked octahedra. In order to improve the electrode performance of $SrFeO_{3-y}$ doping on both the A and B cation sites has been previously examined in the literature [191, 192]. Promising performance has been observed for such systems, particularly by co-doping with La (for Sr) and Co (for Fe). In this work the effect of Si doping was examined, to determine if improvements could be observed in a system where no change in the linkages of the transition metal octahedra would be expected.

5.2.1. Experimental

High purity $SrCO_3$, MnO_2, Fe_2O_3 and SiO_2 were used to prepare a range of $SrM_{1-x}Si_xO_{3-y}$ samples (M=Mn and Fe). These starting materials were ground together in the correct stoichiometric ratios and heated to a temperature of 1100^{o}C for 12 hours. The samples were then ballmilled (350rpm for 1 hour, Fritsch Pulverisette 7 planetary ballmill) and further heated to 1300^{o}C (M=Mn) and 1250^{o}C (M=Fe) for another 12 hours. The samples were then furnace cooled to 350^{o}C and held at this temperature for 12 hours to ensure full oxygenation.

Powder X-ray diffraction experiments, using a Bruker D8 transmission diffractometer with Cu $K\alpha_1$ radiation, were employed to determine phase purity. Neutron diffraction data were collected for the $SrFe_{1-x}Si_xO_{3-y}$, x=0.1 and 0.15 samples, using the HRPT diffractometer at SINQ (PSI Villigen). The GSAS suite of programs was used for the structure refinements.

Oxygen contents were estimated from thermogravimetric analysis (Netzsch STA 449 F1 Jupiter Thermal Analyser). The samples were heated to a temperature of 1200^{o}C at a rate of 10^{o}C/min and held for 30 minutes. This reduces the transitional metal state to 3+ allowing the original oxygen content to be determined from the mass loss observed.

Raman spectroscopy measurements were performed on the powder samples (Renishaw inVia Raman Microscope) using the 532nm laser at a 5% power level with 30 seconds exposure and 10 accumulations.

Pellets for conductivity measurements were prepared by ball milling the samples for an hour and adding a small amount of polyvinyl alcohol before pressing as pellets and sintering at 1350^{o}C (M=Mn) and 1300^{o}C (M=Fe). The conductivities were then measured using the 4 probe d c method. The 4 platinum electrodes were attached to the pellet using platinum paste and then fired to 1000^{o}C for an hour to ensure bonding, before lowering the temperature to 350^{o}C for 12 hours to ensure oxygenation.

In order to further test the potential of these systems for use in SOFCs, compatibility studies were performed with fuel cell electrolytes. These compatibility studies were performed on 0.5g of the sample mixed thoroughly with 0.5g of the electrolyte (YSZ and CGO). This mixture was then examined by XRD both before being placed in a furnace at 1000^{o}C for 48 hours, and afterwards to determine whether there were any changes.

In terms of analysing the potential for use in low temperature alkaline fuel cells, preliminary electrode tests were performed. For the electrochemical measurements, inks were made by ball milling 0.3g of the samples with 2ml of propanol for 2 hours. After ball milling, another 6ml of propanol was added along with 0.1g of polytetrafluoroethylene, 60wt% dispersion in water. The inks were deposited on a glassy carbon electrode, dried, and then examined by cyclic voltammetry and rotating disk measurements in oxygen saturated 0.1M KOH with a variety of rotation rates (400, 800, 1200,1600 and 2000 rpm) with the Invium Stat, Invium A07026 model 636 equipment.

5.2.2. Results and Discussion

5.2.2.1. Structural Studies

The X-ray diffraction data from the $SrMn_{1-x}Si_xO_{3-y}$ series clearly show a phase change on doping, changing from a hexagonal to a cubic perovskite on doping with ≥15% silicon (Figure 91). For silicon levels lower than 15% the data show the presence of both hexagonal and cubic phases, with the cubic phase becoming more prominent with increasing levels of silicon incorporated. In the $SrFe_{1-x}Si_xO_{3-y}$ system there was a change in cell symmetry from tetragonal to cubic on Si doping into the system. Higher Si contents were possible in the manganese system, with the incorporation of up to 20% Si before Sr_2SiO_4 impurities formed, compared to 15% silicon for the Fe system.

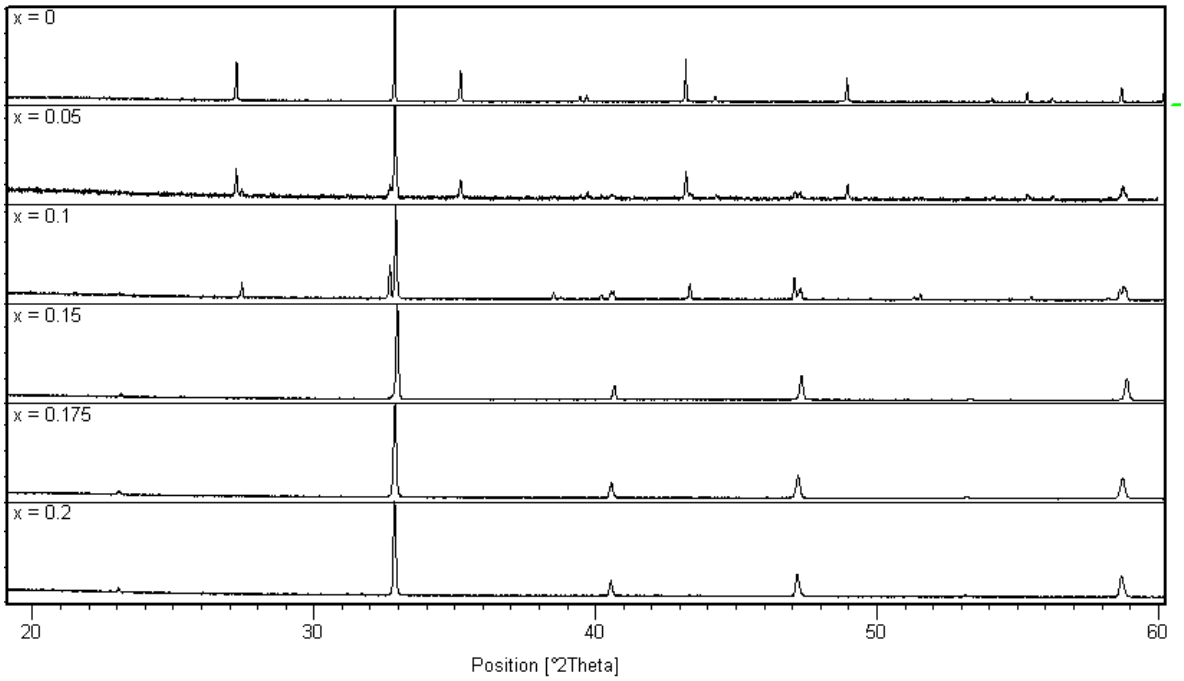

Figure 91: Powder X-ray diffraction patterns for $SrMn_{1-x}Si_xO_{3-y}$ showing the phase change from hexagonal to cubic on Si doping.

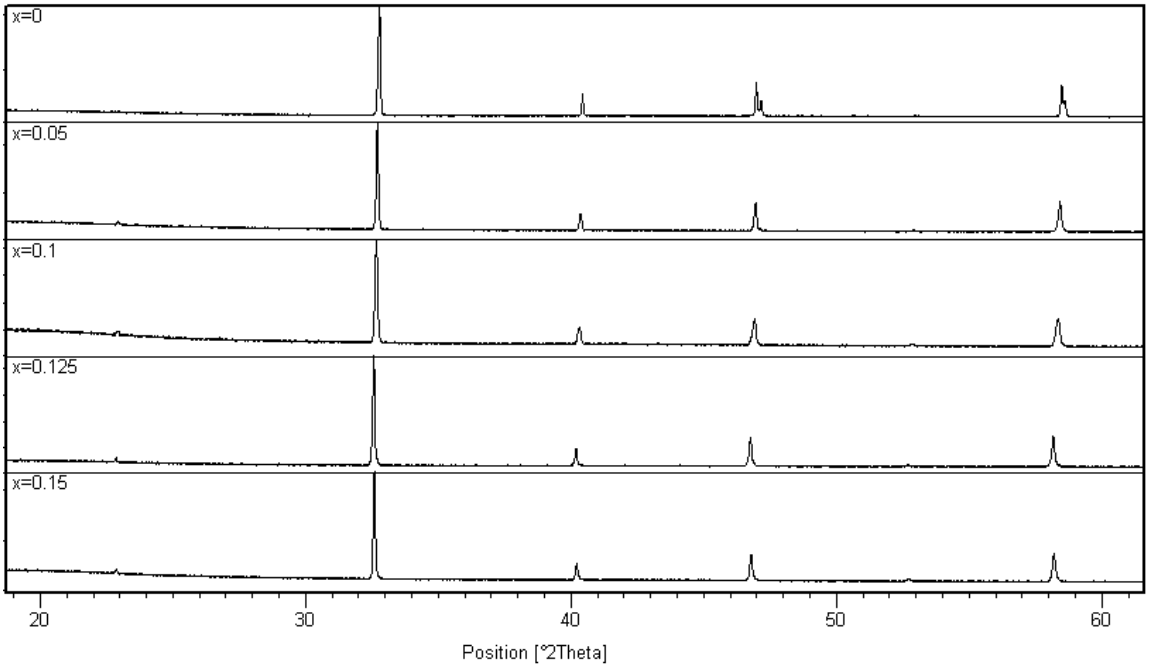

Figure 92: Powder X-ray diffraction patterns for $SrFe_{1-x}Si_xO_{3-y}$.

Structure refinements for the $SrMn_{1-x}Si_xO_{3-y}$ (x=0.15, 0.175 and 0.2) samples were performed using the X-ray data. The structural data for these phases are given in Table 38 and 39. The cell parameters show a slight increase in cell volume on doping of silicon into the system. This increase of the size is due to the increasing reduction of the Mn^{4+} to the larger Mn^{3+} cations countering the effect of the smaller Si^{4+} being added (Equation 24).

Equation 24 $SiO_2 + 3Mn_{Mn} + O_O \rightarrow Si_{Mn} + 2Mn_{Mn}' + V_O^{\bullet\bullet} + 1/2O_2 + MnO_2$

This was supported by TGA studies which indicated the oxygen contents and oxidation states given in Table 40.

Table 38: Structural parameters for $SrMn_{1-x}Si_xO_{3-y}$.

Atom	Multiplicity	X	Y	Z	X = 0.15		X = 0.175		X = 0.2	
					Uiso	Occ	Uiso	Occ	Uiso	Occ
Sr	1	0	0	0	1.06 (3)	1	1.13 (7)	1	1.00 (7)	1
Mn	1	0.5	0.5	0.5	1.4 (1)	0.90 (1)	1.4 (1)	0.81 (1)	1.3 (1)	0.82 (2)
O	3	0.5	0.5	0	2.4 (3)	0.90 (1)	2.8 (3)	0.90 (1)	3.0 (4)	0.90 (2)
Si	1	0.5	0.5	0.5	1.4 (1)	0.10 (1)	1.4 (1)	0.19 (1)	1.3 (1)	0.18 (2)
$SrMn_{0.85}Si_{0.15}O_{3-x}$, Space Group Pm-3m, $\chi^2 = 1.199$, $R_{wp} = 6.02\%$, a = 3.83695 (5) $SrMn_{0.825}Si_{0.175}O_{3-x}$, Space Group Pm-3m, $\chi^2 = 1.241$, $R_{wp} = 5.52\%$, a = 3.84555(5) $SrMn_{0.8}Si_{0.2}O_{3-x}$, Space Group Pm-3m, $\chi^2 = 1.131$, $R_{wp} = 6.4\%$. a = 3.84752 (6)										

Table 39: Bond distances for $SrMn_{1-x}Si_xO_{3-y}$.

	X = 0.15	X = 0.175	X = 0.2
Sr1-O1	2.71313 (3) x12	2.71921 (4) x12	2.72061 (4) x12
Mn/Si-O1	1.91847 (2) x6	1.92277 (3) x6	1.92376 (3) x6

Table 40: Oxygen deficiencies (y) and Mn oxidation state for $SrMn_{1-x}Si_xO_{3-y}$.

Si Content	Oxygen Deficiency	Mn Oxidation State
0.15	0.25	3.40
0.175	0.27	3.34
0.2	0.28	3.31

The structures of the $SrFe_{1-x}Si_xO_{3-y}$, x = 0.1 and 0.15, samples were examined using neutron diffraction data. The data indicated a cubic cell (Pm-3m), with no evidence for extra peaks contrary to Si doped $SrCoO_{3-y}$. The refined structural data and selected bond distances are shown in Table 41 and 42 along with the diffraction profiles in Figure 93 and 94.

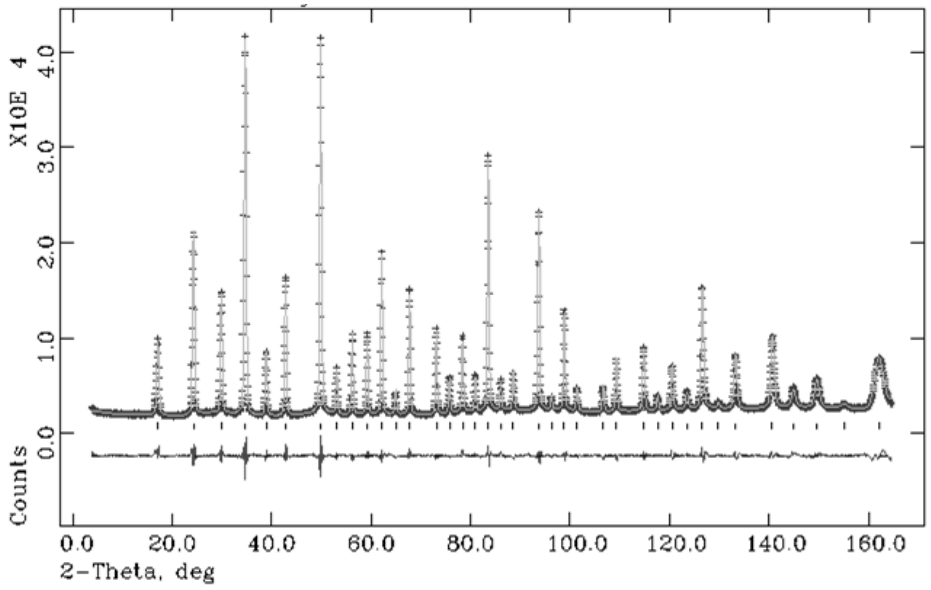

Figure 93: Observed, calculated and difference neutron diffraction profiles for $SrFe_{0.9}Si_{0.1}O_{3-y}$.

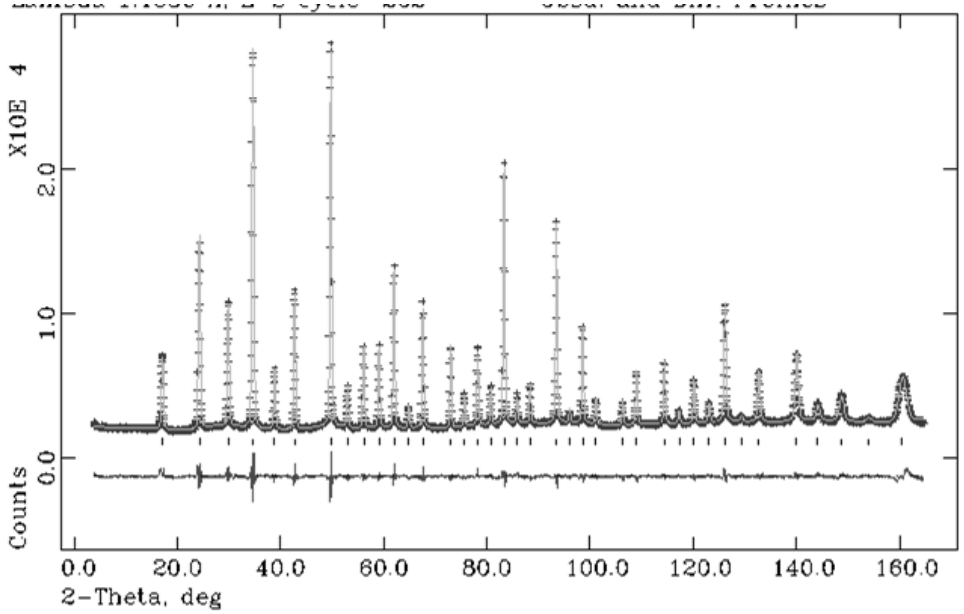

Figure 94: Observed, calculated and difference neutron diffraction profiles for $SrFe_{0.85}Si_{0.15}O_{3-y}$.

For the refinement the atomic displacement parameters for the Fe and Si were constrained to be equal. The Fe and Si occupancies were refined, with the constraint that their sum equalled 1.0. As can be seen from Table 41 the oxygen atomic displacement parameters are higher than the other atoms which can be related to the local distortions caused by the presence of the silicate groups. Due to the likely disorder in the orientation of the SiO_4^{4-} group and the relatively low Si content it was not possible to refine separate O positions for the silicate groups. On increasing the Si content the Fe/Si-O bond distance increases due to the partial reduction of the Fe^{4+} to Fe^{3+} outweighing the effect of the smaller Si^{4+}.

Table 41: Structural parameters for $SrFe_{1-x}Si_xO_{3-y}$.

Atom	Multiplicity	x	y	Z	X=0.1		X=0.15	
					Uiso	Occupancy	Uiso	Occupancy
Fe1	1	0	0	0	0.766 (8)	0.934 (5)	0.94 (1)	0.880 (6)
Sr1	1	0.5	0.5	0.5	1.07 (1)	1	1.22 (1)	1
O1	3	0.5	0.5	0	1.65 (1)	0.897 (3)	1.75 (1)	0.871 (3)
Si1	1	0	0	0	0.766 (8)	0.066 (5)	0.94 (1)	0.120 (6)
$SrFe_{0.93}Si_{0.07}O_{2.91}$: Space Group Pm-3m, a=3.87829(4) Å, χ^2=5.090, R_{wp}=3.73% $SrFe_{0.88}Si_{0.12}O_{2.613}$: Space Group Pm-3m, a=3.88671(2)Å, χ^2=3.810, R_{wp}=3.47%								

Table 42: Bond distances for $SrFe_{1-x}Si_xO_{3-y}$.

Bond	X=0.1 Bond Distance/ Å	X=0.15 Bond Distance/ Å
Fe/Si-O	1.93914 (1) (x 6)	1.94335 (1) (x 6)
Sr-O	2.74236 (1) (x 12)	2.74832 (1) (x 12)

Table 43: Oxygen deficiencies (y) and Fe oxidation state for $SrFe_{1-x}Si_xO_{3-y}$.

Si Content	Oxygen Deficiency	Fe Oxidation State
0.05	0.2	3.6
0.1	0.23	3.48
0.125	0.25	3.46
0.15	0.25	3.42

Confirmation of local cubic symmetry was provided by Raman spectroscopy experiments. As can be seen in Figure 95 there is a clear difference between the undoped and doped systems. The latter show no peaks consistent with the result expected, since a perfect perovskite has cubic symmetry which results in all the lattice sites having inversion symmetry causing first order Raman scattering to be forbidden. In contrast for the hexagonal system, peaks are shown due to the fact that in this case there are Raman allowed bands.

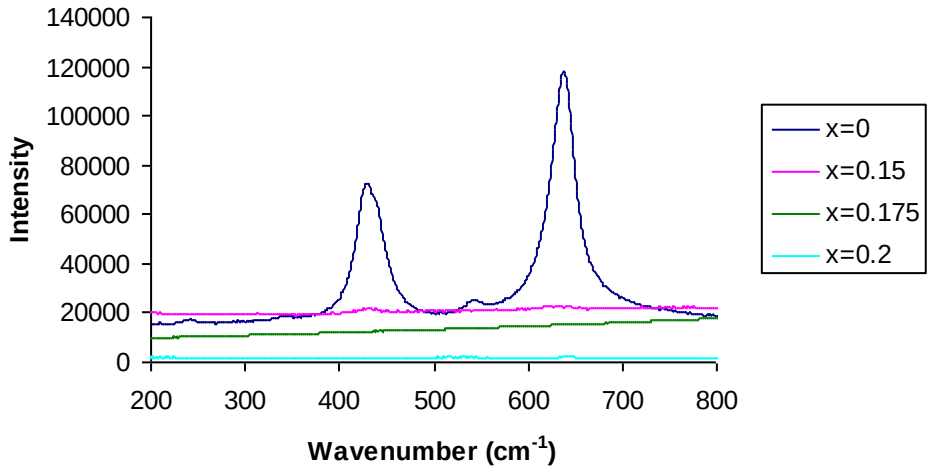

Figure 95: Raman spectra of $SrMn_{1-x}Si_xO_{3-y}$ showing that there are Raman active bands for the undoped hexagonal sample compared to no observed bands for the doped cubic system.

Since the previous results for the Co systems, $SrCo_{1-x}Z_xO_{3-y}$ (Z=P, S, Si) indicated that these phases were metastable, the $SrMn_{1-x}Si_xO_{3-y}$ samples were annealed at 750°C for 14hrs. X-ray

diffraction experiments were performed before and after annealing, and indicated no change, thus showing that in this case the higher Si content fully stabilizes the cubic phase.

In addition to examining the stability in air, the stability of these systems in H_2 was examined to determine if they could also be used as SOFC anodes. From these experiments it was interesting to observe that the doped Fe systems were shown to be stable in H_2; for the Si doped phases, the cell remained cubic after heating to 800^{o}C in 10% H_2/Ar_2 while the undoped phase converted to brownmillerite type $Sr_2Fe_2O_5$. In the Mn systems both the doped and undoped systems were also shown to be stable up to this temperature in H_2, but the data indicated a conversion to a brownmillerite type $Sr_2Mn_2O_5$. A future study of the conductivity of these samples in a hydrogen atmosphere is planned to characterise their potential as SOFC anode materials.

5.2.2.2. Conductivity Measurements

In order to examine the potential of these materials for use as SOFC cathodes, the conductivities were measured. The results showed a large difference between the undoped and doped samples for the Mn system. The undoped x=0 hexagonal perovskite showed very low conductivity of 0.008-0.03 Scm^{-1} between 600–800^{o}C compared to the cubic, Si doped samples $0.15<x<0.2$ which showed a large increase to higher conductivities (9–14 Scm^{-1} in the same temperature range). For the higher dopant levels a small decrease in the conductivity was observed (Figure 96), albeit the conductivities were still much higher than for the undoped system.

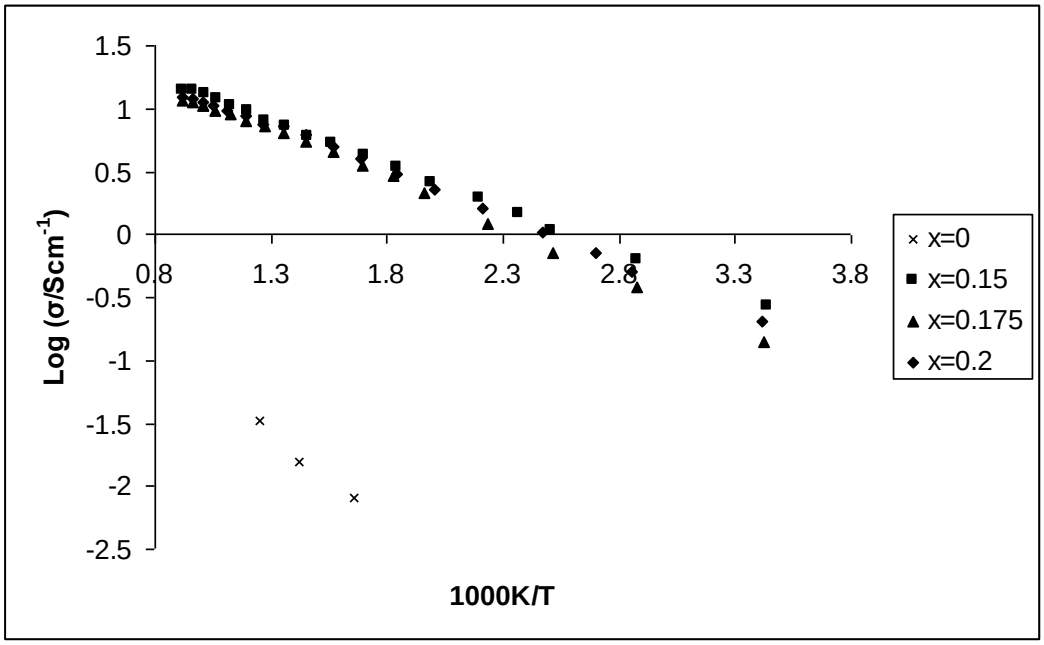

Figure 96: Temperature dependence of the electronic conductivity of $SrMn_{1-x}Si_xO_{3-y}$.

The enhancement of the conductivity for the Mn systems can be attributed to the change from the hexagonal phase which has face sharing of MnO_6 octahedra to the cubic phase which has corner sharing of the octahedral (Figure 97) along with the introduction of mixed valent Mn^{3+}/Mn^{4+}.

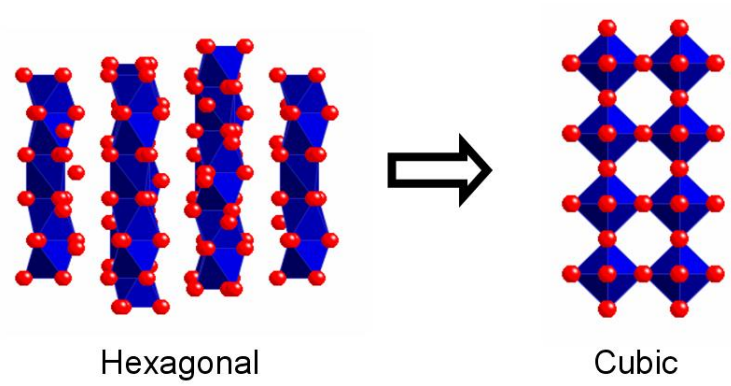

Figure 97: Phase change from hexagonal to a cubic perovskite on silicon doping.

The change from the hexagonal to the cubic phase on silicon doping seems unusual at first glance due to the Mn^{4+} being replaced by the much smaller isovalent Si^{4+}. This decrease in size would be expected to cause a decrease in the average B site cation size causing an increase for the tolerance factor, which would further favour the hexagonal perovskite. However, as seen for the Co based systems, the cubic perovskite is stabilized due to the silicon entering the system as tetrahedral

SiO_4^{4-} replacing the MnO_6 octahedra. This causes the formation of oxide ion vacancies, hence resulting in a reduction in oxygen content and therefore the Mn oxidation state. The presence of the larger Mn^{3+} will then cause the tolerance factor to decrease resulting in the observed cubic perovskite. This reduction of Mn can be illustrated by the relevant defect equation (Equation 24).

These systems were shown to be thermodynamically stable, most likely due to the higher amount of silicon doping compared to other systems. However due to this increase of silicon content, the conductivities are lower than the lightly oxyanion doped Co systems, most likely due to the high levels of silicon leading to a partial disruption of the electronic pathways. Overall the results showed some promise for these Si doped $SrMnO_3$ systems although there is a need to improve their conductivities further. In this respect it is planned to investigate strategies to lower this Si content through codoping (Ca^{2+} for Sr^{2+}) to reduce the starting tolerance factor.

For the Fe systems, an increase in conductivity was observed for the 10% doped (x=0.1) sample, with further increases in Si content lowering the conductivity (Figure 98).

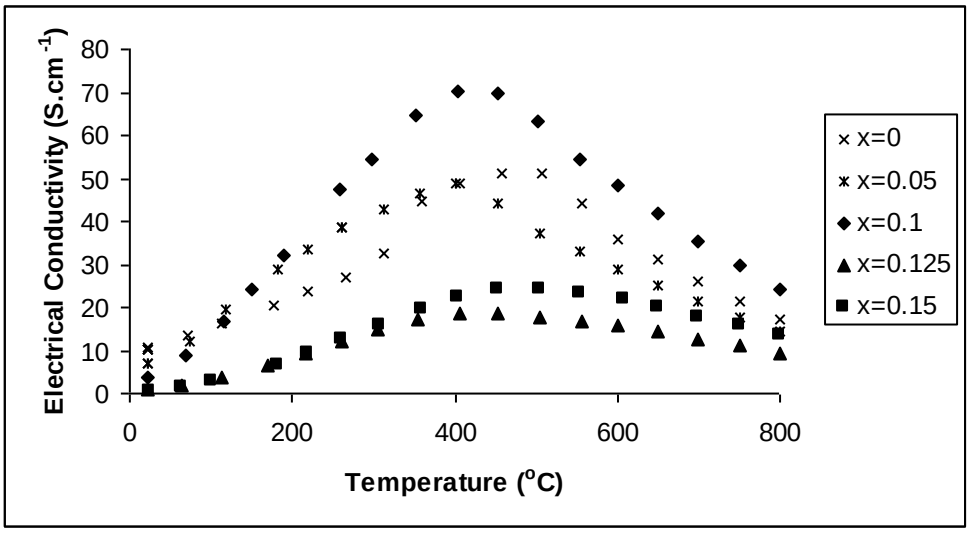

Figure 98: Temperature dependence of the electronic conductivity data for $SrFe_{1-x}Si_xO_{3-y}$.

The initial increase in conductivity for x=0.1 may result from the observed changes in the Fe oxidation state as well as possibly an improvement in the conduction pathways from the change from tetragonal to the more symmetrical cubic system. When the dopant level increases further, the conductivity then decreases due to the silicate disrupting the Fe-O network (Figure 98). All samples

showed a decrease in the conductivity above 400°C, due to oxygen loss at these higher temperatures reducing the Fe^{4+} content.

5.2.2.3. Chemical Compatibility Studies

In order to determine whether these systems could be used in high temperature SOFCs, compatibility tests with YSZ and CGO electrolytes were performed and the results can be seen in Figure 99. As can be seen from these results, the $SrMn_{1-x}Si_xO_{3-y}$ system appears to be more compatible with the CGO electrolyte compared with the YSZ, which formed insulating $SrZrO_3$.

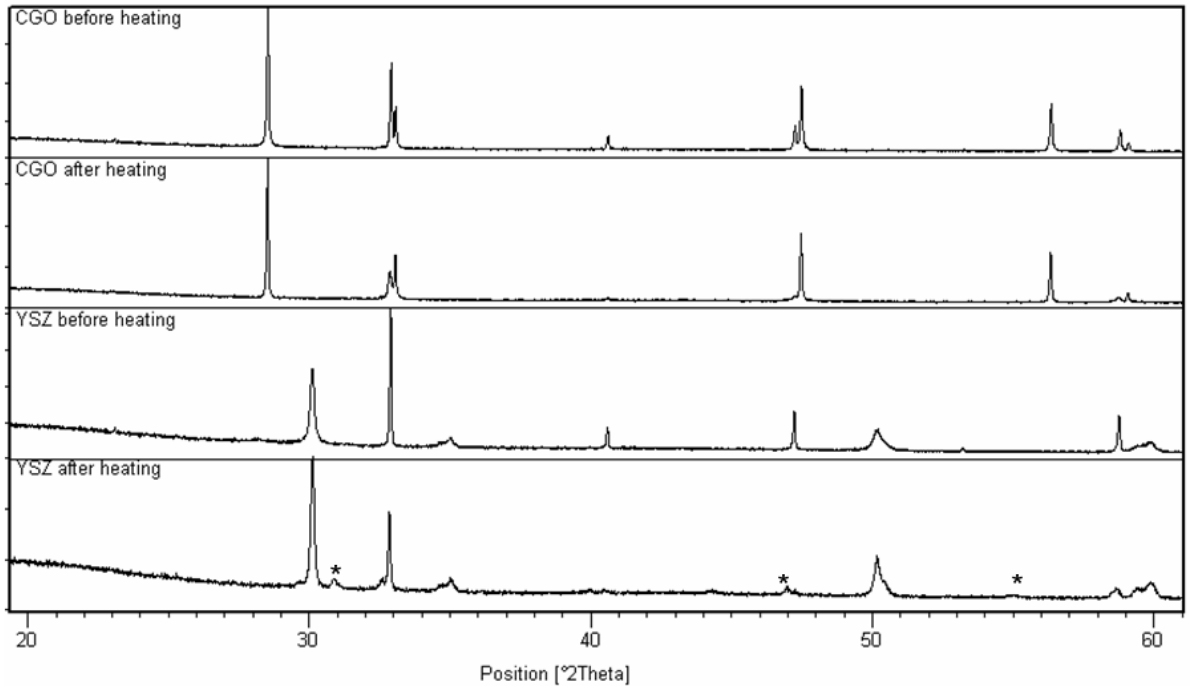

Figure 99: Powder X-ray diffraction patterns for compatibility studies between $SrMn_{0.85}Si_{0.15}O_{3-y}$ and electrolytes CGO and YSZ before and after heating at 1000°C for 2 days * = $SrZrO_3$.

5.2.2.4. Electrochemical Testing

In order to analyse the potential to use these systems as cathode catalysts in low temperature alkaline fuel cells, preliminary electrochemical tests were performed to determine the effectiveness of the oxygen reduction reaction. Figure 100 and 101 show the cyclic voltammogram of the doped and undoped samples. The data show that the onset potential decreases on doping with silicon in $SrMnO_{3-y}$ and improves on doping in $SrFeO_{3-y}$ resulting in a better performance for the

reduction of oxygen in the latter. Despite this improvement, all performances are still poor compared to Pt, and so no further testing was performed on these systems.

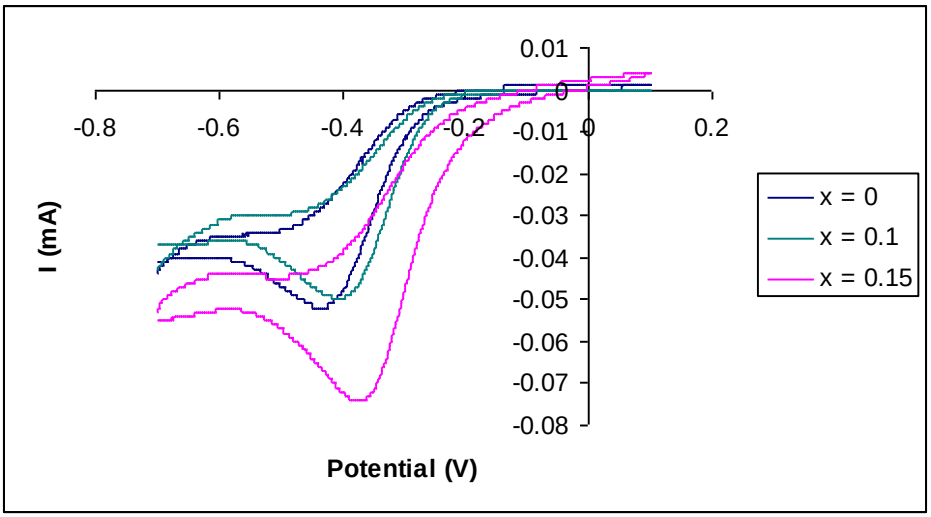

Figure 100: Cyclic voltammograms of $SrMn_{1-x}Si_xO_{3-y}$ showing how the onset potential varies on doping with Si.

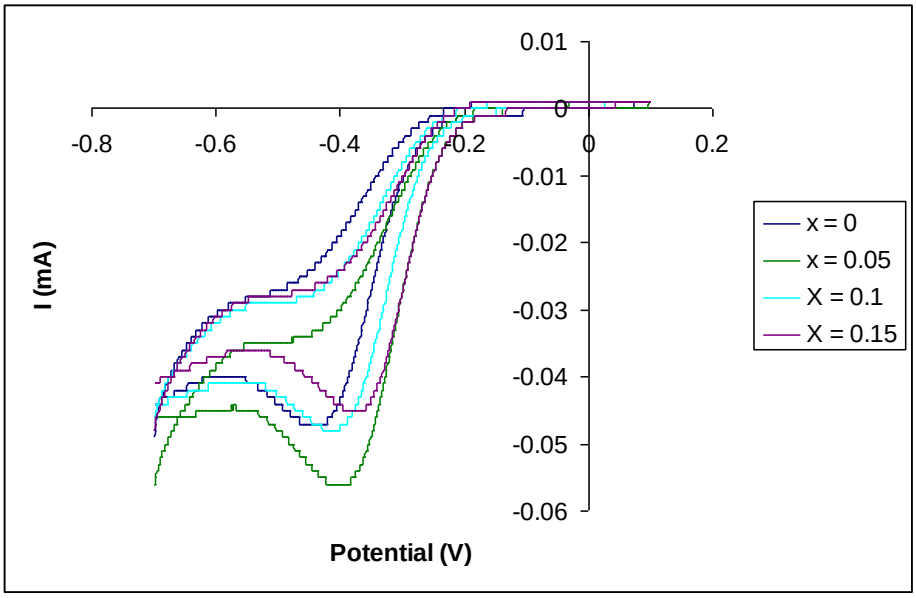

Figure 101: Cyclic voltammogram of $SrFe_{1-x}Si_xO_{3-y}$ showing how the onset potential varies on doping with Si.

5.2.3. Conclusions

Si has been successfully incorporated into the perovskite $SrMnO_{3-y}$ leading to a change from a hexagonal cell to a cubic cell. This Si incorporation results in higher conductivities suggesting a potential as cathodes in SOFCs. Si has also been successfully doped into $SrFeO_{3-y}$ showing a phase

change from tetragonal cell to a cubic cell. This increase of conductivity on initial Si doping along with the stability of these $SrFe_{1-x}Si_xO_{3-y}$ materials in reducing conditions suggest potential for use as SOFC cathodes and possibly anodes. The observed beneficial effect of Si is in contrast to previous assumptions that silicon has a detrimental effect on fuel cell materials. Further work is required to investigate the potential of these materials as SOFC cathode materials. Preliminary results into their performance as cathodes for low temperature alkaline fuel cells however, showed generally poor performance.

5.3. $CaMn_{1-x}Si_xO_{3-y}$

The work on Mn perovskites was extended to examine Si doping in $CaMnO_{3-y}$. In this case the undoped $CaMnO_{3-y}$ system is orthorhombic, containing corner linked octahedra in contrast to hexagonal $SrMnO_{3-y}$ [186]. This system has attracted a lot of interest in the literature, and it has been shown that, on doping on the A site with elements such as Ho and Ce, there is no change to a cubic cell along with an increase in conductivity due to partial reduction of Mn^{4+} to Mn^{3+} [193-195]. In this work we examined whether a similar improvement in conductivity could be achieved through oxyanion doping, with a focus on Si doping. The compounds were also examined for the potential as cathodes for low temperature alkaline fuel cells and following on from some promising initial electrochemical results doping with Ru was also examined.

5.3.1. Experimental

High purity $CaCO_3$, MnO_2, SiO_2 and RuO_2 were used to prepare a range of $CaMn_{1-x}(Si/Ru)_xO_{3-y}$ samples (x = 0, 0.05, 0.1 and 0.15). These starting materials were ground together in the correct stoichiometric ratios and heated to a temperature of 1100^{o}C for 12 hours. The samples were then ball milled (350rpm for 1 hour, Fritsch Pulverisette 7 planetary ball mill) and further heated to 1300^{o}C for another 12 hours. The samples were then furnace cooled to 350^{o}C and held at this temperature for 12 hours to ensure full oxygenation.

Powder X-ray diffraction experiments, using a Bruker D8 transmission diffractometer with Cu $K\alpha_1$ radiation, were employed to determine phase purity, and the GSAS suite of programs used for the structure refinements.

Oxygen contents were estimated from thermogravimetric analysis (Netzsch STA 449 F1 Jupiter Thermal Analyser). The samples were heated to a temperature of 1200^{o}C at a rate of 10^{o}C/min and held for 30 minutes. This reduces the transitional metal oxidation state to 3+, allowing the original oxygen content to be determined from the mass loss observed.

Pellets for conductivity measurements were prepared by ball milling the samples for an hour, and adding a small amount of polyvinyl alcohol before pressing as pellets and sintering at

1350^{o}C. The conductivity was then measured using the 4 probe d c method. The 4 platinum electrodes were attached to the pellet using platinum paste and then fired to 1000^{o}C for an hour to ensure bonding, before lowering the temperature to 350^{o}C for 12 hours to ensure oxygenation.

In order to further test the potential of these systems for use as SOFC cathodes, compatibility studies were performed with fuel cell electrolytes. The compatibility studies were performed on 0.5g of the sample mixed thoroughly with 0.5g of the electrolyte (YSZ and CGO). This mixture was examined by X-ray diffraction before being placed in a furnace at 1000^{o}C for 48 hours, as well as afterwards, to determine whether there was any change.

In terms of analysing the potential for use in low temperature alkaline fuel cells, preliminary electrochemical test were performed. For the electrochemical measurements the inks were made by ball milling 0.3g of the samples with 2ml of propanol for 2 hours. After ballmilling another 6ml of propanol was added along with 0.1g of polytetrafluoroethylene (60 wt% dispersion in water). The inks were then examined by to cyclic voltammetry and rotating disk measurements in oxygen saturated 0.1M KOH with a variety of rotation rates (400, 800, 1200, 1600 and 2000 rpm) with the Invium Stat, Invium A07026 model 636 equipment.

5.3.2. Results and Discussion

In previous oxyanion doping experiments on $SrMnO_{3-y}$ there has been a phase change from a perovskite with face sharing of octahedra to one with corner sharing of octahedra on the introduction of the oxyanion. In the case of $CaMnO_{3-y}$ the undoped system already contains corner sharing octahedra, and consequently for the $CaMn_{1-x}Si_xO_{3-y}$ system there is no change in cell symmetry, with both the undoped and doped materials being orthorhombic (Figure 102). The cell parameter data (Table 44) show an increase in the unit cell size on the addition of the silicon despite the fact that Si^{4+} is smaller than Mn^{4+}. This increase in cell size can be correlated in with partial reduction of the Mn from 4+ to the larger Mn^{3+}, corroborated by TGA studies (Table 44). This reduction of the Mn counters the effect of the smaller Si^{4+} being added. The limit of incorporation

for silicon in this system was shown to be 15 mole %, and above this level, Ca_2SiO_4 impurities can be detected.

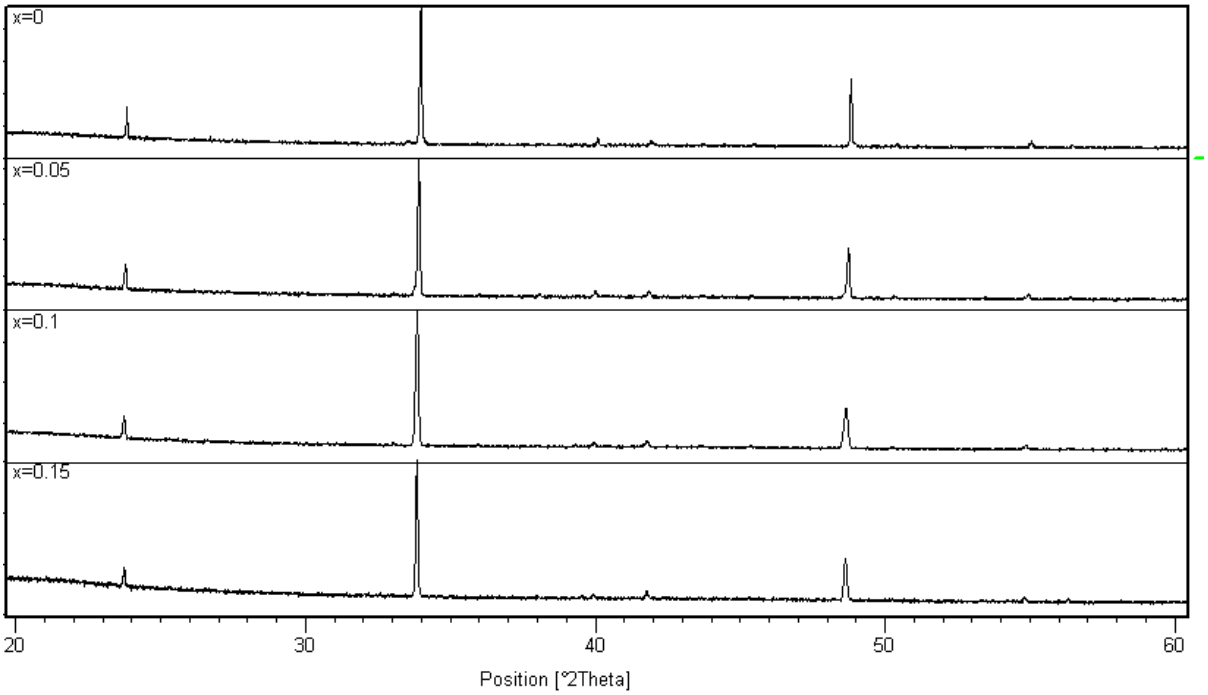

Figure 102: Powder X-ray diffraction patterns for $CaMn_{1-x}Si_xO_{3-y}$.

Table 44: Cell parameters, oxygen deficiencies (y) and manganese oxidation states for $CaMn_{1-x}Si_xO_{3-y}$.

Si content x	Oxygen deficiency (y)	a (Å)	b (Å)	c (Å)	Cell Volume (Å^3)	Mn oxidation state
0	0	5.2739 (9)	7.4482 (4)	5.2621 (8)	206.70 (3)	4
0.05	0.21	5.2817 (8)	7.4643 (4)	5.2774 (5)	208.06 (3)	3.55
0.1	0.21	5.2836 (9)	7.4722 (4)	5.2812 (6)	208.50 (3)	3.53
0.15	0.27	5.2903 (9)	7.84850 (4)	5.2959 (5)	209.71 (3)	3.37

The thermal stability of the materials are important if they are to be used in intermediate temperature fuel cells. In previous studies with the $SrCo_{1-x}Z_xO_{3-y}$ (Z=Si,P,S) system it was discovered that on annealing or thermal cycling the material was metastable. To determine if the $CaMn_{1-x}Si_xO_{3-y}$ system was metastable, it was annealed overnight at 750^{o}C with X-ray diffraction being performed before and after the heat treatment to monitor if there was any change. The X-ray diffraction profiles showed no change indicating that the system is thermally stable. Another stability issue that needed to be addressed is the stability in alkaline conditions. This is because if the material is used in

an AFC, it needs to be stable in basic environments. In this case the material was immersed overnight in a 1M KOH solution at 50°C. X-ray diffraction profiles before and after showed no decomposition indicating that the material was stable for use in AFC systems.

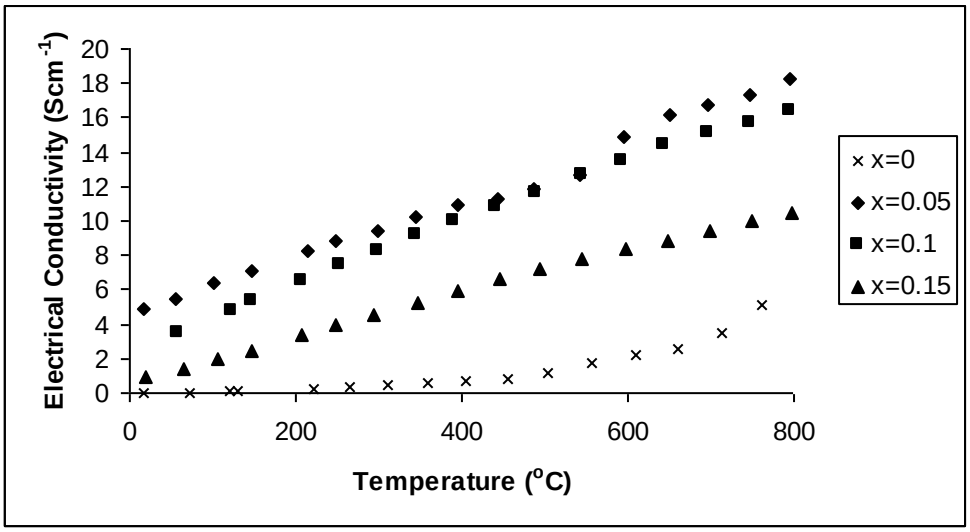

Figure 103: Temperature dependence of the electronic conductivity data for $CaMn_{1-x}Si_xO_{3-y}$.

In order to examine the effect of Si doping on the properties, the conductivities were measured. As can be seen in Figure 103 there is a significant difference between the undoped and doped materials, with the 5% Si doped sample showing a 2 orders of magnitude increase in the conductivity compared to the undoped material at room temperature. In previous studies on related $SrMnO_{3-y}$ system such an enhancement in the conductivity was attributed to the phase change from a hexagonal to a cubic phase perovskite. However in this case there is no phase change on doping with both systems having a similar orthorhombic cell. The explanation for the increase in conductivity is due to the electron doping that occurs from the doping of the tetrahedral Si in the place of octahedral Mn. This can be seen from the defect equation shown in (Equation 24).

The important factor here is the preference for Si to be tetrahedral leading to reduction by the introduction of oxide ion vacancies. The novel features of Si doping can be compared to the effect of doping with other isovalent dopants, such as Ti^{4+}. In contrast with doping with Si there is no enhancement of the conductivity on Ti^{4+} doping as there is no incorporation of oxygen vacancies (and hence no electron doping) resulting in a similar conductivity as the undoped material (Figure

104). Indeed the conductivity at higher temperatures is lower for the Ti doped sample due to partial disruption of the Mn-O conduction pathway. This illustrates the rich potential of exploiting the geometry requirements of oxyanion forming dopant, such as Si, for electron doping perovsite systems.

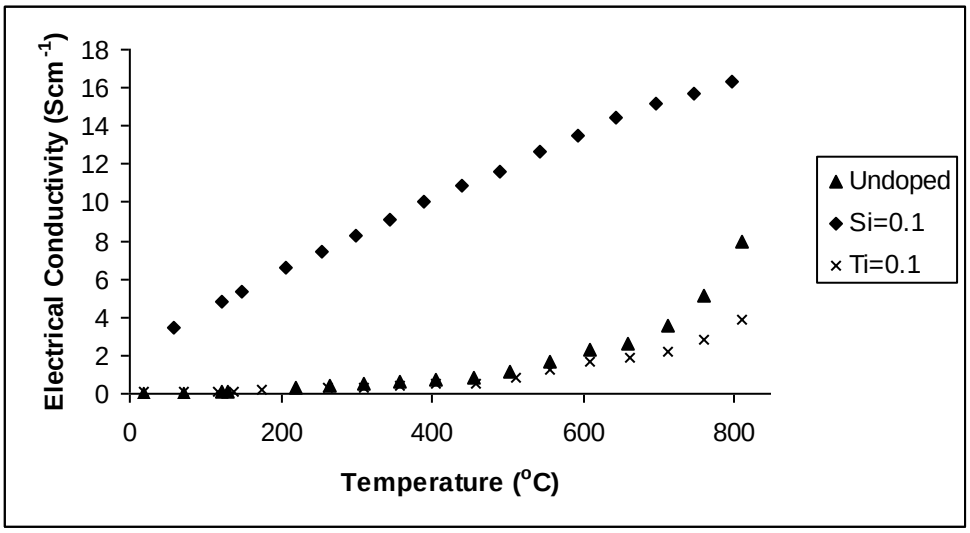

Figure 104: Temperature dependence of the electrical conductivity data for $CaMn_{0.9}Z_{0.1}O_{3-y}$ (z=Si and Ti) and $CaMnO_{3-y}$.

As with the other perovskite systems, while an increase in conductivity was observed for low levels of Si doping, the conductivity then decreased on further increasing the Si content due to the increasing amount Si hindering the electronic transport in the Mn-O network. However, even for the 15% Si doped sample, the conductivity was still higher than the undoped $CaMnO_3$.

In order to examine further the potential of these systems for use as SOFC cathodes their compatibility with SOFC electrolytes was examined. To do this compatibility tests were performed on $CaMn_{0.95}Si_{0.05}O_{3-y}$ and YSZ/CGO mixture. X-ray diffraction analysis was performed before and after heating at 1000°C for 2 days, which are shown in Figure 105. The data showed no evidence for reaction with YSZ, but the presence of weak Mn_3O_4 peaks with CGO, suggesting a small degree of reaction with this electrolyte. Further experiments are required to examine what effect this would have on cathode performance.

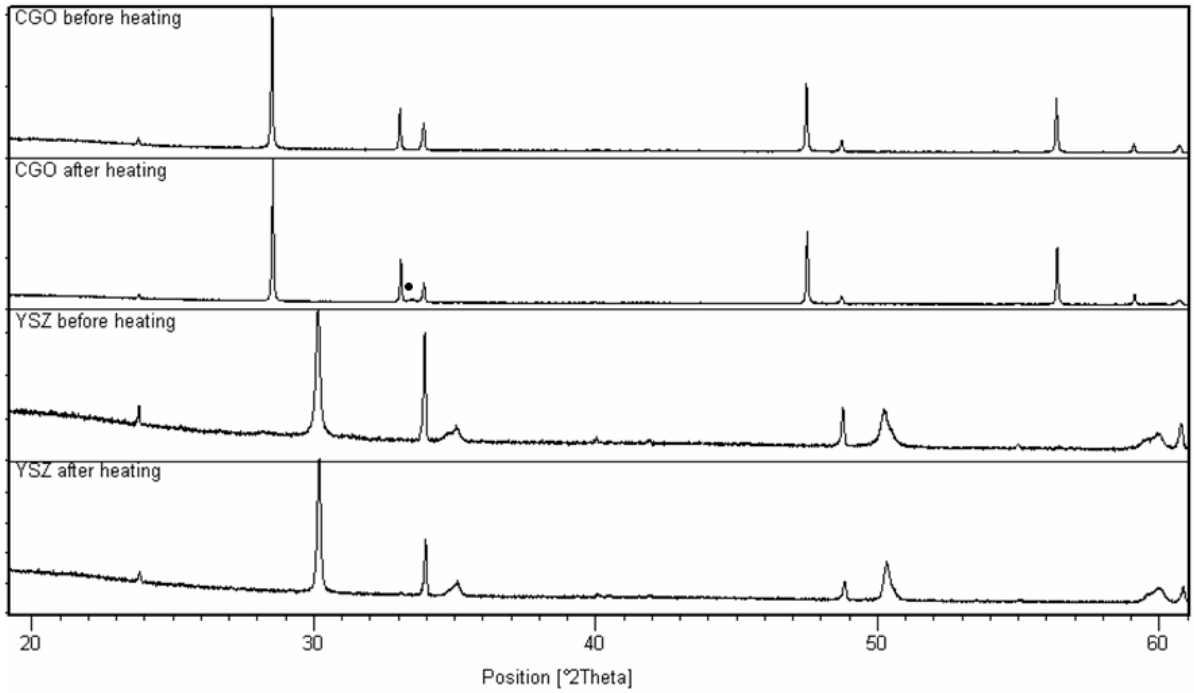

Figure 105: Powder X-ray diffraction patterns for compatibility studies between $CaMn_{0.95}Si_{0.05}O_{3-\gamma}$ and electrolytes YSZ and CGO before and after heating at 1000°C for 2 days (• = Mn_3O_4).

In order to investigate the potential of these materials as cathode catalysts for low temperature alkaline fuel cells preliminary electrochemical tests were performed on the $CaMnO_{3-\gamma}$ systems which showed interesting results. In comparison to the other systems so far reported in this thesis, the onset potential, which is a measure of the effectiveness of the oxygen reduction reaction, was shifted by a significant amount in the positive direction for the undoped material, more so than LSM and LSCF materials which have attracted recent interest by other groups as cathode catalysts for alkaline fuel cells [45] (Figure 106).

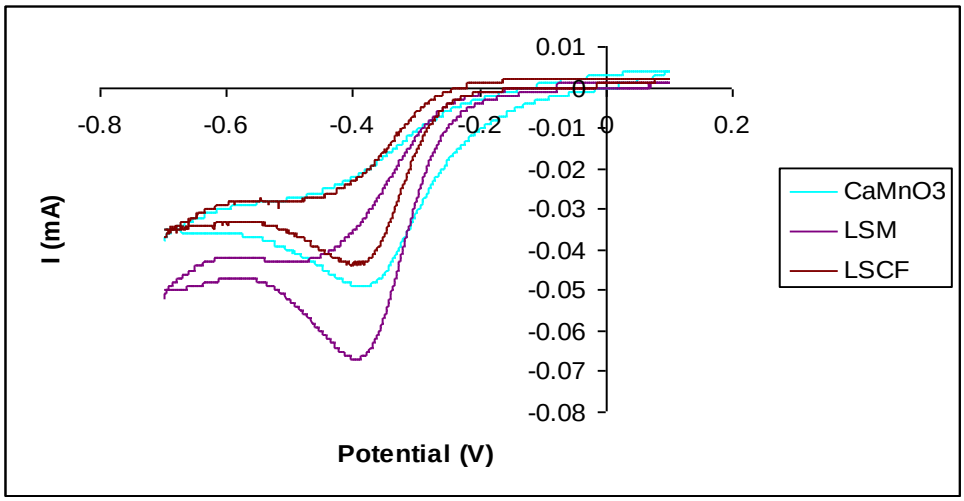

Figure 106: Cyclic voltammograms comparing $CaMnO_{3-y}$ and currently used electrode materials LSM and LSCF, showing a significant shift in the onset potential for $CaMnO_3$ consistent with improved oxygen reduction behaviour.

Following the promising results for $CaMnO_3$, it was hoped that the Si doping would improve the performance further due to the resultant mixed valency Mn. However, doping with Si showed a detrimental effect; the onset potential became more negative (Figure 107) meaning the doped material performed less effectively than the parent material. Due to the promising performance of the parent undoped material, however, more investigation of this system was warranted. Therefore the introduction of Ru was examined, since Ru is known to display good catalytic potential.

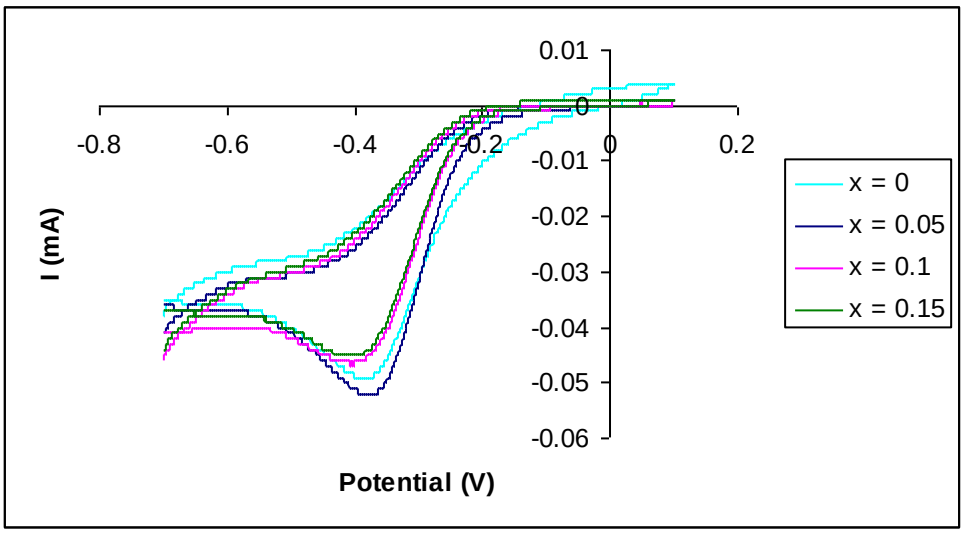

Figure 107: Cyclic voltammograms of $CaMn_{1-x}Si_xO_{3-y}$.

On doping with Ru the cell remains orthorhombic, as for Si doping. The cell volume increases on Ru doping as seen in Table 45 which is attributed to the larger size of Ru, along with partial reduction of Mn^{4+} to Mn^{3+}. This reduction was corroborated by TGA measurements with the Ru oxidation state fixed at 4^{+} as seen in Table 45.

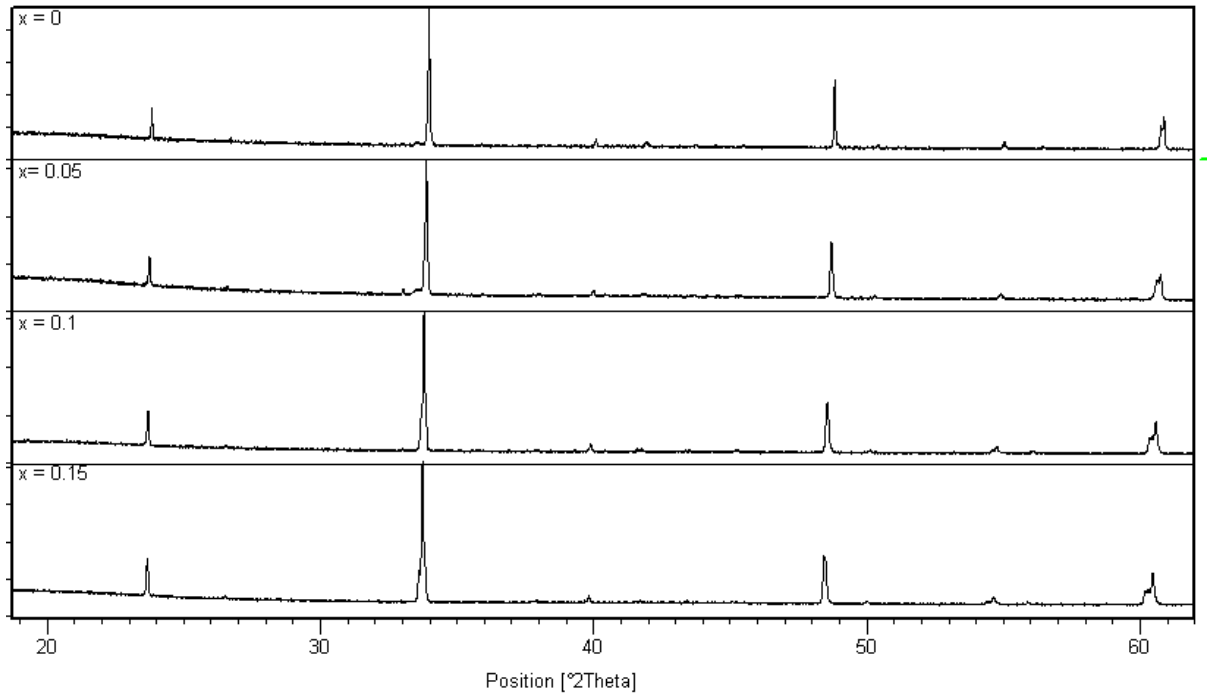

Figure 108: Powder X-ray diffraction patterns for $CaMn_{1-x}Ru_xO_{3-y}$.

Table 45: Cell parameters, oxygen deficiencies (y) and oxidation states for $CaMn_{1-x}Ru_xO_{3-y}$.

Ru content x	Oxygen deficiency	a (Å)	b (Å)	c (Å)	Mn oxidation state
0	0	5.2739 (9)	7.4482 (4)	5.2621 (8)	4.00
0.05	0.17	5.2817 (4)	7.4602 (3)	5.2696 (6)	3.65
0.1	0.16	5.2920 (3)	7.4817 (3)	5.2874 (5)	3.65
0.15	0.16	5.3253 (3)	7.4995 (3)	5.3005 (4)	3.63

The conductivity of the Ru doped system was shown to be significantly higher than that of the undoped and Si doped samples, with the conductivity increasing with higher doping levels of Ru (Figure 109). This increase is due to Ru entering the system as Ru^{4+}/Ru^{5+} which provides extra electrons which increases the conductivity unlike the isovalent Ti^{4+} doping [196, 197]. In addition Ru does not interfere with the electronic transport of the system as is the case with Si doping.

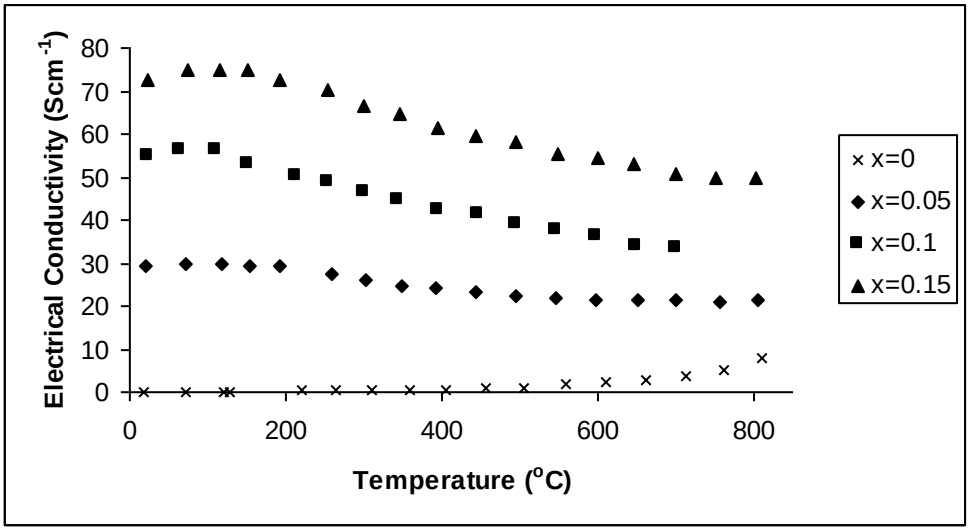

Figure 109: Temperature dependence of the electronic conductivity data for $CaMn_{1-x}Ru_xO_{3-y}$.

As already stated, the undoped $CaMnO_{3-y}$ showed potential for use as electrode materials in low temperature alkaline fuel cells from the promising preliminary electrochemical tests performed. Therefore the Ru doped samples were similarly analysed. For these Ru doped samples the cyclic voltammograms (Figure 110), showed that doping with Ru induced a shift in onset potential to more positive values which was a promising result. In light of this successful result further more detailed electrochemical measurement were performed on these systems and these will be discussed in chapter 7.

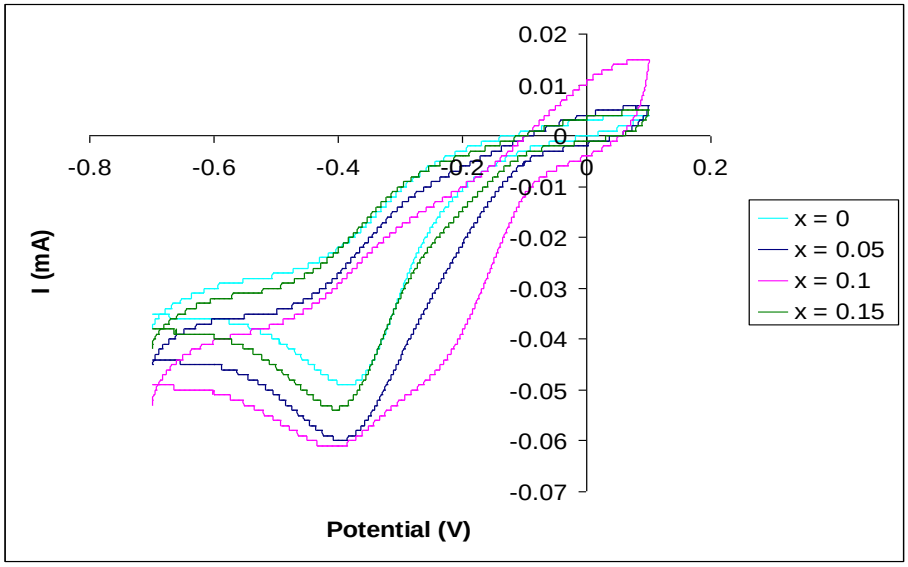

Figure 110: Cyclic voltammograms of $CaMn_{1-x}Ru_xO_{3-y}$.

5.3.3. Conclusions

The results show that Si can be incorporated into $CaMnO_{3-x}$ resulting in an increase of conductivity. This increase in conductivity can be attributed to electron doping due to oxygen loss from the preference for Si to be incorporated as a tetrahedral SiO_4^{4-} ion. In terms of low temperature alkaline fuel cells promising results were observed for the undoped $CaMnO_{3-x}$ although Si doping in this case was shown to give poorer performance. Other doping strategies in $CaMnO_{3-x}$ were also examined, and promising results were achieved for Ru doping which gave evidence for improved performance in alkaline conditions and these Ru doped systems will be analysed further in chapter 7. In terms of potential applications as cathodes in solid oxide fuel cells, the enhanced conductivity on Si doping suggests further studies are also required in this area.

6. Fluorination of Perovskite and Perovskite Related Systems

6.1. Synthesis and Analysis of Reduced and Fluorinated $SrFe_{0.9}Si_{0.1}O_{3-x}$

As already stated, perovskite systems have generated substantial interest in recent years due to the wide range of useful properties found in materials with this structure type. In addition, there has been interest in the substitution of F^- for O^{2-} in perovskite phases by low temperature fluorination leading to compounds with interesting electrical and magnetic properties [198-200]. In this work the effect of fluorination on oxyanion doped $SrFe_{1-x}Si_xO_{3-y}$ has been examined, with a view to comparing the results with previous studies on fluorination of undoped $SrFeO_{3-y}$. In this respect, detailed Mössbauer spectroscopy studies have been performed on the fluorinated phase. In addition, following the results which showed that $SrFe_{1-x}Si_xO_{3-y}$ was stable up to 800°C in H_2, the reduced phase was also analysed by Mössbauer spectroscopy.

6.1.1. Experimental

Fluorination was achieved by mixing $SrFe_{0.9}Si_{0.1}O_{3-y}$ with poly(vinylidene fluoride) (PVDF) in a ratio of 1:1 (Precursor oxide:CH_2CF_2 monomer unit). Once mixed the samples were heated at 375°C for 24hrs with an intermediate regrind in a furnace within a fume hood.

Reduction of $SrFe_{1-x}Si_xO_{3-y}$ was achieved by heating the samples in hydrogen to 800°C for 12 hours.

Powder X-ray diffraction experiments, using a Bruker D8 transmission diffractometer with Cu $K\alpha_1$ radiation, were employed to determine phase purity and perform structural characterisation of the systems. The structural characterisation was performed with the GSAS suite of programs.

Raman spectroscopy measurements were performed on the powder samples (Renishaw inVia Raman Microscope) using a 532nm laser at a 5% power level, with 30 seconds exposure and 10 accumulations.

^{57}Fe Mössbauer spectra were recorded in constant acceleration mode using a *ca*.25mCi^{57}Co/Rh source and a helium closed-cycle cryo-refrigerator. All the spectra were computer fitted and the chemical isomer shift data are quoted relative to metallic Fe at room temperature.

The Mössbauer measurements were performed by Professor Frank Berry and the researchers from the Instituto de Physica, Madrid.

6.1.2. Results and Discussion

The X-ray diffraction patterns showed that the parent $SrFe_{0.9}Si_{0.1}O_{3-y}$, reduced $SrFe_{0.9}Si_{0.1}O_{3-y}$ and the fluorinated derivative were cubic (Figure 111, 112 and 113 respectively). Structure refinements were performed for the parent and fluorinated $SrFe_{0.9}Si_{0.1}O_{3-y.}$ The X-ray diffraction data were used for these structure refinements, with the atomic displacement parameters for the Fe and Si, as well as the O and F in the fluorinated phase, being constrained as equal. The occupancies were originally varied and gave Si contents of 0.14 (2) and 0.07 (2) for the parent and fluorinated material respectively. However to compare the samples the total occupancy for the Fe/Si site was also constrained to 1. As can be seen from the data (Table 46 and 47) there is an increase in the cell parameters on fluorination, as well as an increase in the Fe-O bond lengths. This increase is due to the reduction of the Fe^{4+} to the larger Fe^{3+} cation on fluorination. This reduction of Fe can also be confirmed visually with the colour of the sample changing from black to brown/red on fluorination.

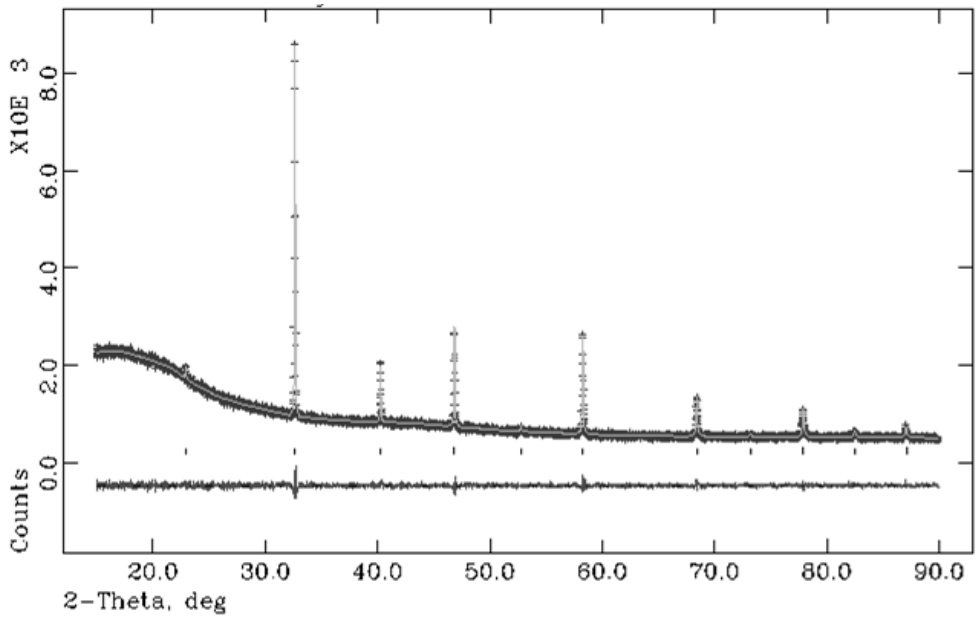

Figure 111: Observed, calculated and difference X-ray diffraction profiles for $SrFe_{0.9}Si_{0.1}O_{3-y}$.

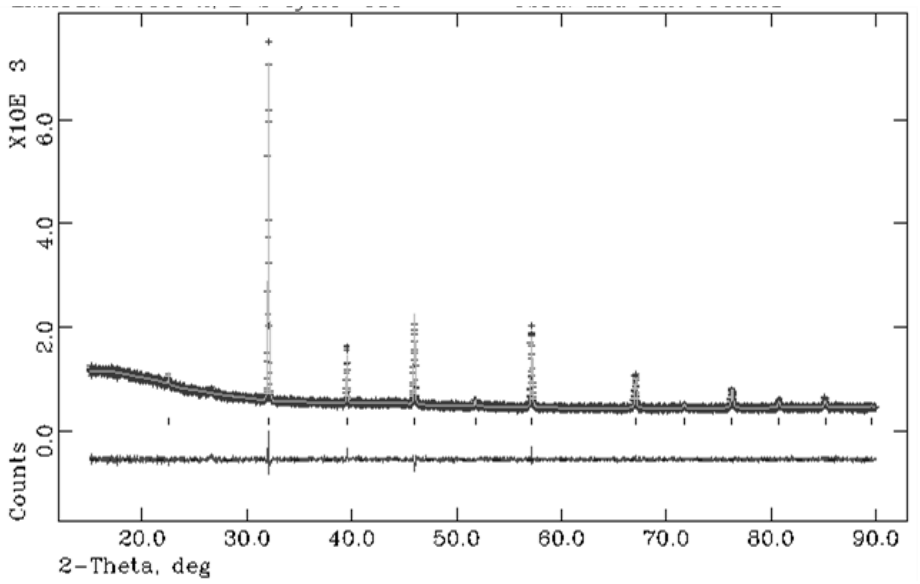

Figure 112: Observed, calculated and difference X-ray diffraction profiles for fluorinated $SrFe_{0.9}Si_{0.1}O_{3-y}$.

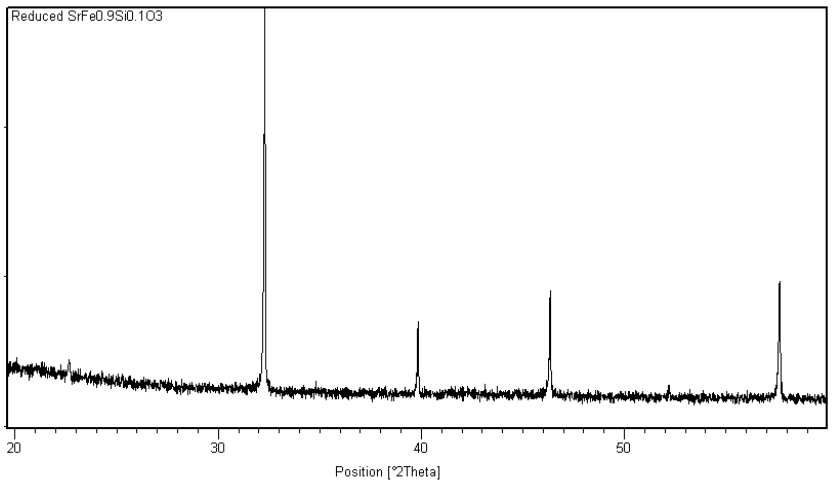

Figure 113: X-ray diffraction profile for reduced $SrFe_{0.9}Si_{0.1}O_{3-y}$.

Somewhat surprisingly the data suggested no change in anion content on fluorination, although this may be related to the insensitivity of X-rays to lighter atoms (O, F), along with issues relating to the displacement of the anion positions on Si incorporation.

Table 46: Structural parameters for unfluorinated and fluorinated $SrFe_{0.9}Si_{0.1}O_{3-y}$.

					Parent		Fluorinated	
Atom	Multiplicity	X	Y	Z	Uiso	Occupancy	Uiso	Occupancy
Fe1	1	0	0	0	0.7 (1)	0.9	2.8 (1)	0.9
Sr1	1	0.5	0.5	0.5	0.26 (7)	1	0.91 (7)	1
O1	3	0.5	0.5	0	2.8 (4)	0.90 (2)	2.4 (4)	0.88 (2)
Si1	1	0	0	0	0.7 (1)	0.1	2.8 (1)	0.1
$SrFe_{0.9}Si_{0.1}O_{2.70}$: Space Group Pm-3m, a=3.87264(5)Å, χ^2=1.201, R_{wp}=3.62%								
$SrFe_{0.9}Si_{0.1}(O/F)_{2.64}$: Space Group Pm-3m, a=3.94109(7)Å, χ^2=1.148, R_{wp}=4.35%								

Table 47: Bond distances for unfluorinated and fluorinated $SrFe_{0.9}Si_{0.1}O_{3-y}$.

Bond	Unfluorinated Bond Distance/ Å	Fluorinated Bond Distance/ Å
Fe/Si-O	1.93632 (3) (x 6)	1.97054 (3) (x 6)
Sr-O	2.73837 (4) (x 12)	2.78677 (3) (x 12)

Raman spectroscopy can also be used to characterise changes in the material after fluorination. For the unfluorinated sample no peaks were observed, which is consistent with the situation expected for a cubic perovskite. When the sample is fluorinated there is a large change with many peaks now being visible (Figure 114). This would indicate that while the XRD suggests an average cubic symmetry, the actual local symmetry is lower than cubic, which may be due to local structural distortions induced by the presence of F.

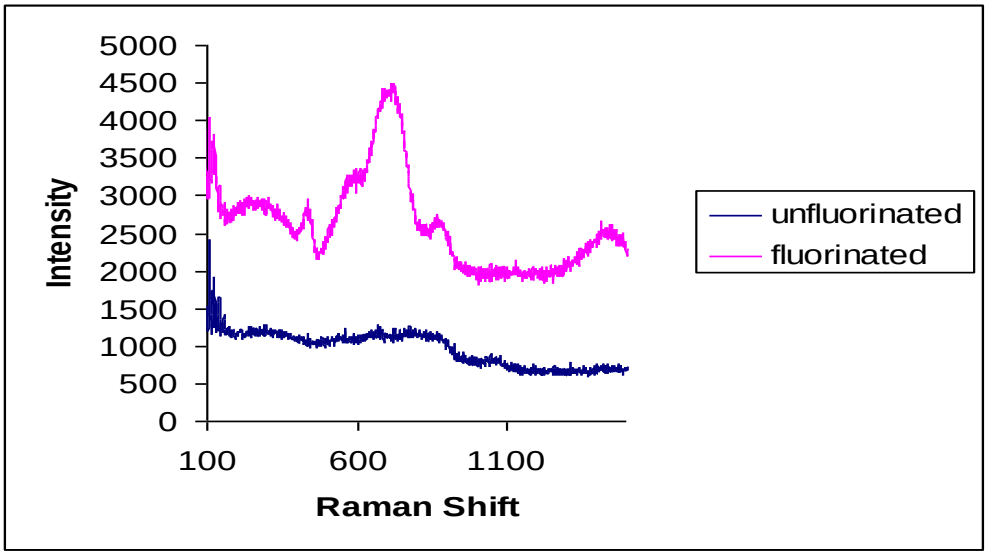

Figure 114: Raman spectra of unfluorinated and fluorinated $SrFe_{0.9}Si_{0.1}O_{3-y}$.

^{57}Fe Mössbauer data were collected in order to gain further information on the Fe environment. These data confirmed the reduction of the Fe to Fe^{3+} when fluorinated. For the unfluorinated phase as 298K (Figure 115) there are 3 doublets seen. The first with a chemical isomer shift of $\delta \approx -0.05$ mms^{-1} is from Fe^{5+} while the other shifts at $\delta \approx 0.37$ and $\delta \approx 0.18$ mms^{-1} are typically from Fe^{3+} in an octahedral co-ordination and Fe^{3+} in a lower coordination respectively. This suggests that the substitution of Fe^{4+} with Si^{4+} results in disproportionation of the Fe^{4+} into Fe^{3+} and Fe^{5+}. This has previously been observed by substituting the larger Sn^{4+} in place of Fe^{4+} causing lattice strain which can be mitigated by incorporating smaller Fe^{5+} ions. In this case the situation is most likely reversed with the smaller Si^{4+} causing significant local strain resulting in the Si^{4+} being surrounded by the large Fe^{3+} to relieve the strain with the adjacent cells incorporating the smaller Fe^{5+} ions.

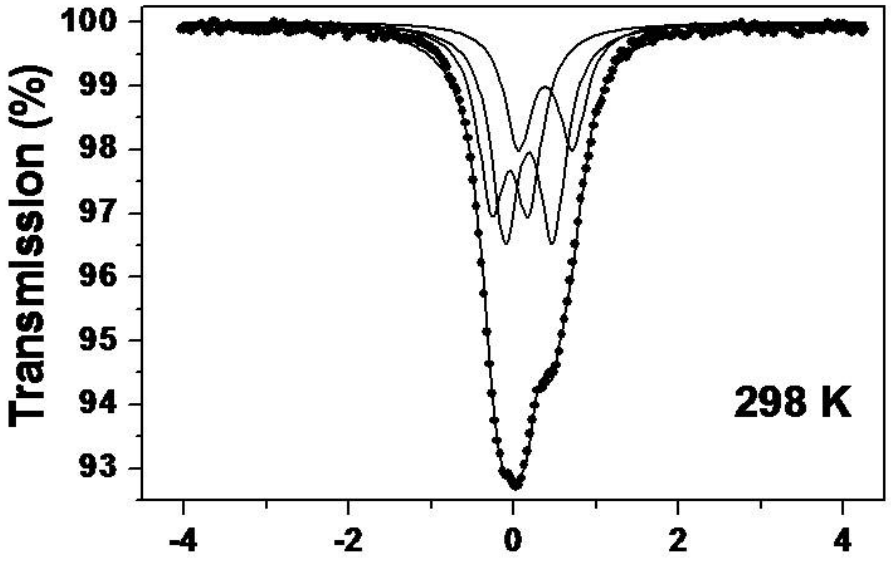

Figure 115: ^{57}Fe Mössbauer spectrum recorded from $SrFe_{0.9}Si_{0.1}O_{3-y}$ at 298K.

The unfitted ^{57}Fe Mössbauer spectra for $SrFe_{0.9}Si_{0.1}O_{3-y}$ between 298 and 15K (Figure 116) show that the material becomes magnetically ordered between 68 and 42K. The spectra recorded were complex due to the complexity of the interactions between Fe^{3+} and Fe^{5+} at low temperatures hence the difficulty in fitting.

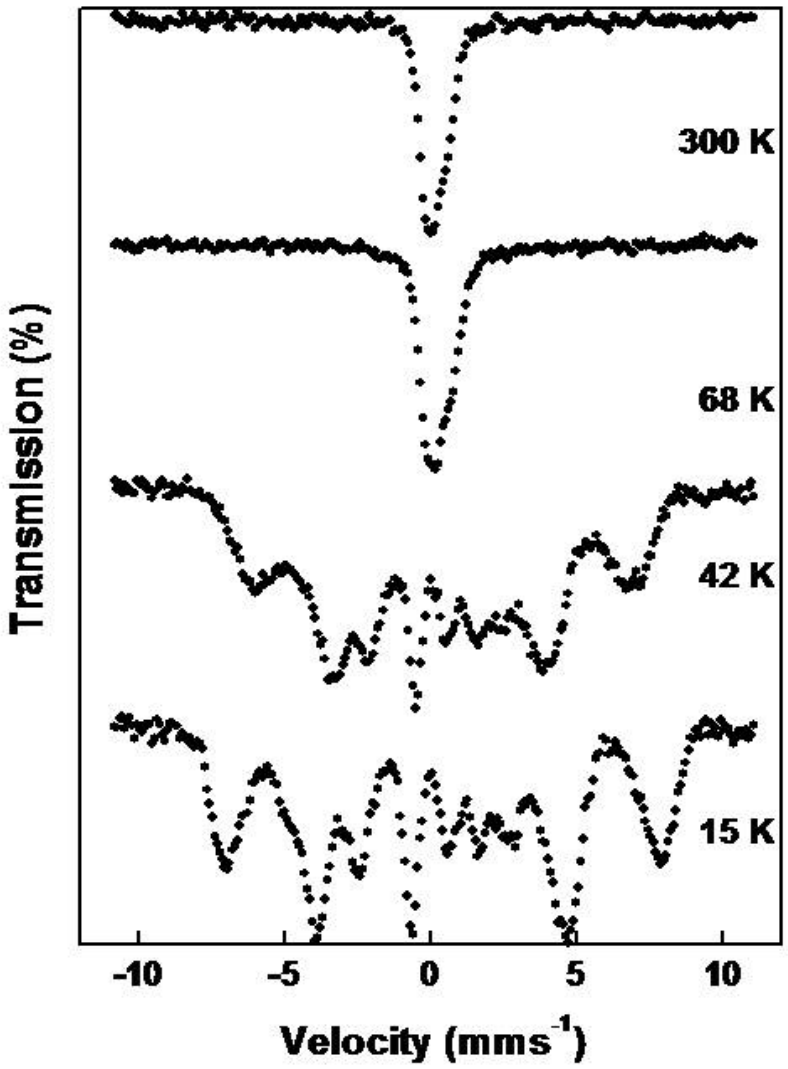

Figure 116: ^{57}Fe Mössbauer spectra recorded from $SrFe_{0.9}Si_{0.1}O_{3-y}$ at 298, 68, 42 and 15K.

The spectra at 298 and 16K from the H_2 reduced parent material (Figure 117) were fitted best to three sextets with chemical isomer shifts characteristic of Fe^{3+}. The results show that the reducing conditions cause the conversion of Fe^{5+} to Fe^{3+} resulting in a composition of the $SrFe_{0.9}Si_{0.1}O_{2.55}$. As can be seen, the spectra at 16K for the reduced material is less complex compared to its prereduced counterpart due to only Fe^{3+} superexchange interactions being observed, compared to the complex interactions in the prereduced material between the iron in different oxidation states. Prior studies have shown that when the undoped $SrFeO_{3-y}$ is reduced it results in brownmillerite-related $Sr_2Fe_2O_5$ where the oxide ion vacancies are ordered [201] . In comparison to previously literature reported Mössbauer data for $Sr_2Fe_2O_5$ the spectra for $SrFe_{0.9}Si_{0.1}O_{2.55}$ were

significantly different. This can be explained by the extra oxygen in $SrFe_{0.9}Si_{0.1}O_{2.55}$ ($Sr_2Fe_{1.8}Si_{0.2}O_{5.1}$) leading to disorder on the oxygen sublattice.

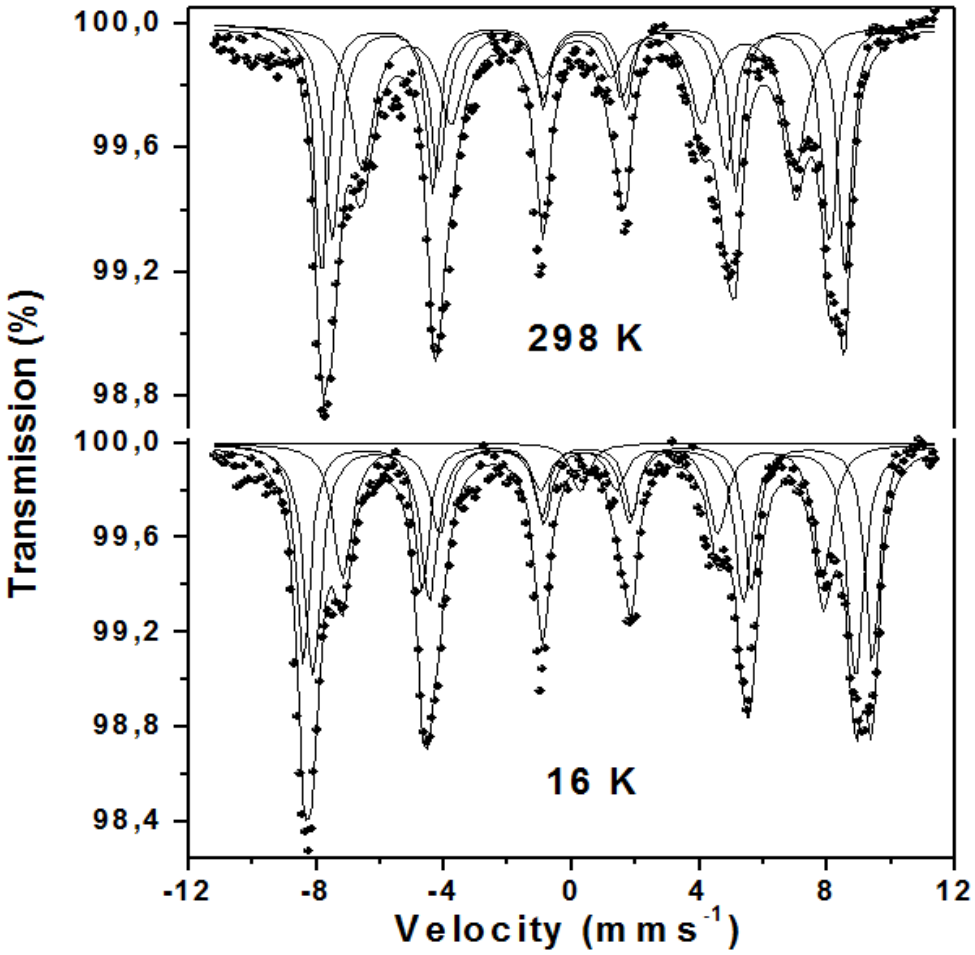

Figure 117: ^{57}Fe Mössbauer spectra recorded from reduced $SrFe_{0.9}Si_{0.1}O_3$ at 298 and 16K.

The ^{57}Fe Mössbauer spectra for fluorinated $SrFe_{0.9}Si_{0.1}O_{3-y}$ showed a quadrupole split absorption on a magnetically split sextet at 298K. The two chemical isomer shifts are due to Fe^{3+} confirming the complete reduction to Fe^{3+}. A composition of $SrFe_{0.9}Si_{0.1}O_{2.2}F_{0.7}$ can be predicted from the complete reduction of Fe to Fe^{3+}, assuming the likely tetrahedral coordination of the Si. The spectrum recorded at 20K (Figure 118) showed two sextet patterns with chemical isomer shifts that are characteristic of Fe^{3+}. The results therefore show that fluorination causes a reduction of Fe to Fe^{3+} which has also been seen in previous studies of fluorination of $SrFeO_{3-y}$ and $SrFe_{1-x}Sn_xO_{3-y}$ [198, 199].

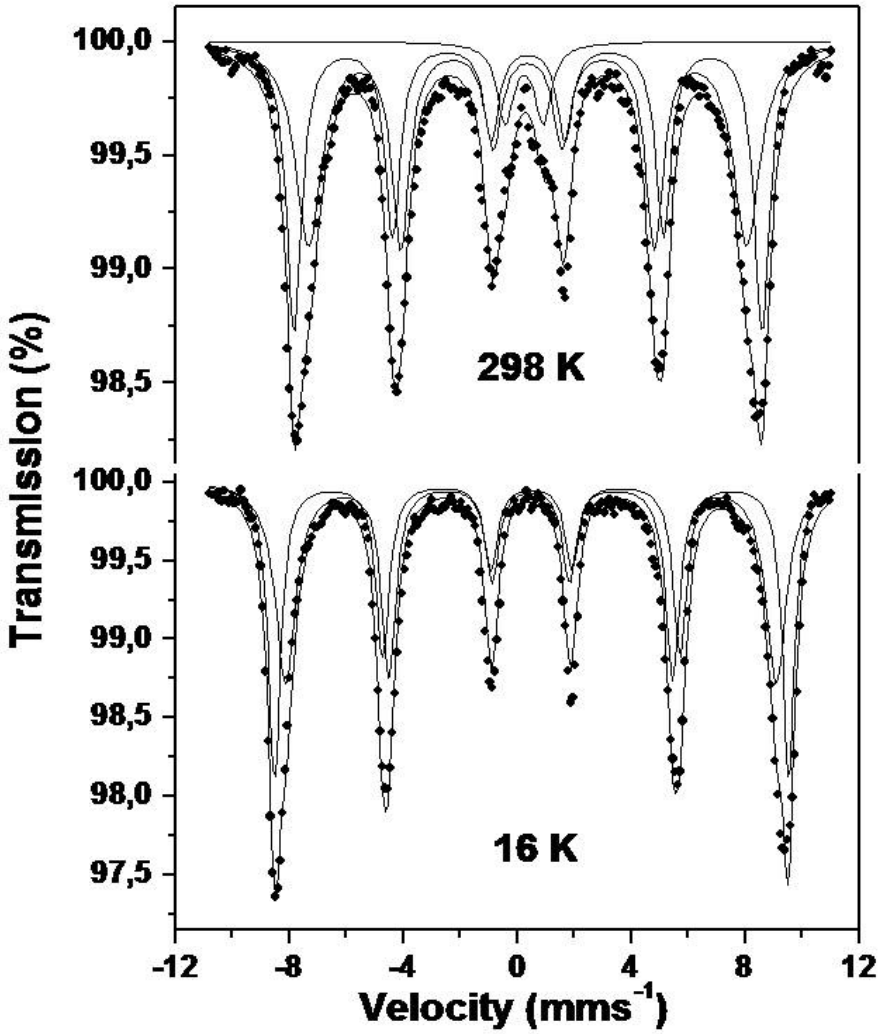

Figure 118: ^{57}Fe Mössbauer spectra recorded from fluorinated $SrFe_{0.9}Si_{0.1}O_{3-y}$.

6.1.3. Conclusions

As shown earlier, Si can be incorporated into $SrFeO_{3-y}$, with the Mössbauer data indicating a disproportionation of Fe^{4+} to Fe^{3+} and Fe^{5+} for such doped samples. When the material is reduced in H_2/Ar, or fluorinated with PVDF, a complete reduction to Fe^{3+} can be seen, and Mossbauer spectra show magnetic ordering in these phases at room temperature. Further studies (e.g. neutron diffraction) are required to gain more information on the magnetic ordering.

6.2. Synthesis and Fluorination of $Sr_3Fe_2O_{7-x}$ Systems

Perovskite related materials have generated a lot of interest due to the wide range of important properties displayed by materials with this structure type. Most research has focused on simple oxide systems; however oxide fluoride materials have opened up new areas of interesting research. The incorporation of two different anions in the structure allows further opportunities to control and enhance the chemical and physical properties. For example the O and F are about the same size, but have different charges and electronegativity, which can modify the electronic configuration of the transition metal [104, 202].

A lot of this oxide fluoride work has concentrated on Cu containing materials due to the discovery of superconductivity in oxide fluorides with the composition of $Sr_2CuO_2F_{2+x}$ [99-101, 108]. This work is now being expanded to investigate oxide fluoride systems with different transition metals such as Mn, Ru and in this case Fe [75, 203, 204]. For example, fluorination of the perovskite $(Sr/Ba)FeO_{3-x}$ [199, 200, 205, 206] system has produced interesting results. The results implied that using PVDF as the fluorination method can be a powerful means of controlling the oxidation states of the transition metal. This is due to the replacement of the O by F, and hence a reduction of the oxidation state of the Fe^{4+} to Fe^{3+} and the appearance of magnetic ordering. In the present study the aim was to investigate the similar fluorination of the Ruddlesden Popper system, $Sr_3Fe_2O_{7-x}$. The interesting additional feature of Ruddlesden Popper phases is the potential for the incorporation of anions into interstitial sites within the rock salt layers. $Sr_3Fe_2O_{7-x}$ has been examined by various researchers and until recently only small amounts of F had been incorporated by reacting with F_2 gas i.e. $Sr_2Fe_2O_6F_{0.87}$ [104]. However at the same time as the results in this thesis were collected, higher amounts of F were shown to be incorporated into the structure by using alternative low temperature routes such as PTFE, in this case a composition of $Sr_3Fe_2O_{5.44}F_{1.56}$ was reported [202]. Low temperature routes are needed to introduce F due to the high thermodynamic stability of the simple binary fluorides, in this case the SrF_2. In this thesis the PVDF method is used to fluorinate the $Sr_3Fe_2O_{7-x}$ material to allow control of the fluorination level (by the amount of PVDF added). The

study's aim was to investigate the level of F incorporation possible with a subsequent aim to perform F^-/OH^- exchange to prepare new oxide hydroxides with potential applications as alkaline fuel cell cathodes as shown in the $La_2NiO_{4-x}F_y$ system earlier.

6.2.1. Experimental

High purity $SrCO_3$ and Fe_2O_3 were used to prepare the unfluorinated parent $Sr_3Fe_2O_{7-x}$ phase. The starting materials were ground together in the correct stoichiometric ratio and heated to a temperature of 1100°C for 24hrs with an intermediate regrinding. Fluorination was achieved by mixing the single phase $Sr_3Fe_2O_{7-x}$ with poly(vinylidene fluoride) (PVDF) in various ratios of 1:1, 1:2 and 1:2.8 (Precursor oxide:CH_2CF_2 monomer unit). Once mixed the samples were heated at 375°C for 24hrs with an intermediate regrind in a furnace within a fume hood.

Powder X-ray diffraction experiments, using a Bruker D8 transmission diffractometer with Cu $K\alpha_1$ radiation, were employed to determine phase purity and for structural characterisation of the systems. The structural characterisation was performed using the GSAS suite of programs.

The ^{57}Fe Mössbauer spectra were recorded in constant acceleration mode using a *ca*.25mCi^{57}Co/Rh source and a helium closed-cycle cryo-refrigerator. All the spectra were computer fitted and the chemical isomer shift data are quoted relative to metallic Fe at room temperature. The Mössbauer measurements were performed by Professor Frank Berry and researchers from the Instituto de Physica, Madrid.

6.2.2. Results and Discussion

X-ray diffraction data confirmed the successful fluorination of the $Sr_3Fe_2O_{7-x}$ system. The XRD patterns for the parent and fluorinated phases are shown in Figure 119. As can be seen in Figure 119, higher amounts of impurities (SrF_2 and $SrFe(O/F)_3$) are formed on increasing the level of fluorination.

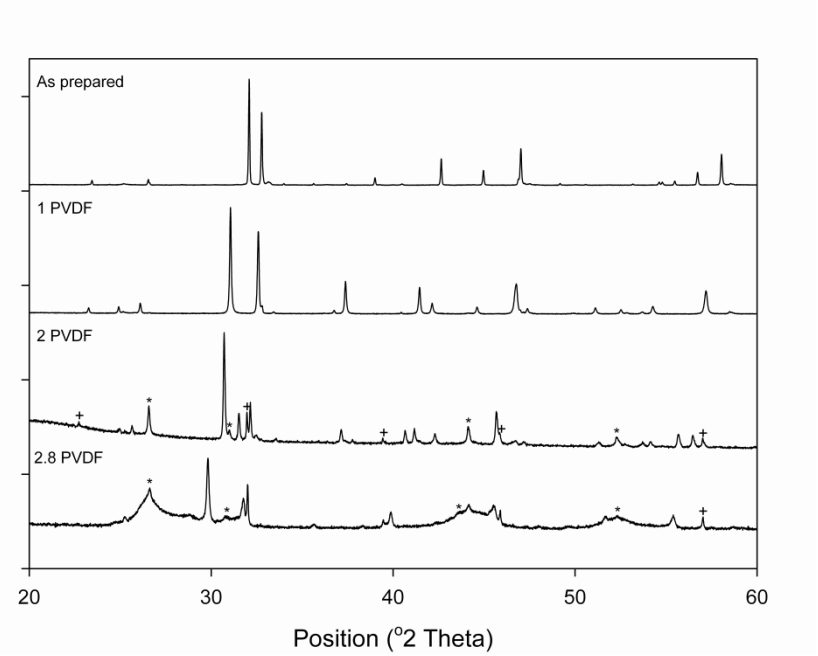

Figure 119: Powder X-ray diffraction patterns for $Sr_3Fe_2O_{7-x}$ as prepared, and after fluorination with 1, 2 and 2.8 mole equivalent of PVDF (* = SrF_2 phase and + = $SrFe(O/F)_3$ impurity phase).

On fluorination the cell volume increases as seen in Table 48 and Figure 120. For the 1:1 phase the main effect is the increase of the c parameters from the undoped. When the fluorination level is increased to 2:1 there is a slight decrease in the c parameter but an increase in the a and b parameters leading to an overall increase in cell volume. Along with this increase in cell volume, the X-ray pattern shows peak splitting due to a change from tetragonal to orthorhombic. For the highest fluorinated phase (1:2.8) there was a large increase of the c parameter along with the a and b parameters, leading to a further large increase in cell volume. Attempts to increase the fluorination level further (e.g. 1:3 ratios) led to nearly complete decomposition.

Table 48: Cell parameters for $Sr_3Fe_2O_{7-x}$ and fluorinated phases.

	a (Å)	b (Å)	c (Å)	Equivalent Cell Volume (Å^3)
$Sr_3Fe_2O_{7-x}$	3.86543 (2)	3.86543 (2)	20.1633 (1)	301.271 (4)
$Sr_3Fe_2O_{7-x}$: 1 PVDF	3.88379 (4)	3.88379 (4)	21.4285 (2)	323.223 (8)
$Sr_3Fe_2O_{7-x}$: 2 PVDF	5.6707 (3)	5.5644 (2)	21.359 (1)	336.98 (8)
$Sr_3Fe_2O_{7-x}$: 2.8 PVDF	3.9837 (2)	3.9837 (2)	22.717 (2)	360.53 (3)

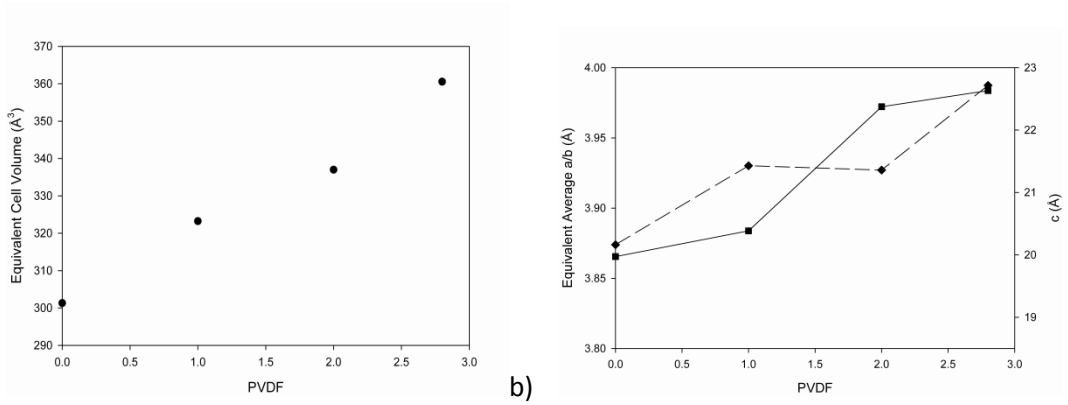

Figure 120: a. Variation of equivalent cell volume and (b) variation in cell lengths (full line a/b, dotted line c) with amount of PVDF used for fluorination. To allow for direct comparison the 2 PVDF sample the average a/b length has been divided by √2 for the 1:2 PVDF sample.

Successful fluorination was also confirmed by the colour change observed on fluorination with the parent and 1:1 fluorinated phase being black compared to the higher fluorinated phases which had a red/brown colour attributed to the complete reduction of the iron to Fe^{3+}.

The X-ray data from the parent, 1:1 and 1:2 fluorinated phases were refined using the GSAS suite of programs. The 1:2.8 phase showed large impurities and so the structure of this phase was not analysed.

The structure for the parent phase (Figure 121) was based on the prior reported tetragonal I4/mmm model [207]. The atomic displacement parameters for the anion sites were all constrained to be equal to aid in the refinement. The occupancy of the O1 and O3 sites were allowed to refine which gave the formula $Sr_3Fe_2O_{6.3144}$. The structural parameters along with selected bond distances can be found in Table 49 and 50 with the diffraction profile in Figure 122.

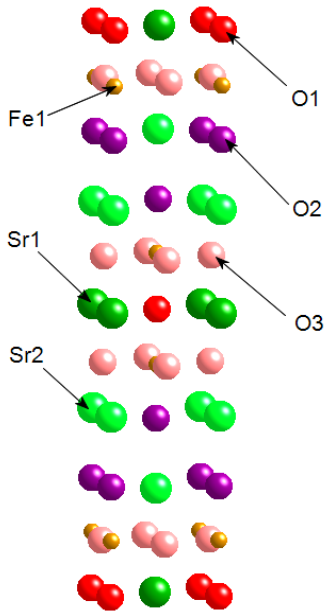

Figure 121: Structure of the parent material $Sr_3Fe_2O_{7-x}$ showing the different oxygen positions.

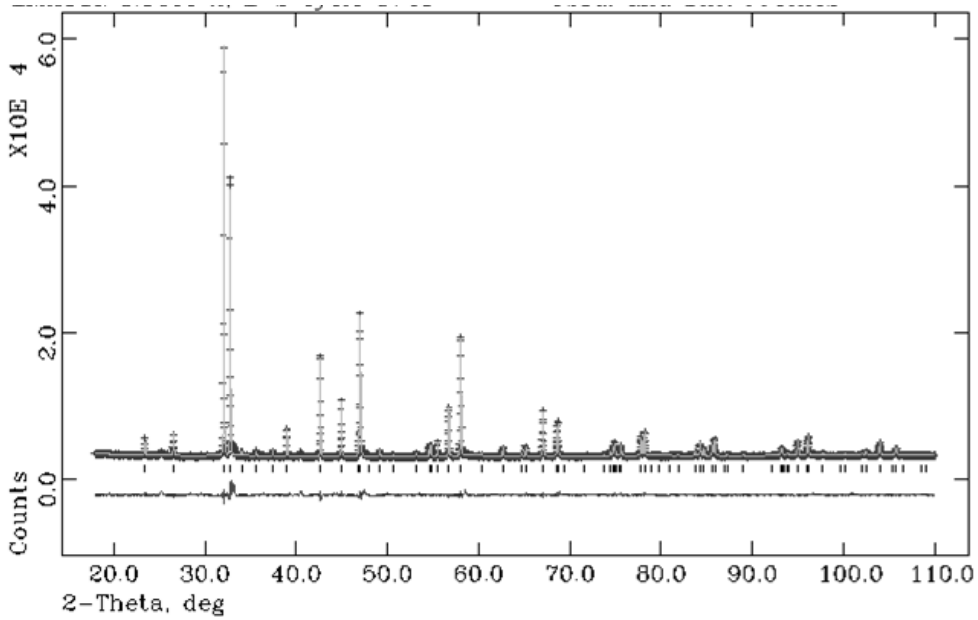

Figure 122: Observed, calculated and difference X-ray diffraction profiles for $Sr_3Fe_2O_{7-x}$.

Table 49: Structural parameters for $Sr_3Fe_2O_{7-x}$.

Atom	Multiplicity	X	Y	Z	Uiso	Occupancy
Sr1	2	0	0	0.5	0.43 (5)	1
Sr2	4	0	0	0.31744 (4)	0.52 (4)	1
Fe1	4	0	0	0.09854 (9)	0.32 (4)	1
O1	2	0	0	0	0.1 (1)	0.77 (1)
O2	4	0	0	0.1939 (2)	0.1 (1)	1
O3	8	0	0.5	0.0931 (2)	0.1 (1)	0.885 (7)
Space Group I4/mmm, a = 3.86543(2) Å, c = 20.1633(1) Å, $\chi 2$ = 3.55, R_{wp} = 3.19%						

Table 50: Selected bond distances for $Sr_3Fe_2O_{7-x}$.

Bond	Bond Length (Å)
Sr1-O1	2.73327(1) x4
Sr1-O3	2.6748(33) x8
Sr2-O2	2.492(5) x1
	2.7427(4) x4
Sr2-O3	2.6432(33) x4
Fe1-O1	1.9868(19) x1
Fe1-O2	1.922(5) x1
Fe1-O3	1.93578(28) x4

The Rietveld refinement for the 1:1 phase was also based on the I4/mmm model. The atomic displacement parameters for all the anion sites were constrained to be equal to aid in refinement. The fluorine atoms were at first allowed to occupy the interstitial sites, but the refinement indicated that there was no occupancy indicating only occupancy of the normal anion sites. The data indicated that the normal anion sites were completely filled (Table 51). From previous work on fluorinated Ruddlesden popper systems [104, 202], the F is presumed to occupy the apical O2 site (Figure 123). The refined pattern along with the structural parameters and selected bond distances are given in Figure 124, Table 51 and 52.

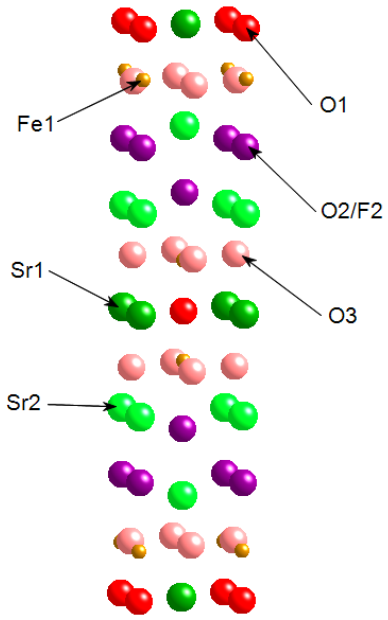

Figure 123: Structure of $Sr_3Fe_2O_{7-x}$:1PVDF showing the different oxygen and fluorine positions.

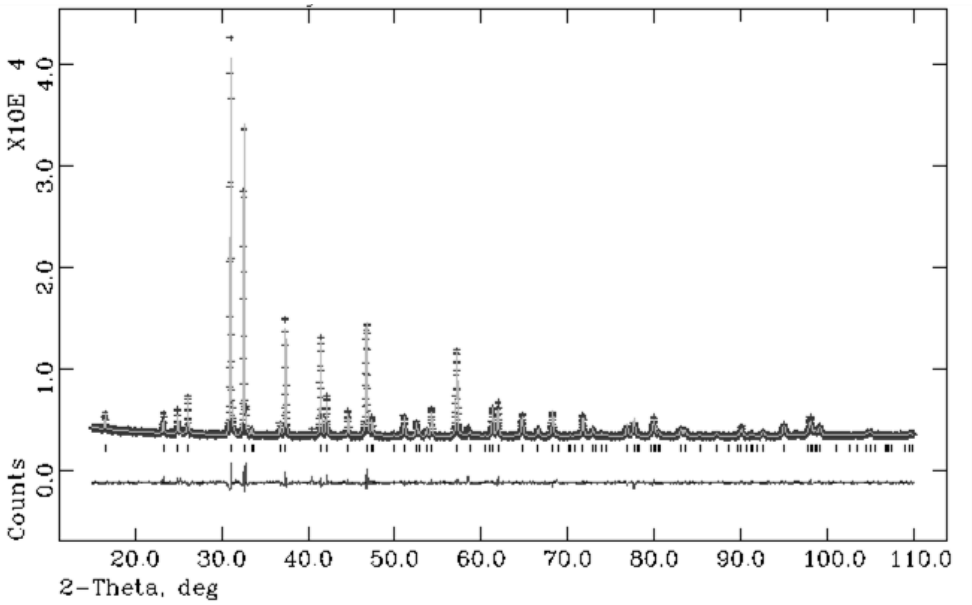

Figure 124: Observed, calculated and difference X-ray diffraction profiles for $Sr_3Fe_2O_{7-x}$:1 PVDF.

Table 51: Structural parameters for $Sr_3Fe_2O_{7-x}$:1 PVDF.

Atom	Multiplicity	X	Y	Z	Uiso	Occupancy
Sr1	2	0	0	0.5	1.58 (6)	1
Sr2	4	0	0	0.32294 (4)	1.05 (5)	1
Fe1	4	0	0	0.08788 (8)	0.74 (5)	1
O1	2	0	0	0	2.45 (9)	1
O2/F2	4	0	0	0.2072 (3)	2.45 (9)	1
O3	8	0	0.5	0.0979 (2)	2.45 (9)	1
Space Group I4/mmm, a = 3.88379(4) Å, c = 21.4284(2) Å, $\chi 2$ = 2.850, R_{wp} = 2.73%						

Table 52: Selected bond distances for $Sr_3Fe_2O_{7-x}$: 1 PVDF.

Bond	Bond Length (Å)
Sr1-O1	2.74625(2) x4
Sr1-O3	2.8579(33) x8
Sr2-O2/F2	2.480(6) x1
	2.8213(13) x4
Sr2-O3	2.579(3) x4
Fe1-O1	1.8831(17) x1
Fe1-O2/F2	2.557(6) x1
Fe1-O3	1.9536(5) x4

As can be seen from the table, the expansion in the c parameter is due to the expansion of the Fe-O2/F2 bond. This expansion is similar to what is observed in the previous studies of $Sr_3Fe_2O_6F_{0.87}$ and $Sr_3Fe_2O_{5.44}F_{1.56}$ supporting the assumption that the fluorine occupies the O2 anion site.

Mössbauer experiments were performed on the system and this spectrum at 298K showed the presence of paramagnetic Fe^{4+} and Fe^{3+} from the observation of a singlet with a shift of 0.08mms^{-1} and paramagnetic doublet with a 0.34mms^{-1} shift respectively (Figure 125). In addition there are 2 magnetic sextets which are also typical of Fe^{3+} being present which is in contrast to $Sr_3Fe_2O_{7-x}$, which shows no magnetic ordering. As the temperature is lowered, the paramagnetic Fe^{4+} singlet decreases in intensity as opposed to an increase in intensity for a magnetic Fe^{4+} sextet. The Fe^{4+} content can be estimated from the intensities of the totally magnetically ordered low temperature spectra to give a Fe^{4+} content of 14 ± 2%. From this estimate the composition can be evaluated as $Sr_3Fe_2O_{5.28(4)}F_{1.72(4)}$. The higher fluorine content in this sample is consistent with the XRD

data, which showed a larger cell volume than observed for $Sr_3Fe_2O_6F_{0.87}$ and $Sr_3Fe_2O_{5.44}F_{1.56}$ reported previously [104, 202]. For the lower content fluorine systems the Mössbauer spectroscopy suggested disproportionation of Fe^{4+} to Fe^{3+} and Fe^{5+} whereas no Fe^{5+} was detected in the present study, which suggests that higher levels of fluorine are needed to suppress the disproportionation of Fe^{4+}.

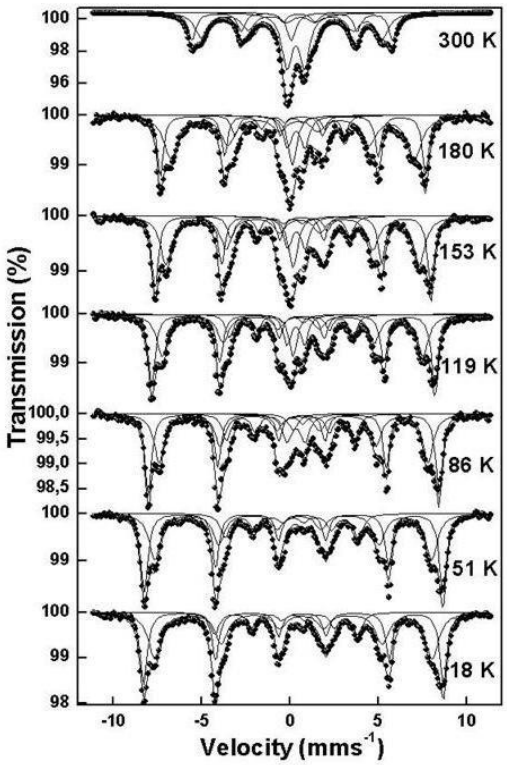

Figure 125: ^{57}Fe Mössbauer spectra recorded for $Sr_3Fe_2O_{7-x}$: 1 PVDF.

For the 1:2 phase (Figure 126) the data indicated an orthorhombic cell with the F222 space group giving a good fit to the data. As for the 1:1 phase the atomic displacement parameters for the anion were constrained to be equal to allow ease of convergence for the refinement. These atomic displacement parameters show rather high values which suggest significant local displacements, which are probably due to the presence of the interstitial anions. As in the 1:1 phase all the normal anion sites are filled with the refinement suggesting filling also of half the interstitial sites to give a composition of $Sr_3Fe_2O_4F_4$. This formula is supported by the decomposition products SrF_2 and

$SrFeO_2F$, which corroborates with the high thermal stability of the SrF_2 which drives the decomposition reaction as shown in Equation 25.

Equation 25: $Sr_3Fe_2O_4F_4 \rightarrow SrF_2 + 2SrFeO_2F$

The structural parameters and bond distances can be found in Table 53 and 54, with the diffraction profiles shown in Figure 127.

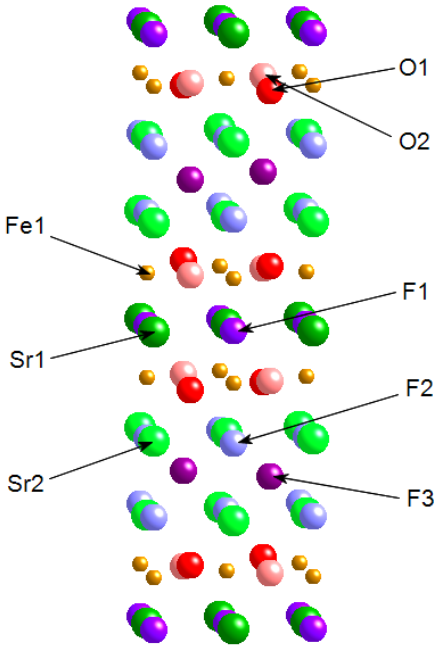

Figure 126: Structure of $Sr_3Fe_2O_{7-x}$:2PVDF showing the different oxygen and fluorine positions.

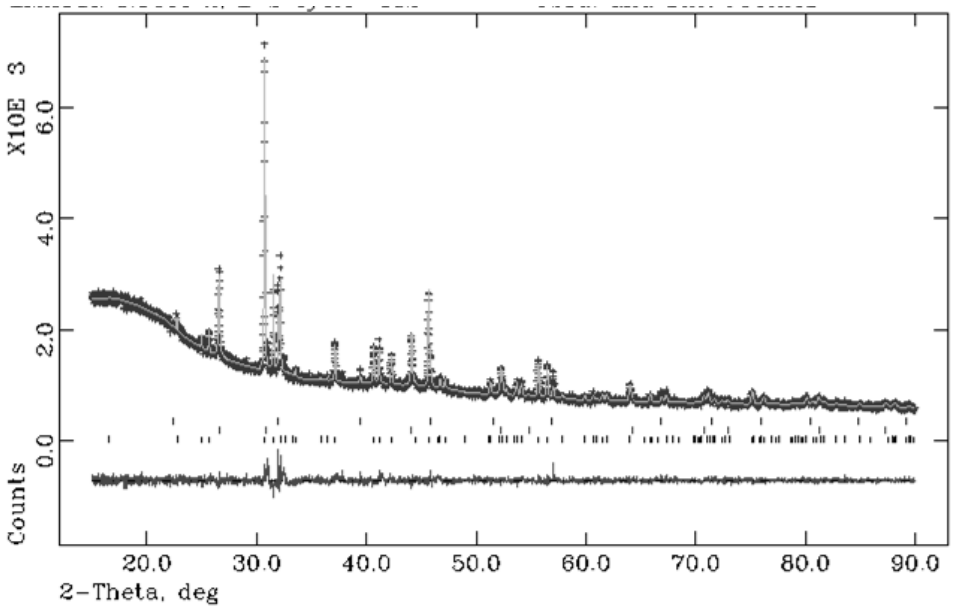

Figure 127: Observed, calculated and difference X-ray diffraction profiles for $Sr_3Fe_2O_{7-x}$:2 PVDF (Lower tick marks: $Sr_3Fe_2O_4F_4$, middle tick marks: $SrFeO_2F$, upper tick marks: SrF_2).

Table 53: Structural parameters for $Sr_3Fe_2O_{7-x}$: 2 PVDF

Atom	Multiplicity	X	Y	Z	Uiso	Occupancy
Sr1	4	0	0	0.5	1.1 (2)	1
Sr2	8	0	0	0.3177 (2)	1.3 (2)	1
Fe1	8	0	0	0.0877 (4)	2.0 (2)	1
O1	8	0.25	0.25	0.103 (2)	5.2 (3)	1
O2	8	0.25	0.25	0.911 (2)	5.2 (3)	1
F1	4	0	0	0	5.2 (3)	1
F2	8	0	0	0.189 (1)	5.2 (3)	1
F3	4	0.25	0.25	0.75	5.2 (3)	1
Space Group F222, a=5.6615(1)Å, b=5.5540(1)Å, c=21.3249(6)Å, χ^2=1.698, R_{wp}=3.76%						

Table 54: Selected bond distances for $Sr_3Fe_2O_{7-x}$: 2 PVDF.

Bond	Bond Length (Å)
Sr1-F1	2.77697(6) x2
	2.83076(7) x2
Sr1-O1	2.954(32) x4
Sr1-O2	2.738(32) x4
Sr2-F2	2.752(22) x1
	2.7802(11) x2
	2.8339(11) x2
Sr2-O1	2.611(29) x2
Sr2-O2	2.816(33) x2
Sr2-F3	2.4523(22) x2
Fe1-F1	1.870(8) x1
Fe1-F2	2.152(2) x1
Fe1-O1	2.008(7) x2
Fe1-O2	1.9828(4) x2

As reported earlier, there was a surprising decrease in the c parameter compared to the 1:1 phase, while there was a large increase in the a and b parameters. This decrease along the c axis can be explained by the decrease in the Fe apical anion (the rock salt layer) distance, which counterbalances the expected expansion due to the partial filling of the interstitial sites. Due to X-ray data not being able to distinguish the difference between O and F anions it is not possible to know the exact location of the F, but it is presumed that the F anions occupy the interstitial and apical sites leaving the O anions to occupy the equatorial sites in the FeO_2 layers. To make a more detailed conclusion neutron diffraction studies are required to provide more accurate descriptions of the anion sites as well as the magnetic structure.

The Mössbauer spectra for the 1:2 phase show chemical isomer shifts that correspond to a number of components containing Fe^{3+} (Figure 128) consistent with the colour change in this sample to red/brown. The spectrum at 298K showed the presence of an intense, asymmetric broad magnetic component which indicates the presence of hyperfine magnetic fields. In addition two weak sextets are observed which are compatible with the $SrFeO_2F$ being present, which confirms the observation from the X-ray data. From the Mössbauer data it is also possible to state that there is a

distorted electronic or anionic environment around the Fe^{3+} due to the relatively large values of both the $e^2Qq/2$ factors, the asymmetry of the spectral lines and the large quadrupole shift values.

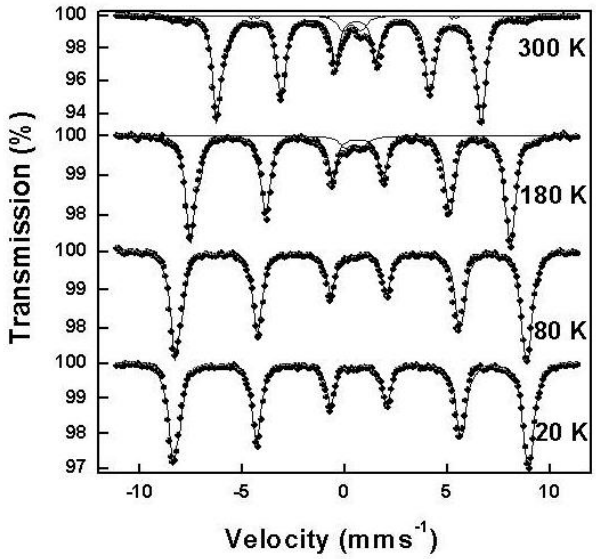

Figure 128: ^{57}Fe Mössbauer spectra recorded for $Sr_3Fe_2O_{7-x}$: 2 PVDF.

As stated earlier it was not possible to perform Rietveld analysis on the 1:2.8 phase because of the large impurities found in the system. Cell parameters were able to be calculated, however, and the expansion of the c parameter is thought to be from the complete filling of the normal anion sites, as well as complete filling of the interstitial sites, resulting in a composition near to $Sr_3Fe_2O_3F_6$. This composition agrees with the decomposition products, SrF_2 and Fe_2O_3, which were observed by XRD (Equation 26).

Equation 26: $Sr_3Fe_2O_3F_6 \rightarrow 3SrF_2 + Fe_2O_3$

The Mössbauer experiments were consistent with the XRD data with two small but well defined sextets characterized by quite a large magnetic field which can be associated with Fe_2O_3 and $SrFeO_2F$ impurities, the latter can be correlated with the fact that the ratio used was 1:2.8 rather than 1:3. In addition only the presence of Fe^{3+} was detected with the spectrum showing paramagnetic peaks at 300K.

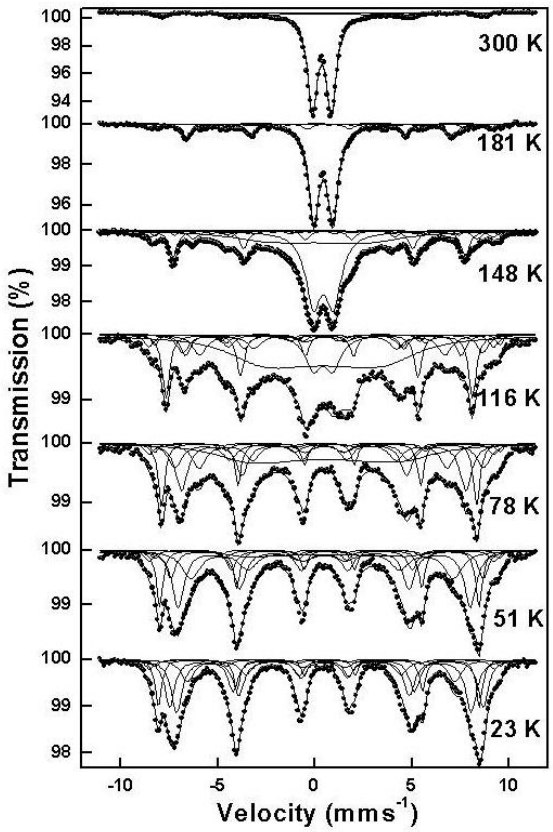

Figure 129: ^{57}Fe Mössbauer spectra recorded for $Sr_3Fe_2O_{7-x}$: 2.8 PVDF.

The results overall show that the Ruddlesden Popper $Sr_3Fe_2O_{7-x}$ material has the ability to incorporate extra anions within its interstitial sites. In addition it has been shown by other research groups that water can be incorporated by exposure to a humid atmosphere [208]. Moreover in a previous chapter it was shown that a significant increase in water content could be achieved in $La_2NiO_{4+\delta}$ by indirect methods. It was therefore decided to investigate whether this method would be viable in the fluorinated $Sr_3Fe_2O_{7-x}$ materials. However preliminary studies showed that immersing the parent material $Sr_3Fe_2O_{7-x}$ in 1M KOH at 200^{o}C resulted in the decomposition of the material, as seen in Figure 130. Due to this instability towards KOH in hydrothermal conditions it was not possible to perform ion exchange on the fluorinated samples.

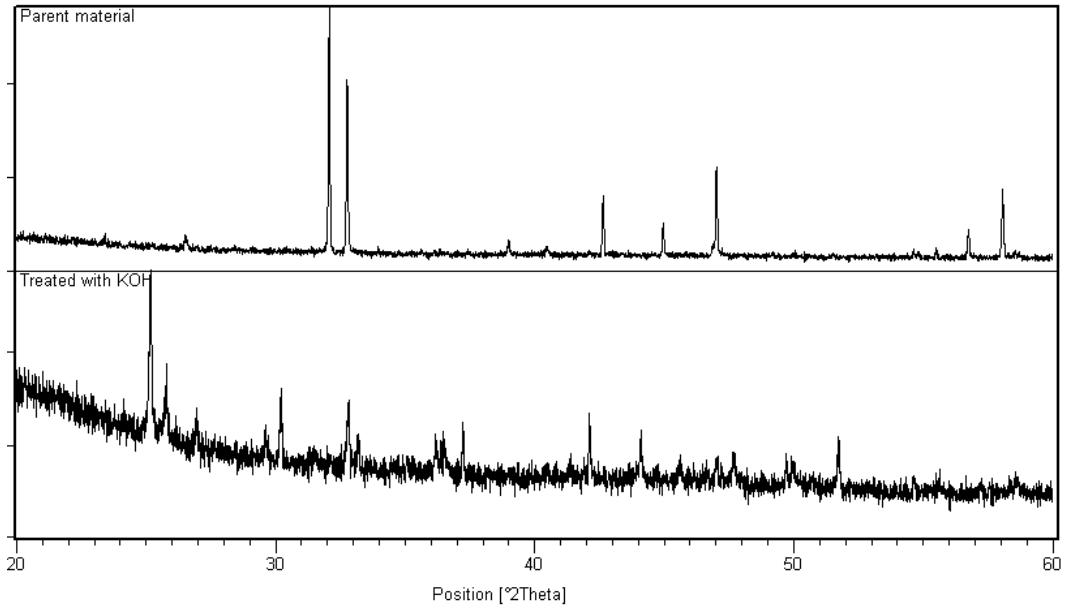

Figure 130: Powder X-ray diffraction patterns for $Sr_3Fe_2O_{7-x}$ (as prepared) and after heat treatment in 1M KOH, showing complete decomposition for the latter.

6.2.3. Conclusions

This work demonstrates that the fluorination of the Ruddlesden Popper phase $Sr_3Fe_2O_{7-x}$ is possible using low temperature fluorination with PVDF. This technique has produced 3 new oxyfluorides with the compositions determined to be $Sr_3Fe_2O_{5.44}F_{1.72}$ (x≈0.28), $Sr_3Fe_2O_4F_4$ and $Sr_3Fe_2O_3F_6$ from X-ray and Mössbauer data. These phases correspond to progressive filling of the normal anion sites; followed by the interstitial sites. It was discovered that for higher fluorine contents, the phases are unstable due to the high thermodynamic stability of the decomposition product SrF_2. The Mössbauer data showed that the Fe oxidation state decreased on fluorination along with complex magnetic interactions being found in all the phases. Attempts to prepare hydroxide variants by F^-/OH^- exchange were unsuccessful, with decomposition observed instead.

7. Electrochemical Testing of Perovskite Systems

As stated earlier it is necessary to replace the expensive platinum that is currently used in low temperature fuel cells with a cheaper alternative. Previous attention has been focused on the catalytic activity of $Ln_{1-x}A_xBO_3$ (Ln=La, Pr, Nd etc, A=Ca and Sr and B=Co, Fe and Mn) systems [60, 209]. It has been reported that the larger the ionic radius of the lanthanide the higher the activity of the electrode [60, 209] with La and Pr giving the best results. In these prior studies, work has been performed on doping on the lanthanide site with Ca doping producing the best performance with an optimum result for x=0.4. In the work reported in this chapter the main focus is on the $CaMnO_{3-y}$ system with different synthesis methods being investigated along with further doping studies with Ru showing promising preliminary results. In addition, results for $Pr_{1-x}Ca_xMnO_{3-y}$ are also reported here to compare with prior literature.

7.1. Experimental

High purity $Pr_6O_{11,}$ CaO and MnO_2 were used to prepare a range of $Pr_{1-x}Ca_xMnO_{3-y}$ (x=0, 0.2, 0.4, 0.6, 0.8 and 1). These materials were ground together in the correct stoichiometric ratios and heated to a temperature of 1100^{o}C for 12 hours. After grinding the materials were heated at 1200^{o}C for a further 12 hours. The Ca end member $CaMnO_{3-y}$ was also prepared by a sol gel combustion route to examine the effect of the synthesis method; In addition a Ru doped sample $CaMn_{0.85}Ru_{0.15}O_{3-y}$ was also prepared by the sol gel combustion route. In this sol gel combustion route high purity $Ca(NO_3)_24H_2O$, $Mn(NO_3)_2H_2O$ and RuO_2 were dissolved and heated on a hot plate with high purity citric acid and EDTA to produce a gel. Once the gel was formed the samples were slowly heated to 350^{o}C to remove all the organic products. These materials were then ground and further heated at 800^{o}C for 12 hours.

The catalyst inks were made by ball milling 0.3g of catalyst in 2ml propanol for 2 hours. After ball milling another 6ml of propanol was added along with 0.1g of polytetrafluoroethylene (60% weight dispersion in water). The inks were deposited and dried on a glassy carbon electrode and then examined by CV and RDE measurements in O_2 saturated 0.1M KOH with a variety of rotation

rates (400, 800,1200 and 1600rpm) using the Invium Stat, Invium A07026 model 636 equipment. For preliminary tests the O_2 was bubbled through the KOH solution for 5mins. For the more detailed tests with $CaMn_{1-x}Ru_xO_{3-y}$ the solution was purged for an hour to ensure full saturation.

For fuel cell testing 0.04g of the catalyst was mixed with 15% total weight of poly(vinylbenzylchloride) (PVBC) and immersed in ethyl acetate. The ink was then painted on a 12.5x12.5mm carbon sheet and then soaked overnight in 1, 6-diaminohexane. After soaking overnight the electrode was soaked for a further hour in 1M KOH, before washing in water. This cathode catalyst was tested in a fuel cell with a Pt anode and University of Surrey's S80 membrane on an Arbin fuel cell test station with the cell temperature and dew point at 50^{o}C and the gas temperature at 60^{o}C with 100% humidity.

7.2. Results and Discussion

At the beginning of this work preliminary tests were performed on a range of materials to determine which materials were most promising. Work performed in the past by other groups suggested that the $Pr_{1-x}Ca_xMnO_{3-y}$ system was interesting with the x=0.4 system showing particular promise. In the work in this thesis, tests were performed on the $Pr_{1-x}Ca_xMnO_{3-y}$ with x=0, 0.2, 0.4, 0.6, 0.8 and 1, with the results showing that the Ca end member (x=1) system displayed the more positive onset potential (Figure 131 and 132) and hence the most favourable oxygen reduction reaction. This increase in performance with increasing Ca content could be due to the increase in the Mn oxidation state.

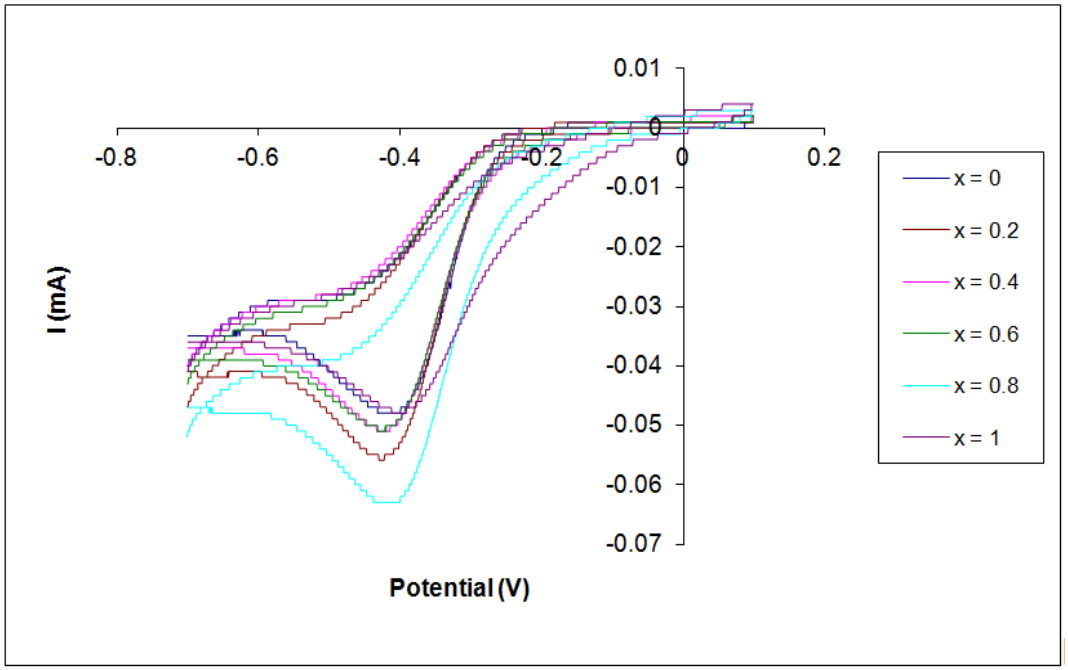

Figure 131: Cyclic voltammograms of $Pr_{1-x}Ca_xMnO_{3-y}$ showing how the onset potential varies on doping.

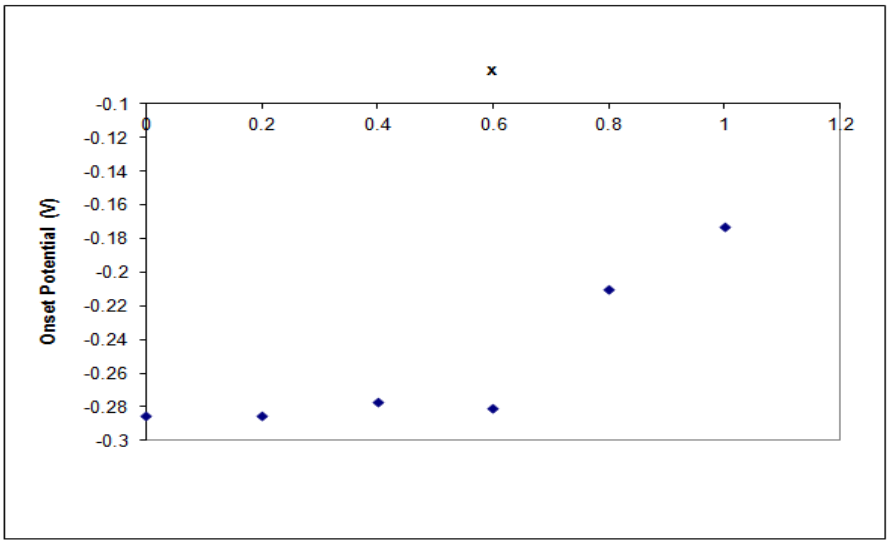

Figure 132: Variation of onset potential of $Pr_{1-x}Ca_xMnO_{3-y}$ on doping with Ca content (x).

Following on from these preliminary results, further work concentrated on the $CaMnO_{3-y}$ system. To determine if the synthesis method had any effect on the onset potential of the catalyst the material was made by both solid state and sol gel methods. As can be seen in Figure 133 the onset potential at around -0.15V for the sol gel sample was shifted further to the right compared to

the solid state prepared sample which had an onset potential around -0.18V. This could be due to the sol gel sample having smaller particle size, and hence a greater surface area. Consequently for the more detailed further testing, the focus was on the sol gel combustion prepared samples.

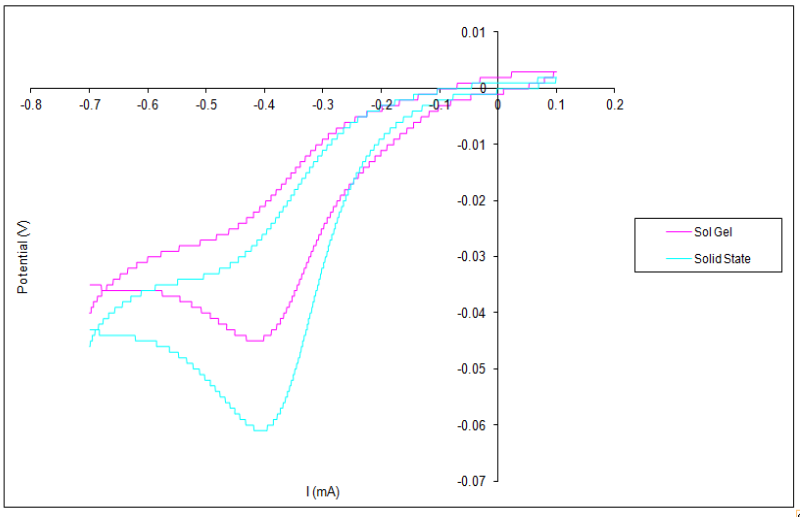

Figure 133: Variation of the onset potential for $CaMnO_{3-\gamma}$ when prepared via different methods.

In the previous chapter ruthenium doping on the Mn site was shown to have a positive effect on the onset potential. To investigate this further, more precise tests were performed on the undoped and the highest doped Ru sample prepared by a sol gel combustion route. The same cyclic voltammetry and rotating disk electrode tests were performed, but a longer purge of the samples with oxygen was used to make sure that the solution was fully oxygenated.

To begin with, cyclic voltammetry was run in nitrogen saturated solution on both the doped and undoped systems. In this case there should be negligible activity which can be confirmed by Figure 134. When performing the cyclic voltammetry experiments in oxygen saturated solution reduction and oxidation peaks can be seen, and the onset potential of the oxygen reduction can be determined. This onset potential indicates the ease of oxygen reduction which improves with the shift in the positive direction. The results show that with Ru doping there is a shift to more positive potentials to around -0.12V, as seen in Figure 135.

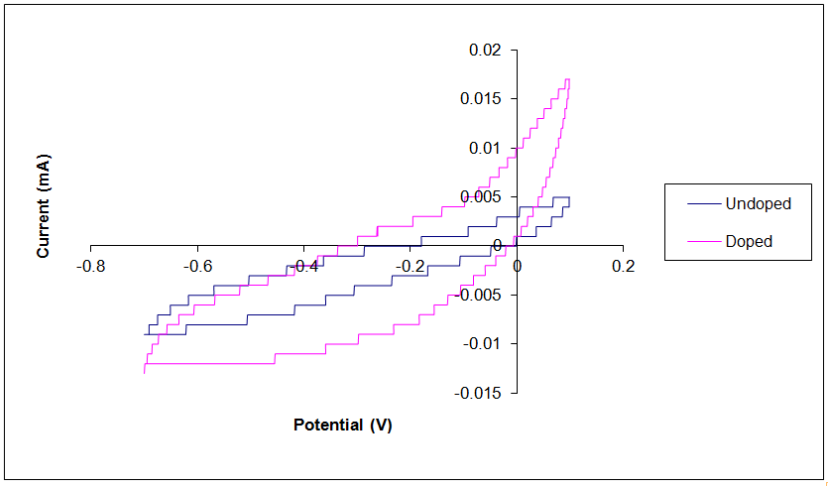

Figure 134: Cyclic voltamograms of $CaMn_{1-x}Ru_xO_{3-y}$ in nitrogen saturated 0.1M KOH solution.

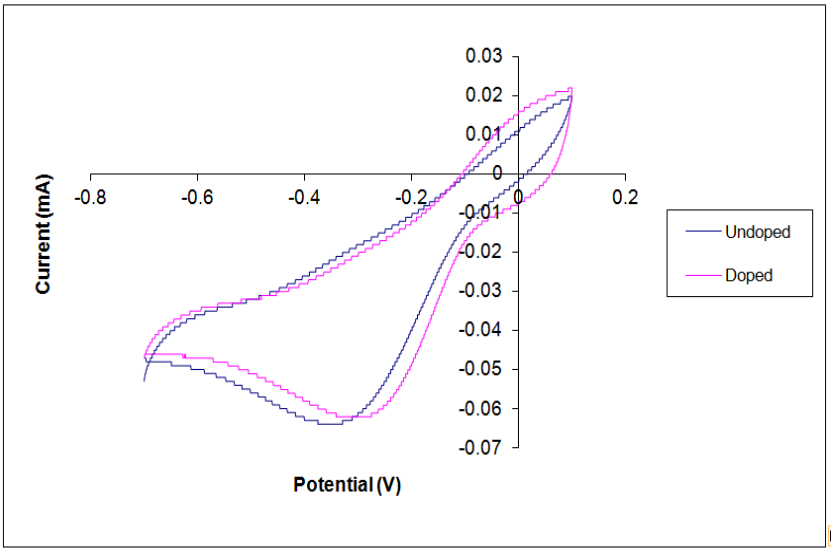

Figure 135: Cyclic voltamograms of $CaMn_{1-x}Ru_xO_{3-y}$ in oxygen saturated 0.1M KOH solution.

As mentioned previously, it is highly desirable to reduce oxygen via the 4 electron pathway (i.e. $O_2 + 4e^- \rightarrow 2O^{2-}$) as this pathway is more efficient, and so the samples were further analysed to determine the electron pathways shown. This was achieved using RDE measurements, which in addition to determining the electron pathway, also measures the onset potential, allowing for correlation with the cyclic voltammetry measurements. Figure 136 and 137 show the RDE measurements for undoped and Ru doped $CaMnO_{3-y}$ materials respectively. In both sets of data the limiting current magnitude increases at higher rotation rates, which is due to the velocity of the solution increasing in speed, which leads to a higher convective transport of electroactive material

along with a thinner diffusion layer thickness. The onset potential follows the results for the cyclic voltammetry with the value for the doped system being more positive at around -0.1V.

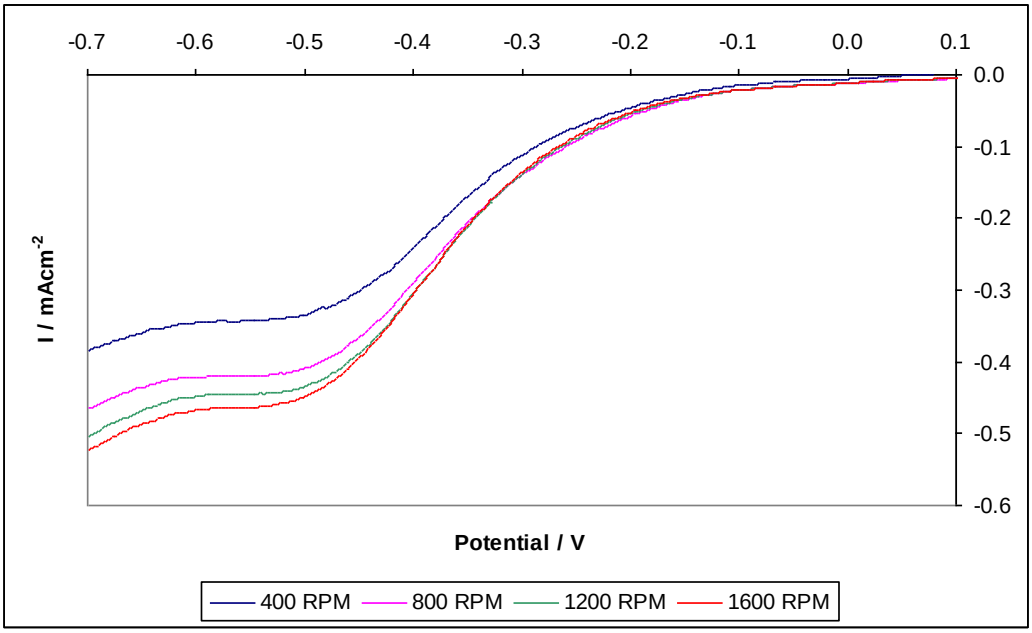

Figure 136: Rotation disk electrode measurements for $CaMnO_{3-y}$ at various rotation rates.

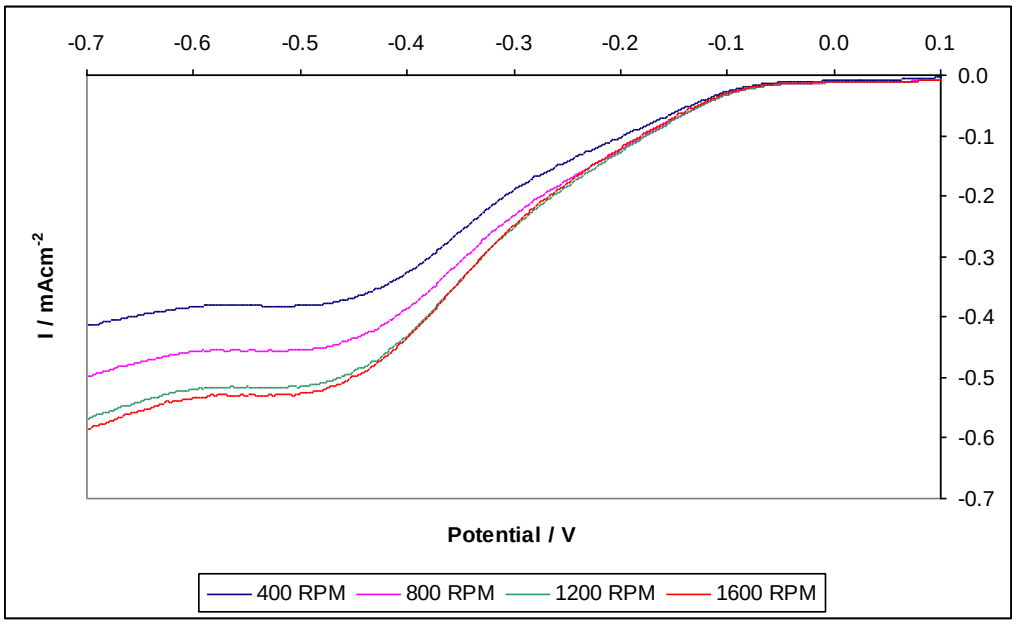

Figure 137: Rotation disk electrode measurements for $CaMn_{1-x}Ru_xO_{3-y}$ at various rotation rates.

The oxygen reduction electron pathway followed by the material is determined by plotting Koutecky-Levich plots ($1/i_{lim}$ vs $1/\omega^{1/2}$) at fixed potentials which are taken from the RDE plots. The

gradient of the slopes (Figure 138, 139 and Table 55) then gives the electron exchange number after applying equation 17.

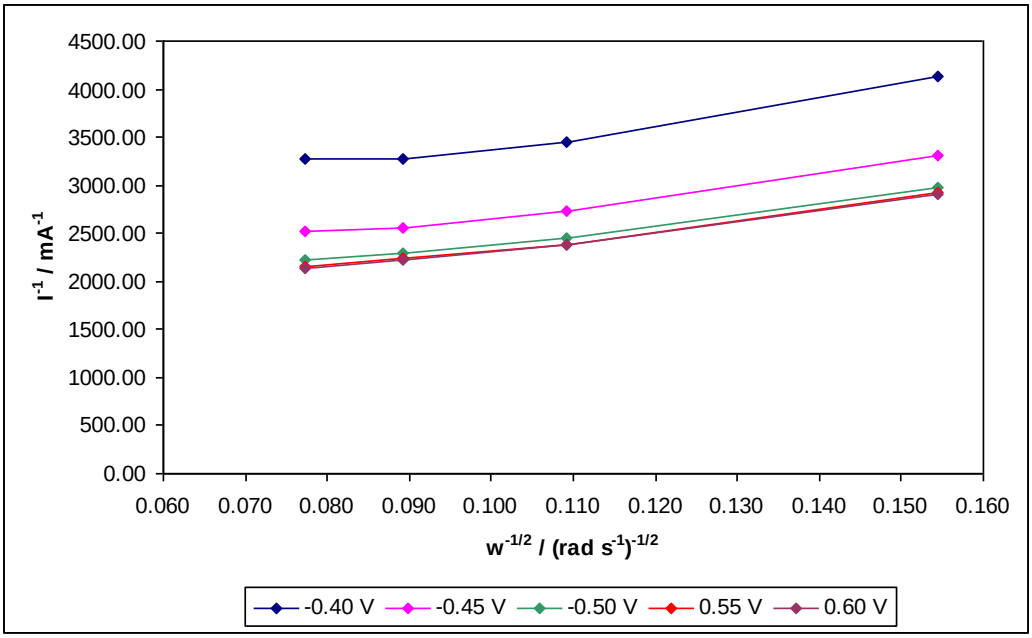

Figure 138: Koutecky-Levich plot for $CaMnO_{3-y}$.

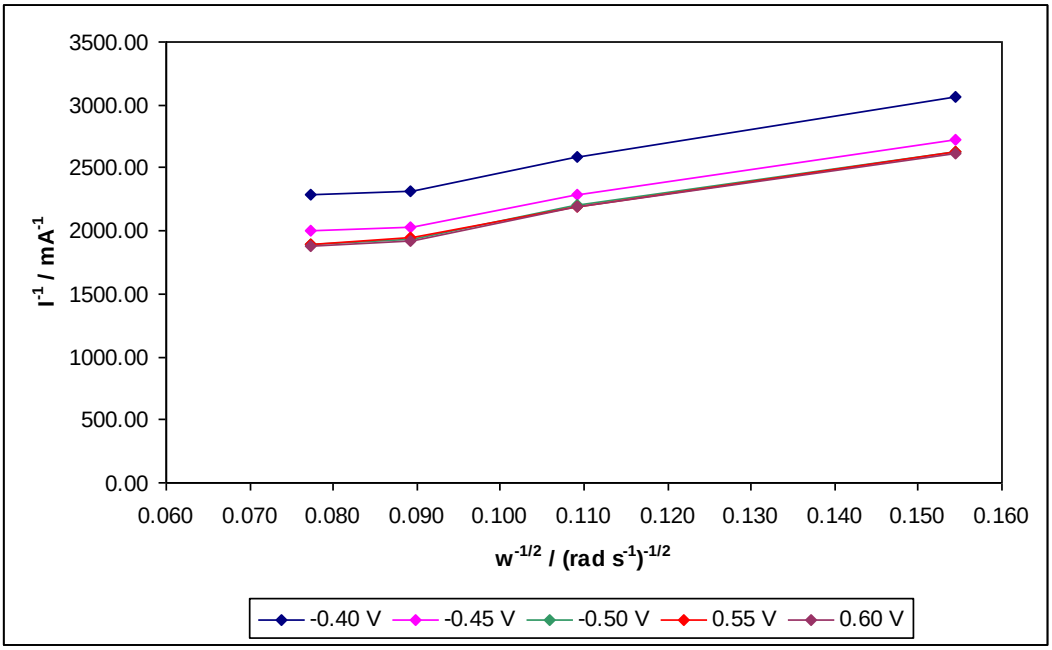

Figure 139: Koutecky-Levich plot for $CaMn_{0.85}Ru_{0.15}O_{3-y}$.

Table 55: Gradient and electron number transfer for $CaMn_{1-x}Ru_xO_{3-y}$ (x=0 and 0.15) calculated from the Koutecky-Levich plots.

	Gradient					Electron Transfer				
Fixed Potential	0.4	0.45	0.5	0.55	0.6	0.4	0.45	0.5	0.55	0.6
$CaMnO_{3-y}$	11752	10551	10005	10008	9902.1	0.8	0.9	0.9	0.9	0.9
$CaMn_{0.85}Ru_{0.15}O_{3-y}$	10500	9665	9827.4	9845.2	9880	0.9	0.9	0.9	0.9	0.9

The data (Table 55) showed that the electron transfer process for the studied materials is around 1. This means that these electrode catalysts are not as efficient as platinum which has an electron transfer pathway of 4. Care must, however, be taken when drawing conclusions from these results, as there may be errors, since the results are based on the area of the electrode and the amount of catalyst in the ink. In the case of these inks this presents some issues as the precise amount of catalyst is not accurately known, since there is some loss from the ball milling process. To determine accurately the electron transfer process it is necessary to perform RRDE which can detect the presence of H_2O_2, which would indicate a lower than 4 electron process. Despite these limitations, the results showed that of the samples tested, these $CaMn_{1-x}Ru_xO_{3-y}$ catalysts had the most potential and so fuel cell testing was performed using them.

The two catalysts $CaMnO_{3-y}$ and $CaMn_{0.85}Ru_{0.15}O_{3-y}$ were investigated for potential use as cathode catalysts in AAEMFC systems supplied with H_2/O_2 at 50^oC. The cathode catalysts were used on prefabricated carbon paper with Pt being used for the anode, and Surrey's S80 membrane as the electrolyte. As can be seen from Figure 140 the Ru doped catalyst out performs the undoped material with a peak power density of 54 $mWcm^{-2}$ at a current density of 160 $mAcm^{-2}$ compared to the lower peak power density of 26 $mWcm^{-2}$ at a current density of 60 $mAcm^{-2}$ for $CaMnO_{3-y}$. The data for $CaMn_{0.85}Ru_{0.15}O_{3-y}$ does show some fluctuations in the power curve, however, which could be blamed on the structure of the electrodes and flooding of the electrode at times during the testing. Further studies are planned to improve the electrode fabrication in this respect.

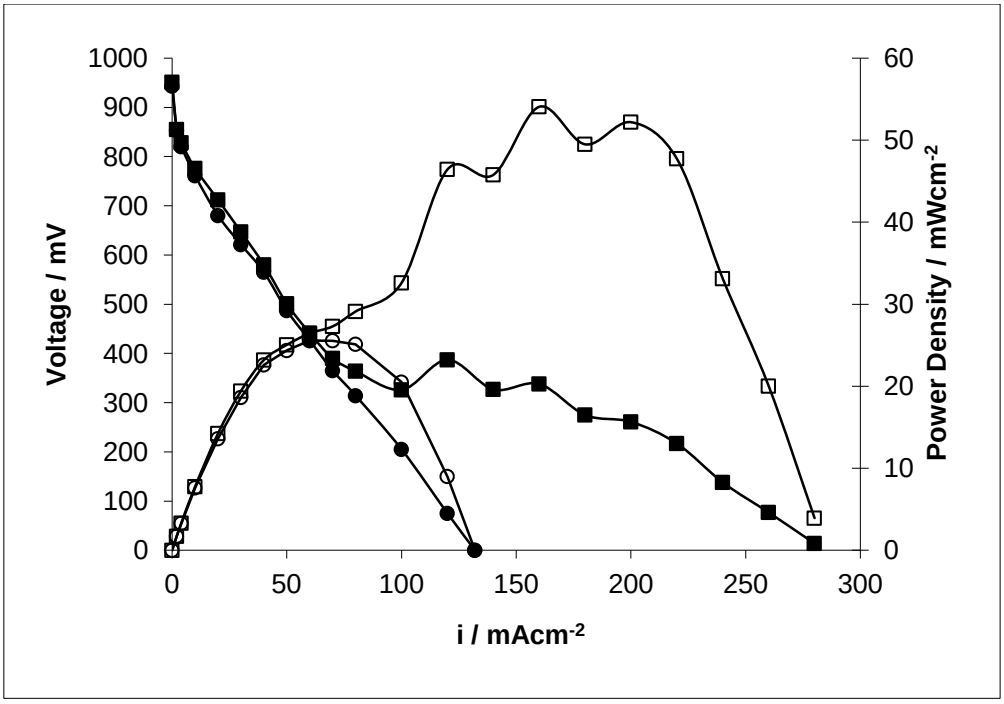

Figure 140: Fuel cell performance at 50°C using Surrey's S80 membrane with a platinum anode. The circles represents the undoped $CaMnO_{3-y}$ and squares the $CaMn_{0.85}Ru_{0.15}O_{3-y}$. The filled shapes show the voltage vs the current density where the empty shapes show the power density vs the current density.

In comparison to existing cathode material, i.e. Pt, the performance of platinum compared to $CaMn_{0.85}Ru_{0.15}O_{3-y}$ is significantly better with a peak power density of 115 $mWcm^{-2}$ at a current density of 300 $mAcm^{-2}$ [210]. However a great deal of optimisation work (e.g. enhancing surface area) has been performed on such Pt catalyst. Consequently the performance of $CaMn_{0.85}Ru_{0.15}O_{3-y}$ is encouraging and with further modifications in processing, further improvements are likely.

7.3. Conclusions

The most promising catalysts, $CaMnO_{3-y}$ and $CaMn_{0.85}Ru_{0.15}O_{3-y}$, discovered from preliminary electrochemical experiments were tested as cathode catalysts for use in an AAEMFC system. The catalysts showed respectable performances, albeit lower than the optimised Pt cathodes. Overall the performances were encouraging, and indicate that further optimisation work in this area is warranted.

8. Conclusions

A variety of Ruddlesden Popper and perovskite materials have been successfully prepared and examined using a variety of techniques in order to determine their structural and physical properties for possible use as fuel cell catalysts in AAEMFCs or SOFCs.

$La_2NiO_{4+\delta}$ and $Nd_2NiO_{4+\delta}$ were prepared by the solid state method, and various methods were employed to incorporate water within their interstitial sites in the hope of improving the performance as a fuel cell catalyst for an AAEMFC. Direct methods of exposing the samples to humid atmospheres were found to be the least successful, while the immersion of the samples in various solutions did lead to the incorporation of additional water. The most effective technique for water incorporation was, however, the novel indirect method of pre-fluorinating the materials and then performing OH^-/F^- ion exchange. A number of fluorinated phases were prepared by reaction with, PVDF, with the purist sample then successfully ion exchanged, resulting in significant levels of water incorporation (0.64 moles per formula unit).

While successful hydration of $La_2NiO_{4+\delta}$ was achieved in this way, the other Ruddlesden Popper materials, $La_2CuO_{4+\delta}$ and $Sr_3Fe_2O_{7-y}$, were unable to incorporate water via this indirect method due to decomposition occurring in the basic conditions employed during the ion exchange process. However some water incorporation was possible using the gentler direct methods. $Sr_3Fe_2O_{7-y}$ was shown to be able to incorporate large levels of fluorine, and this work led to the identification of 3 new oxyfluoride systems. These three new systems correspond to firstly the filling of the anion sites and subsequently the interstitial sites. At the higher levels of fluorination, secondary phases were, however, observed due to the high thermodynamic stability of the decomposition product SrF_2. Mössbauer data showed that the amount of Fe^{3+} increases on fluorination, and for samples containing only Fe^{3+}, were magnetically ordered at room temperature was observed.

Another strategy analysed for the production of new fuel cell catalysts was oxyanion (silicate, phosphate, sulphate) doping in perovskite systems. Successful oxyanion doping with silicate was achieved in the $SrCoO_{3-y}$, $SrMnO_{3-y}$, $SrFeO_{3-y}$ and $CaMnO_{3-y}$ systems. On doping there was a significant increase in the conductivity due to a phase change from hexagonal to cubic/tetragonal on doping in the case for $SrCo_{1-x}Si_xO_{3-y}$, $SrMn_{1-x}Si_xO_{3-y}$ and $SrFe_{1-x}Si_xO_{3-y.}$ In systems where no phase change was observed, e.g. $CaMnO_{3-\delta}$, the increase in the conductivity can be attributed simply due to the incorporation of mixed valency. The silicate doping is particularly interesting as it is gives rise to electron doping (i.e. reduction of the transition metal oxidation state) despite the fact that it is nominally an isovalent doping strategy. This apparent anomaly can be explained by the coordination preference of the silicate group, i.e. it is incorporated as a tetrahedral SiO_4^{4-} ion on an octahedral perovskite site, and hence leads to the creation of oxide ion vacancies, which then account for the observed reduction. In addition, this work is also interesting as in the past the incorporation of Si into fuel cell materials has been said to have a detrimental effect compared, to the positive effect that has been documented here, thus demonstrating that further work is required in this area.

The structures of these materials were also investigated with various heat treatments, which showed changes occurred when some of the material was exposed to different heating conditions. This was particularly true for the $SrCo_{1-x}X_xO_{3-y}$ (X = P, S, Si) system, which were shown to be metastable; slow cooling led to phase transformation from tetragonal back to the hexagonal phase displayed by the undoped parent material.

The materials were then examined for their potential as catalysts in APEMFCs. For this electrochemical testing, preliminary experiments were performed on all systems to determine which materials should be investigated further. These initial data showed that undoped $CaMnO_{3-y}$ had the most promise for use as a fuel cell catalyst due to the material having a higher onset potential compared to the other catalysts tested, even out performing commercial products such as LSM and LSCF. The incorporation of Si caused the onset potential to decrease even though the conductivity

was improved. Further investigation revealed that when doping the $CaMnO_{3-y}$ with ruthenium an improvement in the onset potential could be achieved meaning an improved oxygen reduction reaction. From in-situ fuel cell tests the performance of the Ru doped system was encouraging. The results showed that on doping with ruthenium there was an increase in maximum power density from 26mWcm^{-2} at 60mAcm^{-2} to 54mWcm^{-2} at 160mAcm^{-2}, and further work is planned to take this system further, as well as to analyse these systems as electrode materials in solid oxide fuel cells (see chapter 9).

9. Further Work

The current research indicated that both perovskite and Ruddlesden Popper materials exhibit interesting properties for potential use as electrode materials in either AAEMFC or SOFC.

The research on the Ruddlesden Popper phases showed that it was possible to incorporate extra anions within its structure from low temperature fluorination or water incorporation. Research on the $La_2NiO_{4-x}F_{2x}$ system showed that it was possible to replace F^- by OH^- using ion exchange, and hence showed this to be a novel strategy for the synthesis of new K_2NiF_4 hydroxides. Further work into similar ion exchange of fluorinated Ruddlesden Popper systems would be interesting including $La_2NiO_{4-x}F_{2x}$ phases containing higher F levels. However improvements in the synthetic procedures are required to prepare higher quality samples of these higher fluorinated phases, before the exchange reaction is undertaken. Structure refinements using X-ray data were performed on the exchanged systems, but the positions of the oxygen and hydrogen could not be determined accurately, and so further investigation with neutron diffraction experiments are warranted. In addition it would be interesting to investigate if the magnetic properties change after ion exchange.

For the transition metal containing perovskite materials it was found that doping with oxyanions is an excellent strategy to reduce the tolerance factor due to the incorporation of oxide ion vacancies reducing the transition metal oxidation state. For hexagonal perovskites this can lead to a change to a cubic/tetragonal cell and hence large increases in conductivity. Further neutron diffraction studies are required to accurately determine the positions of the oxide ions in the $(Sr/Ca)Mn_{1-x}Si_xO_{3-y}$ systems, in particular whether there is some degree of oxygen vacancy ordering as in the $SrCoO_{3-y}$ systems. For the oxyanion doped $SrCoO_{3-y}$ material it was shown that codoping with Fe was needed to stabilise the structure, although this did lower the conductivity; further doping studies with other transition metals would be of interest to further improve the stability without having a detrimental effect on the conductivity.

For the $CaMnO_{3-y}$ materials, an improvement in the onset potential and performance was seen on doping with Ru. A doping study to determine the optimum amount of Ru needed to improve the onset potential and performance needs to be performed, in addition to investigating different dopants such as Ir, Re, Pt and Pd. This can then be extended by doping the Ca site with Sr to produce $Ca_{1-y}Sr_yMn_{1-x}Ru_xO_{3-\delta}$ materials, as well as extending to other structures e.g. pyrochlore-type $Ca_2Ru_{2-x}Mn_xO_7$. The structure-type and dopant are not the only areas of work that need to be examined; in particular a detailed investigation into the effect of the synthesis method of these materials is required. Such studies will allow the effect of factors such as particle size/morphology to be examined.

In terms of potential application in SOFCs, all the perovskite materials need more in depth compatibility tests to be performed, to include different electrolyte materials. Once compatibility issues have been determined, the potential usage of these materials in SOFCs needs to be examined. This will initially focus on simple electrode evaluation on electrolyte pellets to determine the ASR (Area Specific Resistance) Values. In this respect, initial work performed by J. Porras-Vasquez has shown that on incorporation of Si into $Sr_{1-y}Ca_yMnO_{3-\delta}$ system there is a significant improvement in the ASR values. Overall the lowest ASR values were observed for the Sr rich system with a value of 0.07 Ωcm^2 for $Sr_{0.8}Ca_{0.2}Mn_{0.925}Si_{0.075}O_{3-\delta}$ at 800^oC compared to 0.36 Ωcm^2 for the undoped system [211]. For electrode materials which show low ASR values, full fuel cell testing would then be performed.

Finally an interesting potential feature of these oxyanion doped phases is their potential to display novel oxide ion conduction pathways, e.g. via SN2 type mechanisms. Therefore in these perovskite systems modelling studies would be of interest to examine the conduction pathways. Such processes have been predicted in modelling studies of apatite germinate SOFC electrolytes [212]. This could be coupled with ^{17}O isotope exchange/NMR studies to examine whether ^{17}O enrichment of the oxyanion occurs, which would indicate some sort of exchange process, although NMR studies on systems containing transition metal are non-trivial.

10. Publication List

Hancock C A and Slater P R, *Synthesis of silicon doped $SrMO_3$ (M=Mn, Co): Stabilisation of the cubic perovskite and enhancement in conductivity.* Dalton Transactions, 2011. **40**, 5599-5603.

Berry F J, Coomer F C, Hancock C A, Helgason O, Moore E A, Slater P R, Wright A J, Thomas M F, *Structure and magnetic properties of the cubic oxide fluoride $BaFeO_2F$.* Journal of Solid State Chemistry, 2011. **184** (6), 1361-1366.

Hancock C A, Slade R C T, Varcoe J R and Slater P R, *Synthesis, structure and conductivity of sulphate and phosphate $SrCoO_3$.* Journal of solid state chemistry, 2011. **184**, 2972-2977.

Hancock C A, Herranz T, Marco J F, Berry F J and Slater P R, *Low temperature fluorination of $Sr_3Fe_2O_{7-x}$ with polyvinylidine fluoride: X-ray powder diffraction and Mössbauer spectroscopy study.* Journal of solid state chemistry, 2012. **186**, 195-203.

Porras J M, Keenan P, Hancock C A, Slater P R, *Investigation into the effect of Si doping on the performance of $Sr_{1-y}Ca_yMnO_{3-\delta}$ SOFC cathode materials.* Journal of Power Sources. Submitted.

Hancock C A, Marco J F, Vergara L, Berry F J and Slater P R, *Synthesis and characterisation of Si doped $SrFeO_{3-x}$ for potential applications in Solid Oxide Fuel Cells.* In Preparation.

Slater P R and Hancock C A, *Oxyanions in Perovskites: From Superconductors to Solid Oxide Fuel Cells.* Review, in preparation.

Hancock C A, Varcoe J, Slade R C T and Slater P R, *Anion incorporation into $La_2NiO_{4+\delta}$ via direct and indirect methods.* In preparation.

11. Conference List

Solid State Christmas Conference	18/12/08	
Birmingham NEC	25/03/09	
University of Birmingham Postgraduate Symposium	00/06/09	
Solid State Christmas Conference	17/12/09	Poster
University of Birmingham Postgraduate Symposium	00/06/10	Poster
Liverpool Conference	20/07/10	Poster
Alan Chadwick Symposium	25/07/10	
Solid State Christmas Conference	21/12/10	Talk
Fundamentals of Fuel Cells, Grenoble	19/01/11	Poster
Solid State Ionics, Warsaw	07/07/11	Poster

12. References

1. BP., *Statistical Review of World Energy 2011.* Cited 2012; Available from: http://www.bp.com/assests/bp_internet/globalbp/globalbp_uk_english/reports_and_publications/statistical_energy_review_2011/STAGING/local_assets/pdf/statistical_review_of_world_energy_full_report_2011.pdf.
2. Song, C.S., *Fuel processing for low-temperature and high-temperature fuel cells – Challenges, and opportunities for sustainable development in the 21st century.* Catalysis Today, 2002. **77**(1-2): p. 17-49.
3. *World Population – The Current World Population.* Cited 2012; Available from: http://geography.about.com/ad/obtainpopulationdata/a/worldpopulation.htm.
4. BP., *BP statistical review of world energy 2011.* Cited 2012; Available from: http://www.bp.com/assets/bp_internet/globalbp_uk_english/reports_and_publications/statistical_energy_review_2011/STAGING?local_assets/spreadsheets/statistical.review_of_world_energy_full_report_2011.xls#'Primary_Energy – Consumption'!A1.
5. Ortiz-Rivera, E.I., Reyes-Hernaandez, A.L. and Febo, R.A., *Understanding the history of fuel cells*. 2000t IEEE Conference on the History of Electric Power, 2007: p. 91-96.
6. Stambouli, A.B. and Traversa, E., *Solid oxide fuel cells (SOFCs): A review of an environmentally clean and efficient source of energy.* Renewable and Sustainability Energy Reviews, 2002. **6**(5): p. 433-455.
7. Carrette, L., Friedrich, K.A. and Stimming, U., *Fuel cells: Principles, types, fuels and applications*. Chemphyschem, 2000. **1**(4): p. 162-193.
8. Andujar, J.M., Segura, F., *Fuel cells: History and updating. A walk along two centuries.* Renewable and Sustainable Energy Reviews, 2009. **13**(9): p. 2309-2322.
9. Grimes, P.G., *Historical pathways for fuel cells – The new electric century.* IEEE Aerospace and Electronic Systems Magazine, 2000. **15**(12): p. 7-10.

10. Douglas, D.L. and Liebhafsky, H.A., *Fuel cells – History, operation and applications.* Physics Today, 1960. **13**(6): p. 26-30.

11. Ilic, D., Holl. K., Birke, P., Wohrle, T., Birke-Salam, F., Perner, A. Ans Haug, P., *Fuel cells and batteries: Competition or separate paths?* Journal of Power Sources, 2006. **155**(1): p. 72-76.

12. McLean, G.F., Niet, T., Prince_Richard, S. and Djilali, N., *An assessment of alkaline fuel cell technology.* International Journal of Hydrogen Energy, 2002. **27**(5): p. 507-526.

13. Warshay, M., Prokopius, P., Le, M. and Voecks, G., *The NASA fuel cell upgrade program for the Space Shuttle Orbiter.* Proceedings of the Thirty-Second Intersociety Energy Conversion Engineering Conference, 1997. **1-4**: p. 228-231.

14. Larminie, J. and Dicks, A., *Fuel Cell Systems Explained.* 2 ed. 2003: Wiley. 406.

15. Cifrain, M. and Kordesch, K., *Hydrogen/oxygen (Air) fuel cells with alkaline electrolytes.* Cited 2011; Available from: http://www.electricauto.com/_pdfs/newspapers/104013_o.pdf.

16. Abdullah, M.O. and Gan, Y.K., *Feasibility study of a mini fuel cell to detect interference from a cellular phone.* Journal of Power Sources, 2006. **155**(2): p. 311-318.

17. Acres, G.J.K., *Recent advances in fuel cell technology and its applications.* Journal of Power Sources, 2001. **100**(1-2): p. 60-66.

18. O'Hayre, R., Cha, S., Colella, W. and Prinz, F.B., *Fuel Cell Fundamentals.* 2006: John Wiley and Sons. 409.

19. Matsuoka, K., Iriyama, Y., Abe, T., Matsuoka, M. And Ogumi, Z., *Alkaline direct alchol fuel cells using an anion exchange membrane.* Journal of Power Sources, 2005. **150**: p. 27-31.

20. Guelzow, E., *Alkaline fuel cells.* Fuel Cells, 2004. **4**(4): p. 251.255.

21. Vielstich, W., Gasteiger, H. A. and Yokokawa, H., *Handbook of Fuel Cells – Advances in Electrocatalysis, Materials, Diagnostics and Durability.* 2009 John Wiley and Sons.

22. Kalhammer, F.R., *Polymer electrolytes and the electric vehicle.* Solid State Ionics, 2000. **135**(1-4): p. 315-323.

23. Deluca, N.W. and Elabd, Y.A., *Polymer electrolyte membranes for the direct methanol fuel cell: A review.* Journal of Polymer Science Part B-Polymer Physics, 2006. **44**(16): p. 2201-2225.

24. Jacobson, A.J., *Materials for solid oxide fuel cells.* Chemistry of Materials, 2010. **22**(3): p. 660-674.

25. Marrero-Lopez, D., Diaz-Carrasco, P., Pena-Martinez, J., Ruiz-Morales, J.C. and Ramos-Barrado, J.R., *Lanthanum germanate-based apatites as electrolytes for SOFCs.* Fuel Cells, 2011. **11**(1): p. 65-74.

26. Orera, A., Baikie, T., Kendrick, E., Shin, J.F., Pramana, S., Smith, R., White, T.J., Sanjuan, M.L. and Slater, P.R., *Apatite germinates doped with tungsten: synthesis, structure and conductivity.* Dalton Transactions, 2011. **40**(15): p. 3903-3908.

27. Orera, A. and Slater, P.R., *New chemical systems for solid oxide fuel cells.* Chemistry of Materials, 2010. **22**(3): p. 675-690.

28. Slater, P.R., Sansom, J.E.H. and Tolchard, J.R., *Development of apatite-type oxide ion conductors.* Chemical Record, 2004. **4**(6): p.373-384.

29. Siemens, *Cylindrical-tube-SOFC-large.gif.* Cited 2011; Available from: http://www.energy.siemens.com/fi/pool/hq/power-generation/fuel-cells/principle-behind/cyclindrical-tube-SOFC-large.gif.

30. *Solid Oxide Fuel Cells.* Cited 2011; Available from: http://people.bath.ac.uk/cf233/sofc.html.

31. Yuh, C., Johnsen, R., Farooque, M. and Maru, H., *Status of carbonate fuel-cell materials.* Journal of Power Sources, 1995. **56**(1): p. 1-10.

32. Sammes, N., Bove, R. and Stahl, K., *Phosphoric acid fuel cells: Fundamentals and applications.* Current Opinion in Solid State and Materials Science, 2004. **8**(5): p. 372-378.

33. Weller, M.T., *Inorganic Materials Chemistry.* 1994: Oxford Chemistry Primers. 92.

34. Morozan, A., Jousselme, B. and Palacin, S., *Low-platinum and platinum-free catalysts for the oxygen reduction reaction at fuel cell cathodes.* Energy and Environmental Science, 2011. **4**(4): p. 1238-1254.

35. Li, C., Soh, K.C.K. and Wu, P., *Formability of ABO_3 perovskites.* Journal of Alloys and Compounds, 2004. **372**(1-2): p. 40-48.

36. Svarcova, S., Wiik, K., Bouwmeester, H.J.M. and Grande, T., *Structual instability of cubic perovskite $Ba_xSr_xSr_{1-x}Co_{1-y}Fe_yO_{3-\delta}$.* Solid State Ionics, 2008. **178**(35-36): p. 1787-1791.

37. Rao, C.N.R. and Raveau, B., *Transition Metal Oxides Structure, Properties and Synthesis of Ceramic Oxides.* 2nd ed.1998: Wiley-VCH.373.

38. Yakel, H.L., *On the structures of some compounds of the perovskite type.* Acta Crystallographica, 1955. **8**(7): p. 394-398.

39. de al Calle, C., Aguader, A., Alonso, J.A. and Fernandez-Diaz, M.T., *Correlation between reconstructive phase transitions and transport properties from $SrCoO_{2.5}$ brownmillerite: A neutron diffraction study.* Solid State Sciences, 2008. **10**(12): p. 1924-1935.

40. Wang, F., Zhou, Q.J., He, T.M., Li, G.D. and Ding, H., *Novel $SrCo_{1-y}Nb_yO_{3-\delta}$ cathodes for intermediate-temperature solid oxide fuel cells*. Journal of materials Chemistry, 2010. **195**(12): p. 3772-3778.

41. Tarancon, A., Skinner, S.J., Chater, R.J., Hernandez-Ramirez, F. and Kilner, J.A., *Layered perovskites as promising cathodes for intermediate temperature solid oxide fuel cells.* Journal of Materials Chemistry, 2007. **17**(30): p. 3175-3181.

42. Plonczak, P., Gazda, M., Kusz, B. and Jasinski, P., *Fabrication of solid oxide fuel cell supported on specially performed ferrite-based perovskite cathode.* Journal of Power Sources, 2008. **181**(1): p. 1-7.

43. Shimakawa, Y., *A-site-ordered perovskites with intriguing physical properties.* Inorganic Chemistry, 2008. **47**(19): p. 8562-8570.

44. Qui, L., Ichikawa, T., Hirano, A., Imanishi, N. and Takeda, Y., *$Ln_{1-x}Sr_xCo_{1-y}Fe_yO_{3-\delta}$ (Ln=Pr, Nd, Gd; x=0.2, 0.3) for electrodes of solid oxide fuel cells.* Solid State Ionics, 2003. **158(**1-2): p. 55-65.

45. Tulloch, J. and Donne, S.W., *Activity of perovskite $La_{1-x}Sr_xMnO_3$ catalysts towards oxygen reduction in alkaline electrolytes.* Journal of Power Sources, 2009. **188**(2): p. 359-366.

46. Meng, X.W., Lu, S.Q., Ji, Y., Wei, T. And Zhang, Y.L., *Characterisation of $Pr_{1-x}Sr_xCo_{0.8}Fe_{0.2}O_{3-\delta}$ (0.2≤x≤0.6) cathode materials for intermediate-temperature solid oxide fuel cells.* Journal of Power Sources, 2008. **183**(2): p. 581-585.

47. Molenda, J., Swierczek, K. and Zajac, W., *Functional materials for the IT-SOFC.* Journal of Power Sources, 2007. **173**(2): p. 657-670.

48. Housecroft, C. E. and Constable, E.C., *Chemistry*. 2 ed. 2002: Prentice Hall.

49. Tao, S.W. and Irvine, J.T.S., *A redox-stable efficient anode for solid-oxide fuel cells.* Nature Materials, 2003. **2**(5): p. 320-323.

50. Marina, O.A., Canfield, N.L. and Stevenson, J.W., *Thermal, electrical, and electrocatalytical properties of lanthanum-doped strontium titanate.* Solid State Ionics, 2002. **149**(1-2): p. 21-28.

51. Li, X., Zhao, H., Shen, W., Gao, F., Huang, X., Li, Y. and Zhu, Z., *Synthesis and properties of Y-doped $SrTiO_3$ as an anode material for SOFCs.* Journal of Power Sources, 2007. **166**(1): p. 47-52.

52. Li, X., Zhao, H., Gao, F., Chen, N. And Xu, N., *La and Sc co-doped $SrTiO_3$ as novel anode materials for solid oxide fuel cells.* Electrochemistry Communications, 2008. **10**(10): p. 1567-1570.

53. Li, X., Zhao, H., Xu, N., Zhou, X., Zhany, C. and Chen, N., *Electrical conduction behaviour of La, Co co-doped $SrTiO_3$ perovskite as anode material for solid oxide fuel cells.* International Journal of Hydrogen Storage, 2009. **34**(15): p. 6407-6414.

54. Tanaka, H. and Kawai, T., *Artificial construction of SrO/(La, Sr)MnO_3 layered perovskite superlattice by laser molecular-beam epitaxy.* Applied Physics Letters, 2000. **76**(24): p. 3618-3620.

55. Yang, L., Wang, S., Blinn, K., Liu, M., Liu, Z., Cheng, Z. and Liu, M., E*nhanced sulfur and coking tolerance of a mixed ion conductor for SOFCs: $BaZr_{0.1}Ce_{0.7}Y_{0.2-x}Yb_xO_{3-\delta}$.* Science, 2009. **326**(5949): p. 126-129.

56. Cowin, P.I., Petit, C.T.G., Lan, R., Irvine, J.T.S. and Tao, S., *Recent progress in the development of anode materials for solid oxide fuel cells.* Advanced Energy Materials, 2011. **1**(3): p. 314-332.

57. Manoharan, R. and Shukla, A.K., *Oxides supported carbon air-electrodes for alkaline-solution power devices*. Electrochimica Acta, 1985. **30**(2): p. 205-209.

58. Weidenkaff, A., Ebbinghaus, S.G., Lippert, T., Montenegro, M.J., Soltmann, C. and Wessicken, R., *Phase formation and phase transition of $Ln_{1-x}Ca_xCoO_{3-\delta}$ (Ln=La, Er) applied for bifunctional air electrodes.* Crystal Engineering, 2002. **5**(3-4): p. 449-457.

59. Kiros, Y., Myren, C., Schwartz, S., Sampathrajan, A. And Ramanathan, M. *Electrode R&D, stack design and performance of biomass alkaline fuel cell module.* International Journal of Hydrogen Energy, 1999. **24**(6): p. 549-564.

60. Hyodo, T., Hayashi, M., Mitsutake, S., Miura, N. and Yamazoe, N., *Praseodymium-calcium manganites ($Pr_{1-x}Ca_xMnO_3$) as electrode catalyst for oxygen reduction in alkaline solution.* Journal of Applied Electrochemistry, 1997. **27**(6): p. 745-746.

61. Bidault, F., Brett, D.J.L, Middleton, P.H. and Brandon, N.P., *Review of gas diffusion cathodes for alkaline fuel cells.* Journal of Power Sources, 2009. **187**(1): p. 39-48.

62. Ruddlesden, S.N. and Popper, P., *The compound $Sr_3Ti_2O_7$ and its structure.* Acta Crysallographica, 1958. **11**(1): p. 54-55.

63. Ruddlesden, S.N. and Popper, P., *New compounds of the K_2NiF_4 type.* Acta Crystallographica, 1957. **10**(8): p. 538-540.

64. McCabe, E.E. and Greaves, C., *Synthesis and structural and magnetic characterization of mixed manganese-copper n=1 Ruddlesden-Popper phases.* Chemistry of Materials, 2006. **18**(24): p. 5774-5781.

65. Amow, G. and Skinner, S.J., *Recent developments in Ruddlesden-Popper nickelate systems for solid oxide fuel cell cathodes.* Journal of Solid State Electrochemistry, 2006. **10**(8): p. 538-546.

66. Greenblatt, M., *Ruddlesden-Popper $Ln_{n+1}Ni_nO_{3n+1}$ nickelates: Structure and properties.* Current Opinion in Solid State and materials Science, 1997. **2**(2): p. 174-183.

67. Nemudry, A., Rudolf, P. and Schollhorn, R., *Room temperature topotactic oxidation of lanthanum cobalt oxide $La_2CoO_{4.0}$.* Solid State Ionics, 1998. **109**(3-4): p. 213-222.

68. Mehta, A. and Heaney, P.J., *Structure of $La_2NiO_{4.18}$.* Physical Review B, 1994. **49**(1): p. 563-571.

69. Cruz, M.M., Carvalho, M.D., Wattiaux, A., Bassat, J.M., Casaca, A., Bonfait, G., Costa, F.M.A. and Godinho, M., *Magnetic properties of lanthanum nickelates.* Physica B, 2000. **284**: p. 1477-1478.

70. Munnings, C.N., Skinner, S.J., Amow, G., Whitfield, P.S. and Davidson, I.J., *Oxygen transport in the $La_2Ni_{1-x}Co_xO_{4+\delta}$ system.* Solid State Ionics, 2005. **176**(23-24): p. 1895-1901.

71. Skinner, S.J. and Amow, G., *Structural observations on $La_2(Ni,Co)O_{4+/-\delta}$ phases determined from in situ neutron powder diffraction.* Journal of Solid State Chemistry, 2007. **180**(7): p. 1977-1983.

72. Vornin, V.I., Berger, I.F., Cherepanov, V.A., Gavrilova, L.Y., Petrov, A.N., Ancharov, A.i., Tolochko, B.P. and Nikitenko, S.G., *Neutron diffraction, synchrotron radiation and EXAFS spectroscopy study of crystal structure peculiarities of the lanthanum nickelates $La_{n+1}Ni_nO_y$ (n=1,2,3).* Nuclear Instruments and methods in Physics Research Section a-Accelerators Spectrometers Detectors and Associated Equipment, 2001. **470**(1-2): p. 202-209.

73. Amow, G., Davidson, I.J. and Skinner, S.J., *A comparative study of the Ruddlesden-Popper series, $La_{n+1}Ni_nO3_{n+1}$ (n=1,2 and 3), for solid-oxide fuel-cell cathode applications.* Solid State Ionics, 2006. **177**(13-14): p. 1205-1210.

74. Zhao, F., Wang, X.F., Wang, Z.Y., Peng, R.R. and Xia, C.R., *K_2NiF_4 type $La_{2-x}Sr_xCo_{0.8}Ni_{0.2}O_{4+\delta}$ as the cathodes for solid oxide fuel cells.* Solid State Ionics, 2008. **179**(27-32): p. 1450-1453.

75. Aikens, L.D., Gillie, L.J., Li, R.K. and Greaves, C., *Staged fluorine insertion into manganese oxides with Ruddlesden-Popper structures: $LaSrMnO_4F$ and $La_{1.2}Sr_{1.8}Mn_2O_7F$.* Journal of Materials Chemistry, 2002. **12**(2): p. 264-267.

76. Zhao, H.L., Shen, W., Zhu, Z.M., Li, X. and Wang, Z.F., *Preparation and properties of $Ba_xSr_{1-x}Co_yFe_{1-y}O_{3-\delta}$ cathode material for intermediate temperature solid oxide fuel cells.* Journal of Power Sources, 2008. **182**(2): p. 503-509.

77. Kumar, M., Srikanth, S., Ravikumar, B., Alex, T.C. and Das, S.K., *Synthesis of pure and Sr-doped $LaGaO_3$, $LaFeO_3$ and $LaCoO_3$ and SrMg-doped $LaGaO_3$ for ITSOFC application using different wet chemical routes.* Materials and Chemistry Physics, 2009. **113**(2-3): p. 803-815.

78. Fontaine, M.L., Laberty-Robert, C., Barnabe, A., Ansart, F. and Tailhades, P., *Synthesis of $La_{2-x}NiO_{4+\delta}$ oxides by polymeric route: non-stoichiometry control.* Ceramics International, 2004. **30**(8): p. 2087-2098.

79. Fontaine, M.L., Laberty-Robert, C., Pielaszeck, J., Lenormand, P., Ansart, F. and Tailhades, P., *Synthesis of $La_2NiO_{4+\delta}$ oxides by sol-gel process: Structural and microstructural evolution from amorphous to nanocrystallized powders.* Materials Research Bulletin, 2006. **41**(9): p. 1747-1753.

80. Li, C., Yu, G.Y. and Yang, N.R., *Supported dense oxygen permeating membrane of mixed conductor $La_2Ni_{0.8}Fe_{0.2}O_{4+\delta}$ prepared by sol-gel method.* Seperation and Purification Technology, 2003. **32**(1-3): p. 335-339.

81. Xu, Y.B., Huang, G.H. and Long, H., *Sol-gel synthesis of $BaTi_2O_5$.* Materials Letters, 2003. **57**(22-23): p. 3570-3573.

82. Zhu, C.J., Liu, X.M., Yi, C.S., Yan, D. and Su, W.H., *Electrochemical performance of $PrBaCo_2O_{5+\delta}$ layered perovskite as an intermediate-temperature solid oxide fuel cell cathode.* Journal of Power Sources, 2008. **185**(1): p. 193-196.

83. Lei, Z., Zhu, Q.S. and Zhao, L., *Low temperature processing of interlayer-free $La_{0.6}Sr_{0.4}Co_{0.2}Fe_{0.8}O_{3-\delta}$ cathodes for intermediate temperature solid oxide fuel cells.* Journal of Power Sources, 2006. **161**(2): p. 1169-1175.

84. Zhu, G.Y., Fang, X.H., Xia, C.R. and Liu, X.Q., *Prepartion and electrical properties of $La_{0.4}Sr_{0.6}Ni_{0.2}Fe_{0.8}O_3$ using a glycine nitrate process.* Ceramics International, 2005. **31**(1): p. 115-119.

85. Bansal, N.P. and Zhong, Z.M., *Combustion synthesis of $Sm_{0.5}Sr_{0.5}CoO_{3-x}$ and $La_{0.6}Sr_{0.4}CoO_{3-x}$ nanopowders for solid oxide fuel cell cathodes.* Journal of Power Sources, 2006. **158**(1): p. 148-153.

86. Bosomoiu, M., Bozga, G., Berger, D. and Matei, C., *Studies on combustion catalytic activity of some pure and doped lanthanum cobaltites.* Applied Catalysis B-Environmental, 2008. **84**(3-4): p. 758-765.

87. Wang, L.X. and Zhang, Q.T., *The effect of pH values on the phase formation and properties of $BaFe_{12}O_{19}$ prepared by citrate-EDTA complexing method.* Journal of Alloys and Compounds, 2008. **454**(1-2): p. 410-414.

88. Feldhoff, A., Arnold, M., Martynczuk, J., Gesing, T.M. and Wang, H., *The sol-gel synthesis of perovskites by an EDTA/citrate complexing method involves nanoscale solid state reactions.* Solid State Sciences, 2008. **10**(6): p. 689-701.

89. Chen, L.Y., Horiuchi, T. and Mori, T., *Catalytic reduction of NO over a mechanical mixture of $NiGa_2O_4$ spinel with a manganese oxide: influence of catalyst preparation method.* Applied Catalysis a-General, 2001. **209**(1-2): p. 97-105.

90. Chen, L.Y., Horiuchi, T. and Mori, T., *Catalytic reduction of NO by hydrocarbons over a mechanical mixture of spinel Ni-Ga oxide and manganese oxide.* Catalysis Letters, 1999. **60**(4): p. 237-241.

91. Cousin, P. and Ross, R.A., *Preparation of mixed oxides – A review.* Materials Science and Engineering a-Structural Materials Properties Microstructure and Processing, 1990. **130**(1): p. 119-125.

92. Han, S.H., Kim, K.S., Kim, H.G., Lee, H.G., Kang, H.W., Kim, J.S. and Cheon, C., *Synthesis and characterization of multifermic $BiFeO_3$ powders fabricated by hydrothermal method.* Ceramics International, 2010. **36**(4): p. 1365-1372.

93. Spooren, J. and Walton, R.I., *Hydrothermal synthesis of the perovskite manganites $Pr_{0.5}Sr_{0.5}MnO_3$ and $Nd_{0.5}Sr_{0.5}MnO_3$ and alkali-earth manganese oxides $CaMn_2O_4$, 4H-$SrMnO_3$, and 2H-$BaMnO_3$.* Journal of Solid State Chemistry, 2005. **178**(5): p. 1683-1691.

94. Spooren, J., Walton, R.I. and Millange, F., *A study of the manganites $La_{0.5}M_{0.5}MnO_3$ (M = Ca, Sr, Ba) prepared by hydrothermal synthesis.* Journal of Materials Chemistry, 2005. **15**(15): p. 1542-1551.

95. Stampler, E.S., Sheets, W.C., Prellier, W., Marks, T.J. and Poeppelmeier, K.R., *Hydrothermal synthesis of $LnMnO_3$ (Ln = Ho-Lu and Y): exploiting amphoterism in late rare-earth oxides.* Journal of Materials Chemistry, 2009. **19**(25): p. 4375-4381.

96. Modeshia, D.R., Walton, R.I., Mitchell, M.R. and Ashbrook, S.E., *Disordered lithium niobate rock-salt materials prepared by hydrothermal synthesis.* Dalton Transactions, 2010. **39**(26): p. 6031-6036.

97. Somiya, A., Hishinuma, K. and Akiba, T., *A new materials processing – Hydrothermal processing.* Bulletin of Materials Science, 1995. **18**(6): p. 811-818.

98. Somiya, S. and Roy, R., *Hydrothermal synthesis of fine oxide powders.* Bulletin of Materials Science, 2000. **23**(6): p. 453-460.

99. Greaves, C. and Francesconi, M.G., *Fluorine insertion in inorganic materials.* Current Opinion in Solid State and materials Science, 1998. **3**(2): p. 132-136.

100. Slater, P.R., Hodges, J.P., Francesconi, M.G., Greaves, C. and Slaski, M., *Fluorination of the Ruddlesden-Popper type cuprates, $Ln_{2-x}A_{1+x}Cu_2O_{6-y}$ (Ln = La, Nd; A = Ca, Sr).* Journal of Materials Chemistry, 1997. **7**(10): p. 2077-2083.

101. Almamouri, M., Edwards, P.P., Greaves, C. and Slaski, M., *Synthesis and superconducting properties of the strontium copper oxy-fluoride $Sr_2CuO_2F_{2+\delta}$.* Nature, 1994. **369**(6479): p. 382-384.

102. Chevalier, B., Tressaud, A., Lepine, B., Amine, K., Dance, J.M., Lozano, L., Hickey, E. and Etourneau, J., *Stabilisation of a new superconducting phase by low-temperature fluorination of La_2CuO_4.* Physica C, 1990. **167**(1-2): p. 97-101.

103. Bhat, V., Rao, C.N.R. and Hinig, J.M., *Fluorination of La_2NiO_4 and $La_2CuO_{4+\delta}$.* Solid State Communications, 1992. **81**(9) p. 751-756.

104. Case, G.S., Hector, A.L., Levason, W., Needs, R.L., Thomas, M.F. and Weller, M.T., *Syntheses, powder neutron diffraction structures and Mossbauer studies of some complex iron oxyfluorides: $Sr_3Fe_2O_6F_{0.87}$, Sr_2FeO_3F and $Ba_2InFeO_5F_{0.68}$.* Journal of Materials Chemistry, 1999. **9**(11): p. 2821-2827.

105. Slater, P.R. and Gover, R.K.B., *Synthesis and structure of the new oxide fluoride $Sr_2TiO_3F_2$ from the low temperature fluorination of Sr_2TiO_4: an example of a staged fluorine substitiution/insertion reaction.* Journal of Materials Chemistry, 2002. **12**(2): p. 291-294.

106. McCabe, E.E. and Greaves, C., *Fluorine insertion reactions into pre-formed metal oxides.* Journal of Fluorine Chemistry, 2007. **128**(4): p. 448-458.

107. Slater, P.R. and Gover, R.K.B., *Synthesis and structure of the new oxide fluoride $Ba_2ZrO_3F_2 \bullet xH_2O$ (x approximate to 0.5).* Journal of Materials Chemistry, 2001. **11**(8): p. 2035-2038.

108. Van Tendeloo, G., Antipov, E.V. and Putilin, S.N., *High-Temperature Superconductors and Novel Inorganic materials.* 1999. p. 133-138.

109. Slater, P.R., *Poly(vinylidene fluoride) as a reagent for the synthesis of K_2NiF_4-related inorganic oxide fluorides.* Journal of Fluorine Chemistry, 2002. **117**(1): p. 43-45.

110. Hyeon, K.A. and Byeon, S.H., *Synthesis and structure of new layered oxides, ($MLa_2Ti_3O_{10}$)-La-II (M = Co, Cu and Zn).* Chemistry of Materials, 1999. **11**(2): p. 352-357.

111. Toda, K., Watanabe, J. and Sato, M., *Crystal structure determination of ion-exchangeable layered perovskite compounds, $K_2La_2Ti_3O_{10}$ and $Li_2La_2Ti_3O_{10}$.* Materials Research Bulletin, 1996. **31**(11): p. 1427-1435.

112. Heap, R., *Synthesis and characterization of K_2NiF_4-related oxides and oxide fluorides.* University of Surrey, 2006. p. 209.

113. *Crystal Structure.* Cited 2011; Available from: http://cnx.org/content/m16927.

114. *Chaper 5: X-ray Generation and Powder Diffraction.* Cited 2011; Available from: http://ruby.colorado.edu/~smyth/G30105.htm.

115. Rietveld, H.M., *A profile refinement method for nuclear and magnetic structures.* Journal of Applied Crystallography, 1969. **2**: p. 65.

116. Rietveld, H.M., *Line profiles of neutron powder-diffraction peaks for structure refinement.* Acta Crystallographica, 1967. **22**: p. 151.

117. Young, R.A., *The Rietveld method.* 1993. Oxford University Press. 298.

118. Toby, B.H., *EXPGUI, a graphical user interface for GSAS.* Journal of Applied Crystallography, 2001. **34**: p. 210-213.

119. *Fitting nuclear and magnetic scattering in GSAS with a Pmmm nucleat phase and a Fmm'm' magnetic phase.* Cited 2009; Available from: http://www.ncnr.nist.gov/xtal/software/magtut/pmmm.html.

120. Cui, J., Huang, Q. and Toby, B.H., *Magnetic structure refinement with neutron powder diffraction data using GSAS: A tutorial.* Powder Diffraction, 2006. **21**(1): p. 71-79.

121. Finger, L.W., Kroeker, M. and Toby, B.H., *DRAWxtl, an open-source computer program to produce crystal structure drawings.* Journal of Applied Crystallography, 2007. **40**: p. 188-192.

122. McCusker, L.B., Von Dreele, R.B., Cox, D.E., Louer, D. and Scardi, P., *Rietveld refinement guidelines.* Journal of Applied Crystallography, 1999. **32**: p. 36-50.

123. Renishaw, *Renishaw User Manual.* 2008.

124. Pelletier, M., *Analytical Applications of Raman Spectroscopy.* 1999. Blackwell Publishing.

125. Smith, G. D. And Clark, R. J. H., *Raman microscopy in archaeological science.* Journal of Archaeological Science, 2004. **31**(8): p. 1137-1160.

126. RSC, *Introduction to Mossbauer spectroscopy.*

127. Herber, R.H., *Introduction to Mossbauer spectroscopy.* Journal of Chemical Education, 1965. **42**(4): p. 180.

128. Rietveld, G., Koijmans, C.V., Henderson, L.C.A., Hall, M.J., Hannon, S., Warnecke, P. and Schumacher, B., *DC conductivity measurements in the Van der Pauw geometry.* IEEE Transactions on Instrumentation and Measurement, 2003. **52**(2): p. 449-453.

129. Bissessur, R., White, W. and Dahn, D.C., *Electrical characterization of conductive polymers and their intercalated nanocomposites with molybdenum disulfide.* Materials Letters, 2006. **60**(2): p. 248-251.

130. Kapil, A., Taunk, M. and Chand, S., *Low temperature charge transport study in p-toluenesulfonic acid doped polyaniline.* Asian Journal of Chemistry, 2009. **21**(10): p. 138-142.

131. Marinsek, M., *Electrical conductivity of sintered LSM ceramics*. Materiali in Technologije, 2009. **42**(2): p. 79-843

132. Kissinger, P.T. and Heineman, W.R., *Cyclic Voltammetry.* Journal of Chemical Education, 1983. **60**(9): p. 702-7063

133. Mabbott, G.A., *An introduction to cyclic voltammetry.* Journal of Chemical Education, 1983. **60**(9): p. 697-702.

134. Vanbenschoten, J.J., Lewis, J.Y., Heineman, W.R., Roston, D.A. and Kissinger, P.T., *Cyclic voltammetry experiment.* Journal of Chemical Education, 1983. **60**(9): p. 772-776.

135. Brett, C.M.A. and Brett, A.M.O., *Electroanalysis.* 1998. Oxford University Press. 88.

136. Deng, X.Y., Zhang, D.Y., Wang, X., Yuan, X.X. and Ma, Z.F., *Preparation and catalytic activity of carbon nanotube-supported metallporphyrin electrocatalyst.* Chinese Journal of Catalysis, 2008. **29**(6): p. 519-523.

137. Bard, A.J. and Faulkner, L.R., *Electrochemical Methods Fundamentals and Applications.* 1980. John Wiley and Sons Inc. 718.

138. Fisher, A.C., *Electrode Dynamics.* 2006. Oxford University Press. 83.

139. Claude, E., Addou, T., Latour, J.M. and Aldebert, P., *A new method for electrochemical screening based on the rotating ring disc electrode and its application to oxygen reduction catalysts.* Journal of Applied Electrochemistry, 1998. **28**(1): p. 57-64.

140. Calderon, E.H., Wuthrich, R., Mandin, P., Foti, G. And Comninellis, C., *Estimation of the effectiveness factor of an outer-sphere redox couple (Fe^{3+}/Fe^{2+}) using rotating disk Ti/IrO_2 electrodes of different loading.* Journal of Applied Electrochemistry, 2009. **39**(8): 1379-1384.

141. Chen, R.R., Li, H.X., Chu, D. And Wang, G.F., *Unraveling oxygen reduction mechanisms on carbon-supported Fe-Phthalocyanine and Co-Phthalocyanine catalysts in alkaline solutions.* Journal of Physical Chemistry, 2009. **113**(48): p. 20689-20697.

142. Hansal, W.E.G., Tury, B., Halmdienst, M., Varsanyi, M.L. and Kautek, W., *Pulse reverse plating of Ni-Co alloys: Deposition kinetics of watts, sulfamate and chloride electrolytes.* Electrochimica Acta, 2006. **52**(3): p. 1145-1151.

143. Matter, P.H., Zhang, L. and Ozkan, U.S., *The role of nanostructure in nitrogen-containing carbon catalysts for the oxygen reduction reaction.* Journal of Catalysis, 2006. **239**(1): p. 83-96.

144. Alden, J., *Computational Electrochemistry*. 1998. Oxford University.

145. Spiegel, C. S., *Designing and building fuel cells.* 1st Edition, 2007: The McGraw Hill Companies. 434.

146. Sayers, R. and Skinner, S.J., *Evidence for the catalytic oxidation of $La_2NiO_{4+\delta}$.* Journal of Materials Chemistry, 2011. **21**(2): p. 414-419.

147. Sayers, R., De Souza, R.A., Kilner, J.A. and Skineer, S.J., *Low temperature diffusion and oxygen stoichiometry in lanthanum nickelate.* Solid State Ionics, 2010. **181**(8-10): p. 386-391.

148. Skinner, S.J., *Characterisation of $La_2NiO_{4+\delta}$ using in-situ high temperature neutron powder diffraction.* Solid State Sciences, 2003. **5**(3): p. 419-426.

149. Odier, P., Leblanc, M. and Choisnet, J., *Structural characterization of an orthorhombic form of La_2NiO_4.* Materials Research Bulletin, 1986. **21**(7): p. 787-796.

150. Read, M.S.D., Islam, M.S., Watson, G.W. and Hancock, F.E., *Surface structures and defect properties of pure and doped La_2NiO_4.* Journal of Materials Chemistry, 2001. **11**(10): p. 2597-2602.

151. Read, M.S.D., Islam, M.S., King, F. and Hancock, F.E., *Defect chemistry of $La_2Ni_{1-x}M_xO_4$ (M = Mn, Fe, Co, Cu): Relevance to catalytic behaviour.* Journal of Physical Chemistry B, 1999. **103**(9): p. 1558-1562.

152. Sayers, R., Liu, J., Rustumji, B. and Skinner, S.J., *Novel K_2NiF_4 type materials for solid oxide fuel cells: Compatibility with electrolytes in the intermediate temperature range.* Fuel Cells, 2008. **8**(5): p. 338-343.

153. Jorgensen, J.D., Dabrowski, B., Pei, S., Richards, D.R. and Hinks, D.G., *Structure of the interstitial oxygen defect in $La_2NiO_{4+\delta}$.* Physical Review B, 1989. **40**(4): p. 2187-2199.

154. Aguadero, A., Alonso, J.A., Martinez-Lopez, M.J., Fernandez-Diaz, M.T., Escudero, M.J. and Daza, L., *In situ high temperature neutron powder diffraction study of oxygen-rich $La_2NiO_{4+\delta}$ in air: correlation with the electrical behaviour.* Journal of Materials Chemistry, 2006. **16**(33): p. 3402-3408.

155. Shpanchenko, R. V., Antipov, E. V. And Kovba, L. M., *Ba_2ZrO_4 and its hydrates.* Materials Science Forum, 1993. **133-136**: p. 639-644.

156. Islam, M. S. and Darco, S., *Defect chemistry of the oxyfluoride $Sr_2CuO_2F_{2+\delta}$: Relationship to high T_c superconductivity.* Chemical Communcations, 1996. (19): p. 2291-2292.

157. Ishikawa, K., Metoki, K. and Miyamoto, H., *Orthorhombic-orthorhombic phase transitions in $Nd_2NiO_{4+\delta}$ ($0.067 \leq \delta \leq 0.224$).* Journal of Solid State Chemistry, 2009. **182**(8): p. 2096-2103.

158. Takeda, Y., Nishijima, M., Imanishi, N., Kanno, R. and Yamamoto, O., *Crystal-chemistry and transport properties of $Nd_{2-x}A_xNiO_4$ (A = Ca, Sr, or Ba, $0 \leq x \leq 1.4$).* Journal of Solid State Chemistry, 1992. **96**(1): p. 72-83.

159. Puche, R.S., Fernandez, F., Carvajal, J.R. and Martinez, J.L., *Magnetic and X-ray diffraction characterization of stoichiometric Pr_2NiO_4 and Nd_2NiO_4 oxides.* Solid State Communications, 1989. **72**(3): p. 273-277.

160. Watanabe, K., Asakawa, H., Fujinawa, G., Ishikawa, K. and Nakamura, T., *Analysis of metal-semiconductor transition of $Ln_2NiO_{4+\delta}$ (La, Pr, Nd) by Rietveld Refinement.* X-sen Bunseki no Shinpo, 1998. **29**: p. 137-152.

161. Mesguich, D., Bassat, J.M., Aymonier, C. and Djurado, E., *Nanopowder synthesis of the SOFC cathode materials $Nd_2NiO_{4+\delta}$ by ultrasonic spray pyrolysis.* Solid State Ionics, 2010. **181**(21-22): p. 1015-1023.

162. Mauvy, F., Bassat, J.M., Boehm, E., Manaud, J.P., Dordor, P. and Grenier, J.C., *Oxygen electrode reaction on $Nd_2NiO_{4+\delta}$ cathode materials: Impedance spectroscopy study.* Solid State Ionics, 2003. **158**(1-2): p. 17-28.

163. Bednorz, J. G., Muller, K. A. And Takashige, M., *Superconductivity in alkaline earth substituted La_2CuO_{4-y}.* Science, 1987. **236**(4797): p. 73-75.

164. Radaelli, P.G., Jorgensen, J.D., Schultz, A.J., Hunter, B.A., Wagner, J.L., Chou, F.C. and Johnston, D.C., *Structure of the superconducting $La_2CuO_{4+\delta}$ phases (δ approximate to 0.08-0.12) prepared by electrochemical oxidation.* Physical Review B, 1993. **48**(1): p. 499-510.

165. Zolliker, P., Cox, D.E., Parise, J.B., McCarron, E.M. and Farneth, W.E., *Neutron and synchrotron X-ray powder-diffraction study of $La_2CuO_{4+\delta}$.* Physical Review B, 1990. **42**(10): p. 6332-6341.

166. Chevalier, B., Tressaud, A., Lepine, B., Robin, C. and Etourneau, J., *Influence of fluorine-gas treatment on the structural and physical properties of La_2CuO_4.* Journal of the Less-Common Metals, 1990. **164**: p. 832-839.

167. Briois, P., Oliveira, J.C., Lapostolle, F., Perry, F., Billard, A. And Cavaleiro, A., *Synthesis and electrical properties of $Ln_2CuO_{4+\delta}$ (Ln : Nd or La) mixed conductor sputter deposited coatings.* Ionics, 2008. **14**(5): p. 455-461.

168. Singhal, S.C., *Advances in solid oxide fuel cell technology.* Solid State Ionics, 2000. **135**(1-4): p. 305-313.

169. Francesconi, M.G. and Greaves, C., *Anion substitutions and insertions in copper oxide superconductors.* Superconductor Science and Technology, 1997. **10**(7A): p. A29-A37.

170. Laverde, M.A.U., Tellez, D.A.L. and Rao-Rojas, J., *Magnetic, electric and equilibrium properties of $YBa_2Cu_{3-x}(PO_4)_xO_{7-\delta}$ high temperature superconducting system.* Modern Physics Letters B, 2009. **23**(6): p. 807-813.

171. Sarmiento, M.P.R., Laverde, M.A.U., Lopez, E.V., Tellez, D.A.L. and Roa-Rojas, J., *Conductivity fluctuation and superconducting parameter of the $YBa_2Cu_{3-x}(PO_4)_xO_{7-\delta}$ material.* Physica B-Condensed Matter, 2007. **398**(2): p. 360-363.

172. Slater, P.R., Greaves, C., Slaski, M. and Muirhead, C.M., *Copper-oxide superconductors containing sulfate and phosphate groups.* Physica C, 1993. **208**(1-2): p. 193-196.

173. Shin, J.F., Orera, A., Apperley, D.C. and Slater, P.R., *Oxyanion doping strategies to enhance the ionic conductivity in $Ba_2In_2O_5$.* Journal of Materials Chemistry, 2011. **21**(3): p. 874-879.

174. Shin, J.F., Apperley, D.C. and Slater, P.R., *Silicon doping in $Ba_2In_2O_5$: Example of a beneficial effect of silicon incorporation on oxide ion/proton conductivity.* Chemistry of Materials, 2010. **22**(21): p. 5945-5948.

175. Shin, J.F., Hussey, L., Orera, A. and Slater, P.R., *Enhancement of the conductivity of $Ba_2In_2O_5$ through phosphate doping.* Chemical Communications, 2010. **46**(25): p. 4613-4615.

176. James, M., Cassidy, D., Wilson, K.F., Horvat, J. and Withers, R.L., *Oxygen vacancy ordering and magnetism in the rare earth stabilized from of "$SrCoO_{3-\delta}$".* Solid State Sciences, 2004. **6**(7): p. 655-662.

177. Harrison, W.T.A., Hegwood, S.L. and Jacobson, A.J., *A powder neutron-diffraction determination of the structure of $Sr_6Co_5O_{15}$, formerly described as the low-temperature hexagonal form of $SrCoO_{3-x}$.* Journal of the Chemical Society-Chemical Communications, 1995. (19): p. 1953-1954.

178. Aguadero, A., Perez-Coll, D., de la Calle, C., Alonso, J.A., Escudero, M.J. and Daza, L., *$SrCo_{1-x}Sb_xO_{3-\delta}$ perovskite oxides as cathode materials in solid oxide fuel cells.* Journal of Power Sources, 2009. **192**(1): p. 132-137.

179. Aguadero, A., Alonso, J.A., Perez-Coll, D., de la Calle, C., Fernández-Diaz, M.T. and Goodenough, J.B., *$SrCo_{0.95}Sb_{0.05}O_{3-\delta}$ as cathode material for high power density solid oxide fuel cells.* Chemistry of Materials, 2010. **22**(3): p. 789-798.

180. Iwasaki, K., Ito, T., Matsui, T., Nagasaki, T., Ohta, S. And Koumoto, K., *Synthesis of an oxygen nonstoichiometric $Sr_6Co_5O_{15}$ phase.* Materials Research Bulletin, 2006. **41**(4): p. 732-739.

181. Zhang, K., Ran, R., Ge, L., Shao, Z.P., Jin, W.Q. and Xu, N.P., *Systematic investigation on new $SrCo_{1-y}Nb_yO_{3-\delta}$ ceramic membranes with high oxygen semi-permeability.* Journal of Membrane Science, 2008. **323**(2): p. 436-443.

182. Aguadero, A., de la Clle, C., Alonso, J.A., Escudero, M.J., Fernandez-Diaz, M.T. and Daza, L., *Structural and electrical characterisation of the ovel $SrCo_{0.9}Sb_{0.1}O_{3-\delta}$ perovskite: Evaluation as a solid oxide fuel cell cathode material.* Chemistry of Materials, 2007. **19**(26): p. 6437-6444.

183. Zeng, P., Shao, Z., Liu, S. And Xu, Z.P., *Influence of M cations on structural, thermal and electrical properties of the new oxygen selective membrane based on $SrCo_{0.95}M_{0.05}O_{3-\delta}$ perovskite.* Seperation and Purification Technology, 2009. **67**(3): p. 304-311.

184. Nagai, T., Ito, W. and Sakon, T., *Relationship between cation substitution and stability of the perovskite structure in $SrCoO_{3-\delta}$ based mixed conductors.* Solid State Ionics, 2007. **177**(39-40): p. 3433-3444.

185. Balamurugan, S. and Takayama-Muromachi, E., *Structural and magnetic properties of high-pressure/high-temperature synthesized $Sr_{1-x}R_xCoO_3$ (R = Y and Ho) perovskites.* Journal of Solid State Chemistry, 2006. **179**(7); p. 2231-2236.

186. Roy, C. and Budhani, R.C., *Raman and infrared-active phonons in hexagonal $BaMnO_3$.* Physical Review B, 1998. **58**(13): p. 8174-8177.

187. Tichy, R.S. and Goodenough, J.B., *Oxygen permeation in cubic $SrMnO_{3-\delta}$.* Solid State Sciences, 2002. **4**(5): p. 661-664.

188. Pandey, N. and Thakur, A.K., *Studies on structural and electrical properties of $SrMnO_{3-\delta}$ prepared in oxidizing medium.* Advances in Applied Ceramics, 2010. **109**(2): p. 83-90.

189. Sondena, R., Stolen, S., Ravindran, P. And Grande, T., *Heat capacity and lattice dynamics of cubic and hexagonal $SrMnO_3$: Calorimetry and density functional theory.* Physical Review B, 2007. **75**(21): p. 214307 1-8.

190. Sacchetti, A., Baldini, M., Postorino, P., Martin, C. and Maignan, A., *Raman spectroscopy on cubic and hexagonal $SrMnO_3$.* Journal of Raman Spectroscopy, 2006. **37**(5): p. 591-596.

191. Ling, Y.H., Zhang, X.Z., Wang, S.L., Zhao, L., Lin, B. and Liu, X.Q., *A cobalt-free $SrFe_{0.9}Sb_{0.1}O_{3-\delta}$ cathode materials for proton-conducting solid oxide fuel cells with stable $BaZr_{0.1}Ce_{0.7}Y_{0.1}Yb_{0.1}O_{3-\delta}$ electrolyte.* Journal of Power Sources, 2010. **195**(20): p. 7042-7045.

192. Ryu, K.S., Lee, S.J. and Yo, C.H., *Studies of nonstoichiometry and physical properties of the perovskite $Sr_xHo_{1-x}FeO_{3-y}$ system.* Bulletin of the Korean Chemical Society, 1994. **15**(3): p. 256-260.

193. Isasi, P.H., Lopes, M.E., Nunes, M.R. and Jorge, M.E.M., *Low-temperature synthesis of nanocrystalline $Ca_{1-x}Ho_xMnO_{3-\delta}$ ($0 \leq x \leq 0.3$) powders.* Journal of Physicas and Chemistry of Solids, 2009. **70**(2): p. 405-411.

194. Ferreira, B.M., Jorge, M.E.M., Lopes, M.E., Nunes, M.R. and Pereira, M.I.D., *Properties of $Ca_{1-x}Ho_xMnO_3$ perovskite-type electrodes.* Electrochimica Acta, 2009. **54**(24): p. 5902-5908.

195. Lucas, C., Eiroa, I., Nunes, M.R., Russo, P.A., Carrott, M., Pereira, M.I.S. and Jorge, M.E.M., *Preparation and characterisation of $Ca_{1-x}Ce_xMnO_3$ perovskite electrodes.* Journal of Solid State Electrochemistry, 2009. **13**(6): p. 943-950.

196. Zhou, Q., Kennedy, B.J., Zhang, Z., Jang, L. Y. and Aitken, J. B., *X-ray absorption near edge structure and crystallographic studies of the mixed valence oxides $CaRu_{1-x}Mn_xO_3$.* Chemistry of Materials, 2009. **21**(18): p. 4203-4209.

197. Pi, L., Herbert, S., Martin, C., Maignan, A. and Raveau, B., *Comparison of $CaMn_{1-x}Ru_xO_3$ and $CaMn_{1-y}Mo_yO_3$ perovskites.* Physical Review B, 2003. **67**(2): p. 024431-7.

198. Berry, F.J., Bowfield, A.F., Coomer, F.C., Jackson, S.D., Moore, E.A., Slater, P.R., Thomas, M.F., Wright, A.J. and Ren, X., *Fluorination of perovskite-related phases of composition $SrFe_{1-x}Sn_xO_{3-\delta}$.* Journal of Physics, Condensed Matter: An Institute of Physical Journal, 2009. **21**(25): p. 943-950.

199. Berry, F.J., Ren, X.L., Heap, R., Slater, P.R. and Thomas, M.F., *Fluorination of perovskite-related $SrFeO_{3-\delta}$.* Solid State Communications, 2005. **134**(9): p. 621.624.

200. Berry, F.J., Heap, R., Helgason, O., Moore, E.A., Shim, S., Slater, P.R. and Thomas, M.F., *Magnetic order in perovskite-related $SrFeO_2F$.* Journal of Physics Condensed Matter, 2008. **20**(21): p. 21507 1-6.

201. Gallagher, P. K., Sanders, J. P., Woodward, P. M. and Lokuhewa, I.N., *Reactions within the system, 2SrCO$_3$-Fe$_2$O$_3$-Part I. CO2 atmosphere.* Journal of Therman Analysis and Calorimetry, 2005. **80**(1): p. 217-223.

202. Tsujimoto, Y., Yamaura, K., Hayashi, N., Kodama, K., Igawa, N., Matsushita, Y., Katsuya, Y., Shorako, Y., Akaogi, M. and Takayama-Muromachi, E., *Topotactic synthesis and crystal structure of a highly fluorinated Ruddlesden-Popper-type iron oxide, Sr$_3$Fe$_2$O$_{5+x}$F$_{2-x}$ (x approximate to 0.44).* Chemistry of Materials, 2011. **23**(16): p. 3652-3658.

203. Li, R.K. and Greaves, C., *Double-layered ruthenate Sr$_3$Ru$_2$O$_7$F$_2$ formed by fluorine insertion into Sr$_3$Ru$_2$O$_7$.* Physical Review B, 2000. **62**(6): p. 3811-3815.

204. Dann, S.E., Weller, M.T., Currie, D.B., Thomas, M.F. and Alrawwas, A.D., *Structure and magnetic properties of Sr$_2$FeO$_4$ and Sr$_3$Fe$_2$O$_7$ studied by powder neutron diffraction and Mossbauer spectroscopy.* Journal of materials Chemistry, 1993. **3**(12): p. 1231-1237.

205. Heap, R., Slater, P.R., Berry, F.J., Helgason, O. and Wright, A.J., *Synthesis and structural determination of the new oxide fluoride BaFeO$_2$F.* Solid State Communications, 2007. **141**(8): p. 467-470.

206. Berry, F.J., Coomer, F.C., Hancock, C., Helgason, O., Moore, E.A., Slater, P.R., Wright, A.J. and Thomas, M.F., *Structure and magnetic properties of the cubic oxide fluoride BaFeO$_2$F.* Journal of Solid State Chemistry, 2011. **184**(6): p. 1361-1366.

207. Prado, F., Mogni, L., Cuello, G. J. and Caneiro, A., *Neutron powder diffraction study at high temperature of the Ruddlesden Popper phase Sr$_3$Fe$_2$O$_{6+\delta}$.* Solid State Ionics, 2007. **178**(1-2): p. 77-82.

208. Matvejeff, M., Lehtimaki, M., Hirasa, A., Huang, Y. H., Yamauchi, H. and Karppinen, M., *New water containing phase derived from the Sr$_3$Fe$_2$O$_{7-\delta}$ phase of the Ruddlesden Popper structure.* Chemistry of Materials, 2005. **17**(10): p. 2775-2779.

209. Hyodo, T., Hayashi, M., Miura, N. and Yamazoe, N., *Catalytic activities of rare earth manganites for cathodic reduction of oxygen in alkaline solution.* Journal of the Electrochemical Society, 1996. **143**(11): p. L266-L267.

210. Poynton, S. D., Kizewski, J. P., Slade, R. C. T. and Varcoe, J. R., *Novel electrolyte membranes and non Pt catalysts for low temperature fuel cells.* Solid State Ionics, 2010. **181**(3-4): p. 219-222.

211. Porras, J. M., Keenan, P., Hancock, C. A. and Slater, P. R., *Investigation into the effect of Si doping on te performance of $Sr_{1-y}Ca_yMnO_{3-\delta}$ SOFC cathode materials.* Journal of Power Sources, Submitted.

212. Panchmatia, P. M., Orera, A., Rees, G. J., Smith, M. E., Hanna, J. V., Slater, P. R. and Islam, M. S., *Oxygen defects and novel transport mechanisms in apatite ionic conductors: Combined O^{17} NMR and modeling studies.* Angewandte Chemie- International Edition, 2011. **50**(40): p. 9328-9333.

13. List of Figures

14. List of Tables